Characterization of Perovskite Solar Cells

Pockett, Adam

Award date:
2017

Awarding institution:
University of Bath

Characterization of Perovskite Solar Cells

Adam Pockett

A thesis submitted for the degree of Doctor of Philosophy

University of Bath

Department of Chemistry

December 2016

Abstract

A range of electrical characterization techniques previously used for DSSC have been transferred to the study of planar perovskite devices. These include impedance spectroscopy (EIS), intensity modulated photovoltage spectroscopy (IMVS) and open-circuit voltage decay measurements (OCVD). An investigation into the observed response from these measurements has been carried out in order to gain a deeper understanding of device operation.

Multiple processes with time constants on the microsecond, millisecond and second timescale were observed. The complimentary frequency and time domain techniques have been employed, showing excellent agreement between the two types of measurement.

The high frequency (microsecond) process was found to be purely electronic in nature, which was linked to recombination. The geometric capacitance was shown to dominate this response, with accumulation of charge in the planar perovskite layer not observed.

The lower frequency (millisecond and second timescale) processes were found to be linked to the coupling between recombination and the movement of ions. The low frequency EIS and IMVS measurements revealed that the recombination resistance was frequency dependent. The rate of change of the recombination resistance was found to be linked to the diffusion of ionic species. Activation energies for these processes were obtained (E_A=0.55-0.66 eV) and shown to be in good agreement to computationally calculated values from literature for iodide vacancy migration.

The same slow processes were also studied in the time domain using open-circuit photovoltage rise and decay measurements from well-defined equilibrium conditions. Comparable activation energies were also found using these techniques. The vacancy defect concentration was calculated to be 3×10^{19} cm^{-3}, which is high enough for ionic double layers at the contacts to completely screen the built-in voltage across the perovskite at equilibrium in the dark. The slow dynamic processes observed under illumination or applied bias are therefore due to the rearrangement of ions in response to a changing electric field. As this rearrangement occurs, the rate of recombination is altered.

Declaration of work done in conjunction with others

The solar cell devices studied in this work were made at the University of Oxford by Giles Eperon and Nobuya Sakai under the supervision of Professor Henry Snaith.

The modelling of the perovskite cell capacitance was performed by Timo Peltola under the supervision of Professor Alison Walker at the University of Bath. The result of this calculation has been presented in Chapter 4 to aid with the discussion of experimental results, and the full calculation has been included in Appendix A for clarity.

The equation for the OCVD lifetime for bimolecular recombination (Chapter 6) was derived by Professor Laurie Peter. The full derivation is shown in the Appendix B.

Acknowledgements

Firstly I would like to thank my main supervisor Dr Petra Cameron. Her supervision over the course of this work has helped to guide the work and understand the results. None of this would have been possible without her guidance. I also have to thank my second supervisor Professor Alison Walker, and her group, for helpful discussions in understanding the underlying device physics.

I was fortunate to have the input of Professor Laurie Peter throughout this work.

I would like to thank Giles Eperon and Nobuya Sakai, and their supervisor Professor Henry Snaith, for supplying the perovskite cells for this study.

My thanks also go to the entire Petra Cameron group, from the people who first helped me when I joined to the newer members who I hope I was able to pass some useful skills onto.

I also have to thank my family, especially my wife Charlotte, in case they read this and wonder why I have left them out. I'm not usually one for expressing emotions, but their support definitely helps.

Contents

1 Introduction

1.1 Global energy crisis

A strong case can be made for issues related to "energy" being amongst the most serious problems facing the world today. Indeed, it has recently been included by the United Nations as one of the top sustainable development targets for the next 15 years[1]. On closer inspection, the topic of energy can be related to many other broader issues. Whether that be the availability of clean drinking water and food, the destruction of ecosystems, economic growth, conflict or climate change; the production, distribution and usage of energy is fundamental.

Perhaps the most direct link can be made between energy usage and climate change. Since the commencement of the industrial revolution in the 18th century anthropogenic greenhouse gas levels have risen dramatically. Corresponding trends in average global temperature, sea levels and snow coverage have also been observed. It has been determined, with a high level of certainty, that the greatest contributor to this climate change is due to the burning of fossil fuels for energy generation[2]. Add to this the significant global dependence on fossil fuels, a finite resource, for energy production and it is apparent that there is or soon will be a global energy crisis.

This clearly highlights the need to find alternative methods for producing energy from clean, renewable sources. There are a variety of methods for potentially achieving this, each with a number of technical challenges that require a great deal of research and development before commercially viable solutions can be implemented. It is quite likely that several technologies will have to be synchronized in order to achieve continuous and uninterrupted energy supply, and this is likely to depend upon specific geographical location.

1.2 The case for solar power

The fundamental driving force behind most natural processes on Earth is the Sun. It is therefore an obvious source from which to try to artificially extract heat or light energy and convert it to a useable form. This can include growing biomass via photosynthesis which can be burnt to release heat, exploiting the potential energy of large volumes of water to drive hydroelectric turbines, and harnessing wind as a result of the differential heating of the atmosphere.

A more direct approach is to convert the light energy incident on a material to electricity using photovoltaics. In principal, this requires lower arable land usage, less infrastructure and a reduced visual impact than many of the other renewable technologies. It is also suited to developing regions of the world, such as Africa, where the growing of energy crops or the utilization of hydroelectricity or wind power is not as feasible. In theory it is possible to generate electricity at the point of use, with solar panels mounted on buildings, thus minimizing losses associated with long range distribution of power.

Of course there are still a number of issues that must be addressed with solar and other renewable energy technologies. These include the incorporation of several technologies to eliminate potential shortfalls such as in higher latitudes where solar insolation is lower. Energy storage is also another challenge that must be overcome to help deal with the inherent intermittency of solar power; i.e. generation only during daytime, but power used at night.

What is clear is that solar power has the theoretical potential to supply much of the world's energy demand[3], as shown in Figure 1-1. In fact, relatively small areas of land would have to be covered in solar panels in order to produce enough electricity to satisfy the global demand, particularly if this was done in desert regions. In practice it would be more sensible to produce this power nearer to where it is utilized, but it nevertheless highlights the potential of solar power.

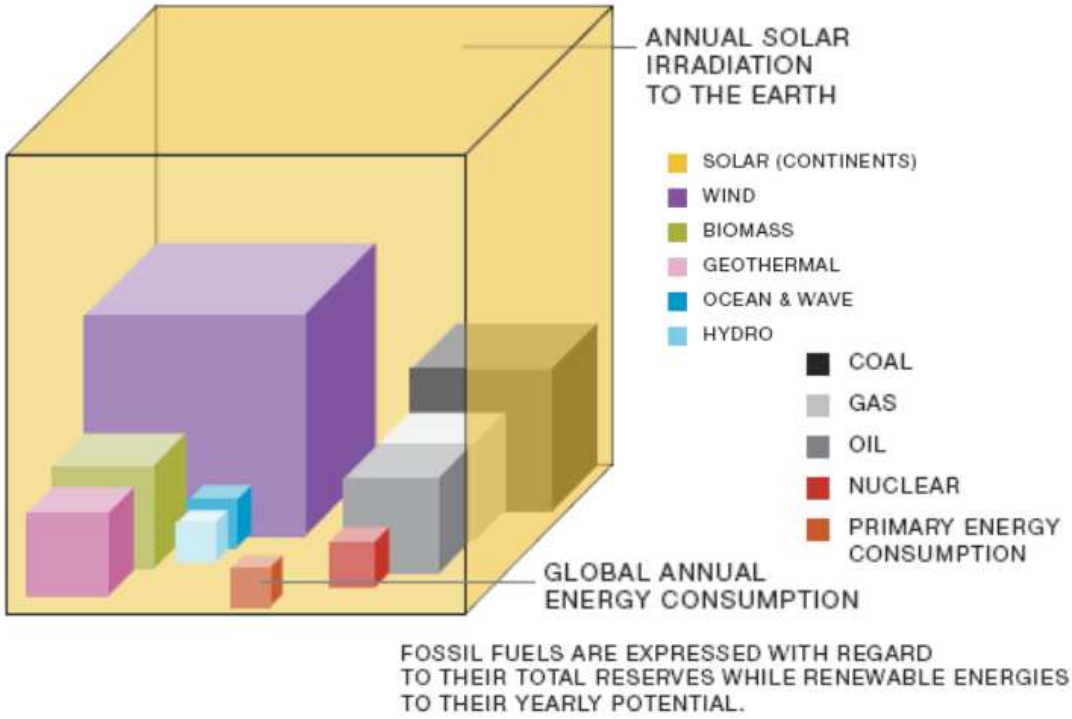

Figure 1-1: Typical renewable energy generation potential figures[3].

As with all technologies there is a never ending search for continued efficiency improvement with regards to solar cell light to electricity conversion efficiency. This will help reduce the area required for solar cells as well as help to bring down costs on a price per unit of energy basis.

1.3 Solar cell history

1.3.1 First-generation solar cells

The prospect of large-scale electricity generation from solar photovoltaics has been imagined since the 1950s[4]. For several decades the research focus has been on silicon technologies, with initial development helped in part by the interest in solar cell use in the space programme. The typical device structure of a silicon solar cell is that of a pn-junction, formed from n-type and p-type doped silicon regions. Today silicon dominates the commercial solar energy generation market with over an 80% share. In recent years there has been a rapid decline in the cost of silicon PV, largely due to oversupply from China. The price of modules has decreased from around $2.00 /watt in 2010, to approximately $0.50 /watt in 2013[5]. This makes it increasingly difficult for new and emerging technologies to compete.

Crystalline silicon PV cells have a record efficiency of over 25%[6, 7]. This corresponds to real-world module efficiencies of around 21-22%[8]. Despite achieving high efficiencies crystalline silicon solar cells are expensive owing to the high-grade silicon required, which is produced via an energy intensive process. Crystalline silicon modules lend themselves well to rooftop applications where area is restricted and the high cost is offset by the need for maximum power production.

For utility based PV applications (solar farms) area is not usually such a limiting factor and it is more cost effective to utilise cheaper panels with a slightly lower efficiency. In this case it is often panels made from multi-crystalline silicon. These are capable of achieving efficiencies of 15-17% and are 40-50% cheaper than crystalline devices[5]. Lab based multi-crystalline silicon cells have reached efficiencies of 20.4%. The record efficiencies for crystalline and multi-crystalline silicon cells were obtained in 1999 and 2004 respectively[9]. This indicates that research into silicon cell technologies is no longer focused on improving absolute efficiency. However, module efficiencies continue to be improved, closing the gap to the cell record efficiencies.

1.3.2 Second-generation solar cells

Silicon is certainly not an ideal solar PV material owing to its indirect band gap. Its consequent low absorption coefficient means that layers of the order of ~100 μm are required to obtain sufficient light absorption. An alternative to this large quantity use of material are second-generation solar cells, otherwise known as thin film solar cells. These utilise films, of the order of ~1 μm thick, of materials with good photovoltaic properties, including cadmium telluride (CdTe) and copper indium gallium selenide (CIGS).

Cadmium telluride PV is the second largest commercial technology after silicon. Device structure is based on pn-junction architecture, with a thin cadmium sulphide layer to act as the n-type material. With device efficiencies approaching that of silicon modules, it has become commercially viable particularly when temperature effects are taken into account. CdTe has a temperature coefficient approximately half that of silicon. This means that at an operating temperature of 65 °C CdTe would suffer a relative efficiency loss of approximately 8.4%, whereas for silicon this loss would be around 18%[10]. As the efficiency of CdTe modules is around 14% this means that in operation it would have an efficiency of approximately 12.8%. A silicon cell of 16% standard efficiency would have a similar efficiency. In warm climates with high solar irradiances the temperature of a panel can far exceed this example making CdTe potentially more efficient than silicon alternatives.

1.3.3 Third-generation solar cells

The definition of third-generation solar cells is broad, encompassing a wide range of different technologies. Most commonly it refers to organic, quantum dot and dye-sensitized solar cells but can also include multi-junction solar cells. There has been limited commercial success of third-generation solar cells with dye sensitized solar cells perhaps being the most successful to date, although a number of promising alternatives are beginning to emerge.

First created in the early 1990s, dye-sensitized solar cells operate via a biomimetic process that can be likened to photosynthesis[11, 12]. Visible light is absorbed by dye molecules that sensitize a wide-bandgap semiconductor. To increase light absorption this semiconductor is in the form of mesoporous titanium dioxide (typically around 10 microns thick) to give a high surface area for dye molecules to be adsorbed to its surface. Common dyes are ruthenium based metal complexes which are adsorbed onto the TiO_2 nanoparticle surface through carboxylate groups. Stimulated electrons in the dye are rapidly injected into the conduction band of the mp-TiO_2, through which they diffuse to the electrode contact (Figure 1-2). Oxidised dye molecules are regenerated by a redox electrolyte, most commonly in the form of an iodide-triiodide redox couple in an organic solvent. More recently record efficiencies have been obtained using cobalt (III/II) redox complexes which have more favourable redox potentials resulting in higher open-circuit voltages[13]. Dye cells typically also contain a dense TiO_2 layer underneath the mesoporous layer to act as a blocking layer to recombination of electrons in the FTO substrate with triiodide in the electrolyte.

DSSC device efficiencies have reached 14% for lab based tests[14]. Whilst these are relatively low compared to that of silicon devices, DSSCs do present a number of advantages. They can be produced using low-cost, abundant materials, using roll-to-roll processing on flexible substrates, and also have very good response in diffuse light conditions due to the scattering nature of the porous film. However, the main factor limiting scale-up has been their instability. This is mainly associated with the use of a liquid electrolyte. The redox species is corrosive to sealing materials, and the volatile solvent is prone to leaking. Ingress of water also substantially effects performance. Attempts have been made to create DSSCs using a solid state "electrolyte". Essentially this needs to be a hole transport material to reduce the dye molecules before they degrade. The best results have been obtained using a heavily

doped organic hole-conducting material, Spiro-OMeTAD[15]. However, device efficiencies have so far failed to exceed 8%, largely due to issues regarding the thickness of the titania layer. An optimum thickness of 2 μm has been suggested for efficient hole transport in solid state cells, but this greatly limits light absorption[16].

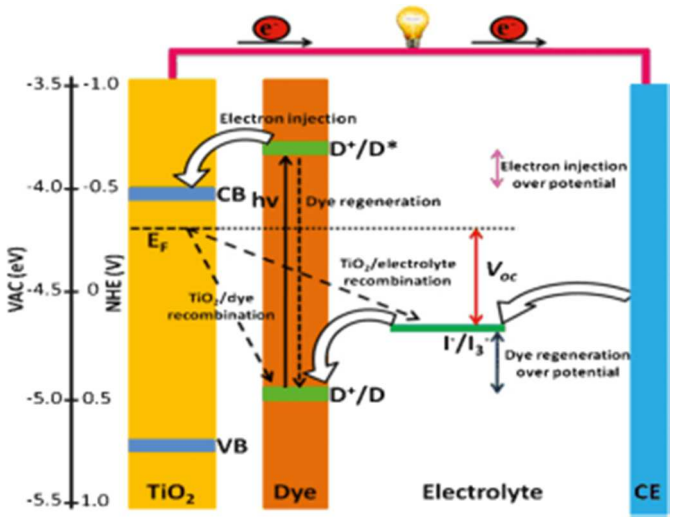

Figure 1-2: Energy level diagram of a liquid DSSC showing main transport and recombination pathways[17].

1.4 Perovskite solar cells

In the past few years a new class of material for solar photovoltaics has emerged known as perovskite solar cells. Initially the perovskite material was incorporated into the familiar dye-sensitized solar cell device architecture with efficiencies quickly bettering those of conventional solid state dye cells[18]. Efficiencies have now surpassed 20%, far exceeding that of DSSC and rivalling other thin film technologies such as CdTe and CIGS, as shown in Figure 1-3[7]. The ability to produce highly efficient solar cells via a straight forward solution based method, using low cost materials may make it possible for perovskite solar cells to become commercially viable.

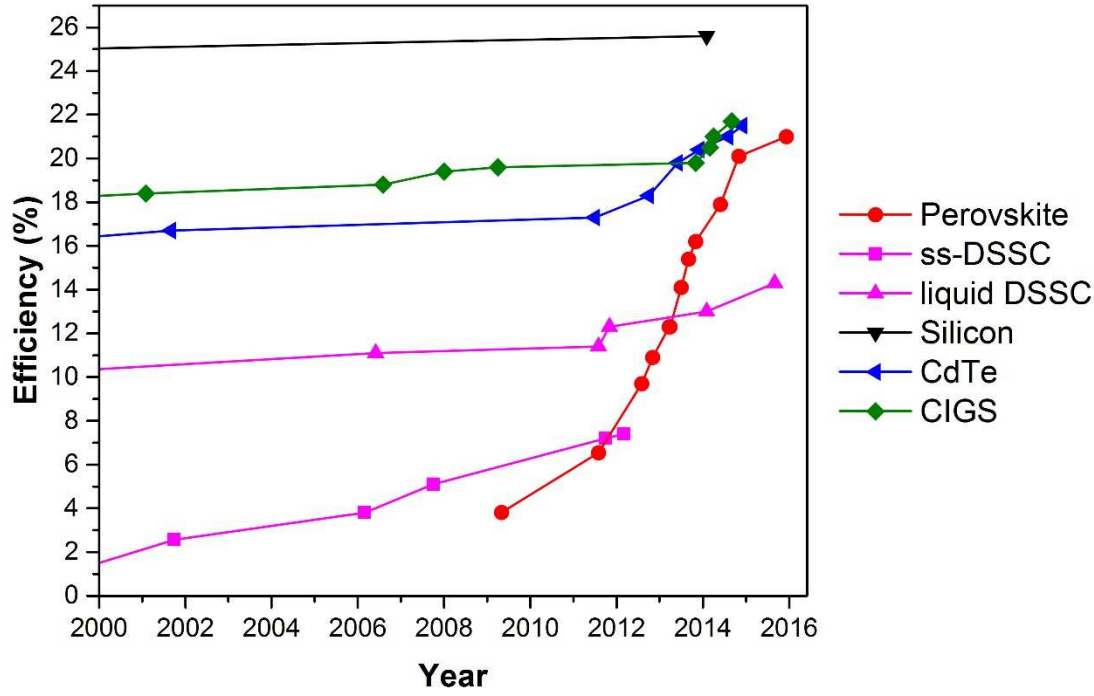

Figure 1-3: Solar cell efficiency progress showing the rapid improvement in perovskite cell efficiencies.

'Perovskite' refers to the crystal structure of the materials used. It refers to a material with a crystal structure comparable to the archetypal perovskite calcium titanate, $CaTiO_3$. They have a general formula of ABX_3, with a structure of corner sharing BX_6 octahedra with the A cation positioned in the centre of the unit cell as shown in Figure 1-4. In the case of perovskite materials for solar cells, the A cation is typically a methylammonium ion, B is lead, and X is a halide. Methylammonium lead iodide is a direct bandgap semiconductor, with an energy bandgap of around 1.55eV

making it an efficient absorber of light across the visible spectrum. Herein, 'perovskite' will generally refer to methylammonium lead iodide, $CH_3NH_3PbI_3$.

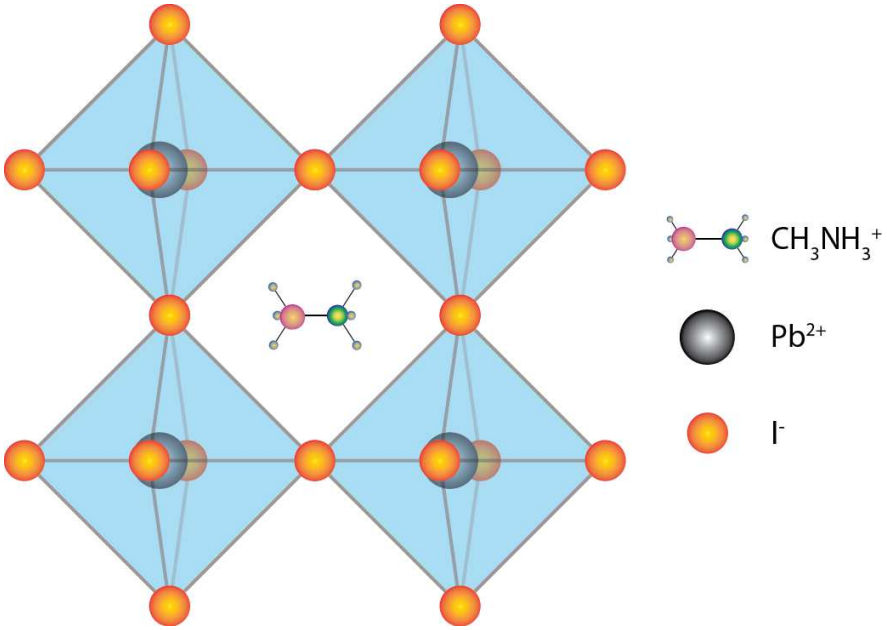

Figure 1-4: Perovskite structure of methylammonium lead iodide.

1.4.1 Initial perovskite solar cells

Initial research into organometallic perovskite materials for applications in optoelectronic devices was carried out over 10 years ago[19], but their first use in solar cells was as recent as 2009[20]. Kojima et al. demonstrated the use of both methylammonium lead iodide and bromide as sensitizers in a dye cell with a mesoporous titania thickness of 10 µm and a liquid iodide-triiodide electrolyte. The perovskite was deposited onto the TiO_2 by spin coating a DMF solution containing methylammonium halide and lead halide. Efficiencies of up to 3.8% were achieved for $CH_3NH_3PbI_3$, with a high photovoltage of 0.96 V measured for the $CH_3NH_3PbBr_3$ perovskite. These devices were very unstable due to dissolution of the perovskite in the liquid electrolyte. The method of perovskite deposition on the TiO_2 employed by Kojima still forms the basis for many of today's devices. Im et al. constructed devices in a similar fashion, with a TiO_2 thickness of 3.6 µm, and achieved efficiencies of around 6.5%[21].

An inorganic perovskite, $CsSnI_3$, has been used as the hole transport material in dye cells incorporating the common ruthenium sensitizer N719. The device configuration

was identical to that used in liquid dye cells, simply with the electrolyte replaced with the solid state perovskite. A device efficiency of 8.51% was recorded, which exceeds all other efficiencies for solid state dye cells achieved[18]. Despite this promising result, the study of tin based perovskites has been hampered due to their instability[22].

The first use of a methylammonium lead halide perovskite in a solid state cell was not reported until late 2012, and the subsequent rate of improvement can be seen in Figure 1-3. A number of different device architectures were reported at the time, but all demonstrated surprisingly high performance. The perovskite can be seen to act as a very efficient light absorber as the mesoporous layer thickness was generally reduced to a few hundred nanometres. The sensitization of TiO_2 with $CH_3NH_3PbI_3$ using spiro-OMeTAD as the hole transporter (see Figure 1-5 for device architecture), resulted in an efficiency of over 9%[23]. Interestingly, the same configuration without a hole transport material was shown to still give a very good efficiency of 5.5%[24]. This showed that the perovskite is able to transport holes as well as simply acting as a sensitizer.

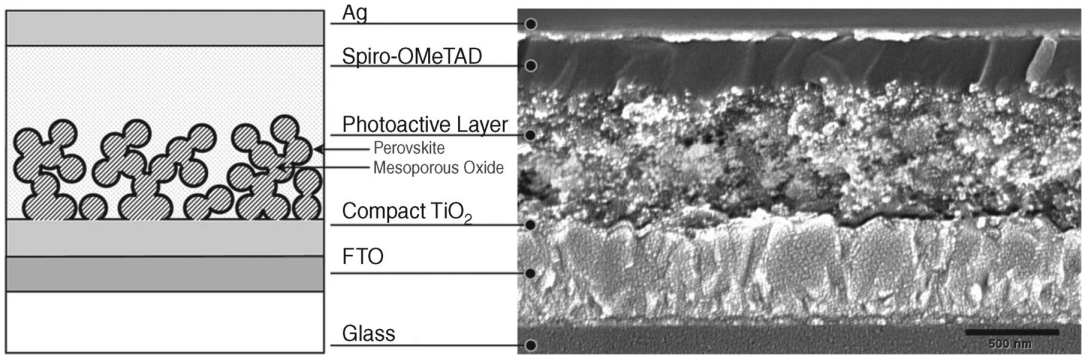

Figure 1-5: Device architecture and cross-sectional SEM image for a mesoporous oxide based perovskite solar cell using spiro-OMeTAD as the hole transport material[25].

A significant finding was made by Lee et al. in that the use of a TiO_2 mesoporous layer was not needed in order to achieve efficient performance[25]. The titania layer was replaced with an insulating mesoporous Al_2O_3 layer in devices using a $CH_3NH_3PbI_{3-x}Cl_x$ perovskite. The higher conduction band of Al_2O_3 does not allow injection of electrons from the perovskite. The transport of the electrons must then be through the perovskite, with the charge collected in the underlying compact TiO_2 layer[25]. These devices exhibited efficiencies of over 10%. This signified the first major step away from the dye-sensitized solar cell, as the perovskite can no longer be thought of as a sensitizer.

Another significant improvement in device efficiency was made when forming the perovskite using a sequential deposition method, resulting in a 14.1% efficiency[26]. Lead iodide was first introduced into a mesoporous TiO_2 film, before being briefly dipped into a dilute CH_3NH_3I solution. The perovskite forms quickly, with the increase in performance associated with improved perovskite morphology as a result of forming the perovskite within the pores.

This influence of perovskite morphology is further evidenced in planar junction cells in which no mesoporous layer is used. As the perovskite has a very high absorption coefficient, the increased surface area of a mesoporous structure is not required. A high film coverage however is necessary. Spin coating of the perovskite often leads to films with numerous pin-holes which can lead to shorting of the device. In order to produce films with greater surface coverage, evaporation of the perovskite precursor materials onto the substrate has been employed[27]. These $CH_3NH_3PbI_{3-x}Cl_x$ planar devices have reached efficiencies of 15.4%. These devices indicate a significant shift away from DSSC architecture and operating principles, so much so that perovskite solar cells must be thought of as a new class of photovoltaics, perhaps having more in common with other p-i-n junction devices.

The use of the chloride "doped" perovskite initially resulted in better performance than for the iodide alone. It is produced by mixing CH_3NH_3I and $PbCl_2$ in a 3:1 molar ratio as the perovskite precursor solution. The iodide perovskite has generally been formed from equimolar mixing of CH_3NH_3I and PbI_2. The actual mechanism for the effect of Cl doping is not well defined, although it does appear that it is not incorporated into the perovskite lattice[28], unlike for bromide ions[29]. There is very little change in bandgap between the iodide perovskite and chloride incorporated perovskite. The improvements seen due to the use of the chloride are largely thought to be related to the improved perovskite crystallisation process rather than an actual doping effect[28].

Efficiencies of over 15% were achieved within one year of the first solid-state perovskite device. However, understanding of the device operation lagged far behind.

1.4.2 Further developments

A number of different device architectures are common in perovskite solar cells. These include the mesoporous TiO_2/Spiro devices that are derived from solid state DSSC. It is also possible to produce highly efficient cells in a planar device structure by contacting a thin film of perovskite with electron (n-type) and hole (p-type) selective contacts. The perovskite is considered to act as an essentially intrinsic semiconductor[30, 31], giving a p-i-n device configuration. Common selective contacts for these devices are compact TiO_2/Spiro and PCBM/PEDOT:PSS. Initial reports suggested that planar cells could only be produced using the mixed halide perovskite precursor. The measured diffusion lengths in the chloride-containing film were 10 times greater than for the iodide alone[32]. However, using various deposition techniques it is possible to deposit high quality films of the chloride-free triiodide perovskite that perform just as well.

The basic structure of a planar perovskite cell with compact TiO_2/Spiro selective contacts is illustrated in Figure 1-6. As will be shown in this thesis the energy level profile of this type of cell is complicated by slow dynamic effects.

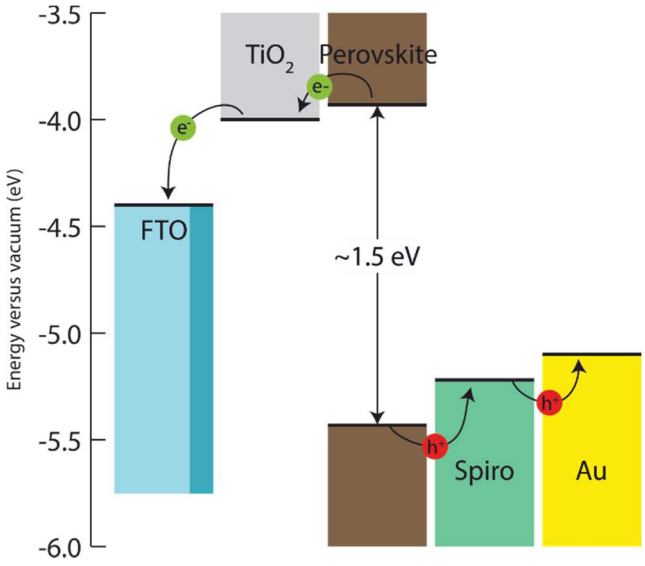

Figure 1-6: Simplified energy level diagram of a planar perovskite cell.

These slow effects were first observed as hysteresis in the current voltage curve when measuring the devices efficiency[33]. This leads to uncertainty in the cells performance characteristics depending on the measurement profile employed. This effect will be discussed in the next chapter, and the investigation into the origins of these slow processes is the main focus of this thesis.

1.5 References

1. United Nations, *General Assembly*, 2015.
2. W. Collins, R. Colman, J. Haywood, M. R. Manning and P. Mote, *Scientific American*, 2007, **297**, 64-73.
3. European Photovoltaic Industry Association *Solar Generation 6*, 2011, 14.
4. F. Daniels, in *The New York Times*, March 18 edn., 1956.
5. Seeking Alpha, *How First Solar Will Win In The Solar Market*, http://seekingalpha.com/article/1889311-how-first-solar-will-win-in-the-solar-market?source=google_news, Accessed Nov 2016.
6. J. Zhao, A. Wang, M. A. Green and F. Ferrazza, *Appl. Phys. Lett.*, 1998, **73**, 1991-1993.
7. M. A. Green, K. Emery, Y. Hishikawa, W. Warta and E. D. Dunlop, *Progress in Photovoltaics: Research and Applications*, 2016, **24**, 905-913.
8. SunPower Corporation, Analyst Day report, 2013.
9. M. A. Green, K. Emery, Y. Hishikawa, W. Warta and E. D. Dunlop, *Progress in Photovoltaics: Research and Applications*, 2013, **21**, 827-837.
10. D. P. A. Virtuani, G. Friesen, in *25th European Photovoltaic Solar Energy Conference and Exhibition*, Valencia, Spain, 2010, pp. 4248 - 4252.
11. N. Vlachopoulos, P. Liska, J. Augustynski and M. Graetzel, *J. Am. Chem. Soc.*, 1988, **110**, 1216-1220.
12. B. O'Regan and M. Grätzel, *Nature*, 1991, **353**, 737-740.
13. J.-H. Yum, E. Baranoff, F. Kessler, T. Moehl, S. Ahmad, T. Bessho, A. Marchioro, E. Ghadiri, J.-E. Moser, C. Yi, M. K. Nazeeruddin and M. Grätzel, *Nat Commun*, 2012, **3**, 631.
14. K. Kakiage, Y. Aoyama, T. Yano, K. Oya, J.-i. Fujisawa and M. Hanaya, *Chem. Commun.*, 2015, **51**, 15894-15897.
15. J. Burschka, A. Dualeh, F. Kessler, E. Baranoff, N.-L. Cevey-Ha, C. Yi, M. K. Nazeeruddin and M. Grätzel, *J. Am. Chem. Soc.*, 2011, **133**, 18042-18045.
16. H. J. Snaith and L. Schmidt-Mende, *Adv. Mater.*, 2007, **19**, 3187-3200.
17. J. Theerthagiri, A. R. Senthil, J. Madhavan and T. Maiyalagan, *ChemElectroChem*, 2015, **2**, 928-945.
18. I. Chung, B. Lee, J. He, R. P. H. Chang and M. G. Kanatzidis, *Nature*, 2012, **485**, 486-489.
19. D. B. Mitzi, in *Prog. Inorg. Chem.*, John Wiley & Sons, Inc., 2007, pp. 1-121.
20. A. Kojima, K. Teshima, Y. Shirai and T. Miyasaka, *Journal of the American Chemical Society*, 2009, **131**, 6050-6051.
21. J.-H. Im, C.-R. Lee, J.-W. Lee, S.-W. Park and N.-G. Park, *Nanoscale*, 2011, **3**, 4088-4093.

22. C. C. Stoumpos, C. D. Malliakas and M. G. Kanatzidis, *Inorg. Chem.*, 2013, **52**, 9019-9038.

23. H.-S. Kim, C.-R. Lee, J.-H. Im, K.-B. Lee, T. Moehl, A. Marchioro, S.-J. Moon, R. Humphry-Baker, J.-H. Yum, J. E. Moser, M. Gratzel and N.-G. Park, *Sci. Rep.*, 2012, **2**, 1-7.

24. L. Etgar, P. Gao, Z. Xue, Q. Peng, A. K. Chandiran, B. Liu, M. K. Nazeeruddin and M. Grätzel, *J. Am. Chem. Soc.*, 2012, **134**, 17396-17399.

25. M. M. Lee, J. Teuscher, T. Miyasaka, T. N. Murakami and H. J. Snaith, *Science*, 2012, **338**, 643-647.

26. J. Burschka, N. Pellet, S.-J. Moon, R. Humphry-Baker, P. Gao, M. K. Nazeeruddin and M. Gratzel, *Nature*, 2013, **499**, 316-319.

27. M. Liu, M. B. Johnston and H. J. Snaith, *Nature*, 2013, **501**, 395-398.

28. S. Colella, E. Mosconi, P. Fedeli, A. Listorti, F. Gazza, F. Orlandi, P. Ferro, T. Besagni, A. Rizzo, G. Calestani, G. Gigli, F. De Angelis and R. Mosca, *Chem. Mater.*, 2013, **25**, 4613-4618.

29. J. H. Noh, S. H. Im, J. H. Heo, T. N. Mandal and S. I. Seok, *Nano Lett.*, 2013, **13**, 1764-1769.

30. C. C. Stoumpos, C. D. Malliakas and M. G. Kanatzidis, *Inorg. Chem.*, 2013, **52**, 9019-9019.

31. A. Walsh, D. O. Scanlon, S. Chen, X. G. Gong and S.-H. Wei, *Angew. Chem. Int. Ed.*, 2015, **54**, 1791-1794.

32. S. D. Stranks, G. E. Eperon, G. Grancini, C. Menelaou, M. J. P. Alcocer, T. Leijtens, L. M. Herz, A. Petrozza and H. J. Snaith, *Science*, 2013, **342**, 341-344.

33. H. J. Snaith, A. Abate, J. M. Ball, G. E. Eperon, T. Leijtens, N. K. Noel, S. D. Stranks, J. T.-W. Wang, K. Wojciechowski and W. Zhang, *J. Phys. Chem. Lett.*, 2014, **5**, 1511-1515.

2 Theory

2.1 Hysteresis in current-voltage measurements

Hysteresis relates to the history dependent behaviour of a system under test. It is most commonly associated with ferromagnetic materials. If a ferromagnetic material is subjected to an applied magnetic field, domains within the material align. When the field is removed a significant proportion of the alignment will remain, leaving the material magnetized. This is often observed in the magnetization of iron nails. If the magnetic field is then applied in different directions the magnetization of the material changes in a way that is dependent on the previous magnetization state, creating a hysteresis loop as shown in Figure 2-1.

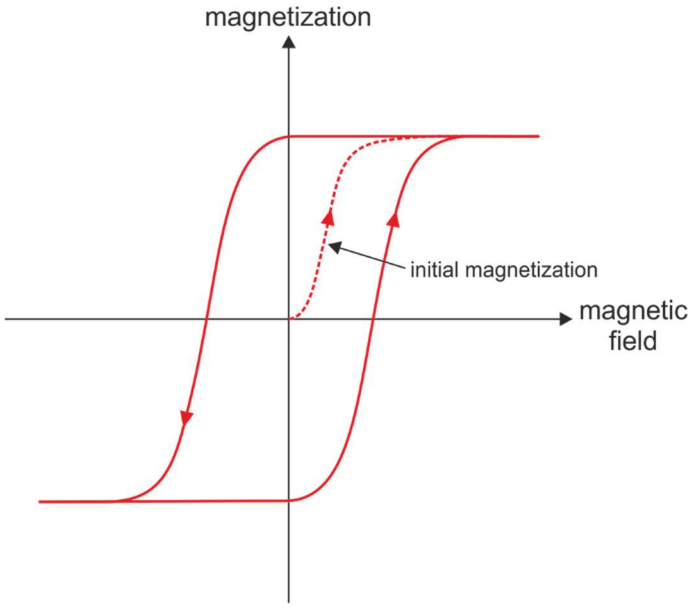

Figure 2-1: Example of a magnetic hysteresis loop for a ferroelectric material. The material is initially magnetized to a saturation value. Subsequent change in the magnetic field causes the magnetization to change relative to the previous condition (the history of system).

Similar history dependent behaviour has been observed in the measurement of solar cell current-voltage (J-V) curves. The purpose of a J-V sweep is to quickly assess the steady-state power output over a range of different bias levels. The bias is usually swept across a wide voltage range, covering at least the range from short-circuit to the open-circuit voltage. A small delay at each potential step is often incorporated to allow the current to settle to the steady state value. In theory the measured J-V curve should be independent of the sweep direction in order to be representative of steady state behaviour.

Hysteresis may occur due to the small current that arises as a result of a potential step charging certain capacitances within a cell. This current decays at the rate of the RC time constant of the cell, meaning a delay time on the order of milliseconds is often required. If the potential is swept too quickly the current can be over or underestimated depending on the direction of the potential step (sweep direction). This effect has been observed in dye-sensitized solar cells when the delay time is less than 20 ms due to the relatively large cell capacitance (long RC time constant)[1]. In order to overcome this effect the delay time should be increased to at least 5 times the RC time constant at which point the charging current should have decayed to less than 1%.

Hysteresis has been shown to be very pronounced in some perovskite solar cells[2]. The extent of the hysteresis has been shown to be highly dependent on the preconditioning of the cell as well as sweep direction and rate. This leads to uncertainty of the true steady state efficiency of the device.

The origins of this hysteresis effect in perovskite solar cells does not seem to be solely related to the cells RC time constant as in other technologies. This is evidenced by the fact that a slower sweep rate does not necessarily minimize the level of hysteresis between J-V scans in opposing directions as shown in Figure 2-2[3]. When sweeping the potential in the reverse direction (from forward bias to short circuit) the measured efficiency can be much higher than for the forward scan in the opposite direction. The main impact is a reduction in fill factor and V_{oc}. The hysteresis is shown to be most pronounced at intermediate sweep rates, although there can be a large difference in the determined cell parameters at very slow and very fast sweep rates.

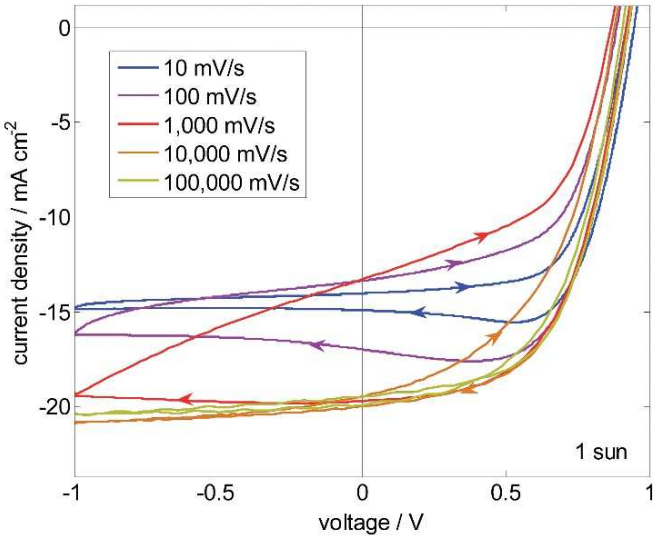

Figure 2-2: J-V sweeps under 1 sun illumination for different voltage sweep rates[3].

The observed J-V characteristics are also dependent on the cell preconditioning. Pre-biasing and/or light soaking can result in different cell responses[4-6]. In general, forward biasing of the cell or illuminating at open-circuit gives favourable effects. In the case of J-V measurements this appears to give improved charge extraction when the voltage is then swept towards short circuit[7]. These preconditioning effects have also been investigated using a range of transient measurements[3, 8, 9].

Potential sweeps with long time periods between voltage steps show that the relaxation of the current to steady state can be on the order of seconds[3, 10]. This decay appears to be too slow to be related to a purely electronic process. A number of theories as to the origin of the hysteresis have been investigated including the alignment of ferroelectric domains in the perovskite[4, 11, 12], high interfacial defect densities[13], and the movement of ionic species[14-16].

There is significant experimental evidence to suggest that hysteresis is linked to ionic migration. It has been shown that the hysteresis is strongly temperature dependent[9, 17], with rates that have been related to computationally derived activation energies for ionic migration[14, 18]. The observed hysteresis has also been simulated in models incorporating ion movement[7, 19].

Whilst clear links between J-V hysteresis and ionic migration have been found, the impact of selective contacts on hysteresis is not fully understood. It has been shown that in an inverted architecture with organic contacts, most commonly PCBM and

PEDOT:PSS, that the J-V hysteresis is significantly reduced as shown in Figure 2-3[20, 21]. Bryant et al. showed that hysteresis could be observed in these devices at low temperature[17]. Ion migration is not likely to be affected greatly by the choice of contact material. Van Reenen et al. showed that their computational model also required the inclusion of interfacial recombination via trap states in order to predict the observed hysteresis phenomenon[19]. This together with the findings of Bryant et al. suggests that interfacial recombination is significantly different between the PCBM and TiO_2 electron selective contacts that are commonly used in perovskite solar cells.

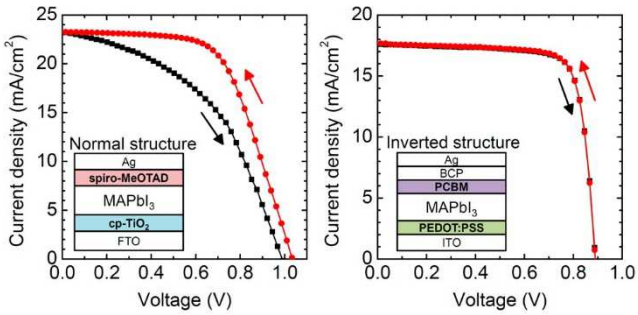

Figure 2-3: J-V curves for a planar TiO_2/Spiro and PCBM/PEDOT:PSS device showing reduced hysteresis in the organic contact cell[21].

The use of a mesoporous TiO_2 scaffold for the perovskite is also shown to reduce hysteresis[2, 22]. This could be due to the effect it has on perovskite morphology or the increased surface area for charge extraction resulting in reduced interfacial recombination rates.

Due to the uncertainty in device efficiency values obtained from cells displaying significant hysteresis, it has been suggested that the steady state power output should be obtained by maximum power point tracking[2, 6].

Slow dynamic processes are also observed in a wider range of measurement techniques including photovoltage and photocurrent transient measurements[8, 23, 24], photoluminescence[25] and impedance spectroscopy[26-29]. Clear links between these slow processes and the observed J-V hysteresis have been shown[24, 27]. It is advantageous to study the underlying mechanisms of the hysteresis process using these techniques as a more quantitative interpretation can be gathered from them. Often they are performed at a steady state with only one variable perturbed. A J-V sweep under illumination is quite a complicated system to study as it is a dynamic measurement performed with a swept voltage over time.

2.2 Mobile ionic species

The presence of ionic vacancy migration in the perovskite material is one of the most credible explanations for the observed slow dynamic behaviour of perovskite cells. The presence of mobile vacancy defects in the class of perovskite structured materials is not uncommon. Oxide perovskite materials with the general formula ABO_3 are used for applications including electrodes in solid oxide fuel cells[30-32]. Materials such as $LaBO_3$ (B=Co, Mn, Fe, etc.) are known to be mixed electronic and oxide ion conductors.

Computational calculations of the ionic vacancy formation in methylammonium lead iodide suggests high defect concentrations at room temperature. Walsh et al. calculated the formation energies for Schottky disorder defects in the perovskite[33]. They calculated a low formation energy which relates to a high vacancy concentration exceeding 10^{19} cm^{-3} at room temperature. Even with such a high vacancy concentration it appears that the defects do not directly effect electronic processes, i.e. do not act as recombination centres.

The activation energies for migration of ions via these vacancy defects have been calculated from first principles. Eames et al. showed that iodide ions are the most mobile, followed by the methylammonium cation[34]. The lead is considered to be immobile. An activation energy of 0.58 eV for iodide vacancy migration was calculated, from which a diffusion coefficient of 10^{-12} cm^2 s^{-1} was predicted. The activation energy for MA^+ migration was only slightly higher at 0.84 eV. However this was thought to be a lower limit as the MA^+ exhibits a high degree of rotation, and only the ideal migration pathway was assumed. The estimated diffusion coefficient was four orders of magnitude lower than for iodide.

The activation energy relates to the energy barrier that must be overcome for the migration of an ion to a neighbouring vacancy via a hopping mechanism. This can be determined experimentally using the Arrhenius relationship

$$k = Ae^{-E_A/RT}$$

where k is the rate constant, A is a pre-exponential factor that is related to the attempted hopping frequency, R is the gas constant and E_A is the activation energy.

This relationship can be rearranged as

$$\ln k = \ln A - \frac{E_A}{RT}$$

Which shows that a plot of ln(k) against 1/T, will have a slope $-E_A/R$ from which the activation energy can be determined. The intercept of the plot gives the attempt frequency.

There is a possibility that there are other mobile ions present in the completed perovskite cell due to processing methods and contact layers. The perovskite layer is often deposited from a mixed-halide precursor solution containing methylammonium iodide and lead chloride. This was commonly given the stoichiometry, $CH_3NH_3PbI_{3-x}Cl_x$, implying that some chloride was present in the final material. However, values of the residual chloride content remaining in the film after annealing have ranged from being undetectable to 2-5%[35, 36]. There is also the possibility of lithium ions diffusing into the perovskite from the Spiro layer, or the presence of highly mobile protons[37].

There are several reports which directly observe the effects of ionic migration. These include rapid halide ion exchange between iodide, bromide and chloride. Pellet et al. showed that when a film of $CH_3NH_3PbX_3$ (where $X=I^-$, Br^-, Cl^-) was dipped into a solution of MAX in 2-propanol (where X was a different halide ion to in the film), the film quickly converted to the other halide perovskite[38]. Hoke et al. showed reversible iodide and bromide phase segregation in mixed halide films, measuring an activation energy of 0.27 eV from the evolution of photoluminescence peaks[39]. Tracking of this process using emission and transient absorption spectroscopies shows that this process takes place on the order of seconds, which would agree with the timescales of the hysteresis effects in J-V measurements[40].

Perhaps more surprising is evidence of the organic cation being mobile. Similarly to the anion exchange experiments, it has also been found that perovskite films can be converted between the methylammonium and formamidinium lead triiodide perovskites. The time constant for this exchange was measured to be of the order of tens of minutes, from the rate of peak shifts observed in XRD measurements[41]. This finding is consistent with the lower diffusion coefficient for the organic cation, as calculated by Eames et al.

2.3 Frequency domain techniques

The frequency domain techniques used in this thesis are examples of transfer function analysis of a linear input-output system. A transfer function relates the linear output response of a system to an input stimulus, typically in the frequency domain. This type of analysis is commonly used in electrical circuit analysis.

$$\text{Transfer function} = \frac{\text{Output}}{\text{Input}}$$

A linear system has an output response that is given by a constant multiplied by the input function, i.e. the current-voltage response of a resistance given by Ohm's law, V=R×I. Many real systems have non-linear responses to input stimuli. However, the response can be linearized by making the amplitude of the stimulus small. An example of linearizing a diode current-voltage curve is illustrated in Figure 2-4.

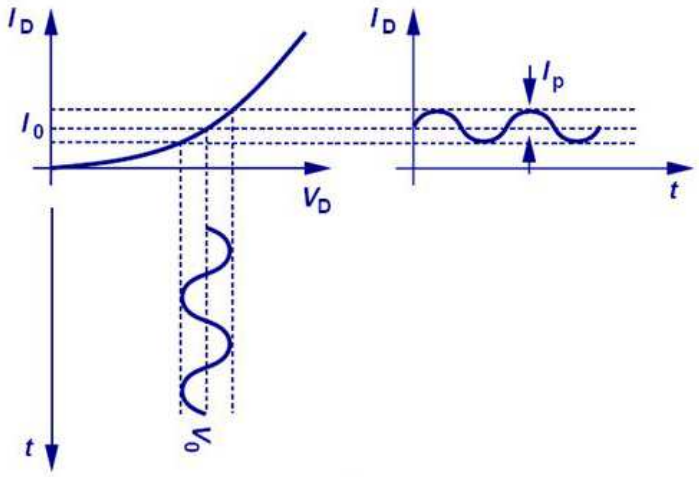

Figure 2-4: A small amplitude voltage input can linearize the response of a real system so that the input/output relationship obeys Ohm's law. The current voltage curve could relate to that of a diode.

2.3.1 Impedance spectroscopy

Impedance spectroscopy is an example of a small perturbation frequency domain technique. It has been extensively used in the characterization of a range of materials with both electronic and ionic behaviours, including solar cells[42, 43] and ceramic materials for fuel cells[44, 45]. These are complex systems that require small perturbation techniques in order to be analysed using linear functions.

In impedance spectroscopy the input signal is most commonly a small amplitude AC voltage signal superimposed on a DC offset. Typically an amplitude of around V_{rms} =10 mV is used, although this can be varied depending on the linearity of the response. The output current signal will be at the same frequency as the input signal, but may have a different amplitude and be phase shifted depending on the impedance of the system as illustrated in Figure 2-5. The impedance transfer function gives the AC form of Ohm's law, i.e. Z=V/I, where Z is the complex impedance.

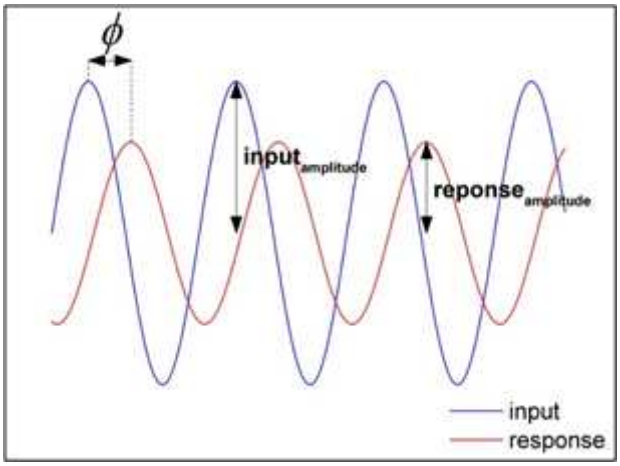

Figure 2-5: Illustration of input and output signals showing a change in amplitude and phase shift.

The sinusoidal input voltage signal can be written as

$$V = V_0 \cos(\omega t)$$

where V_0 is the amplitude, and ω is the angular frequency given by $\omega=2\pi f$, where f is the frequency.

The current response to this input signal will be

$$I = I_0 \cos(\omega t - \phi)$$

where ϕ relates to any phase shift in the output signal, and I_o is the amplitude.

It is often convenient to rewrite these equations in complex form using the Euler relationship

$$e^{j\omega t} = \cos(\omega t) + j\sin(\omega t)$$

This gives the input and output signals as

$$V = V_0 e^{j\omega t}$$
$$I = I_0 e^{j\omega t} e^{-j\phi}$$

The impedance is therefore given by

$$\begin{aligned} Z &= \frac{V}{I} \\ &= \frac{V_0}{I_0} e^{j\phi} \\ &= |Z| e^{j\phi} \end{aligned}$$

The impedance therefore relates to the magnitude of the amplitude decrease between the input and output signals, $|Z|$, and the phase shift, $e^{j\phi}$. This impedance can be represented in vector form on a Nyquist plot as shown in Figure 2-6.

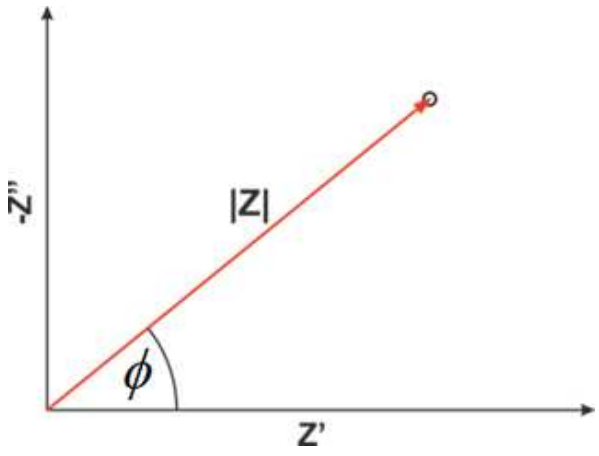

Figure 2-6: Nyquist plot of impedance transfer function.

The real and imaginary components of the impedance are represented on the Nyquist plot by Z' and Z'' respectively. These are given by

$$Z' = |Z| \cos\phi$$
$$Z'' = |Z| j \sin\phi$$

2.3.1.1 Impedance response of simple circuit elements

Systems are modelled using a combination of simple electrical components such as resistors and capacitors. These have well defined responses to AC signals. For a resistor, the AC voltage and current are in phase, $\phi = 0$, which means the impedance is given by Ohm's law

$$Z_R = \frac{V_0}{I_0} = R$$

The impedance has no imaginary component, and the magnitude of the impedance is just the resistance. This is represented on a Nyquist plot as a single point on the real axis as shown in Figure 2-7.

The current-voltage relationship for a capacitor is given by

$$\begin{aligned} Q(t) &= C \cdot V(t) \\ \int I(t)\,dt &= C \cdot V(t) \\ I(t) &= C \cdot dV(t)/dt \end{aligned}$$

For the voltage input $V = V_0 e^{j\omega t}$, the current is

$$\begin{aligned} I(t) &= C \cdot dV(t)/dt \\ &= C \cdot V_0 j\omega e^{j\omega t} \end{aligned}$$

Therefore the impedance is given by

$$\begin{aligned} Z_C &= V / I \\ &= \frac{1}{j\omega C} = -\frac{j}{\omega C} \end{aligned}$$

The impedance of a capacitor therefore has no real component. The current leads the voltage by 90°. The impedance increases with decreasing frequency, which is represented by a vertical line (at Z'=0) on the Nyquist plot (Figure 2-7).

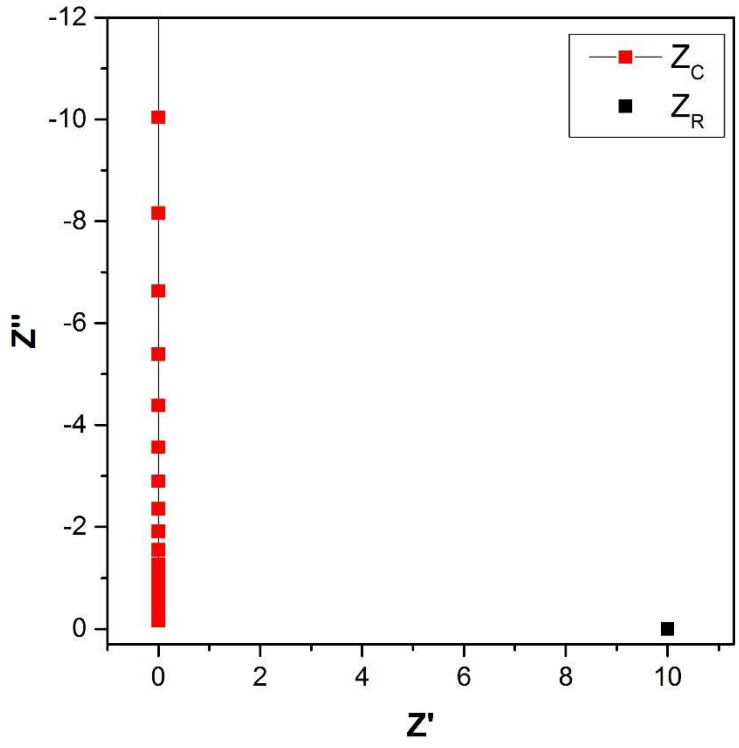

Figure 2-7: Impedance response of an individual resistor and capacitor presented on a Nyquist plot.

2.3.1.2 Impedance response of circuits

The response from combinations of these components can also be calculated. Impedance combinations are calculated in a similar way to resistor combinations.

In series

$$Z_{tot} = Z_1 + Z_2$$

and in parallel

$$\frac{1}{Z_{tot}} = \frac{1}{Z_1} + \frac{1}{Z_2}$$

The impedance response for a series connected resistor and capacitor is therefore given by

$$Z = Z_R + Z_C = R + \frac{1}{j\omega C}$$

On a Nyquist plot this is represented by the capacitor impedance response (vertical line) offset along the real axis by the resistance as shown in Figure 2-8.

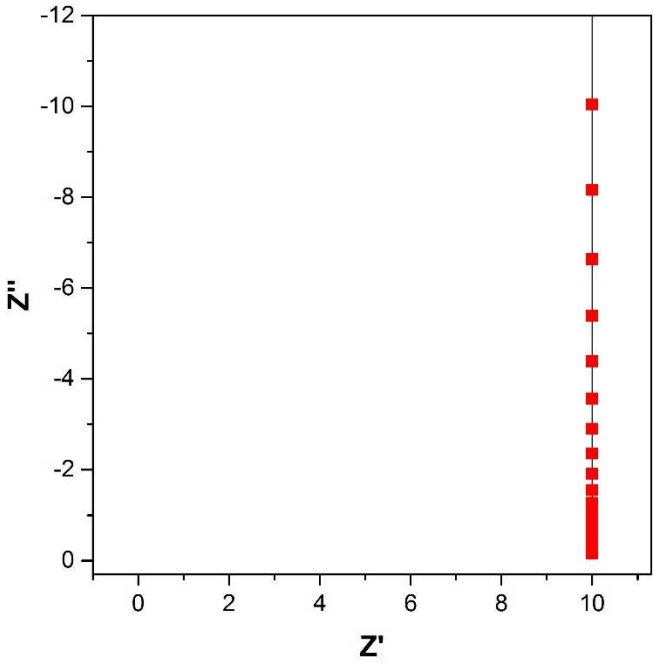

Figure 2-8: Nyquist plot of series connected RC.

The impedance of a resistor and capacitor in parallel is given by

$$Z = \frac{1}{\frac{1}{Z_R} + \frac{1}{Z_C}} = R\frac{(1 - j\omega RC)}{(1 + \omega^2 R^2 C^2)}$$

At high frequency ($\omega \rightarrow \infty$) the impedance tends to zero. The capacitor cannot charge/discharge at such high frequencies and behaves as a short-circuit. At low frequency ($\omega \rightarrow 0$), the impedance tends to R. The impedance of the capacitor becomes very large (no current flows through capacitor once fully charged) so the current flows through the resistor. The impedance response on a Nyquist plot is in the form of a semicircle, with high and low frequency real-axis intercepts at 0 and R. At the particular frequency, ω^{-1}=RC; Z' = R/2 and Z'' = -R/2, which relates to the maximum point of the semicircle. This is known as the characteristic frequency and gives what is called the 'RC time constant' of the system.

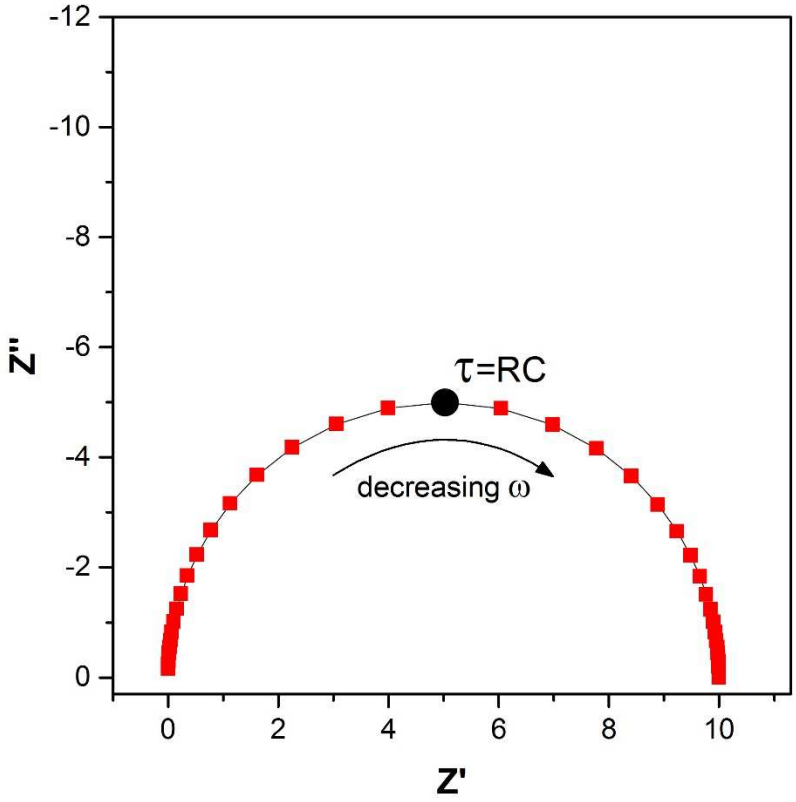

Figure 2-9: Nyquist plot of parallel connected RC. The frequency of the maximum point of the semicircle can be related to the RC time constant.

2.3.1.3 Impedance model of a real system

For real systems, resistors are used to model charge transfer resistances including transport and recombination. Capacitors are used to model charge storage. A common process studied using impedance measurements is the charge transfer at the semi-conductor electrolyte interface. The equivalent circuit to model this process is shown in Figure 2-10, along with the simulated response in Figure 2-11. The electrical double layer, due to the build-up of charge at the interface, is modelled as a capacitor. The Faradaic charge transfer of electrons across the interface is modelled as a resistance in parallel to the capacitor. The circuit also contains a resistor in series with this parallel combination to represent the series resistance of the system.

The observed impedance spectra shows the semi-circular response expected from the parallel RC element, offset by the series resistance as at high frequency the capacitor acts as a short-circuit. The value of the series resistance, R_s, is therefore easily obtained from the high frequency intercept of the semicircle. The diameter of the semicircle gives the charge transfer resistance, R_{ct}. The time constant relating to

$R_{ct}C_{dl}$, can be divided by the charge transfer resistance to obtain the capacitance. Visually, the Nyquist plot gives no information regarding the frequency of each point. It is more informative to also present the impedance data on a Bode plot as shown in Figure 2-12, which shows the magnitude and phase components as a function of frequency.

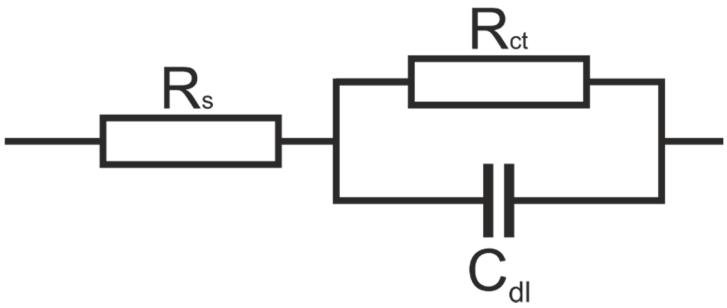

Figure 2-10: Simplified Randles circuit used to model charge transfer at the semi-conductor electrolyte interface.

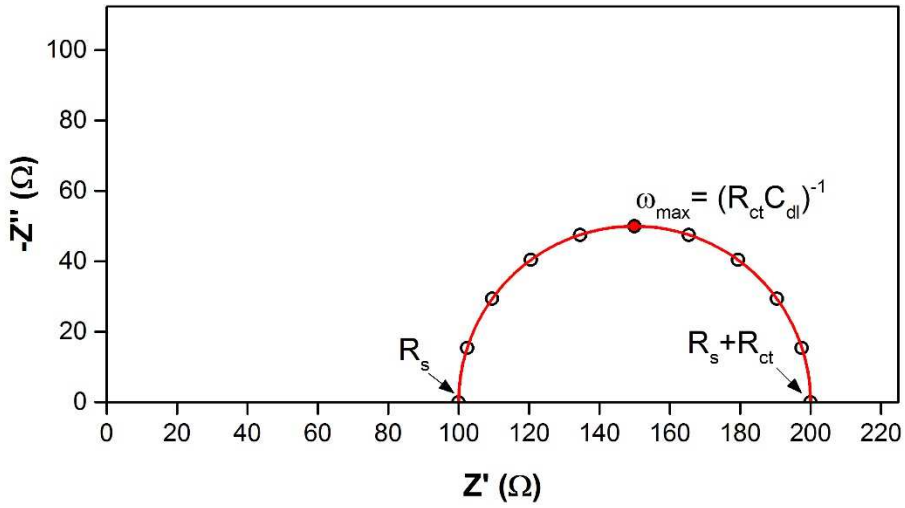

Figure 2-11: Simulated impedance response for the above Randles circuit. R_s=100 Ω, R_{ct}=100 Ω, C_{dl}=1 μF.

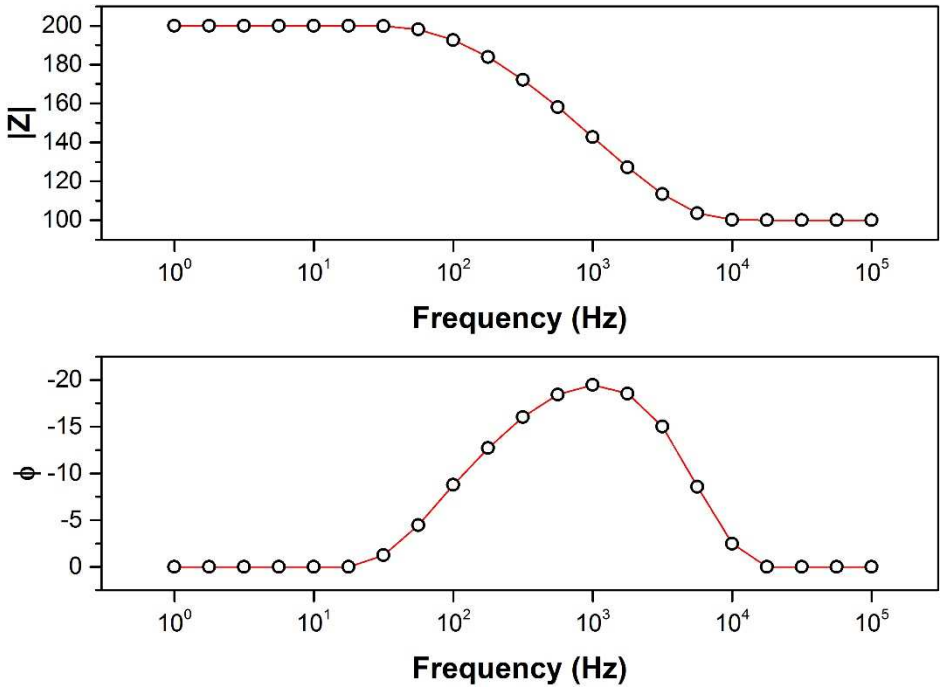

Figure 2-12: Bode plot of simulated impedance from the Randles circuit above. R_s=100 Ω, R_{ct}=100 Ω, C_{dl}=1 μF.

The basic principles behind the charge transfer at the semiconductor-electrolyte interface are similar to many other processes. For example, recombination of electrons from the mesoporous TiO_2 with triiodide ions in the electrolyte in DSSC involves a similar process. In that instance the parallel RC element represents the charge stored in the TiO_2 (chemical capacitance) and the recombination resistance. The basic semi-circular response is observed in many systems relating to capacitances discharging through a resistance. Often impedance spectra will show multiple semicircles to represent multiple interfaces or discharge processes.

In practice impedance data is often fitted using non-linear least squares fitting software. This involves first developing a physically relevant model and then fitting it to the data. In cases where a model cannot be determined or fitting a capacitance is not physically relevant, for instance in the case of a frequency dependent recombination process, information can still be obtained about the rates of the processes observed. The frequency of the maximum point of the semicircle (or frequency of the maximum imaginary component) can be taken to calculate the time constant of the process. Fitting software, such as Z-View (Scribner Associates), may also contain an option to perform a 'simple circle fit'. This fits a semicircle to the specified data range, from which it computes the resistance (diameter) and capacitance (from τ/R).

2.3.1.4 Impedance response of other processes

There are a number of complications to consider when modelling real systems using linear circuit elements. The main issue involves the appearance of non-perfect capacitances. In principal, anything other than a perfectly flat parallel plate capacitor may show some frequency variation. Material interfaces normally show some degree of inhomogeneity which leads to non-ideal capacitance behaviour. In these situations the circuit can be modelled using a 'constant phase element' (CPE). The impedance of a constant phase element is given as

$$Z_{CPE} = \frac{1}{T(j\omega)^P}$$

where T is a constant with units F cm^{-2} s^{P-1} and P is related to the angle a purely capacitive response needs to be rotated in a complex plane plot. The impedance response of a CPE is therefore a straight line at a phase angle of -90×P degrees. A 'P' value of 1 therefore relates to a true capacitance (vertical line on Nyquist plot).

A constant phase element with P < 1, in parallel with a resistor gives a depressed semicircle on a Nyquist plot as shown in Figure 2-13. Whilst it is possible to fit such impedance spectra with a CPE element, as the capacitance becomes less ideal it is difficult to obtain a physically relevant interpretation of the capacitance behaviour. It is possible to calculate an equivalent capacitance using the equation derived by Brug et al.[46]

$$C_{eq} = T^{1/P}\left(R_s^{-1} + R_p^{-1}\right)^{(P-1)/P}$$

where R_s and R_p relate to the series and parallel resistances connected to the CPE. To be related to a capacitor the 'P' value should be between 0.8 and 1.

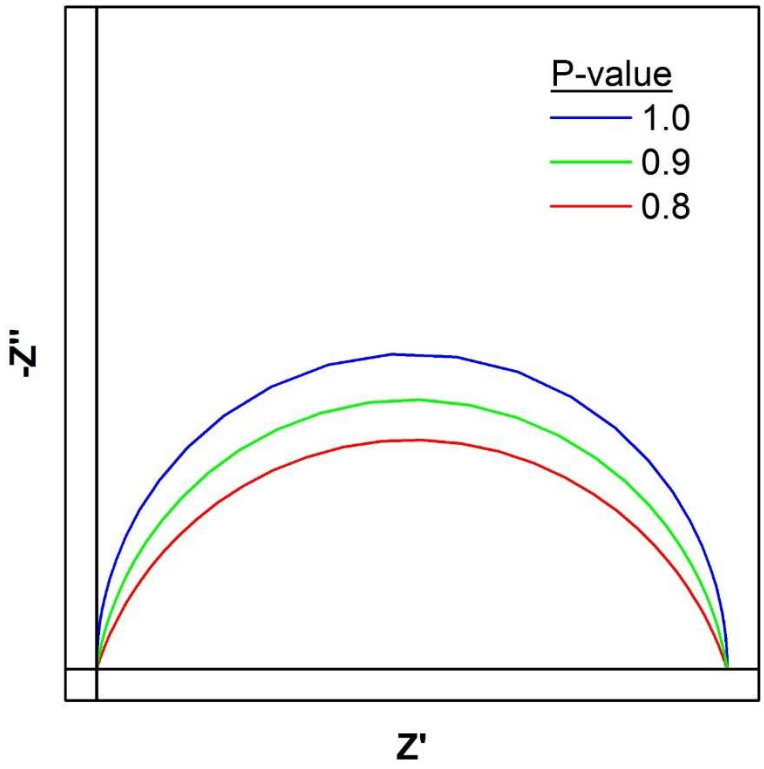

Figure 2-13: Nyquist plot of simulated impedance response of a CPE in parallel with resistor. The semicircle becomes more depressed as P gets smaller.

A CPE with a phase angle of 45 ° (P = 0.5) represents a Warburg diffusion process. This could be used to represent the diffusion of electrons or ions through a material. On short length scales this Warburg response is terminated in a resistance or capacitance at low frequency depending on the nature of the interface. If the electrode is blocking for the diffusing species, a capacitance will build up at low frequency. If the electrode is permeable the Warburg is shorted with a diffusion resistance. These types of Warburg response are shown in Figure 2-14.

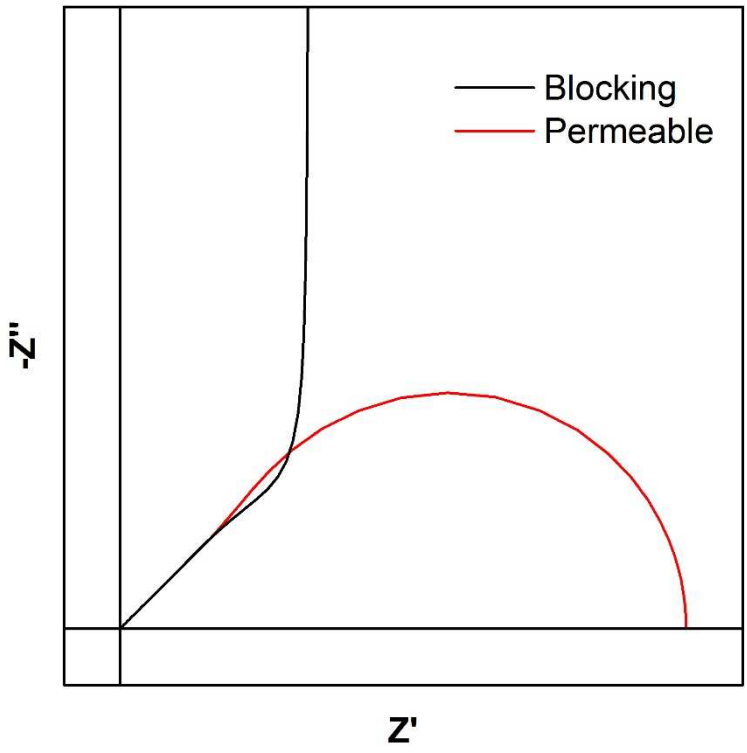

Figure 2-14: Warburg responses for finite diffusion to a blocking or permeable interface.

2.3.2 Intensity modulated spectroscopies

Instead of using a voltage signal as the input signal to test a system, it is possible to use other stimuli. One example of alternative transfer function analysis is to use modulated light as the perturbation signal. Again this involves superimposing a small amplitude AC signal on a DC offset. For photoactive semiconductor materials this will produce a comparable effect to impedance spectroscopy.

In intensity modulated photovoltage spectroscopy (IMVS) the cell is held at open-circuit under the DC illumination. The small AC signal (usually <10 % of the DC light intensity) is used to modulate the Fermi levels due to modulated generation and recombination rates within the cell. This is measured as the modulated photovoltage, $\tilde{U}_{photo}$, in response to the modulated input photon flux, $\tilde{\Phi}$. The IMVS transfer function is therefore given as

$$H_{IMVS}(\omega) = \frac{\tilde{U}_{photo}(\omega)}{\eta q \tilde{\Phi}}$$

Where, η, is the quantum efficiency for charge generation and, q, is the elementary charge. The transfer function therefore has units of Ω cm^2 showing it's relation to the impedance technique.

As IMVS is carried out open-circuit no charge is extracted and therefore the decay is as a result of recombination. The comparable measurement at short-circuit is called intensity modulated photocurrent spectroscopy (IMPS). This can give information about charge transport as is the case for DSSC, however the response is limited by the RC time constant of the device. IMPS has also been used to study interfacial charge transfer and recombination at illuminated semiconductor-electrolyte interfaces. The IMPS transfer function is

$$H_{IMPS}(\omega) = \frac{\tilde{j}_{photo}(\omega)}{\eta q \tilde{\Phi}}$$

The spectra obtained from intensity modulated measurements are similar to those obtained from impedance measurements. Time constants for the observed processes are obtained by taking the inverse of the radial frequency at the maxima of the semi-circular response as shown in Figure 2-15.

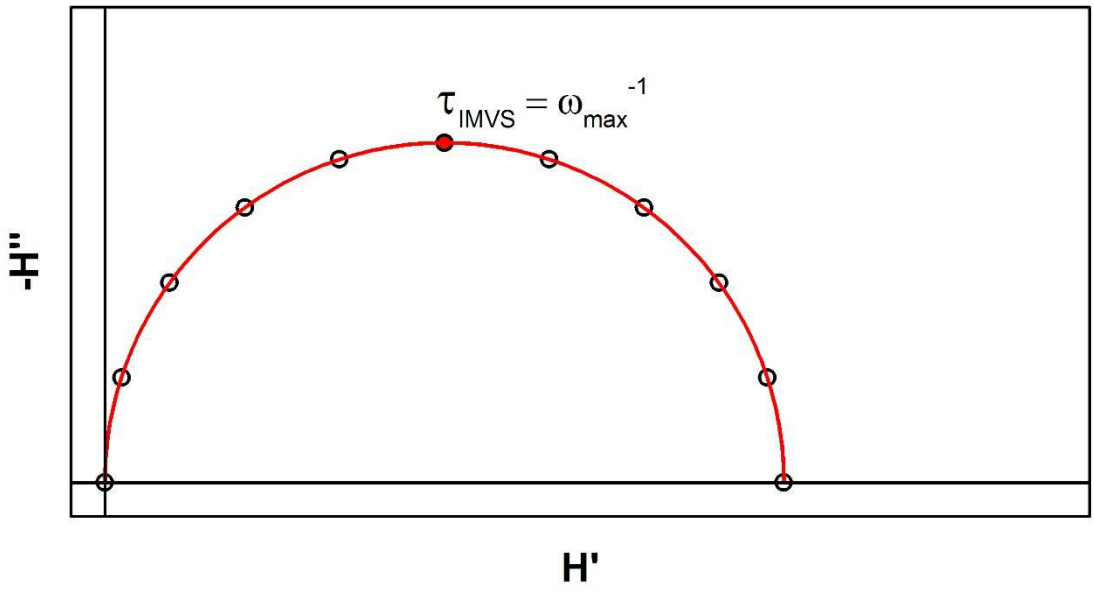

Figure 2-15: Example IMVS response showing the time constant extraction from the frequency of the maximum point of the semicircle.

It has been shown by Halme[47] that the EIS, IMVS and IMPS methods are related by definition as

$$Z(\omega) = \frac{H_{IMVS}(\omega)}{H_{IMPS}(\omega)}$$

In this thesis IMVS and IMPS measurements will be used to calculate equivalent impedance spectra.

2.4 References

1. K. Naoki, C. Yasuo and H. Liyuan, *Japanese Journal of Applied Physics*, 2005, **44**, 4176.
2. H. J. Snaith, A. Abate, J. M. Ball, G. E. Eperon, T. Leijtens, N. K. Noel, S. D. Stranks, J. T.-W. Wang, K. Wojciechowski and W. Zhang, *J. Phys. Chem. Lett.*, 2014, **5**, 1511-1515.
3. W. Tress, N. Marinova, T. Moehl, S. M. Zakeeruddin, M. K. Nazeeruddin and M. Gratzel, *Energy Environ. Sci.*, 2015, **8**, 995-1004.
4. H.-W. Chen, N. Sakai, M. Ikegami and T. Miyasaka, *J. Phys. Chem. Lett.*, 2015, **6**, 164-169.
5. M. Lyu, J.-H. Yun, R. Ahmed, D. Elkington, Q. Wang, M. Zhang, H. Wang, P. Dastoor and L. Wang, *J. Colloid Interface Sci.*, 2015, **453**, 9-14.
6. J. A. Christians, J. S. Manser and P. V. Kamat, *J. Phys. Chem. Lett.*, 2015, **6**, 852-857.
7. G. Richardson, S. E. J. O'Kane, R. G. Niemann, T. A. Peltola, J. M. Foster, P. J. Cameron and A. B. Walker, *Energy Environ. Sci.*, 2016, **9**, 1476-1485.
8. B. C. O'Regan, P. R. F. Barnes, X. Li, C. Law, E. Palomares and J. M. Marin-Beloqui, *J. Am. Chem. Soc.*, 2015, **137**, 5087-5099.
9. L. K. Ono, S. R. Raga, S. Wang, Y. Kato and Y. Qi, *Journal of Materials Chemistry A*, 2015, **3**, 9074-9080.
10. E. L. Unger, E. T. Hoke, C. D. Bailie, W. H. Nguyen, A. R. Bowring, T. Heumuller, M. G. Christoforo and M. D. McGehee, *Energy Environ. Sci.*, 2014, **7**, 3690-3698.
11. J. Wei, Y. Zhao, H. Li, G. Li, J. Pan, D. Xu, Q. Zhao and D. Yu, *J. Phys. Chem. Lett.*, 2014, **5**, 3937-3945.
12. J. M. Frost, K. T. Butler and A. Walsh, *APL Mat.*, 2014, **2**, 081506.
13. Y. Shao, Z. Xiao, C. Bi, Y. Yuan and J. Huang, *Nat. Commun.*, 2014, **5**, 5784.
14. S. Meloni, T. Moehl, W. Tress, M. Franckevičius, M. Saliba, Y. H. Lee, P. Gao, M. K. Nazeeruddin, S. M. Zakeeruddin, U. Rothlisberger and M. Graetzel, *Nat. Commun.*, 2016, **7**, 10334.
15. H. Zhang, C. Liang, Y. Zhao, M. Sun, H. Liu, J. Liang, D. Li, F. Zhang and Z. He, *PCCP*, 2015, **17**, 9613-9618.
16. Y. Zhang, M. Liu, G. E. Eperon, T. C. Leijtens, D. McMeekin, M. Saliba, W. Zhang, M. de Bastiani, A. Petrozza, L. M. Herz, M. B. Johnston, H. Lin and H. J. Snaith, *Materials Horizons*, 2015, 315-322.
17. D. Bryant, S. Wheeler, B. C. O'Regan, T. Watson, P. R. F. Barnes, D. Worsley and J. Durrant, *J. Phys. Chem. Lett.*, 2015, **6**, 3190-3194.
18. C. Li, S. Tscheuschner, F. Paulus, P. E. Hopkinson, J. Kießling, A. Köhler, Y. Vaynzof and S. Huettner, *Adv. Mater.*, 2016, **28**, 2446-2454.
19. S. van Reenen, M. Kemerink and H. J. Snaith, *J. Phys. Chem. Lett.*, 2015, **6**, 3808-3814.

20. J. H. Heo, H. J. Han, D. Kim, T. K. Ahn and S. H. Im, *Energy Environ. Sci.*, 2015, **8**, 1602-1608.

21. H.-S. Kim, I.-H. Jang, N. Ahn, M. Choi, A. Guerrero, J. Bisquert and N.-G. Park, *J. Phys. Chem. Lett.*, 2015, **6**, 4633-4639.

22. H.-S. Kim and N.-G. Park, *J. Phys. Chem. Lett.*, 2014, 2927-2934.

23. A. Baumann, K. Tvingstedt, M. C. Heiber, S. Väth, C. Momblona, H. J. Bolink and V. Dyakonov, *APL Mat.*, 2014, **2**, 081501.

24. R. S. Sanchez, V. Gonzalez-Pedro, J.-W. Lee, N.-G. Park, Y. S. Kang, I. Mora-Sero and J. Bisquert, *J. Phys. Chem. Lett.*, 2014, **5**, 2357-2363.

25. S. Chen, X. Wen, R. Sheng, S. Huang, X. Deng, M. A. Green and A. Ho-Baillie, *ACS Appl. Mater. Interfaces*, 2016, **8**, 5351-5357.

26. J. Bisquert, L. Bertoluzzi, I. Mora-Sero and G. Garcia-Belmonte, *J. Phys. Chem. C*, 2014, **118**, 18983-18991.

27. M. Bag, L. A. Renna, R. Y. Adhikari, S. Karak, F. Liu, P. M. Lahti, T. P. Russell, M. T. Tuominen and D. Venkataraman, *J. Am. Chem. Soc.*, 2015, **137**, 13130-13137.

28. E. J. Juárez-Pérez, R. S. Sánchez, L. Badia, G. Garcia-Belmonte, Y. S. Kang, I. Mora-Sero and J. Bisquert, *J. Phys. Chem. Lett.*, 2014, **9**, 2390-2394.

29. A. Guerrero, G. Garcia-Belmonte, I. Mora-Sero, J. Bisquert, Y. S. Kang, T. J. Jacobsson, J.-P. Correa-Baena and A. Hagfeldt, *J. Phys. Chem. C*, 2016, **120**, 8023-8032.

30. A. Jun, J. Kim, J. Shin and G. Kim, *ChemElectroChem*, 2016, **3**, 511-530.

31. S. J. Skinner, *Int. J. Inorg. Mater.*, 2001, **3**, 113-121.

32. B. A. Boukamp, *Nat Mater*, 2003, **2**, 294-296.

33. A. Walsh, D. O. Scanlon, S. Chen, X. G. Gong and S.-H. Wei, *Angew. Chem. Int. Ed.*, 2015, **54**, 1791-1794.

34. C. Eames, J. M. Frost, P. R. F. Barnes, B. C. O/'Regan, A. Walsh and M. S. Islam, *Nat Commun*, 2015, **6**, 1-8.

35. C. Ludmila, U. Satoshi, J. A. Kumar, M. Tsutomu, N. Jotaro, K. Takaya and S. Hiroshi, *Chem. Lett.*, 2015, **44**, 1089-1091.

36. E. L. Unger, A. R. Bowring, C. J. Tassone, V. L. Pool, A. Gold-Parker, R. Cheacharoen, K. H. Stone, E. T. Hoke, M. F. Toney and M. D. McGehee, *Chem. Mater.*, 2014, **26**, 7158-7165.

37. D. A. Egger, L. Kronik and A. M. Rappe, *Angew. Chem. Int. Ed.*, 2015, **54**, 12437-12441.

38. N. Pellet, J. Teuscher, J. Maier and M. Grätzel, *Chem. Mater.*, 2015, **27**, 2181-2188.

39. E. T. Hoke, D. J. Slotcavage, E. R. Dohner, A. R. Bowring, H. I. Karunadasa and M. D. McGehee, *Chemical Science*, 2015, **6**, 613-617.

40. S. J. Yoon, S. Draguta, J. S. Manser, O. Sharia, W. F. Schneider, M. Kuno and P. V. Kamat, *ACS Energy Letters*, 2016, **1**, 290-296.

41. G. E. Eperon, C. E. Beck and H. J. Snaith, *Materials Horizons*, 2016, **3**, 63-71.

42. J. Bisquert, *J. Phys. Chem. B*, 2001, **106**, 325-333.

43. F. Fabregat-Santiago, J. Bisquert, E. Palomares, L. Otero, D. Kuang, S. M. Zakeeruddin and M. Grätzel, *J. Phys. Chem. C*, 2007, **111**, 6550-6560.

44. F. S. Baumann, J. Fleig, H.-U. Habermeier and J. Maier, *Solid State Ionics*, 2006, **177**, 1071-1081.

45. J. Jamnik and J. Maier, *PCCP*, 2001, **3**, 1668-1678.

46. G. J. Brug, A. L. G. van den Eeden, M. Sluyters-Rehbach and J. H. Sluyters, *J. Electroanal. Chem. Interfac.*, 1984, **176**, 275-295.

47. J. Halme, *PCCP*, 2011, **13**, 12435-12446.

3 Experimental

3.1 Introduction

This chapter describes the general equipment used and its relevant setup. Specific experimental details are given in each results chapter.

The solar cell devices were manufactured by Giles Eperon and Nobuya Sakai at the University of Oxford. Their experimental procedure is given where relevant as it may be important to understand device structure and fabrication techniques when interpreting the results. These cells were stored in a nitrogen glovebox in the dark when they were not being tested.

All measurements were performed inside a light-tight Faraday cage to avoid stray light and minimize electrical interference.

3.2 Impedance spectroscopy

Impedance measurements were carried out at open-circuit under illumination. Impedance data was fitted using Z-View software (Scribner Associates).

For the measurements focusing on the high frequency cell response the impedance measurements were performed using an Autolab PGSTAT30 incorporating an FRA and potentiostat. This was controlled using the NOVA software (version 1). The illumination was provided by a red 625 nm LED (Thorlabs MRLED) which was adjusted using the attached driver (Thorlabs DC2100) so that the test cell produced a photocurrent equivalent to 0.1 sun AM 1.5 illumination. Neutral density filters were used to attenuate the light to lower intensities. The open-circuit voltage of the cell was monitored until it reached a steady-state, at which point the impedance measurement was started. Measurements were carried out over the frequency range 1.5 MHz to 1 Hz.

For the remaining impedance measurements to low frequency a Solartron ModuLab XM Photoelectrochemical Test System was used, controlled by the ModuLab PhotoEchem software. This system utilized a blue 470 nm LED (Thorlabs M470L2) with the maximum intensity calibrated to give a 1 sun equivalent photocurrent from the solar cells. The software generates an intensity calibration curve using its NIST calibrated reference photodiode and controls the LED intensity directly via the LED driver (Thorlabs DC2100). Again, the open-circuit voltage of the cell was allowed to reach steady state before the measurement was started. Measurements were performed over the frequency range 1 MHz to 3 mHz.

3.3 Intensity modulated spectroscopies

IMVS measurements were also carried out on two different equipment setups.

For the high frequency response chapter, a Solartron 1260 Frequency Response Analyser was used. For IMVS measurements the cell was connected to the FRA via a high impedance voltage follower (>10^{12} Ω input impedance) to hold the cell at open-circuit and ensure no current was drawn from the cell. For IMPS measurements a low noise current amplifier (Femto DLPCA-200) was used to hold the cell at short circuit. The light intensity was controlled using neutral density filters. The AC modulation depth was <10 % of the DC value to ensure a linear cell response.

For the low frequency measurements the same Solartron ModuLab system was used as for impedance measurements. The cell was connected directly to the potentiostat, which held the cell at open or short circuit. DC light intensity was controlled in the same way as for impedance measurements. The AC modulation depth was <10 % of the DC value to ensure a linear cell response.

For both of these systems the same reference detection method was used to allow for accurate high frequency measurements. The LED driver (Thorlabs DC2100) delivered an LED driving current proportional to a sinusoidal input signal that was supplied by the generator channel of the FRA. A beam splitter and reference photodetector was used to measure the modulated photon flux of the LED (Figure 3-1). At high frequencies the modulated amplitude of the LED may become attenuated, and a significant phase lag between the light signal and FRA generator signal may exist. To compensate for this a high bandwidth reference photodiode was used to obtain a true measure of the modulated photon flux. This photodiode signal was used as the reference signal for the transfer function. In simple terms the measured transfer function is essentially

$$H = \frac{\text{Cell signal}}{\text{Ref PD signal}}$$

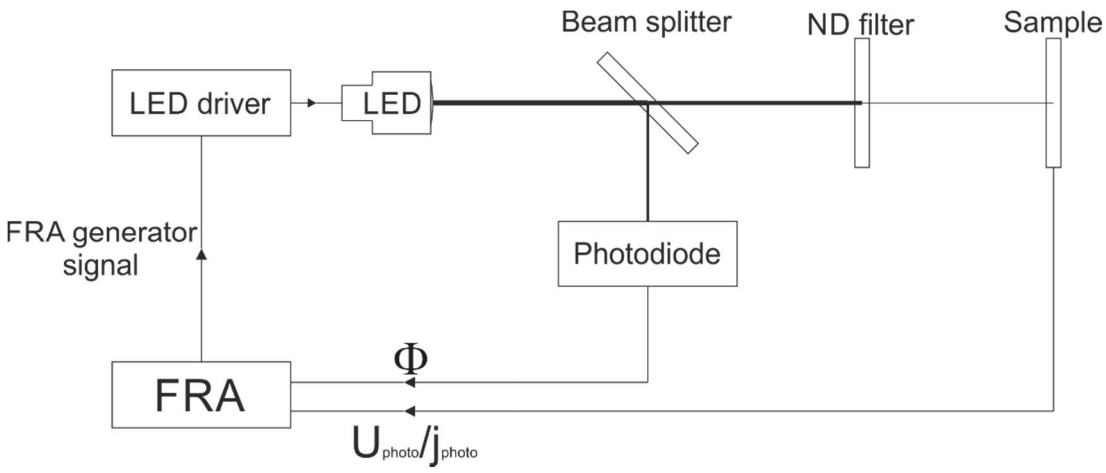

Figure 3-1: Experimental setup for high frequency IMVS/IMPS measurements utilizing a reference photodiode to compensate for high frequency attenuation and lag of the LED light output.

3.4 Open-circuit voltage decay

For the initial cell batch the OCVD measurements were performed manually at a single light intensity (equivalent to 0.1 sun). The cell was connected via the high impedance voltage follower to a digital storage oscilloscope (Tektronix TDS3012). The cell was illuminated with a 625nm LED (Thorlabs MRLED) which was switched on and off via the LED driver (Thorlabs DC2100). Measurements were repeated using different oscilloscope timebases to improve resolution at short times.

For the second cell batch OCVD measurements were performed using the Solartron ModuLab system. The illumination was provided by a 470 nm LED (Thorlabs M470L2). The LED intensity and switching was controlled by the ModuLab system via the LED driver signal input. Traces were recorded at a variable sampling rate to improve data resolution at short times.

3.5 Dark voltage/current measurements

The dark voltage and current measurements were performed using the ModuLab XM system.

4 The high frequency response of planar perovskite cells

4.1 Abstract

In this chapter a variety of electrical characterization techniques are used to study planar perovskite solar cells. These techniques, including impedance spectroscopy and intensity modulated photovoltage/photocurrent spectroscopy, have been frequently used to study transport and recombination in dye-sensitized solar cells. Here they are also shown to be suitable for investigations into perovskite solar cells, however the interpretation of results is shown to be quite different.

The electrical response at high frequency is shown to be dominated by the effects of the cells geometric capacitance. No chemical capacitance has been observed, showing a clear difference to the operation of dye-sensitized solar cells. It is shown that recombination can be observed on the time-scales monitored by these techniques, however charge transport is believed to be too fast.

A clear difference in the performance of seemingly identical cells is observed when measurements are made at low light intensity. This reveals large differences in ideality factors, between m=2.6 and m=5.2, which represent different recombination mechanisms occurring in these devices even though their 1 Sun performance is comparable.

4.2 Introduction

Much of the early electrical characterization work on perovskite solar cells was performed on mesoporous structured cells[1-5]. This presents difficulties in the deconvolution of the effect of the mesoporous layer from the intrinsic behaviour of the perovskite active layer. The main reason for the focus on mesoporous cells is that it appears to be simpler to make high-performance cells, with good steady state properties (low hysteresis), using the mesoporous rather than planar heterojunction architecture[6]. To be able to study the electronic properties of the perovskite layer itself it is preferable to study planar heterojunction devices. In this type of device the flat perovskite layer is contacted by two different carrier extracting contact materials. The most common choice of contact materials is a compact layer of titanium dioxide as an electron transport layer (ETL) and spiro-OMeTAD as the hole transport layer (HTL). These materials were commonly used in the manufacture of solid state dye-sensitized solar cells and were carried over into initial perovskite solar cell investigations[7, 8]. They have been shown to act as good contact layers for perovskite cells with the efficiencies for planar heterojunction TiO_2/Spiro cells in excess of 15%[9, 10].

Due to the similarities in the mesoporous perovskite device structure with that of the dye-sensitized solar cell (DSSC), initial perovskite studies tended to interpret the device response in comparable ways. Predominantly this focused on the use of a transmission line model to fit the perovskite impedance spectrum[1-3]. In a DSSC electron transport occurs through the mesoporous TiO_2 layer via a diffusion process. There is little or no electric field across this layer due to screening by ions in the electrolyte. The main competing recombination process to this diffusion pathway is the charge transfer of an electron from the TiO_2 to the oxidized electrolyte species, typically triiodide ions. This related diffusion-recombination mechanism is modelled using a transmission line (Figure 4-1), similar to the case for many types of porous electrodes, as defined by Bisquert for the application of DSSC[11, 12].

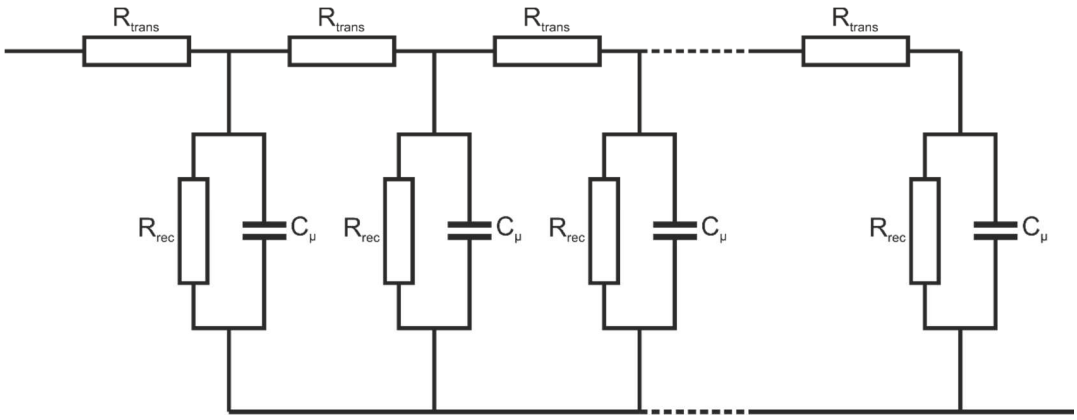

Figure 4-1: Transmission line model for electron transport through mesoporous titania. The model includes charge accumulation in the TiO_2 in the form of a chemical capacitance as well as recombination of this stored charge. R_{trans} and R_{rec} relate to the transport and recombination resistances, and C_μ corresponds to the chemical capacitance.

A simulated impedance spectrum for the above transmission line model is shown in Figure 4-2. The characteristic response shows a 45° line at high frequency representing the diffusion of the electrons (similar response is seen for other diffusion processes). At lower frequencies this 45° line transitions into a semi-circular arc representing the parallel combination of the recombination resistance and chemical capacitance. Software utilising non-linear least squares fitting can be used to quickly fit an equivalent circuit to an impedance spectrum. As highlighted in Figure 4-2, for a relatively simple model the parameters can be quickly estimated from the diameter of semi-circles and by knowing the frequency of the maximum imaginary component. In the case of the DSSC transmission line, values for the transport resistance, recombination resistance and chemical capacitance can be obtained. These values can be used to calculate important solar cell parameters[13]. The time constant obtained from $R_{rec}C_\mu$ gives the electron lifetime, τ_n. The ratio of the transport and recombination resistances can be related to the electron diffusion length.

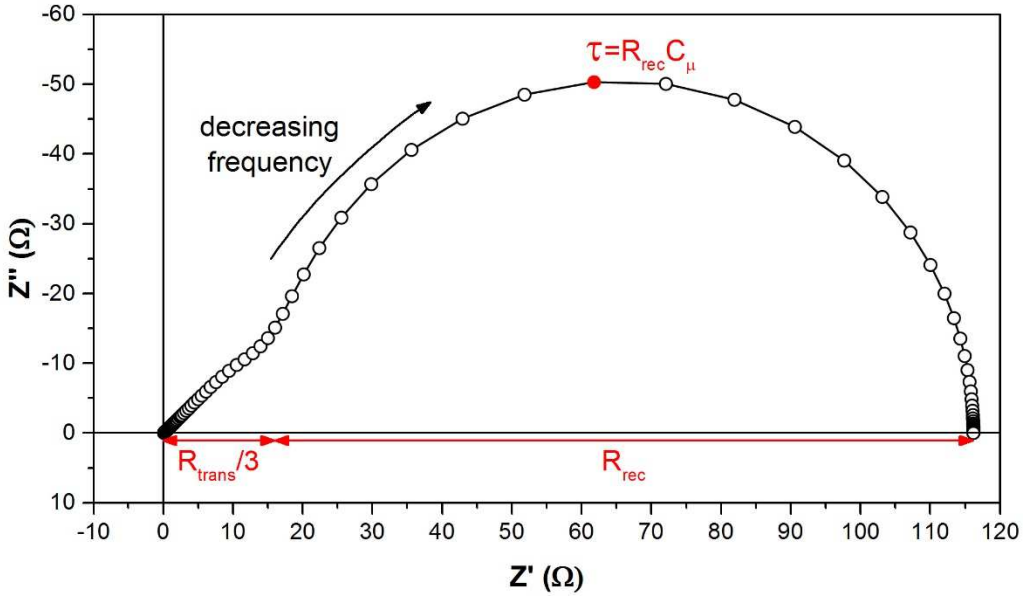

Figure 4-2: Simulated impedance spectrum for the transmission line model shown in Figure 4-1. R_{trans}=50 Ω, R_{rec}=100 Ω, C_{μ}=1 mF.

Figure 4-3 provides a literature example of impedance spectra obtained from a planar and mesoporous titania based perovskite solar cell[2]. The equivalent circuit shown has been used to fit spectra from both types of cell. The high frequency arc was related to transport in the Spiro-OMeTAD layer. The authors do not quote any frequency range for the presence of the transmission line, but the entire measurement is over the range 400 kHz to 0.05 Hz. This suggests that the transmission line feature starts to appear at around 1 kHz, with the maximum frequency of the recombination arc occurring at around 0.1 Hz. This would give electron transit times on the millisecond timescale and an electron lifetime of around 0.6 s close to open-circuit under 1 sun illumination.

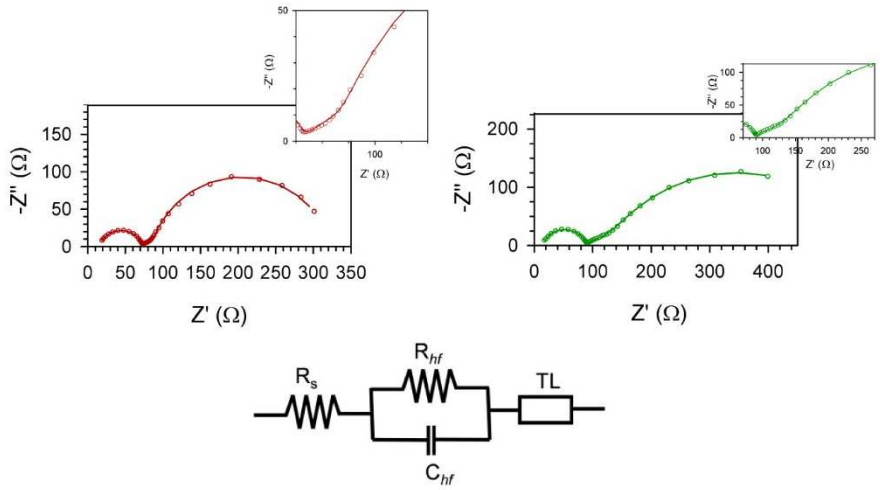

Figure 4-3: Example of impedance spectra (left: planar, right: mesoporous TiO_2) and equivalent circuit used in literature[2]. Insets show the part of the spectra believed to represent the diffusion of electrons, although a true 45° slope does not appear clear.

Early measurements of recombination lifetimes derived from time-resolved photoluminescence measurements suggested values on the hundreds of nanoseconds timescale[14]. Mobility values of around 10 $cm^2\ V^{-1}\ s^{-1}$ were also determined from terahertz spectroscopy[15]. Considering the high mobility of the perovskite material charge transit times are likely to be on the order of nanoseconds. It is therefore unlikely that transport processes will be observed on the timescale of impedance measurements, let alone at the lower end of the measured frequency range.

The use of the transmission line led to calculations of the electron diffusion length, L_d, using the relationship, $L_d/d = \sqrt{R_{rec}/R_{trans}}$ where, d, is the film thickness. Diffusion lengths around 1 μm were calculated[2] (for L~0.5 μm), which agreed with literature reported values from time-resolved PL measurements[14, 16]. However, all that is required to calculate a diffusion length that is greater than the film thickness using a transmission line element is for $R_{trans} \leq R_{rec}$. If the transmission line has been assigned incorrectly then it is merely fortuitous that these values of diffusion length appear to be sensible.

The chemical capacitance (also called the diffusion capacitance) is related to the accumulation of charge within the device due to the filling of conduction band states[17]. In the case of DSSC this corresponds to trapped charge in the mesoporous TiO_2[18]. Due to the large interfacial surface area of this layer, capacitance values of the order of mF cm^{-2} can be expected. The chemical capacitance is given by

$$C_\mu = \frac{q^2}{k_B T} n$$

where, n, is the density of conduction band electrons. This shows that the chemical capacitance is proportional to the density of conduction band electrons, which is given by

$$n = n_0 e^{(E_{Fn} - E_{F0})/k_B T} = n_0 e^{qV_F/k_B T}$$

where, V_F, is the potential relating to the splitting of the Fermi levels. The chemical capacitance can therefore be seen to have an exponential dependence on the Fermi level splitting (applied voltage).

The total capacitance measured in a solar cell may have contributions from a number of layers or interfaces. For example, in the case of a DSSC there will also be a capacitance due to the electrolyte contact with the underlying substrate[19]. For solar cells without a mesoporous layer, such as in bulk heterojunction OPV there will be a capacitance associated with the active layer acting as a dielectric[20, 21]. These capacitances are geometric in nature, varying with active area and layer thickness, and are not bias dependent. The measured capacitance will therefore be a combination of multiple capacitances which have different bias dependences.

At low bias potentials the chemical capacitance will be low, and the geometric capacitance will dominate the total capacitance measured. As the Fermi level splitting is increased at higher forward bias potentials, the chemical capacitance will increase exponentially and begin to dominate as shown in Figure 4-4[22].

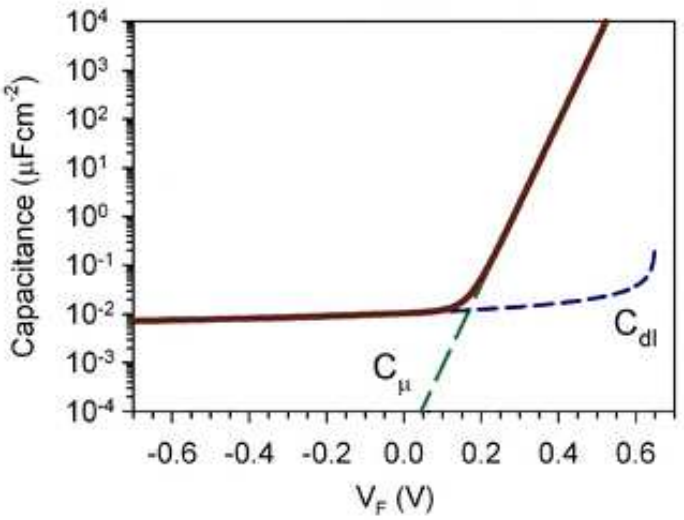

Figure 4-4: Capacitance-voltage relationship for a solar cell with a geometric double layer capacitance and chemical capacitance. The solid line represents the total effective capacitance showing a clear transition in capacitance behaviour under forward bias as charge is accumulated in the conduction band[22].

The presence of a chemical capacitance has been observed in mesostructured perovskite solar cells[3, 5]. The measured capacitance values show a clear exponential relationship with applied voltage or open-circuit voltage at different illumination intensities. It is however unclear whether this capacitance is associated with a build-up of charge in the perovskite itself, or from just the mesoporous TiO_2 scaffold employed. Kim et al. showed the capacitance behaviour for a range of nanostructured samples, but did not identify a clear chemical capacitance for planar samples[3]. O'Regan et al. showed a comparable extracted charge-voltage trend between a mesostructured perovskite cell and DSSC when they took the different layer thicknesses into account[5]. This suggests that electrons are indeed injected into the mesoporous titania, resulting in an increase in its chemical capacitance. It is also clear that transport is possible through the perovskite, as shown from functioning planar cells and those with insulating scaffolds[7].

Intensity modulated voltage and current spectroscopy (IMVS/IMPS) measurements have also been performed on mesoporous perovskite solar cells[4, 23, 24]. These measurements were also common techniques to study recombination and transport in DSSC and have been shown to be complimentary to impedance measurements utilizing the transmission line[25-27]. Guillén et al. observed two time constants in IMPS measurements[4]. They attributed the slower of these two time constants to transport in the mesoporous TiO_2. It was suggested that the faster process could

relate to transport in the HTL or through the perovskite itself. Time constants from IMVS measurements showed excellent agreement with those from EIS[4]. The IMVS time constant was related to the recombination lifetime, $R_{rec}C_{\mu}$.

It is clear from the range of optoelectronic measurements previously presented in the literature that it is difficult to deconvolve the processes relating to the perovskite from those due to the mesoporous TiO_2. It is therefore necessary to study planar devices to get a clearer interpretation of what behaviour is intrinsic to the perovskite material. Whilst theories developed for mesoporous semiconductor electrodes and more specifically DSSC may be applicable in the mesostructured perovskite devices, it does not necessarily follow that they are suitable for planar devices. In fact, despite having their origins based in DSSC technologies, perovskite cells with planar architecture may operate in comparable ways to other thin film technologies, e.g. thin film a-Si p-i-n devices[28].

4.3 Experimental

The perovskite cell fabrication was carried out by Giles Eperon and Nobuya Sakai at the University of Oxford.

Perovskite precursor preparation: Methylamine iodide (MAI) was prepared by reacting methylamine, 33 wt% in ethanol (Sigma-Aldrich), with hydroiodic acid (HI),57 wt% in water (Sigma-Aldrich), at room temperature. HI was added dropwise while stirring. Upon drying at 100°C, a white powder was formed, which was washed with ethanol and dried overnight in a vacuum oven before use.

To form the non-stoichiometric $CH_3NH_3PbI_{3-x}Cl_x$ precursor solution, methylammonium iodide and lead (II) chloride (98%, Sigma-Aldrich) are dissolved in anhydrous *N*,*N*-Dimethylformamide (DMF) at a 3:1 molar ratio of MAI to $PbCl_2$, with final concentrations 0.88M lead chloride and 2.64M methylammonium iodide. This solution is stored under a dry nitrogen atmosphere.

Substrate preparation: Devices were fabricated on fluorine-doped tin oxide (FTO) coated glass (Pilkington, 7Ω $\square^{-1}$). To prevent shunting upon contact with measurement pins, FTO was removed from regions under the anode contact by etching with 2M HCl and zinc powder. Substrates were then cleaned sequentially in 2% Hellmanex detergent, acetone, propan-2-ol and oxygen plasma. A hole-blocking layer of compact TiO_2 was deposited by spin-coating a mildly acidic solution of titanium isopropoxide in anhydrous ethanol (350µl in 5ml ethanol with 0.013M HCl), and annealed at 500°C for 30 minutes. Spin-coating was carried out at 2000rpm for 60 seconds.

Perovskite solar cell fabrication: A total of 12 cells was fabricated in groups of 3 cells on one substrate, each with a pixel area of 0.15 cm^2. To form the perovskite layer, the non-stoichiometric precursor was spin-coated on the substrate in a nitrogen-filled glovebox at 2000rpm for 45 seconds. After spin-coating, the films were left to dry at room temperature in the glovebox for 30 minutes, to allow slow solvent evaporation. They were then annealed on a hotplate in the glovebox at 90°C for 180 minutes and subsequently at 120°C for 15 minutes.

A hole-transporting layer was then deposited via spin-coating a 0.79M solution of 2,2',7,7'-tetrakis-(N,N-di-p-methoxyphenylamine)9,9'-spirobifluorene (spiro-

OMeTAD) in chlorobenzene, with additives of lithium bis(trifluoromethanesulfonyl)imide (0.0184M) and 4-tert-butylpyridine (0.0659M). Spin-coating was carried out at 2000rpm for 45 seconds. Devices were then left overnight in air for the spiro-OMeTAD to dope via oxidation. Finally, gold electrodes were thermally evaporated under vacuum of ~10^{-6} Torr, at a rate of ~0.1 nm s^{-1}, to complete the devices.

Solar cell characterization: The current density–voltage (J-V) curves were measured (2400 Series SourceMeter, Keithley Instruments) under simulated AM 1.5 sunlight at 100 $mWcm^{-2}$ irradiance generated by an Abet Class AAB sun 2000 simulator, with the intensity calibrated with an NREL calibrated KG5-filtered Si reference cell. The mismatch factor was calculated to be 1.2% between 400 and 1100nm. The solar cells were masked with a metal aperture to define the active area, typically 0.0625cm^{-2} and measured in a light-tight sample holder to minimize any edge effects.

The cells were stored in a nitrogen glove box between measurements to minimize degradation. Open circuit voltages were measured as a function of light intensity using a 625 nm light emitting diode (LED) (Thorlabs MRLED). The incident photon flux was controlled using neutral density filters (Edmund Optics) and measured using a calibrated silicon photodiode (Newport 818-SL with OD3 neutral density filter). All modulated techniques were also carried out with illumination from a 625 nm LED where appropriate (Thorlabs MRLED). Impedance measurements for different illumination intensities were made at the corresponding open circuit voltage using an Autolab PGSTAT30. Impedance measurements were also made in the dark as a function of applied voltage. Impedance data were fitted using ZView software (Scribner Associates). IMVS and IMPS measurements were made using a Solartron 1260 frequency response analyzer (FRA) combined with a Thorlabs DC2100 controller (bandwidth 100 kHz) driven by the dc and sine wave output of the FRA. The modulation depth was set to be 10% of the dc level. The illumination intensity was varied using calibrated neutral density filters. To ensure long term stability, cells were illuminated with a single wavelength at intensities of 0.1 Sun and lower. By measuring trends with respect to illumination intensity we were able to derive significant amounts of information on cell behaviour. In the environment solar cells need to operate at illumination intensities below 1 Sun, therefore tests of cell

performance at 0.1 Sun can still be considered as the working environment for a cell. To correct for attenuation and phase lag in the modulated light output at higher frequencies, a glass microscope slide was used as a beam splitter enabling provision of a reference signal for the frequency response analyzer from a fast p-i-n photodiode. For IMPS, the cell current was measured using a current amplifier (Femto DLPCA-200). A high impedance ($>10^{12}$ ohm) voltage follower was used for IMVS. The bandwidth of the system was checked using a fast p-i-n photodiode in place of the solar cell.

4.4 Results

4.4.1 Summary of test devices

The results presented in this section were obtained from the study of 5 planar devices, each consisting of 3 separate pixels. This gave a total of 15 solar cells which were made using an identical procedure, at the same time and in the same batch. Pixels are referred to by the cell name followed by the pixel number, e.g. FB06-1 refers to the first pixel of cell FB06. The pixel active area was defined by the overlap of the gold top electrode and the underlying FTO (non-etched area). This gave a total active area of 0.15 cm^2. The perovskite active layer thickness was 600 nm as measured by SEM. The cell structure and layout is illustrated in Figure 4-5.

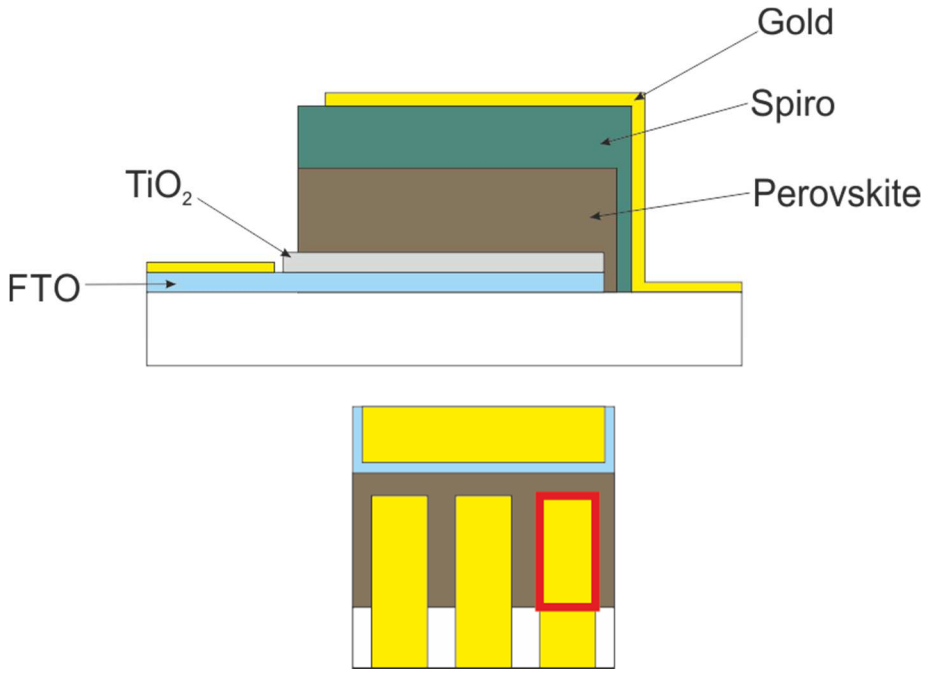

Figure 4-5: Planar perovskite device structure (top) and pixel layout showing active area (bottom).

The device efficiencies were measured under a solar simulator. For this measurement the cells were masked using a metal aperture with an area of 0.0625 cm^2 (cells were unmasked for all subsequent measurements to ensure homogeneous illumination of the complete active area). Example J-V curves are presented in Figure 4-6. These cells were measured by sweeping the potential from forward bias (+1.4V) to short-circuit at a rate of 300 mV/s. The level of hysteresis in these devices was not studied. The cells had an average efficiency of 11.05% under 1 Sun AM1.5 illumination (averages and standard deviation of performance parameters are shown in Table 1). One cell had an efficiency below 5% and so was excluded from further testing.

Another two pixels degraded during transport before further characterization was carried out. A total of twelve cells were therefore studied in detail using the full range of techniques. Two pixels in particular were studied in the most detail; FB06-1 (η=9.60%) and FS43-1 (η=11.98%).

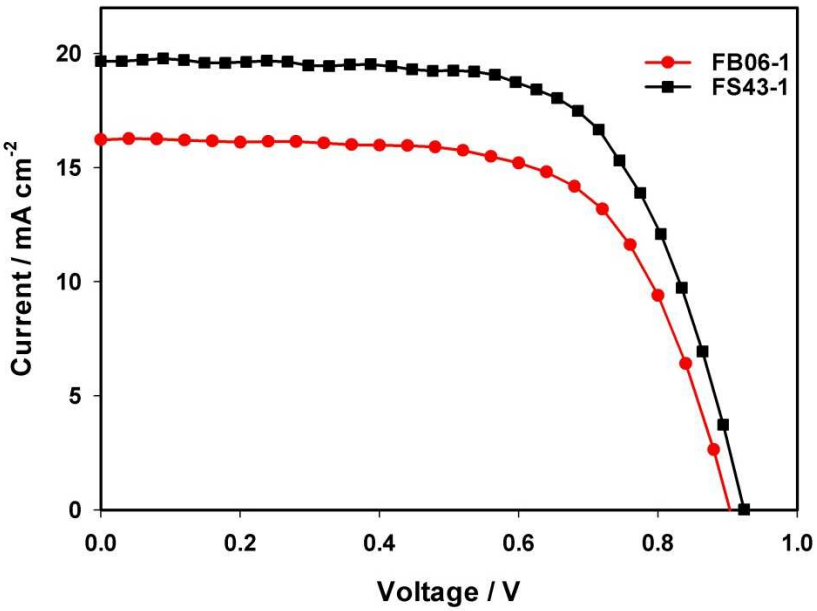

Figure 4-6: Illuminated J-V curves of the two cells studied in most detail.

	Average	Std Dev
Efficiency (%)	11.05	1.02
J_{sc} (mA cm^{-2})	18.32	1.31
V_{oc} (V)	0.91	0.03
FF	0.66	0.02

Table 1: Summary of average device statistics for the batch of cells measured in this chapter.

4.4.2 Intensity dependence of the open-circuit voltage

The intensity dependence of the open-circuit voltage can yield important information regarding the recombination mechanisms occurring within solar cell devices. It can be useful in revealing differences between cells that may not be evident at the standard 1 sun illumination intensity.

The incident intensity of a monochromatic (625 nm) LED was controlled using a series of neutral density filters. The maximum intensity was chosen to give a photocurrent equivalent to that of 0.1 sun AM1.5 illumination. This corresponded to a photon flux of 3.17×10^{16} cm^{-2} s^{-1}. This was then attenuated across 2 orders of magnitude using the ND filters. Voltage values were recorded using the potentiostat at the start of the impedance measurements. The ideality factor was calculated from the slope of the best-fit line to the data plotted on a semi-logarithmic plot using the relationship

$$\frac{\partial V_{oc}}{\partial \ln I_0} = \frac{mk_BT}{q}$$

where, $I_{0,}$ is the incident light intensity and, k_BT/q, is the thermal voltage.

The diode ideality factor, n, is traditionally described in terms of the Shockley diode equation. This describes the dependence of the diode current density on the applied voltage. Here the ideality factor is calculated using different methods under illumination and is given the symbol, m. This differentiation is made to emphasize the fact that the ideality factor for these cells is not equal in the dark and under illumination. This can be seen by the clear crossing of the light and dark JV curves at forward bias (Figure 4-7).

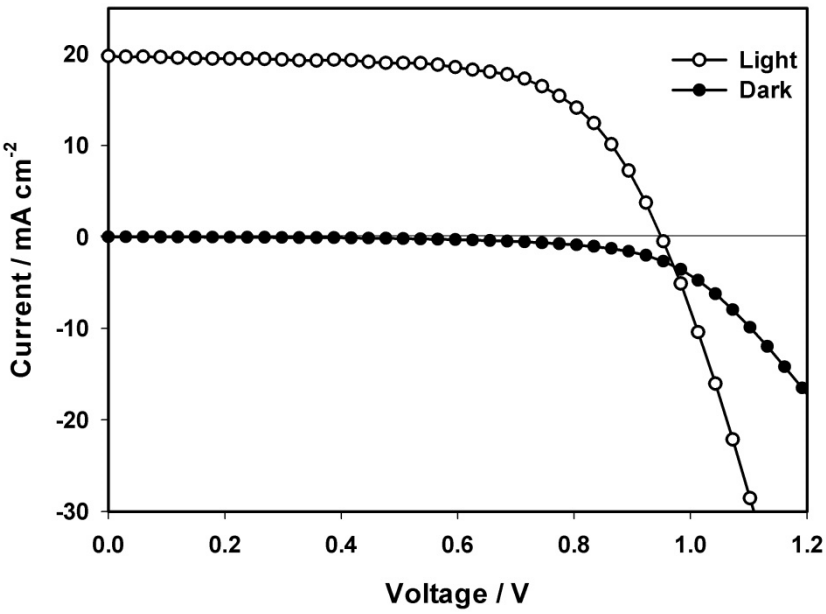

Figure 4-7: Comparison of dark and light J-V curves for cell FS43-1.

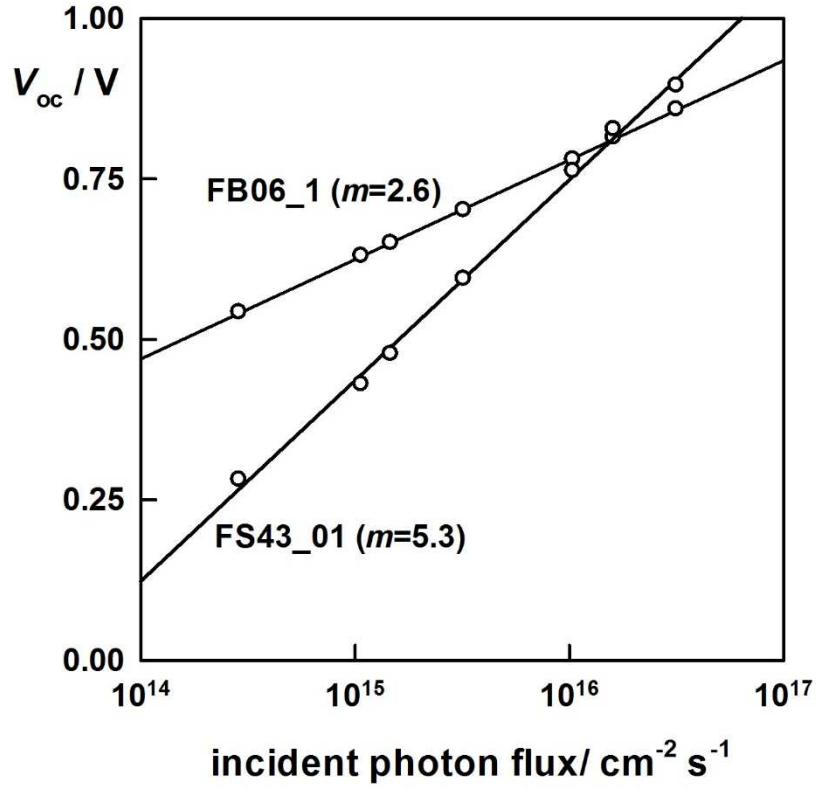

Figure 4-8: Intensity dependence of the open-circuit photovoltage. Ideality factors have been calculated from the slope of the best-fit line.

Despite having comparable performance at 1 sun intensity, including similar V_{oc} values, the range of cells tested showed distinct differences in ideality factor as shown in Figure 4-8. This behaviour was split into two groups. Five of the cells exhibited ideality factors of approximately m=2.6 (average m=2.61; std dev=0.09),

with the other seven having ideality factors around m=5.2 (average m=5.20; std dev=0.31). This behaviour was consistent across pixels on the same device, with the distinct variation only occurring between different substrates. Two of the devices (FB05 and FB06) gave lower ideality factors, whilst the other three (FS43, FS44 and FT48) gave the higher ideality values.

The cell with the higher ideality factor (m=5.3) actually has a higher open-circuit voltage than the low ideality factor cell at the highest intensity measured here (0.1 sun equivalent). The V_{oc} drops off rapidly as the intensity is reduced, with the plots for the two types of cell crossing at around 0.03 suns. It is interesting to note that cells that appear to perform similarly at high light intensity, such as under solar simulator conditions, may actually perform much more differently at lower light intensity. This is an important point for considering their use in real-world conditions where it is important to maintain reasonable performance over a wide range of intensities.

The reasoning behind the differences in ideality is unclear. The cells were nominally identical, being prepared at the same time using the same conditions and material batches. One possibility is that there may have been small differences in annealing temperatures owing to the non-uniformity of heating across the hotplate surface. This may have led to slight variations in crystallisation thus affecting interfaces or trap formation. It was not possible to analyse the material properties once the cells had been manufactured as the deposition of multiple layers of materials obscures those underneath. It is also not clear which layer is the most critical in affecting these properties as both the TiO_2 blocking layer and the perovskite layer undergo an annealing step.

Unexplained variations in device characteristics for seemingly identical samples has also been reported by Gottesman et al[29]. Photoconductivity measurements of perovskite deposited between gold electrodes showed either a direct rise to a steady state photocurrent, or an initial spike then decay to steady state. They too attribute this variation in response to very subtle, unintentional differences in film deposition parameters. As they use a much simpler device configuration with fewer material interfaces it suggests that it is the perovskite layer that is critical for this difference in behaviour.

4.4.3 Impedance spectroscopy

Impedance spectroscopy measurements were carried out over the same range of light intensities as in section 4.4.2, in an attempt to further analyse recombination and transport processes occurring within the devices. Previous impedance measurements had been performed solely on mesostructured perovskite devices with analysis based on models defined originally for DSSC[1]. The impedance response of a DSSC device can reveal a wealth of information about different parts of the cell, particularly concerning electron transport and recombination within the mesoporous titania scaffold. The absence of a substantial electric field and presence of trap states in the TiO_2 means electron transport is relatively slow in a DSSC device. The timescale of electron diffusion in DSSC means that it is clearly identified by impedance spectroscopy measurements below 100 kHz. Electron diffusion coefficients that are several orders of magnitude higher than for mesoporous TiO_2 in DSSC have been measured for perovskite films[30]. It is therefore unlikely that transport will be observed in the planar cells even at the maximum frequency of the potentiostat (1.5 MHz).

The high frequency impedance response of a planar perovskite cell is indeed much simpler than for a DSSC device. The response contains a single semicircle for frequencies down to around 100 Hz, as shown in Figure 4-9 for the highest intensity of 0.1 sun equivalent. Figure 4-10 is the corresponding Bode plot showing a single high frequency process, with a time constant of $\tau = 4\mu s$.

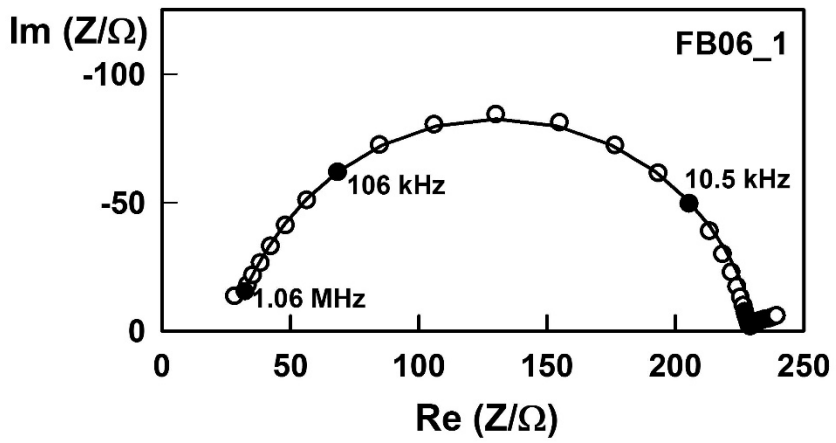

Figure 4-9: Example of the typical high frequency impedance spectra for a measurement at open-circuit under 0.1 sun equivalent illumination.

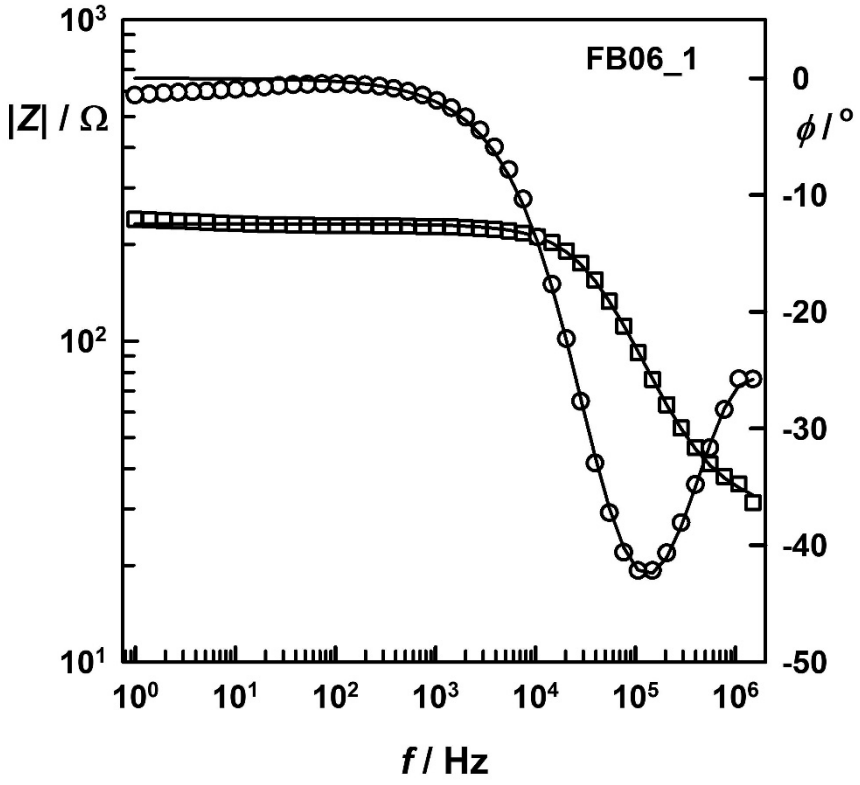

Figure 4-10: Bode plot of impedance response.

A simple equivalent circuit for a planar solar cell is shown in Figure 4-11. It consists of:

a) R_{ser} – the series resistance of the cell. This is mainly attributed to the resistance of the FTO substrate.
b) R_{rec} – the voltage-dependent recombination resistance defined by

$$R_{rec} = \left(\frac{\partial V}{\partial j_{rec}} \right)$$

where, j_{rec}, is the recombination current density.

c) C_{tot} – the total capacitance of the device. This is the sum of any charge stored in the contacts (C_g – geometric capacitance), and any photogenerated charge (C_μ – chemical capacitance).
d) C_{stray} – stray capacitance associated with contacts.

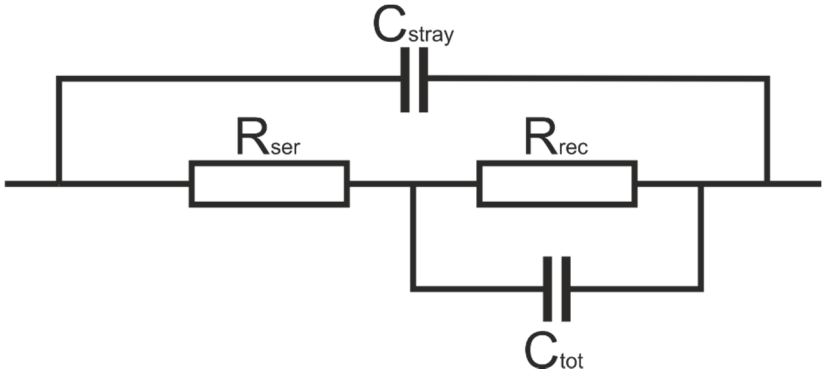

Figure 4-11: Equivalent circuit used to fit the high frequency impedance response.

This equivalent circuit can provide a good fit to the data from the highest frequency down to around 100 Hz. Below this frequency a second feature emerges in the impedance response. At the time of performing these measurements the lower frequency feature could not be clearly resolved. This was in part due to the cells not being stable enough to be measured for the long periods of time needed to reach low frequencies. Measurements were therefore restricted to the range 1.5 MHz to 1 Hz. The V_{oc} of the cell was checked after each measurement to ensure it had not drifted by more than a few mV during each frequency sweep.

Values of the series resistance obtained from all impedance measurements were around 4-6 Ω cm^2 and invariant with light, which is consistent with the FTO resistance. The stray capacitance was typically found to be below 1 nF and was attributed to the effect of wiring and contacts to the cell[31]. The stray capacitance is evident as the slight distortion of the impedance response at the highest frequencies.

The main region of interest is the high frequency arc. This is attributed to the parallel combination of the recombination resistance and total capacitance. The fitted values of the recombination resistance have a strong intensity dependence as shown in Figure 4-12. The linear dependence of resistance on light intensity (as shown by the slope of -1 on the log-log plot) indicates that this is a recombination resistance[32]. Both types of cell (both high and low ideality factor) show a very similar dependence of the recombination resistance on light intensity.

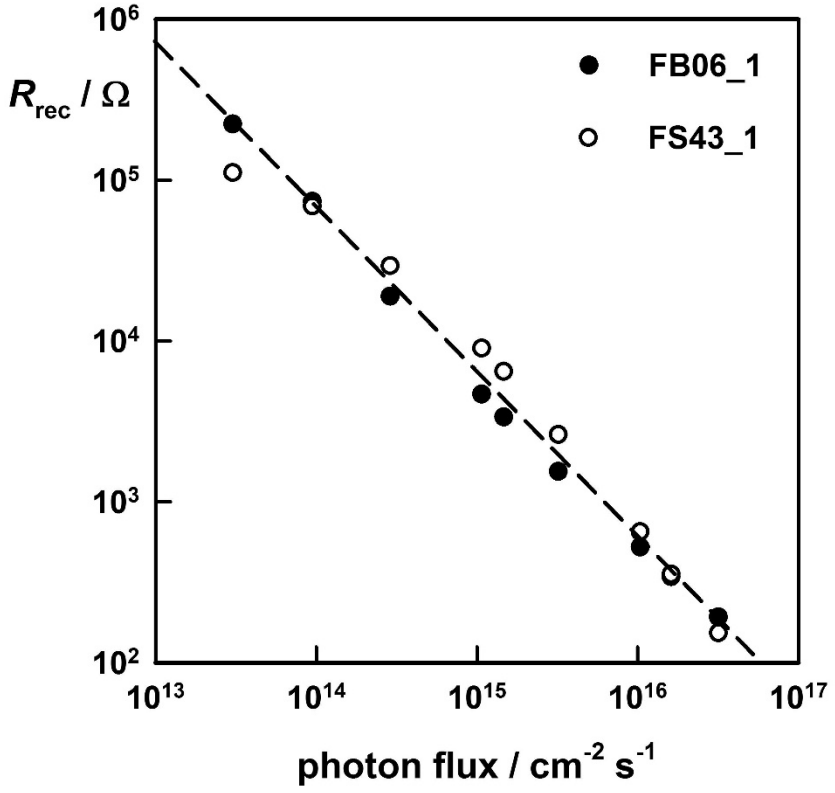

Figure 4-12: Intensity dependence of the recombination resistance. Dashed line corresponds to a linear dependence (slope = -1).

Semi-logarithmic plots of the recombination resistance against open-circuit voltage reveal different trends between the two cells (Figure 4-13). They both show a linear trend over a wide voltage range, but with differing slopes. These slopes can be used to calculate the ideality factor using the relationship

$$\frac{\partial \log R_{rec}}{\partial V} = -\frac{q}{2.303 m k_B T}$$

For FB06-1 and FS43-1 this gives ideality factors of 2.7 and 4.8 respectively, which are in close agreement to the ideality factors obtained from the intensity dependence of their V_{oc} values. Again these ideality factors were consistent across pixels on the same substrate.

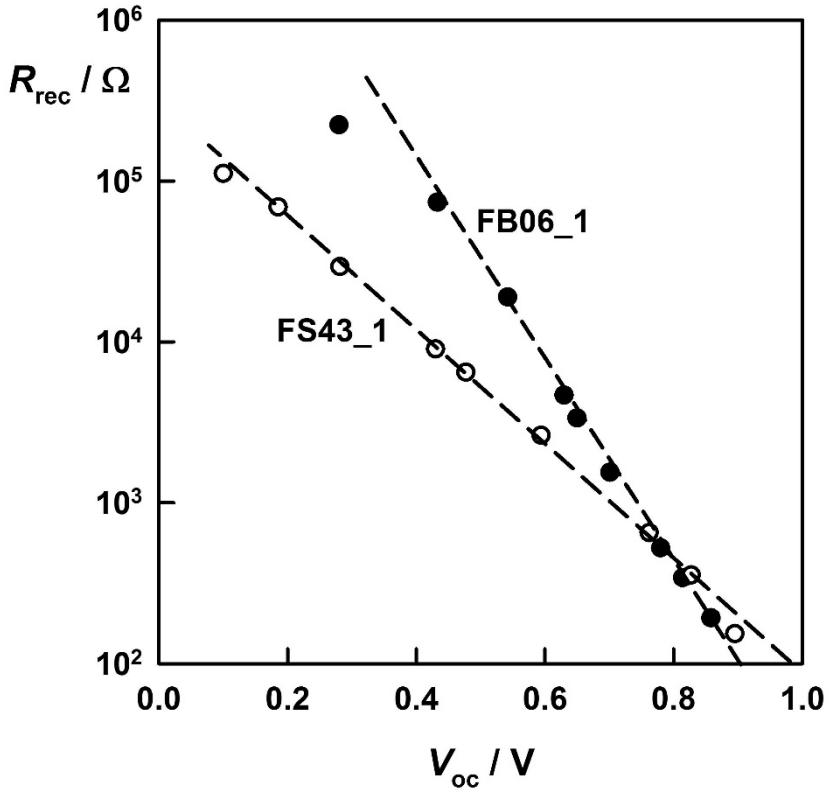

Figure 4-13: Recombination resistance as a function of open-circuit voltage measured under different light intensities.

The assumption that the ideality factor, m, does not equal the ideality factor in the dark was checked by measuring the impedance of the devices in the dark at different applied potentials. The impedance spectra were similar in shape to those obtained under illumination at open-circuit so the same equivalent circuit was used to extract values of the recombination resistance. It can be seen from Figure 4-14 that there is a clear difference in recombination in the dark and under illumination. This gives rise to different ideality factors for the two conditions which can be related to the difference in shape of the JV curves and therefore the apparent crossing of the curves at forward bias.

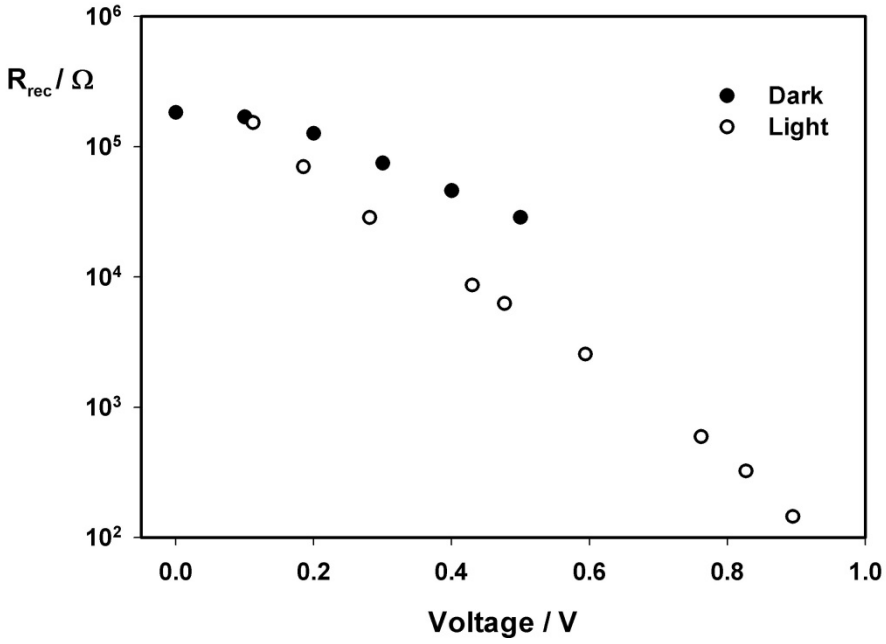

Figure 4-14: Recombination resistance values from dark impedance measurements compared to those obtained at V_{oc} under illumination. Dark impedance measurements were restricted to below 0.5 V forward bias to minimise current flow.

Perhaps the most striking result from the initial impedance analysis is the voltage dependence of the cell capacitance. To obtain a good quality fit to the impedance data it was necessary to replace the capacitor, C_{tot}, with a constant phase element (CPE) due to the depression of the semi-circle response. These are often employed to model inhomogeneity in films, leading to non-ideal capacitances[33, 34]. The impedance of a CPE is given by $Z_{CPE} = \left[T(j\omega)^P \right]^{-1}$. If the parameter 'P' is equal to 1, then the impedance represents a pure capacitance. Therefore values less than 1 represent a non-ideal capacitor, not uncommon in real systems. Figure 4-15 displays the fitting parameters obtained for the CPE representing the junction capacitance for cell FS43-1. Taking into consideration just the 'T' fit value, it appears that the junction capacitance increases with increasing voltage (similar to the build-up of a chemical capacitance). However, it can be seen that the 'P' value exhibits a similar but opposite trend. The effect of this can be seen when the 'equivalent capacitance' is calculated using the equation derived by Brug et al.[35] (see theory for discussion of Brug equation). This suggests that the capacitance is roughly constant, at around 20 nF, across the entire voltage range.

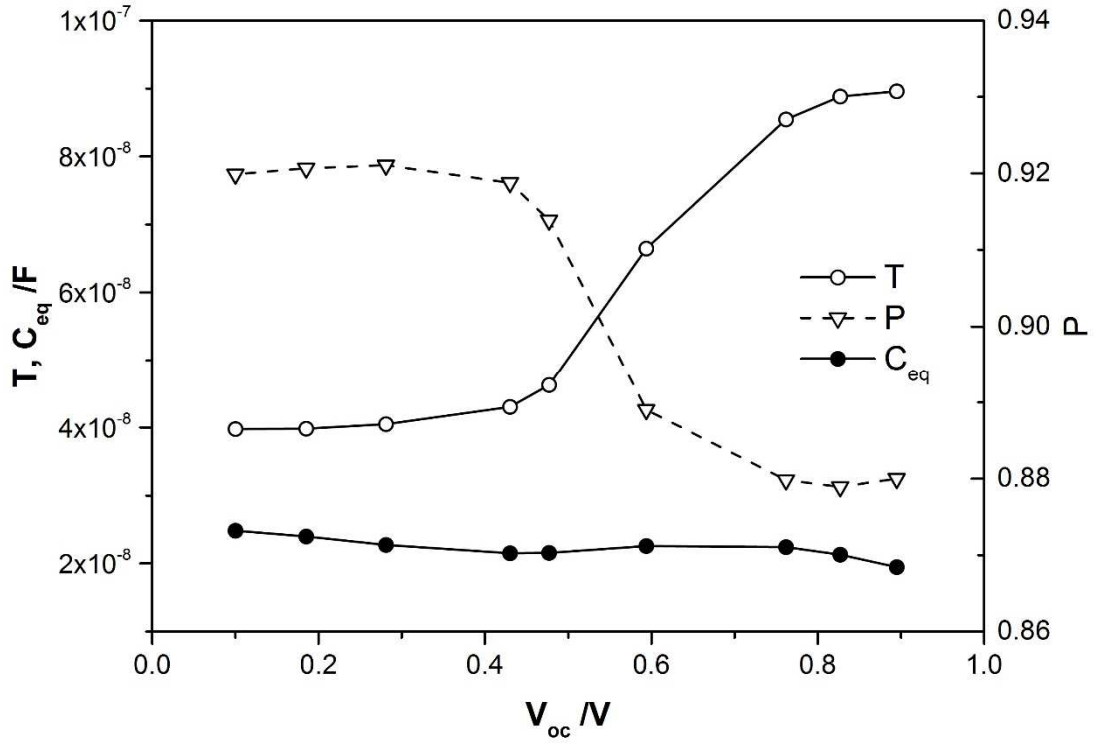

Figure 4-15: Fitting parameters obtained for the constant phase shift element used to represent the geometric capacitance of the cell. The equivalent capacitance, C_{eq}, has been calculated using the Brug equation.

This calculation of the equivalent capacitance was further reinforced in a number of ways. With a 'P' value of over 0.9 it is possible to get a reasonable fit using a pure capacitor. This removes some of the assumptions involved in the calculation of the CPE equivalent capacitance. A fit to the original equivalent circuit for the 0.1 sun data gives a capacitance value of 17 nF, in reasonable agreement with the calculated equivalent capacitance. An alternative method was to take the time constant for this arc, $\tau = 1/\omega_{max}$, and divide it by the recombination resistance. The time constant can be obtained without fitting so no assumption is made about the capacitance behaviour, and the recombination resistance can be fit with high precision using a depressed semi-circle fit. The value of capacitance calculated in this way, $C=\tau/R$, is 19 nF.

The total capacitance of the cell is a sum of the cell geometric capacitance, due to charge stored in the contacts, and the charge related to photogenerated electrons and holes, usually called the chemical capacitance, C_μ. The behaviour of a chemical capacitance is well documented, and is known to increase exponentially with voltage[17, 18]. It is clear from the capacitance-voltage trend shown here that this is not the case. We therefore see no evidence of the chemical capacitance and the constant capacitance measured should be related to the geometric capacitance. The geometric capacitance can be calculated as

$$C_g = \frac{\varepsilon_0 \varepsilon_r A}{d}$$

where ε_0 is the vacuum permittivity, ε_r is the relative dielectric constant of the perovskite, A is the active area and, d is the layer thickness. The perovskite dielectric constant has been calculated from DFT measurements to be 24.1 (the value used here)[36], with similar values found by experiment[37].

For the parameters given for the device active area ($A=0.15$ cm^2, $d=600$ nm) this gives a capacitance value of 5.3 nF. This assumes perfectly flat interfaces with the TiO_2 and spiro-OMeTAD. This is unlikely due to the roughness of the underlying FTO and the perovskite layer itself. The difference between the calculated geometric capacitance and the values calculated from impedance suggest a roughness factor of 4. This seems reasonable as roughness factors as high as 5 have been measured for mechanically polished gold electrodes[34].

The absence of any evidence of a chemical capacitance has been backed up by modelling of a perovskite layer between selective contacts (see Appendix A for full details). The geometric capacitance is shown to exceed the chemical capacitance for V_{oc} values up to around 0.9 V as shown in Figure 4-16. The geometric capacitance therefore dominates the total capacitance measured (C_{tot} is made up of the parallel combination of C_g and C_μ, therefore the largest capacitance dominates). This finding illustrates that there is no significant accumulation of electronic charge occurring within the perovskite itself, either due to conduction band electrons or trapped charge.

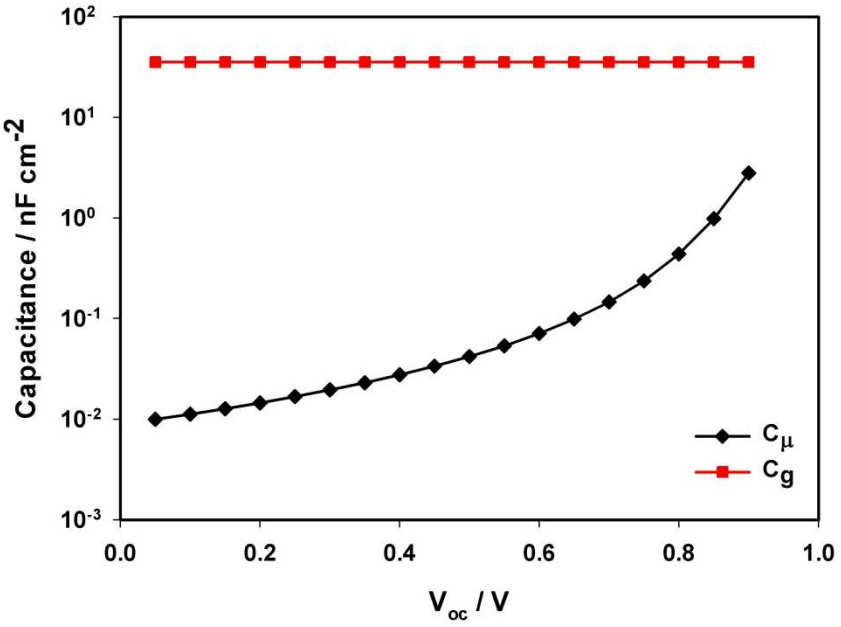

Figure 4-16: Calculated values of chemical capacitance compared to the cells geometric capacitance for a similar voltage range as studied experimentally. Even at the highest V_{oc} of 0.9 V the chemical capacitance is an order of magnitude smaller than the geometric capacitance and so will not be observed. See Appendix for modelling details.

4.4.4 Intensity modulated photovoltage spectroscopy

IMVS measurements were performed to compliment the impedance analysis. Again these were carried out over the same intensity, and therefore V_{oc} range. The technique was widely used in DSSC analysis to investigate recombination. No charge is extracted during IMVS measurements as the cell is held at open-circuit as the light signal is perturbed. It is therefore not possible to study transport processes. As the high frequency impedance response from planar cells is associated to recombination, the IMVS response can be expected to appear similar. Figure 4-17 shows the IMVS response for cell FS43-1 under 0.1 sun illumination. The high frequency arc can be related to the same arc present at high frequencies in impedance. In the absence of the chemical capacitance, these time constants relate to $\tau=R_{rec}C_g$.

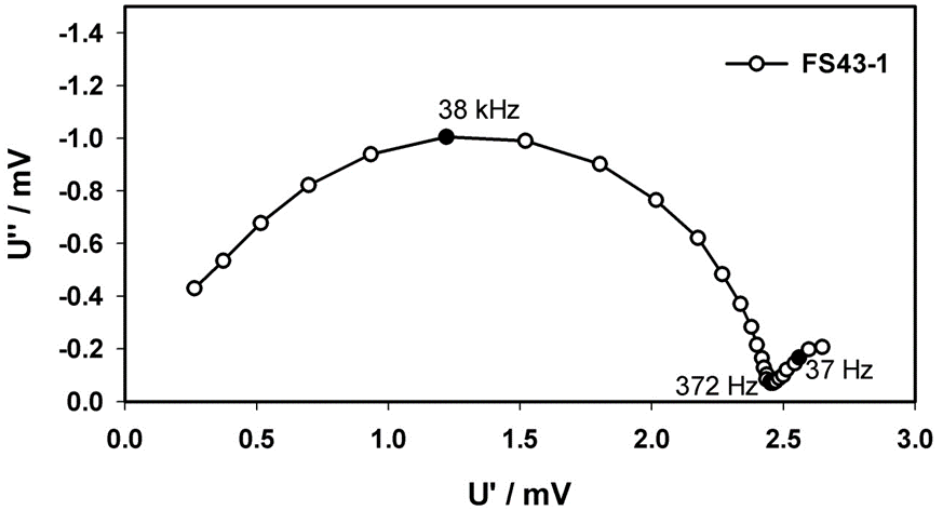

Figure 4-17: IMVS spectra obtained under an illumination intensity equivalent to 0.1 sun.

Time constants were extracted from the IMVS response by taking the inverse of the radial frequency corresponding to the maximum of the imaginary component. Plotted against V_{oc} the time constants are shown to have different trends for the two types of cell (Figure 4-18). Again an ideality factor can be calculated, giving m=2.52 and m=4.86 for cells FB06-1 and FS43-1 respectively. These are consistent with the ideality factors calculated using the other methods. IMVS results are discussed further in Chapter 6.

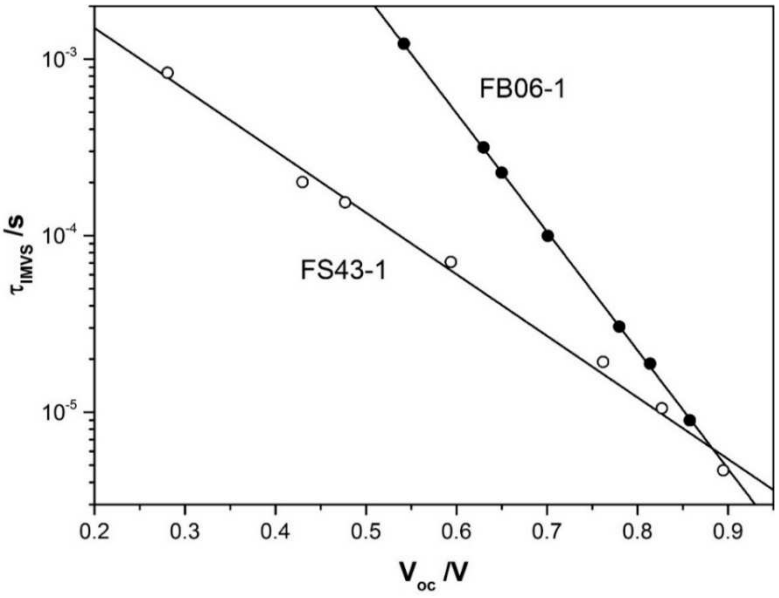

Figure 4-18: IMVS lifetime as a function of open-circuit photovoltage.

The IMVS time constant dependence on light intensity shows a remarkable similarity between the two cells, especially seeing as though the V_{oc} values at each intensity are markedly different (Figure 4-19). The slope of the intensity trend is actually comparable to the recombination resistance dependence on light intensity. This indicates that the capacitance of the cell must be constant and that it does not increase exponentially as it would if a large chemical capacitance was present.

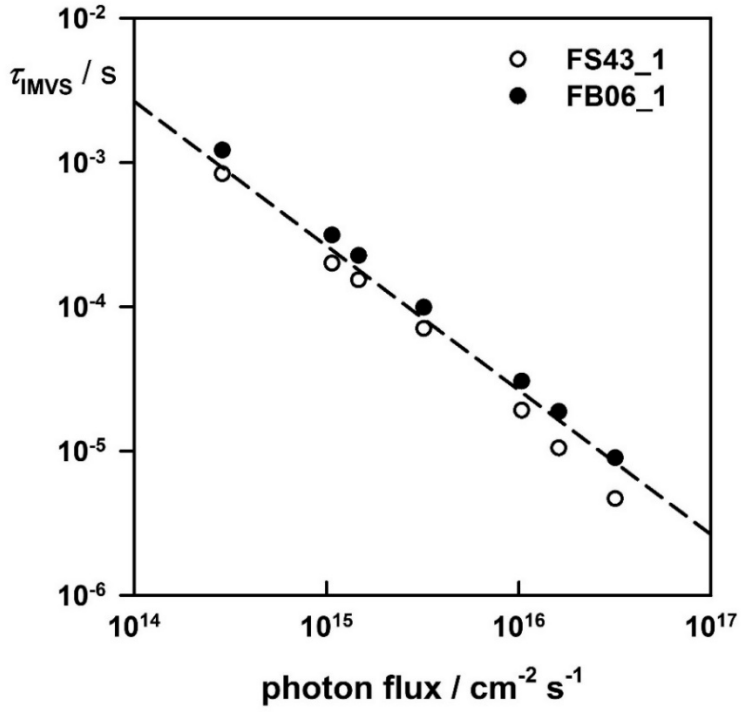

Figure 4-19: IMVS lifetime as a function of light intensity. Dashed line represents a linear dependence.

At the highest light intensity the time constant obtained is 4.7 μs for cell FS43-1. Along with the linear dependence on intensity, this suggests agreement with recombination lifetimes (~1 μs at 1 sun) determined from transient photovoltage measurements by O'Regan et al. for mesoporous samples[5]. The capacitance can once again be calculated by dividing the IMVS time constant by the recombination resistance obtained from EIS. This also gives capacitance values in the region of 20 nF that are constant across the intensity range.

4.4.5 Intensity modulated photocurrent spectroscopy

The IMPS response was used extensively in the DSSC community to measure electron transport through the mesoporous titania. The electron transport is relatively slow as electrons are trapped in shallow states below the conduction band as they diffuse through the TiO_2. They require thermal energy to be released back to the conduction band. However, without a high concentration of trap states carrier transport will be much faster and possibly beyond the range of IMPS measurements. The high frequency IMPS response is limited by the attenuation due to the RC time constant of a solar cell, which corresponds to $R_{ser}C_{tot}$[38]. The lower frequency response may reveal information about recombination at short-circuit, as is the case for measurements on illuminated semiconductor-electrolyte junctions[39].

IMPS measurements were carried out in conjunction with the IMVS measurements at the same intensity, frequency range and modulation amplitude. The cell was held at short-circuit by a low-noise current amplifier. A typical IMPS response is shown in Figure 4-20.

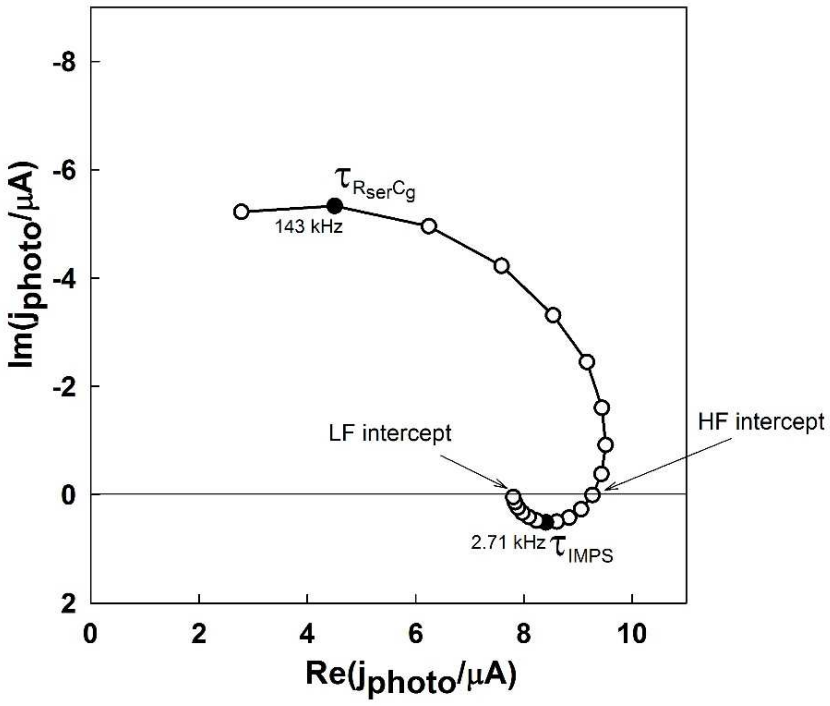

Figure 4-20: IMPS response at 0.1 sun. The maximum of the high frequency arc gives the RC time constant of the cell, $R_{ser}C_g$. The lower frequency arc is related to the rate constants for interfacial transport and recombination.

The high frequency semi-circle in the upper quadrant can be attributed to the RC time constant of the cell, $R_{ser}C_g$. For cell FS43-1 at the highest light intensity, the RC time constant calculated from IMPS is τ =1.04 μs. Taking the series resistance calculated from impedance to be R_{ser}=40 Ω (area normalized series resistance is 6 Ω cm^2) gives a calculated capacitance of C_{tot}=26 nF. This value is slightly higher than the capacitance calculated using the other techniques but it is nevertheless in the same region, and also shows an invariance with light intensity. This reconfirms the previous calculations of the capacitance value without making assumptions about the nature of the capacitor (CPE ideality).

The second lower frequency semicircle in the lower quadrant is similar to that observed for illuminated semiconductor-electrolyte interfaces, where it relates to the change of the minority carrier concentration at short-circuit due to charge transfer and recombination at the electrode surface. The rate constants for these two processes can be calculated from the intercepts of this semi-circle with the x-axis, and the time constant associated to the radial frequency of the minimum point[40]. The high frequency intercept corresponds to the instantaneous photocurrent (before recombination), and the low frequency intercept gives the steady state value. The inverse of the time constant gives the sum of the two rate constants, $\tau_{IMPS}^{-1}=k_{trans}+k_{rec}$. This time constant represents relaxation at short circuit and should not be confused with the recombination time constant measured at open-circuit using IMVS. The ratio of the low frequency intercept to the high frequency intercept gives the charge collection efficiency, $\eta_{cc}= k_{trans}/(k_{trans}+k_{rec})$.

The low frequency IMPS response for these perovskite cells is therefore attributed to interfacial recombination and transport at short-circuit. It is possible that this is related to the perovskite/spiro-OMeTAD interface, due to the spiro essentially acting as a solid electrolyte. Values for the rate constants, relaxation time constant and charge collection efficiency were calculated as a function of light intensity. Figure 4-21 shows the charge collection efficiency calculated for cells FS43-1 and FB06-1. The charge collection efficiency is higher for FS43 across the intensity range, consistent with its higher short-circuit current value. The reasoning behind the minima observed in the charge collection efficiency trend is unclear.

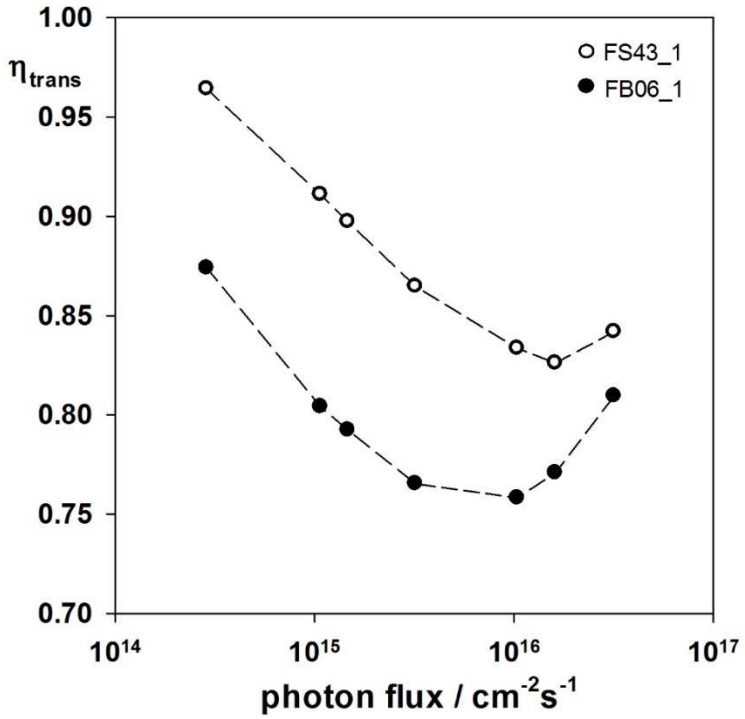

Figure 4-21: Charge collection efficiency at different light intensities.

The relaxation time of the short-circuit photocurrent shows a linear intensity dependence, with similar rates for each cell (Figure 4-22). These short-circuit current relaxation lifetimes are longer than for the recombination lifetimes at open-circuit, τ_{IMVS}.

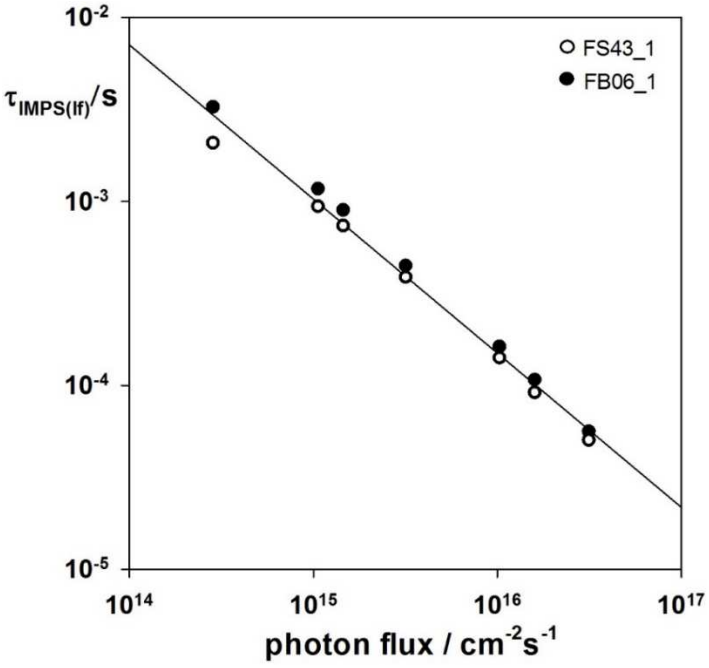

Figure 4-22: Low frequency IMPS time constant dependence on light intensity.

The rate constants for interfacial transport and recombination also have a strong intensity dependence as shown in Figure 4-23. The rate constant for transport, k_{trans}, is roughly an order of magnitude higher than for recombination. This is indicative of a high external quantum efficiency and therefore high short-circuit current. Cell FS43-1 has a greater separation between k_{trans} and k_{rec} than for FB06-1, which again helps to explain its higher photocurrent value under 1 sun illumination.

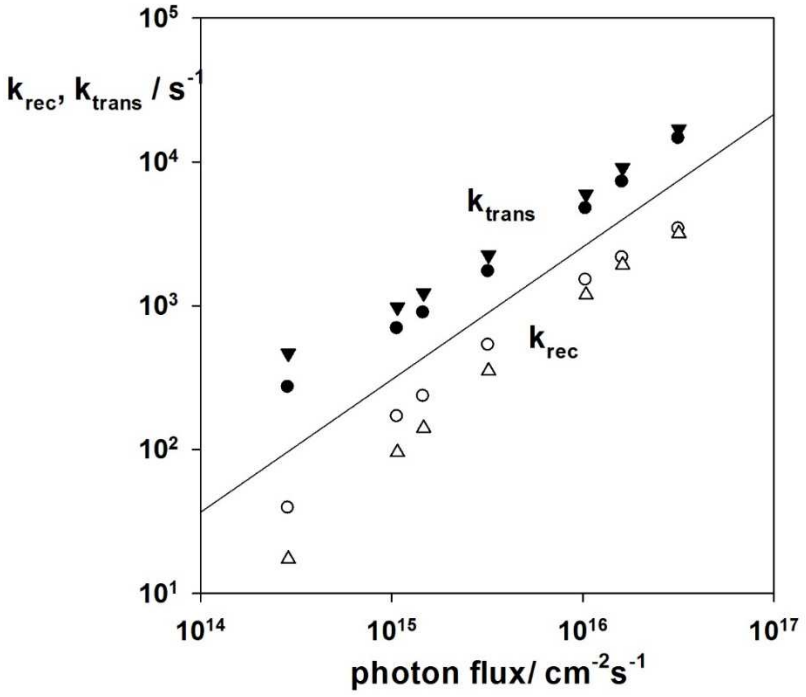

Figure 4-23: Recombination and transport rate constant dependence on light intensity.

4.5 Discussion

A consistent trend existed between two separate groups of cells demonstrating a range of properties that varied with the measured ideality factor. The ideality factor was determined first by the intensity dependence of the open-circuit photovoltage. Roughly half of the measured cells gave ideality factors around m=2.6, with the other half having ideality factors around m=5.2. This grouping of the ideality factors was consistent throughout other measurements, including the voltage dependence of the recombination resistance and IMVS lifetime. It is unclear what the exact mechanism is that determines this difference in ideality factor as all cells were produced at the same time, using seemingly identical methods. The most likely differences between the cells is the potential for differences in morphology due to slight inconsistencies with annealing temperature on the hotplate surface. It is reasonable to expect that variations in the crystallization of the perovskite layer may lead to differences in dominant recombination mechanisms. Diode ideality factors greater than 2 are uncommon. A possible explanation for such high ideality factors is a high rate of interfacial recombination[41-43]. The similarities in 1 sun performance between all cells, regardless of ideality factor, suggests that these recombination mechanisms are supressed at high intensity. However, this is an important consideration for commercially relevant cells where good low light performance is important.

The capacitance associated with the high frequency response has been related to the geometric capacitance of the perovskite layer. No evidence of charge accumulation (chemical capacitance) within the perovskite layer was found as the capacitance was found to be constant across the measured voltage range. The constant capacitance was observed using impedance fitting, analysis of the IMVS time constant and the RC attenuation of the IMPS measurement.

This highlights that the chemical capacitance observed elsewhere for mesostructured cells is due to the TiO_2 and not the perovskite. The capacitance nature of planar perovskite layers has subsequently been studied by Guerrero et al. who confirmed the finding that the geometric capacitance dominates the response[44]. The absence of a chemical capacitance has a consequence on the definition of the time constant derived from the high frequency response. It is not strictly correct to relate this time

constant to the electron lifetime when the capacitance does not relate to charge accumulation in the active layer. The high frequency time constants measured using IMVS and EIS are in agreement, and have been related to

$$\tau = R_{rec} C_g$$

where R_{rec} is the recombination resistance and C_g the geometric capacitance. The parallel resistance has been confirmed as being related to recombination due to its linear dependence on light intensity. The lifetimes measured from these frequency domain measurements therefore relate to the discharge of the geometric capacitance through the recombination resistance.

The IMPS response does not show any evidence of charge transport in the perovskite as this occurs on timescales beyond the limit of the measurement. The high frequency response therefore represents the RC time constant of the cell given by the product of the series resistance and geometric capacitance. Evidence of interfacial recombination at short-circuit has been observed in the low frequency IMPS response. High charge collection efficiencies have been calculated, consistent with the high short-circuit photocurrent values obtained from the devices under 1 sun illumination.

4.6 Conclusion

The high frequency response of planar heterojunction perovskite cells has been studied using a range of complimentary frequency domain techniques. A number of interesting properties have been uncovered which aid the deeper understanding of device operation. The response was shown to be dominated by the time constant corresponding to the geometric capacitance and recombination resistance. No chemical capacitance, relating to photogenerated charge in the perovskite layer, has been observed.

Although all the devices tested showed comparable performance at high light intensity, distinct variations were observed at lower light intensity. This gave rise to differences in ideality factor between m=2.6 and m=5.2. This shows that although performance under the standard testing conditions was similar, there may be very different recombination mechanisms occurring within different devices which become more apparent at low intensity. This difference in operation is also clearly observed in open-circuit voltage decay measurements shown in Chapter 6.

4.7 References

1. A. Dualeh, T. Moehl, N. Tétreault, J. Teuscher, P. Gao, M. K. Nazeeruddin and M. Grätzel, *ACS nano*, 2014, **8**, 362-373.
2. V. Gonzalez-Pedro, E. J. Juarez-Perez, W.-S. Arsyad, E. M. Barea, F. Fabregat-Santiago, I. Mora-Sero and J. Bisquert, *Nano Lett.*, 2014, **14**, 888-893.
3. H.-S. Kim, I. Mora-Sero, V. Gonzalez-Pedro, F. Fabregat-Santiago, E. J. Juarez-Perez, N.-G. Park and J. Bisquert, *Nat. Commun.*, 2013, **4**, 2242.
4. E. Guillén, F. J. Ramos, J. A. Anta and S. Ahmad, *J. Phys. Chem. C*, 2014, **118**, 22913–22922.
5. B. C. O'Regan, P. R. F. Barnes, X. Li, C. Law, E. Palomares and J. M. Marin-Beloqui, *J. Am. Chem. Soc.*, 2015, **137**, 5087-5099.
6. F. Giordano, A. Abate, J. P. Correa Baena, M. Saliba, T. Matsui, S. H. Im, S. M. Zakeeruddin, M. K. Nazeeruddin, A. Hagfeldt and M. Graetzel, *Nat. Commun.*, 2016, **7**, 10379.
7. M. M. Lee, J. Teuscher, T. Miyasaka, T. N. Murakami and H. J. Snaith, *Science*, 2012, **338**, 643-647.
8. I. Chung, B. Lee, J. He, R. P. H. Chang and M. G. Kanatzidis, *Nature*, 2012, **485**, 486-489.
9. H. Zhou, Q. Chen, G. Li, S. Luo, T.-b. Song, H.-S. Duan, Z. Hong, J. You, Y. Liu and Y. Yang, *Science*, 2014, **345**, 542-546.
10. M. Liu, M. B. Johnston and H. J. Snaith, *Nature*, 2013, **501**, 395-398.
11. F. Fabregat-Santiago, G. Garcia-Belmonte, J. Bisquert, A. Zaban and P. Salvador, *J. Phys. Chem. B*, 2002, **106**, 334-339.
12. J. Bisquert, *J. Phys. Chem. B*, 2002, **106**, 325-333.
13. K. Kalyanasundaram, *Dye-sensitized Solar Cells*, EFPL Press, 2010.
14. S. D. Stranks, G. E. Eperon, G. Grancini, C. Menelaou, M. J. P. Alcocer, T. Leijtens, L. M. Herz, A. Petrozza and H. J. Snaith, *Science*, 2013, **342**, 341-344.
15. C. Wehrenfennig, G. E. Eperon, M. B. Johnston, H. J. Snaith and L. M. Herz, *Adv. Mater.*, 2014, **26**, 1584-1589.
16. G. Xing, N. Mathews, S. Sun, S. S. Lim, Y. M. Lam, M. Grätzel, S. Mhaisalkar and T. C. Sum, *Science (New York, N.Y.)*, 2013, **342**, 344-347.
17. J. Bisquert, *PCCP*, 2003, **5**, 5360-5364.
18. J. van de Lagemaat, N. G. Park and A. J. Frank, *J. Phys. Chem. B*, 2000, **104**, 2044-2052.
19. J. Bisquert, D. Cahen, G. Hodes, S. Rühle and A. Zaban, *J. Phys. Chem. B*, 2004, **108**, 8106-8118.
20. G. Garcia-Belmonte, A. Guerrero and J. Bisquert, *J. Phys. Chem. Lett.*, 2013, **4**, 877-886.
21. J. A. Carr and S. Chaudhary, *Appl. Phys. Lett.*, 2012, **100**, 213902.

22. F. Fabregat-Santiago, G. Garcia-Belmonte, I. Mora-Sero and J. Bisquert, *PCCP*, 2011, **13**, 9083-9118.

23. Y. Zhao, A. M. Nardes and K. Zhu, *J. Phys. Chem. Lett.*, 2014, **5**, 490-494.

24. Y. Zhao, A. M. Nardes and K. Zhu, *Farad. Discuss.*, 2014, **176**, 301-312.

25. E. Guillén, L. M. Peter and J. A. Anta, *J. Phys. Chem. C*, 2011, **115**, 22622-22632.

26. J. Bisquert and V. S. Vikhrenko, *J. Phys. Chem. B*, 2004, **108**, 2313-2322.

27. J. Villanueva-Cab, H. Wang, G. Oskam and L. M. Peter, *J. Phys. Chem. Lett.*, 2010, **1**, 748-751.

28. L. Jiang, J. Lyou, S. Rane, E. Schiff, Q. Wang and Q. Yuan, *MRS Proceedings*, 2000, **609**.

29. R. Gottesman, E. Haltzi, L. Gouda, S. Tirosh, Y. Bouhadana, A. Zaban, E. Mosconi and F. De Angelis, *J. Phys. Chem. Lett.*, 2014, **5**, 2662–2669.

30. Y. Li, W. Yan, Y. Li, S. Wang, W. Wang, Z. Bian, L. Xiao and Q. Gong, *Sci. Rep.*, 2015, **5**, 14485.

31. G. Zhang and R. Zhu, *Electroanalysis*, 2010, **22**, 351-358.

32. G. Garcia-Belmonte, P. P. Boix, J. Bisquert, M. Sessolo and H. J. Bolink, *Sol. Energy Mater. Sol. Cells*, 2010, **94**, 366-375.

33. U. Rammelt and G. Reinhard, *Electrochim. Acta*, 1990, **35**, 1045-1049.

34. E. F. Douglass Jr, P. F. Driscoll, D. Liu, N. A. Burnham, C. R. Lambert and W. G. McGimpsey, *Anal. Chem.*, 2008, **80**, 7670-7677.

35. G. J. Brug, A. L. G. van den Eeden, M. Sluyters-Rehbach and J. H. Sluyters, *J. Electroanal. Chem. Interfac.*, 1984, **176**, 275-295.

36. F. Brivio, K. T. Butler, A. Walsh and M. van Schilfgaarde, *Phys. Rev. B*, 2014, **89**, 155204.

37. N. Onoda-Yamamuro, *J. Phys. Chem. Solids*, 1992, **53**, 935-935.

38. L. Dloczik, O. Ileperuma, I. Lauermann, L. M. Peter, E. A. Ponomarev, G. Redmond, N. J. Shaw and I. Uhlendorf, *J. Phys. Chem. B*, 1997, **101**, 10281-10289.

39. L. M. Peter, K. G. U. Wijayantha and A. A. Tahir, *Farad. Discuss.*, 2012, **155**, 309-322.

40. L. M. Peter, *J. Solid State Electrochem.*, 2013, **17**, 315-326.

41. U. Rau, *Appl. Phys. Lett.*, 1999, **74**, 111-113.

42. M. Eron and A. Rothwarf, *J. Appl. Phys.*, 1985, **57**, 2275-2279.

43. J. Verschraegen, M. Burgelman and J. Penndorf, *Thin Solid Films*, 2005, **480–481**, 307-311.

44. A. Guerrero, G. Garcia-Belmonte, I. Mora-Sero, J. Bisquert, Y. S. Kang, T. J. Jacobsson, J.-P. Correa-Baena and A. Hagfeldt, *J. Phys. Chem. C*, 2016, **120**, 8023-8032.

5 The low frequency response of planar perovskite cells

5.1 Abstract

The low frequency response of planar perovskite solar cells is investigated using impedance and intensity modulated voltage spectroscopies. This study required improved cell stability due to the extended length of the measurements when measuring to frequencies as low as 3 mHz.

The combination of impedance and IMVS measurements shows that there are two additional processes occurring to that observed in the high frequency response shown in Chapter 4. These lower frequency processes are shown to be linked to ionic movement using temperature dependent measurements. Activation energies for these two processes of around $E_A = 0.55$ eV are comparable to computationally derived values for iodide migration within the perovskite. It is shown that the recombination rate decreases on the timescale of this ionic migration.

5.2 Introduction

The existence of slow dynamic processes in perovskite solar cells is well established. This is most commonly observed as hysteresis in the current-voltage curve during device efficiency measurements[1, 2]. Slow processes are also frequently observed in a wider range of more diagnostic techniques including photovoltage and photocurrent transient measurements[3-5], photoluminescence[6] and impedance spectroscopy[7-10]. Whilst not studied in detail, additional slow processes were also observed in Chapter 4. For example, an extra feature appeared to emerge in the frequency resolved measurements below 100 Hz.

The origin of the low frequency impedance response has been attributed to several different processes in the literature. These include: the filling and emptying of trap states[11], a giant dielectric effect[9], electron accumulation at the contacts[12], and ionic migration[8].

Early work still focused on the use of models previously implemented for dye-sensitized solar cells. These include the use of a transmission line to describe electron transport and recombination[13, 14]. This model seems unfeasible considering the low frequencies that this apparent feature was observed at (below 1 kHz) and the high carrier mobilities measured for perovskites.

Theories then progressed away from those relating to processes observed in DSSC. It became clear that it was unlikely that transport processes would be observed on the time scales probed by frequency response techniques, typically longer than 100 ns. It was also apparent that the low frequency response was part of a more complex process than being purely electronic in nature. A link between this low frequency behaviour and the commonly observed hysteresis phenomenon was established[5], with initial origins placed in a frequency dependent dielectric constant[9]. This was labelled the 'Giant Dielectric Effect' (GDE) and was thought to be linked to the possibility of methylammonium molecular dipoles becoming aligned in an applied electric field[15, 16]. The extent of ferroelectric domain structure was thought to have a significant effect on electron-hole recombination properties[17, 18]. This hypothesis has since been ruled out by conductance hysteresis measurements that show that the

hysteretic charge density is too high for ferroelectric contributions[19]. It has also been calculated that ferroelectric effects would occur on shorter timescales than the observed JV hysteresis/low frequency response[20].

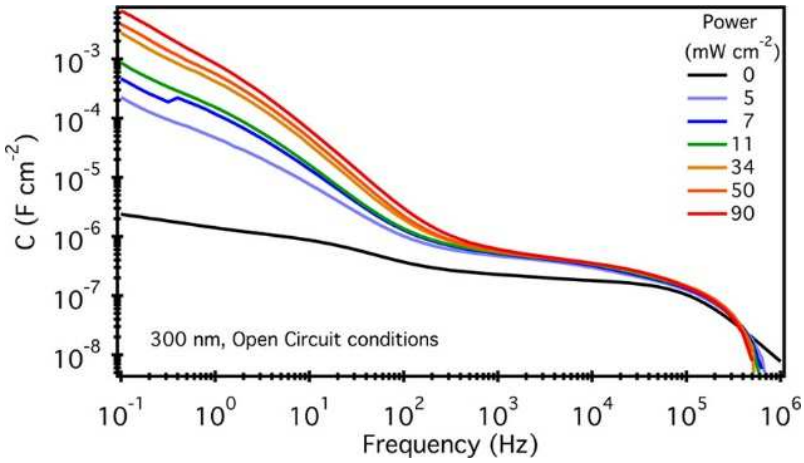

Figure 5-1: Capacitance spectra measured under different light intensities by Zarazua et al. The low frequency capacitance shows a linear dependence on light intensity.

In terms of impedance measurements, this GDE was observed as a large increase in the complex capacitance spectra at low frequencies (Figure 5-1). Whereas at high frequencies the dielectric constant was found to be around 20, at frequencies below 1 Hz it could exceed 1000. Under illumination this could rise to 10^6. This dielectric relaxation effect was included in a complete device model by Bisquert et al.[7], although little experimental evidence was ever shown to support the model. More recently this large increase in capacitance at low frequency has been attributed to electronic accumulation at the TiO_2 interface coupled with ionic defect formation[21].

The presence of mobile ionic species in the perovskite has been shown in a range of measurements including impedance spectroscopy of perovskite pellets[22], XPS measurements of the Pb/I ratio after biasing[23] and microscopy imaging of the degradation near to the contacts during biasing[24, 25]. Computational studies have shown that the ionic defect concentration of the perovskite is high at room temperature[26], and that several possible mobile defects exist with relatively low activation energies[27-30]. The most mobile ionic species are thought to be iodide vacancies.

Bag et al. performed EIS measurements on planar perovskite cells utilizing organic contacts[8]. These measurements showed a similar low frequency feature to that observed elsewhere in literature (shown in Figure 5-2). However, the feature does

appear at higher frequencies than for cells containing TiO_2 and Spiro contacts. This appears to compliment work by Bryant et al. which shows that for organic contact devices hysteresis is observed when the cell is cooled[31]. This suggests that whatever process is influencing the slow dynamic electrical behaviour of these devices occurs at a faster rate for cells with organic contacts.

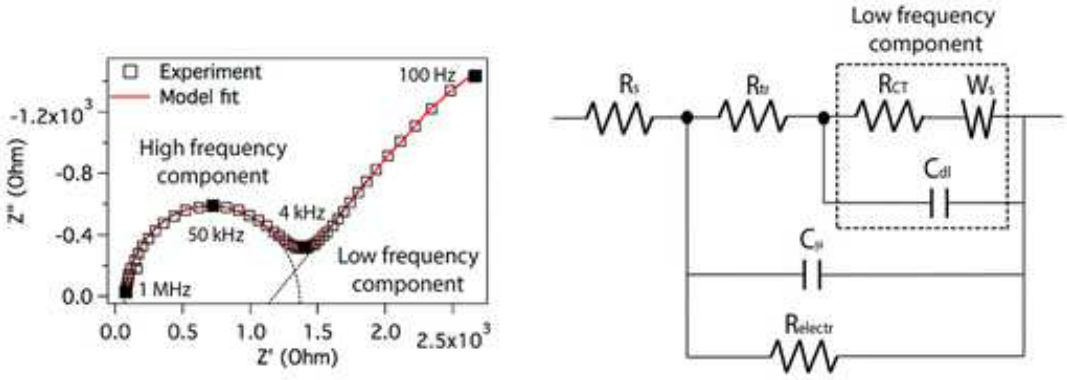

Figure 5-2: Impedance spectra measured and equivalent circuit used to fit the data by Bag et al.[8]

Bag et al. modelled the low frequency response using a finite length Warburg diffusion element to describe ionic diffusion through the bulk perovskite. They assigned this to a pure ionic impedance, but the use of a shorted Warburg (with resistive behaviour at low frequency) would represent the contact materials being permeable to the ionic species, which seems unlikely. Spectra were only recorded down to 100 Hz and so the low frequency feature is not completely resolved. The equivalent circuit is also quite complicated for a relatively simple spectra, with a number of elements that are not well defined. From the time constant of the diffusion process they calculated an activation energy of 0.58 eV, which was assigned to MA^+ migration. This was based on the activation energies calculated by Azpiroz et al.[27] which appear to be inconsistent with other publications. Azpiroz et al. calculated the activation energies for I^- and MA^+ migration to be 0.08 eV and 0.46 eV respectively. Other publications give iodide activation energies in the range 0.3-0.58 eV[28-30]. Activation energies for the MA^+ ion migration are thought to be higher than 0.7 eV due to the ions rotational motion inhibiting its ability to pass through the lattice cage[28, 29].

The primary reason for not investigating these slow processes further in the previous chapter was device stability. For example in impedance spectroscopy, a process with

a time constant of 10 seconds requires measurements to frequencies below 15 mHz in order to be resolved clearly. As at least one complete sinusoidal wave period is required the 15 mHz impedance measurement takes a minimum of around 1 minute. To increase the signal-to-noise ratio of the measurements it is often required that multiple cycles are recorded and then averaged, particularly time consuming at low frequencies. The total time taken to measure a complete impedance spectrum down to a few mHz can often be in excess of 30 minutes, during which the open-circuit voltage of the cell needs to remain stable.

The cells studied in this chapter showed enhanced intrinsic stability compared to those tested in Chapter 4, possibly due to improved perovskite film quality. The perovskite film was deposited using a toluene-assisted drenching method which has been shown to produce larger grains than in the standard annealing method[32]. It has been suggested that degradation due to the presence of oxygen and/or moisture is faster at grain boundaries, therefore a higher quality film may well show increased stability[33, 34].

5.3 Experimental

The perovskite cell fabrication was carried out by Giles Eperon and Nobuya Sakai at the University of Oxford.

Perovskite solar cell fabrication: A batch of planar perovskite cells was fabricated using identical precursor and substrate preparation techniques to those used in Chapter 4. The only difference in the preparation route was a modified perovskite deposition technique. This utilized a "solvent engineering" method similar to those shown in literature to produce high quality perovskite layers[35].

The perovskite layer was deposited onto the TiO_2 compact layer using a two-step spin coating process[36]. The non-stoichiometric mixed halide precursor solution, $MAPbI_{3-x}Cl_x$ in DMF, was spin coated onto the substrate first at 1200 rpm for 25 seconds, followed by a second step at 2000 rpm for 12 seconds. At the beginning of the second step, 350 μL of toluene was dropped onto the pre-crystallized film. The perovskite film was annealed at 100 °C for 90 minutes, then at 120 °C for a further 10 minutes. The resultant thickness of the perovskite layer was 425 nm as measured by SEM.

The cells were completed by spin-coating a Spiro-OMeTAD layer on top of the perovskite film, before thermal evaporation of a gold metal contact. The device active area, as determined by the overlap of the gold contact with the underlying FTO, was 0.119cm^2 (a slightly different evaporation ask was used to in the previous chapter, giving a smaller active area).

Characterization: The cells were characterized by EIS and IMVS using a Solartron ModuLab XM Photoelectrochemical Test System with optical bench attachment. Impedance measurements were performed at different light intensities under open-circuit conditions over a frequency range of 1 MHz to 3 mHz. IMVS measurements were performed from 200 kHz to 3mHz utilizing the Modulab's reference photodiode to correct for phase lag and attenuation of the LED signal at high frequency. Illumination was provided by a blue LED (470 nm) at intensities between 73 mW cm^{-2} and 1 mW cm^{-2}. The highest intensity produced a photocurrent equivalent to the 1 sun AM1.5 value.

Samples were mounted in a desiccated cell holder with quartz window that maintained a dry environment (<10% RH). Additional temperature controlled measurements were performed using a similar cell holder incorporating a Peltier element. The temperature was controlled using a USB controller (Meerstetter Engineering) which delivered a purely DC current to the Peltier module. A different temperature controller was initially tested but its high frequency pulse width modulated (PWM) output signal induced significant interference in the electrical measurements. A 5 kΩ NTC thermistor was placed on the sample surface to monitor the temperature as part of the controllers PID feedback loop. The Peltier element was mounted on a water cooled copper heatsink to extract heat efficiently from the hot side. The water cooling system utilised a pump and radiator with fan that were kept outside of the measurement faraday cage to eliminate sources of interference. The sample holder was also placed inside a desiccated box, with quartz window, to reduce the chances of condensation forming on the cells at low temperatures. The temperature range used was -25 to +65 °C in 10 °C increments. Temperature stability was ±0.01 °C at the set point.

5.4 Results

It is clear from the results shown in Chapter 4 that the complete impedance spectrum has not been resolved at the frequencies measured. In that work, attempts to measure to lower frequencies resulted in a large decrease in the open-circuit voltage of the cell during the measurement. As the measurement was performed under potentiostatic conditions, with the potential held at the steady-state V_{oc}, a background current begins to flow as the cell degrades. It is very important that the device is at steady state during impedance measurements at open-circuit, therefore the analysis becomes invalid when the V_{oc} drifts. It appeared that the V_{oc} decrease over time under illumination was due to degradation, and not as the result of a dynamic process similar to the slow increase in voltage under illumination as the same V_{oc} values could not be achieved in subsequent measurements even after the device was allowed to relax in the dark.

The main focus in preventing this V_{oc} decrease was minimizing the impact of degradation due to moisture. This has been postulated and discussed anecdotally to be the main degradation pathway of the perovskite layer[33, 37-39], although other factors such as light and oxygen have also been shown to have an effect[40]. The use of the desiccated cell holder, and the better-quality perovskite films, enabled continuous measurements to be performed for several hours without any significant drift in cell performance. As an aside, it was noted that the cells were less stable under the highest light intensity and so the longest measurements were performed under slightly lower illumination levels. Although not part of a controlled degradation study this adds weight to the theory of degradation caused by reactive oxygen species under illumination and in the absence of moisture[40-42]. The measurements were performed in a dry air atmosphere rather than an inert nitrogen atmosphere in case the lack of oxygen would impact upon the performance of the titanium dioxide and spiro-OMeTAD layers[43-45].

5.4.1 Summary of test devices

The devices tested in this chapter have the same planar heterojunction architecture as in Chapter 4. The only significant difference between the two batches is the modified perovskite layer deposition method (see experimental section above for details), which resulted in a slightly thinner perovskite layer of 425 nm. The cell arrangement was also changed, with 8 pixels per substrate. There were three device substrates giving a total of 24 pixels. The three best pixels from each device were chosen for further testing. Pixels are numbered 1 to 8, and are referred to by the cell name followed by pixel number, e.g. EY-4. The cells measured in this chapter were labelled EY, CT and CZ. The total active area of each pixel was 0.119 cm^2, again defined by the overlap of the FTO and evaporated gold contact.

Device efficiencies were measured under a solar simulator with the cells masked to an illuminated area of 0.092 cm^2 (cells were unmasked for all subsequent measurements to ensure homogeneous illumination of the complete active area). An example J-V curve is shown in Figure 5-3. For this batch of cells the J-V curves were measured by sweeping the potential in two different directions. Firstly, the voltage was swept from forward bias (+1.4 V) to short-circuit (FB-SC). The sweep direction was then reversed to scan from short-circuit to forward bias (SC-FB). The scan rate was 380 mV s^{-1}. Measuring in this way reveals the extent of J-V hysteresis in the devices. It can be seen in Figure 5-3, that the predominant effect is a reduction in fill factor and slight reduction in V_{oc} for the SC-FB scan direction. Clearly this leads to a reduction in the calculated efficiency value.

In order to try and establish the true device efficiency a potentiostatic measurement was performed at the voltage of the maximum power point for the FB-SC scan as shown in Figure 5-4. The stabilized current value was then used to calculate a more reliable maximum power point and from that the stabilized efficiency.

The cells tested in this chapter had an average stabilized efficiency of 11.90% under 1 Sun AM1.5 illumination (averages and standard deviation of performance parameters are shown in Table 2).

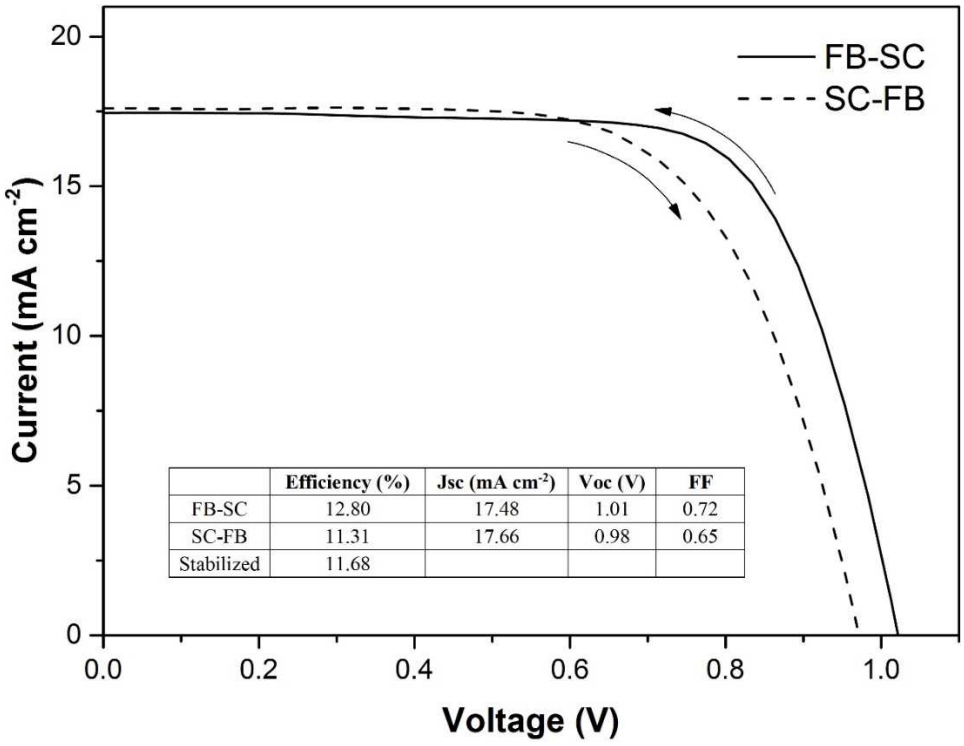

	Efficiency (%)	Jsc (mA cm^{-2})	Voc (V)	FF
FB-SC	12.80	17.48	1.01	0.72
SC-FB	11.31	17.66	0.98	0.65
Stabilized	11.68			

Figure 5-3: J-V curve under 1 sun AM1.5 illumination for cell CT-4. Voltage was swept in both directions at a rate of 380 mV s^{-1}.

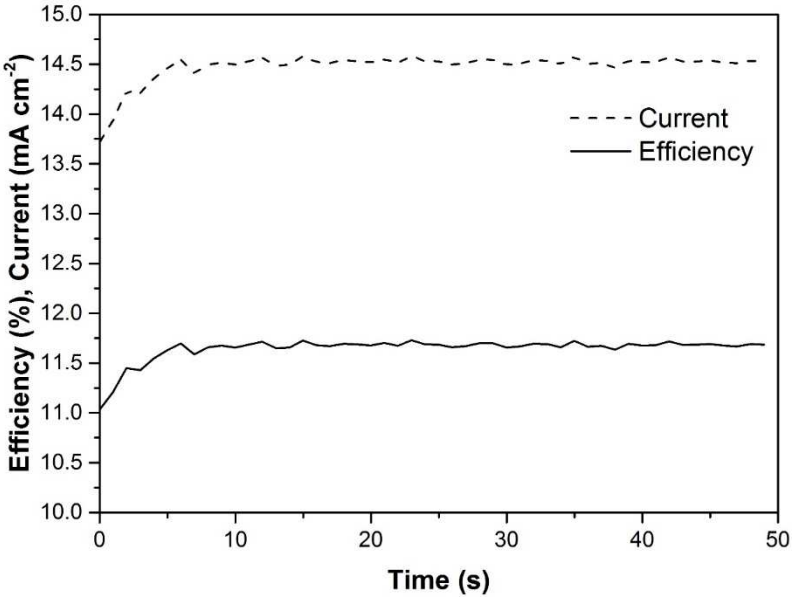

Figure 5-4: Stabilized efficiency measurement for cell CT-4. Potential is held at V_{mp}=0.80 V as measured in the FB-SC J-V sweep.

	Average	Std Dev
Stab eff (%)	11.90	0.80
J_{sc} (mA cm^{-2})	18.79	1.56
V_{oc} (V)	1.02	0.01

Table 2: Average and standard deviation values of main performance parameters of the 9 pixels tested in this study.

5.4.2 Low-frequency impedance spectroscopy

With the added precautions discussed above to improve device stability, a more complete impedance spectrum could be gathered. EIS spectra were measured from 1 MHz to 3 mHz at open-circuit under illumination. Figure 5-5 and Figure 5-6 show the response at the highest light intensity of 73 mW cm^{-2}. Two predominant features are present; the first at high frequency with a time constant of approximately 1 μs, the second at lower frequency with a time constant on the order of seconds. These two time constants will be referred to as τ_{hf} and τ_{lf} respectively.

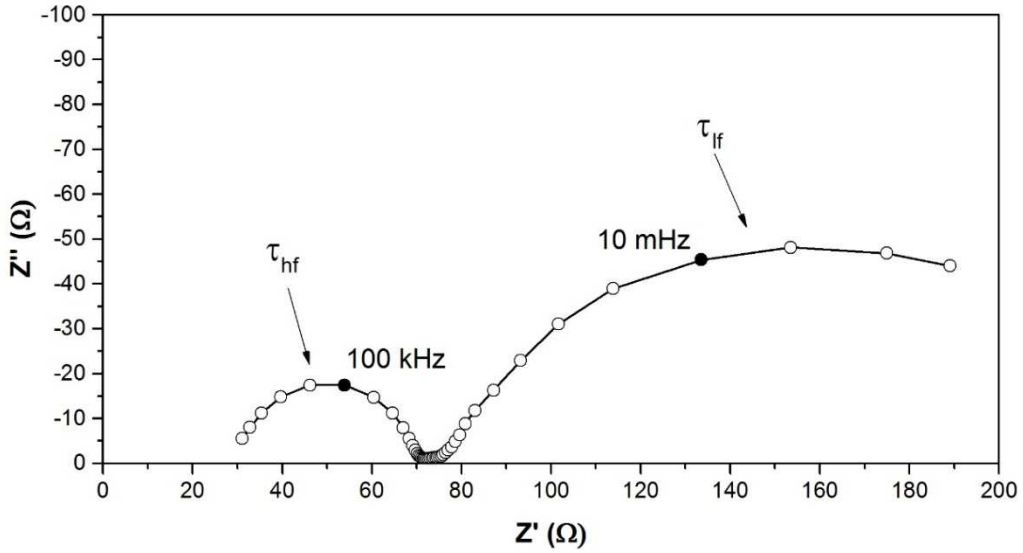

Figure 5-5: Nyquist plot of impedance data measured from 1 MHz to 3 mHz at the highest light intensity of 73 mW cm^{-2}.

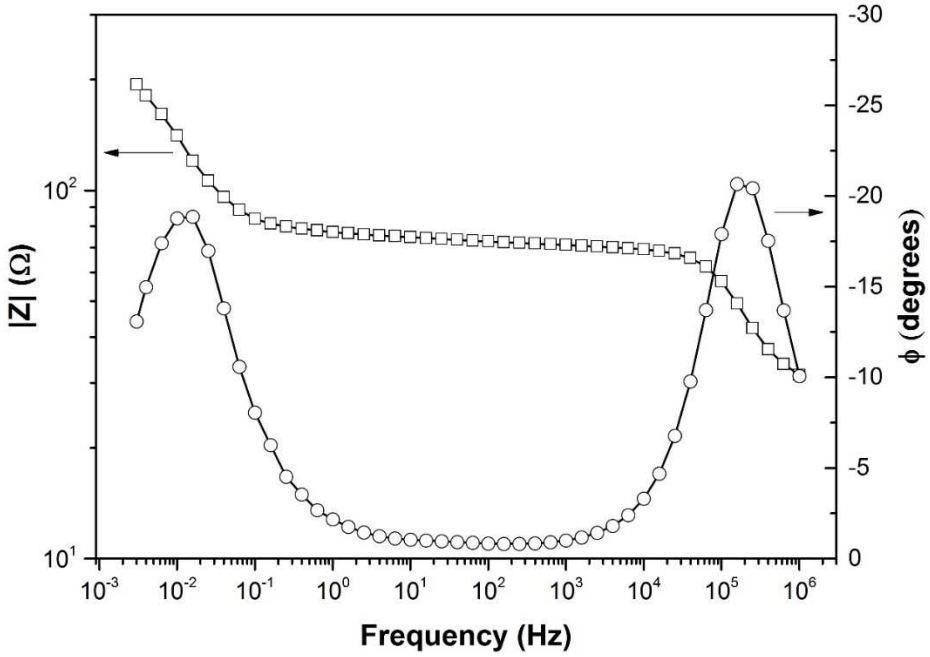

Figure 5-6: Bode plot of impedance data measured from 1 MHz to 3 mHz at the highest light intensity.

The complete impedance spectrum shown in Figure 5-5 took 27 minutes to acquire, during which time the open-circuit potential of the cell did not drift significantly. Figure 5-7 shows the time domain voltage and current signals during the impedance measurement. It can be seen that the current oscillates sinusoidally about zero without drifting by more than 10-15 μA.

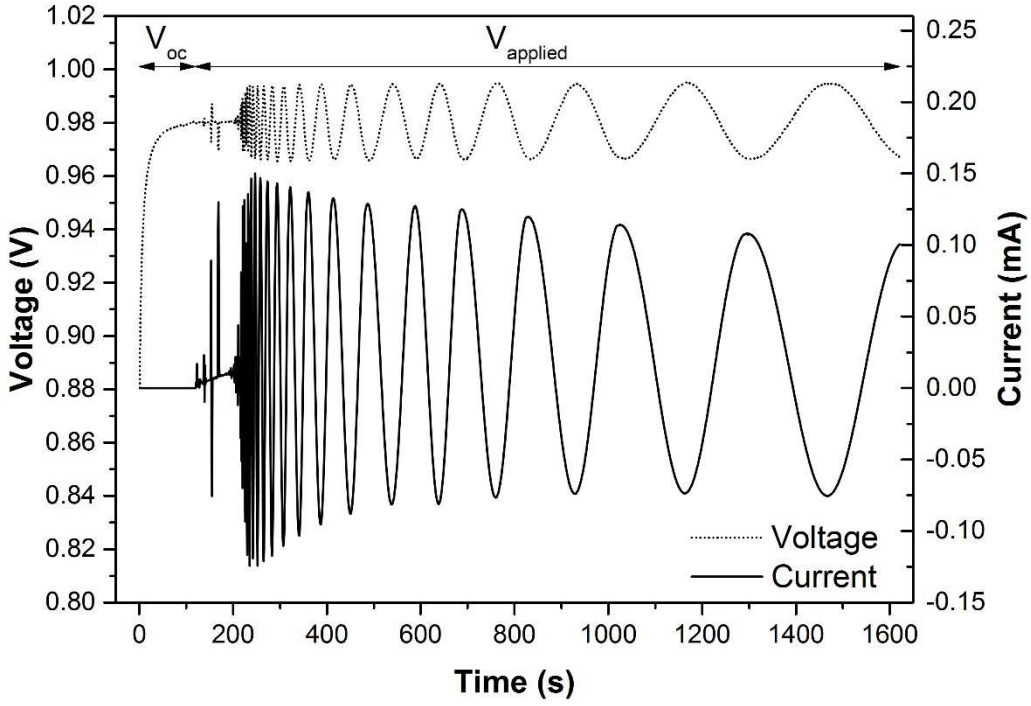

Figure 5-7: Time-domain voltage and current signals for impedance measurement from 1 MHz to 3 mHz. High frequency signal is not resolved in the time-domain due to a sampling rate of 1 point per second.

1.1.1.1 Comparison of high frequency response to previous cell batch

As shown in the previous chapter, the time constant of the high frequency process is attributed to the combination of the geometric capacitance and recombination resistance. To check this is consistent in this batch of cells, the high frequency part of the spectrum was fitted to a simple R(RC) circuit. The behaviour of the capacitance in this batch of cells was more ideal, with a CPE exponent p>0.95. In fact the high frequency part of the spectra could be fit without the use of a constant phase shift element. The use of a simple capacitor in the equivalent circuit yields more reliable capacitance values without the need for interpretation of the CPE values. The improved capacitance fitting in this batch of cells may be indicative of the improved perovskite layer, potentially having fewer grain boundaries and other imperfections.

In agreement with the analysis on the previous batch of cells, the capacitance values were found to be constant over the range of light intensities used. The capacitance for cell EY-4 was 35.4 nF ±0.2 nF across the range of light intensities. All cells in the batch gave similar constant capacitance values. The geometric capacitance expected for these devices with an active area of 0.119 cm^2 and thickness of 425 nm is 6 nF, yielding a roughness factor of less than 6, consistent with previous work in Chapter 4.

The ideality factor obtained from the intensity dependence of the open-circuit voltage was around m=1.4. None of the cells exhibited ideality factors exceeding m=2 as were observed in the previous batch of cells. It is possible that the improved perovskite layer leads to reduced surface and/or interfacial recombination, thus giving a lower ideality factor. The cells also showed comparable trends in recombination resistance with light intensity and voltage.

1.1.1.2 Low-frequency impedance spectroscopy

The impedance spectra demonstrated here appear to be some of the most complete spectra, compared to those displayed in other literature. As previously mentioned, it is challenging to perform impedance measurements to such low frequencies whilst still maintaining meaningful results due to cell instability. Typically measurements have been restricted to frequencies above 50 mHz[13, 46], which limits the ability to fit and interpret the low frequency feature.

In an attempt to gain clarity on the origin of this impedance response, it was studied as a function of light intensity and temperature.

1.1.1.3 Intensity dependence

Impedance spectra were measured over a range of intensities from 73 mW cm^{-2} to 1.4 mW cm^{-2} at the open-circuit potential. The highest intensity generated a photocurrent equivalent to the 1 sun J_{sc} value. Figure 5-8 shows a Nyquist plot for the three highest intensities. It can be seen that the resistances of the two arcs increase with decreasing light intensity. For the high frequency process this has been shown to be related to the recombination resistance varying with light intensity. The low frequency arc also appears to show a similar trend. A simple semi-circle fit to each arc was performed. The fitted resistance values for each process are shown in Figure 5-9. As expected the high frequency arc shows a near linear dependence on light intensity, reaffirming its assignation to the recombination resistance. The low frequency arc shows a similar dependence on light intensity, albeit with slightly less linearity. This suggests that the two processes may be linked to the recombination resistance.

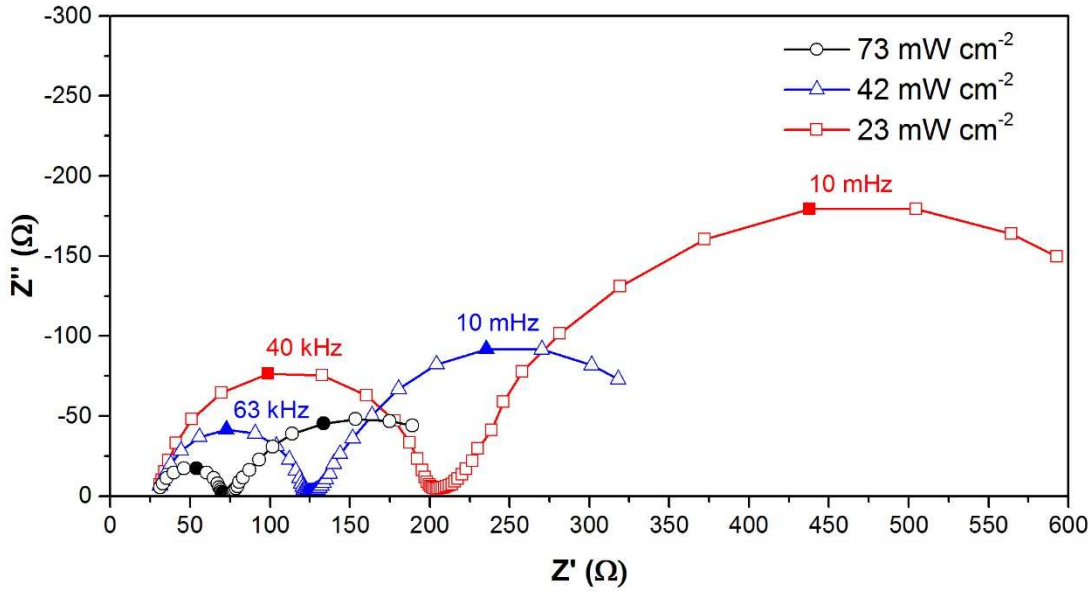

Figure 5-8: Nyquist plot of impedance spectra at different intensities.

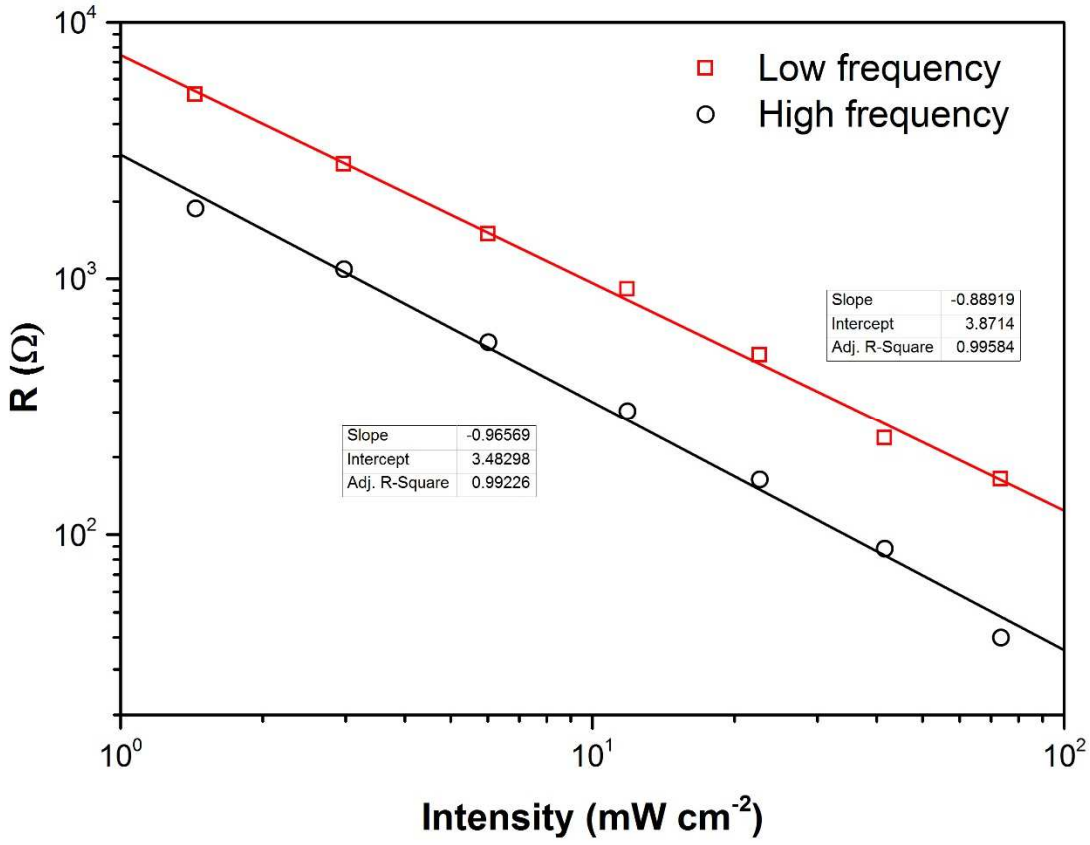

Figure 5-9: Resistance versus intensity for the high and low frequency processes.

To evaluate the time constant dependence on light intensity it is helpful to plot the impedance data as the logarithm of the imaginary component versus the logarithm of frequency, a variation on the standard Bode plot, as shown in Figure 5-10. Maxima in this plot therefore relate to the frequency of the maximum point on a semi-circle in a Nyquist plot, allowing shifts in this point to be easily observed. It can be clearly seen that at high frequencies the time constant, associated to $R_{rec}C_g$, decreases with decreasing light intensity. This result is comparable to previous work shown in Chapter 4. The low frequency process is much less dependent on light intensity, and in fact is shown to have an opposite relationship. Figure 5-11 shows the time constant dependence on light intensity for both of these processes.

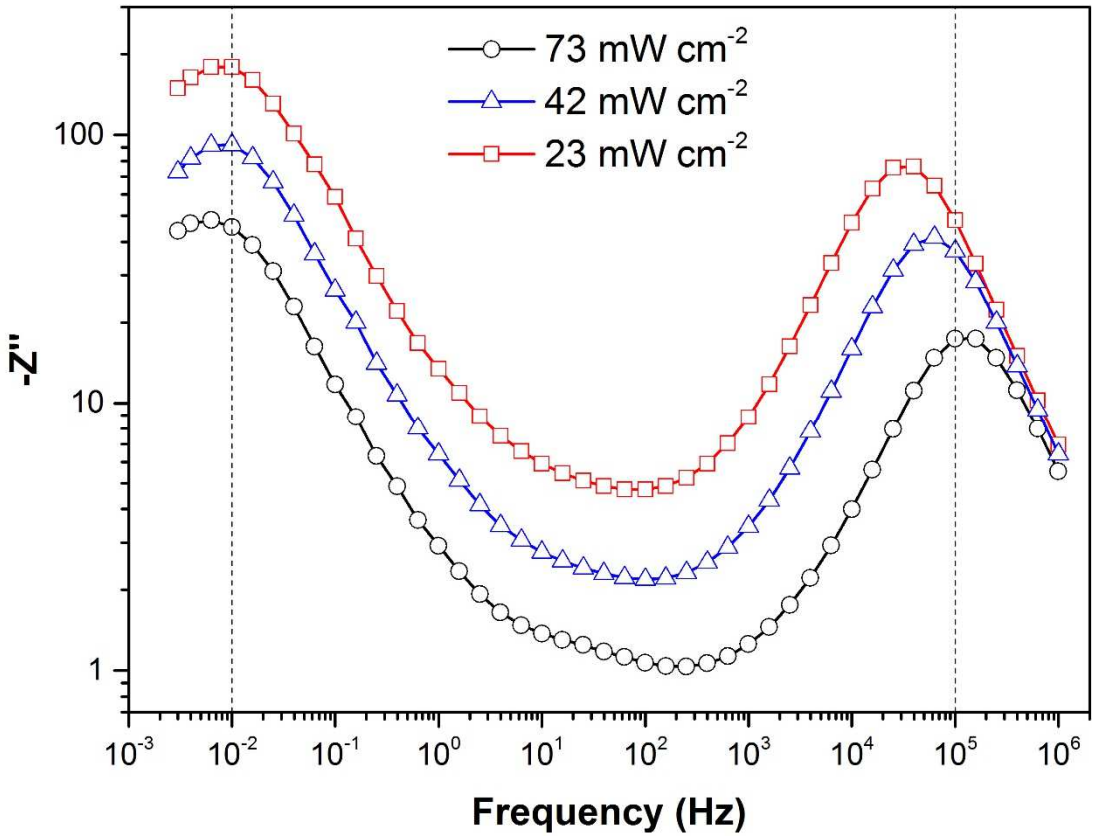

Figure 5-10: Impedance intensity dependence plotted as the logarithm of the imaginary component versus frequency. The peaks therefore relate to the maximum of the semicircle in the Nyquist plot allowing shifts in time constant to be clearly observed. Lines at 10 mHz and 100 kHz act as guides to the eye.

It is interesting to note here that the intensity dependence of the complete impedance spectra gives comparable results to Zarazua et al. and other perovskite GDE literature when plotted as a complex capacitance[9, 21]. The low frequency capacitance scales linearly with the light intensity. This shows that the spectra here are comparable to other literature measurements, although the subsequent interpretation is quite different (see Discussion).

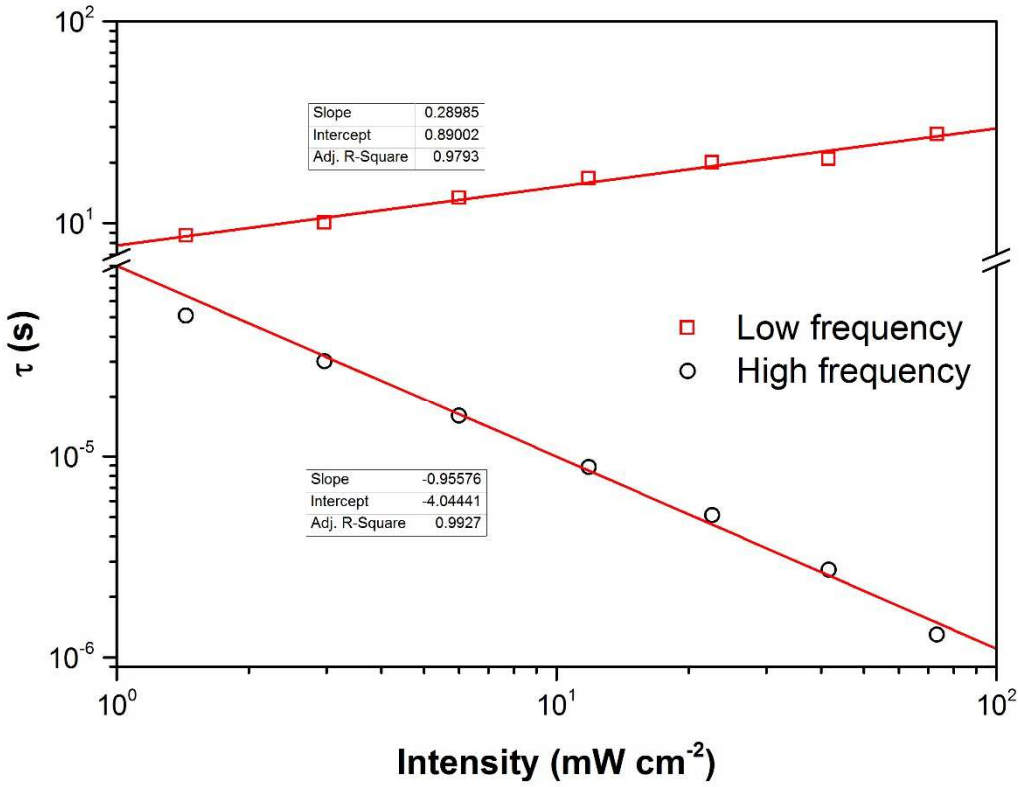

Figure 5-11: Time constant dependence on light intensity for the high and low frequency processes observed in EIS.

5.4.3 Low-frequency intensity modulated voltage spectroscopy

Intensity modulated voltage spectroscopy (IMVS) measurements were also performed over a wide frequency range from 200 kHz to 3 mHz. An example of the complete IMVS spectra is shown in Figure 5-12. Interestingly, the IMVS reveals three apparent processes with time constants on the microsecond, millisecond and second timescale. These processes will be referred to as τ_{hf}, τ_{mf} and τ_{lf} respectively.

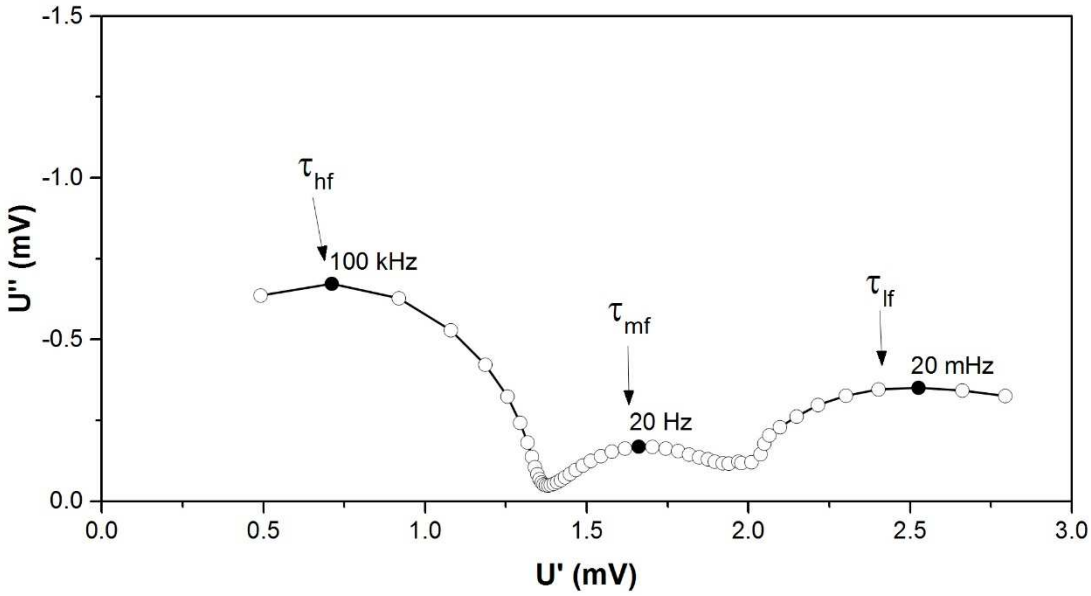

Figure 5-12: IMVS spectra measured to very low frequency.

1.1.1.4 Intensity dependence

The intensity dependence of the IMVS measurements is shown in Figure 5-13. Again, trends in time constants are clearer when plotted as a Bode plot, as shown in Figure 5-14. This shows that the high frequency time constant is strongly dependent on light intensity, as expected from its relation to $R_{rec}C_g$ (shown in EIS here and in previous chapter). The two lower frequency time constants have much weaker dependences on light intensity.

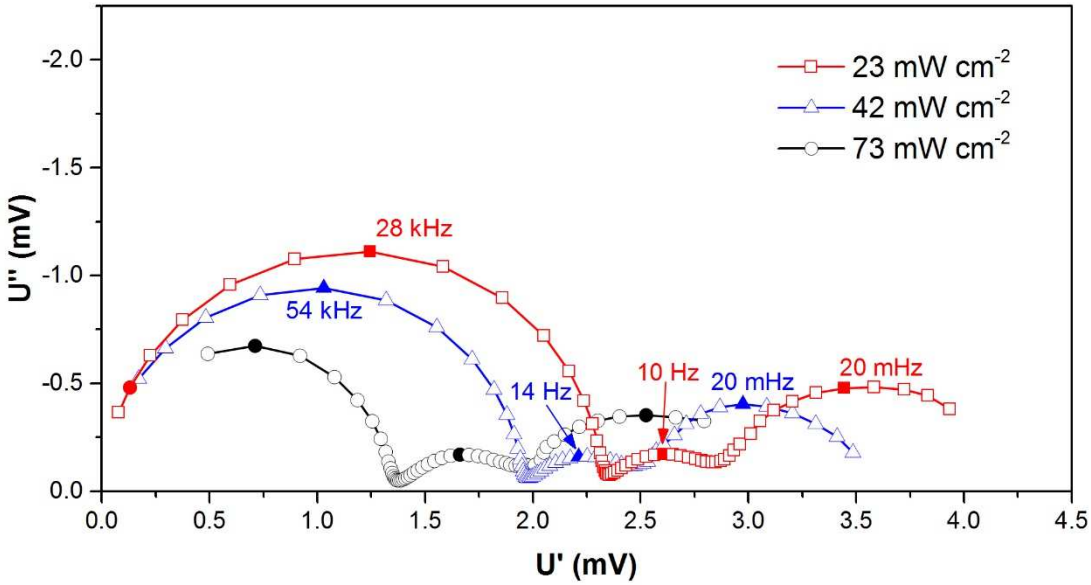

Figure 5-13: Intensity dependence of IMVS spectra.

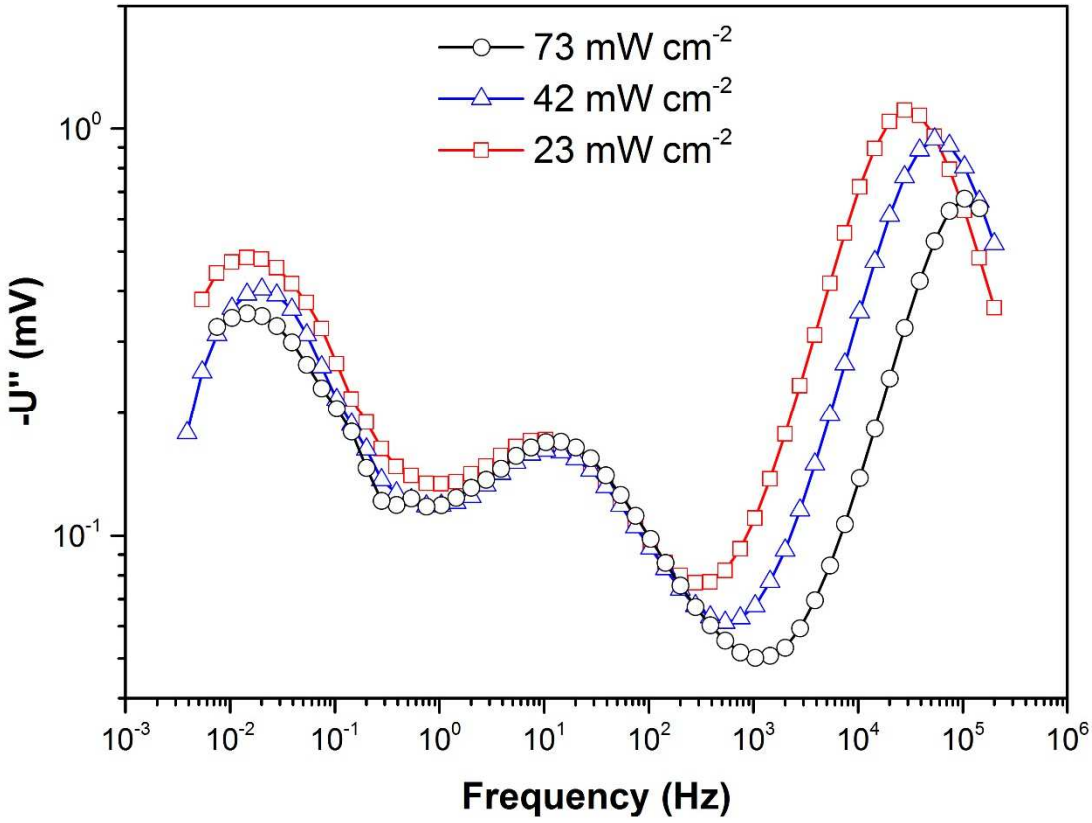

Figure 5-14: Bode plot of IMVS intensity dependence.

The extracted time constants for the three processes are shown in Figure 5-15. Unfortunately data for the complete IMVS spectra was only recorded for three light intensities so it is difficult to draw full conclusions from this alone. However, it does indicate that the low frequency process has a similar time constant associated to it in both EIS and IMVS. The mid frequency time constant is clearly resolved in IMVS, whereas it is not obvious in EIS.

As the same low frequency process appeared to be observed in both IMVS and EIS, it was decided that the low frequency measurements would only be performed for EIS and not IMVS. This was done to prioritize device stability as performing both measurements to a few mHz would have resulted in higher degradation and would have restricted the range of measurements possible.

More data for the high and mid frequency time constants is presented in Figure 5-20.

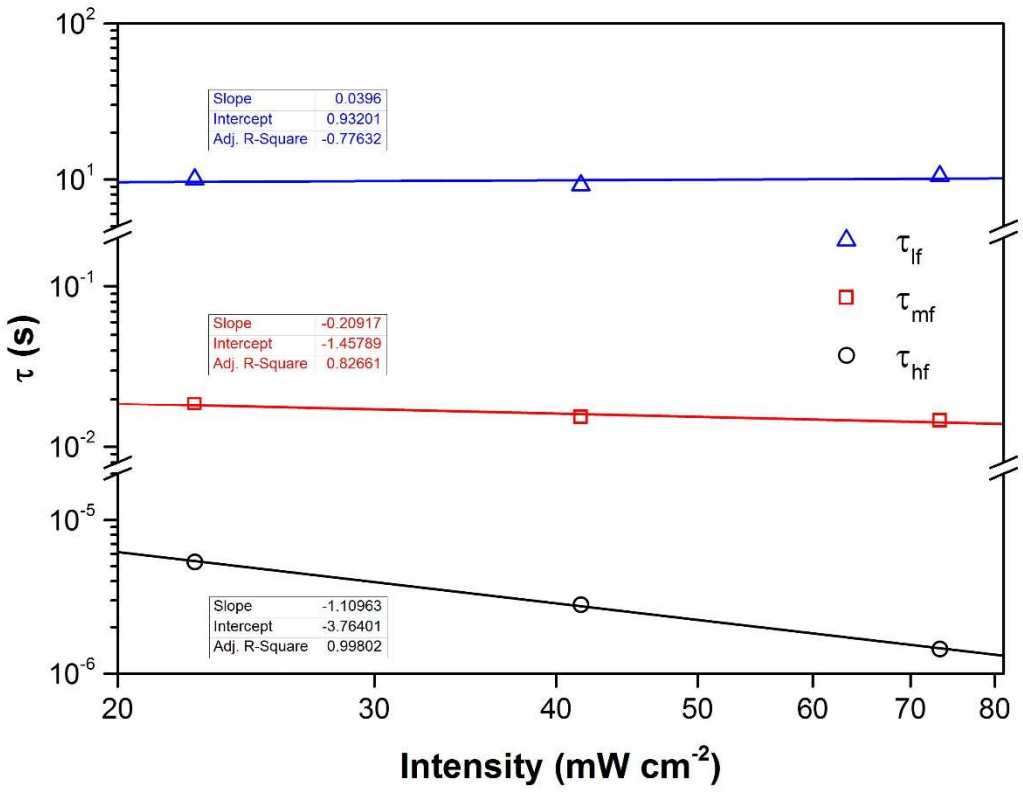

Figure 5-15: IMVS time constant dependence on light intensity.

5.4.4 Conversion of IMVS to impedance

It has been shown that is possible to combine IMVS and IMPS data to generate an impedance spectra[47]. Essentially this involves dividing the modulated photovoltage by the modulated photocurrent that is generated by the same light perturbation. The modulated photocurrent value can be obtained from the dc limit of an IMPS measurement (current in phase with the light signal at low frequency).

Initially this was attempted using a standard IMPS measurement, which is performed at short circuit. Scaling using this photocurrent value gave a large discrepancy between the IMVS and EIS spectrum at the same intensity. It was then realised that the photocurrent measured using the standard IMPS measurement overestimated the true value related to open-circuit conditions. The method was therefore modified to hold the potential at the open-circuit voltage generated by the background illumination, rather than at short-circuit. It is important to emphasize that this is a potentiostatic measurement rather than galvanostatic, as is the case for IMVS. Therefore whilst the cell is held at the open-circuit voltage caused by the background illumination, current will flow as the light intensity is increased or decreased. The AC photocurrent is much lower near open-circuit than at short circuit, as shown in Figure 5-16, indicating higher recombination rates assuming charge generation is equal at open and short circuit. The intensity dependence of the photocurrent is also non-linear near open-circuit.

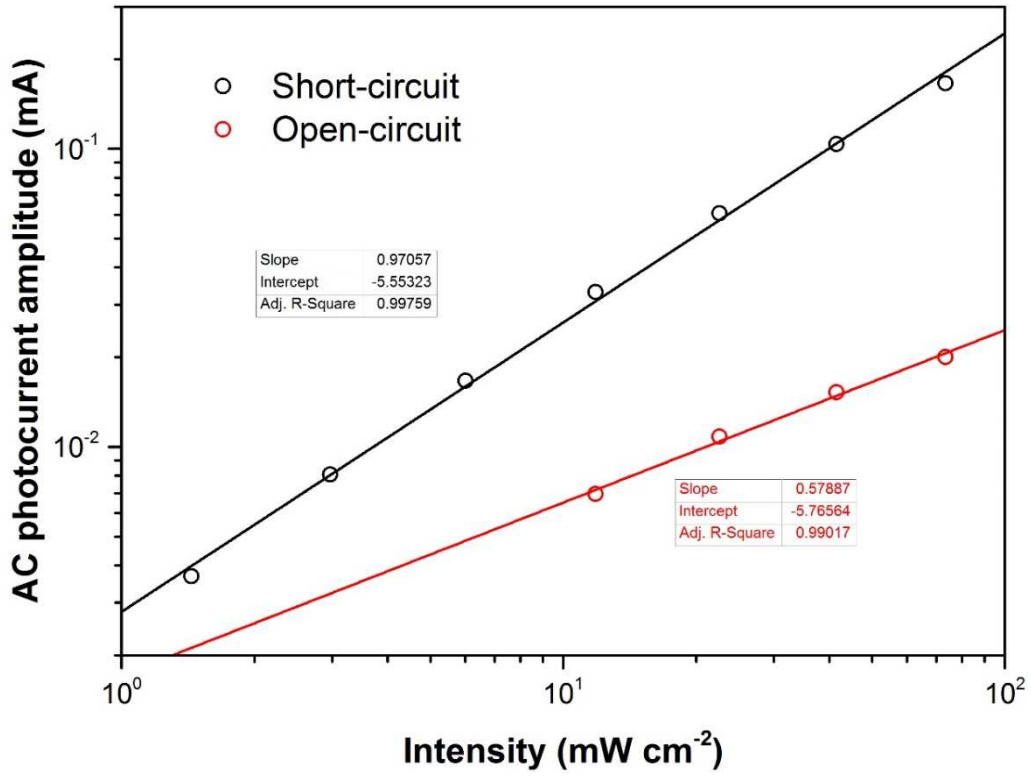

Figure 5-16: Amplitude of the AC photocurrent generated at short-circuit and with the cell held at the open-circuit potential for the same AC light signal.

Using the values of the AC photocurrent at open-circuit gives good agreement between the EIS and converted IMVS as shown in Figure 5-17. The series resistance has been subtracted from the impedance spectra as charge does not flow through the series resistance in IMVS, so its impact is not measured.

There is good agreement between the resistance values for the high frequency arc, but less so for the lower frequency part of the spectrum. The magnitude of the lower frequency response appears to be smaller from the IMVS measurement when compared to the impedance. Differences between the two methods are perhaps not surprising as although converting the IMVS gives a response equivalent to an impedance measurement, the cell is not quite in the same state for both. For example, during impedance measurements at open-circuit a small AC current flows through the device and is measured at the contacts to the cell. For IMVS no current flows and all generated charge recombines. It appears to be this distinction that allows the same processes to be measured in the two methods (high and low frequency time constants show good agreement between EIS and IMVS) but causes a process such as the one occurring at mid frequency to be well resolved in one measurement and not the other.

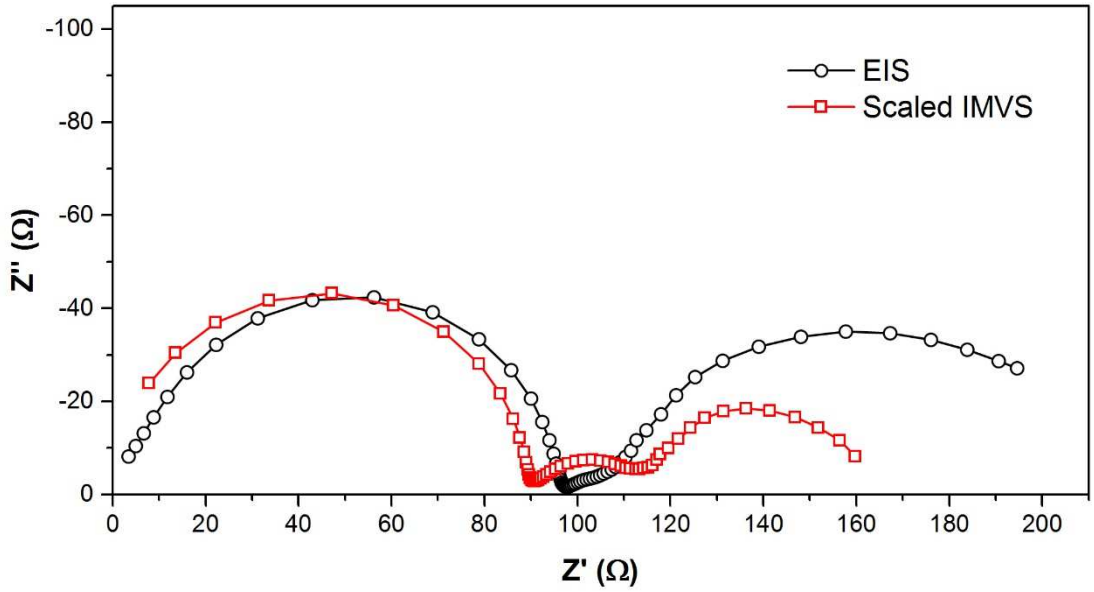

Figure 5-17: IMVS scaled using the AC photocurrent at the open-circuit potential for the same light perturbation. EIS spectra recorded at same light intensity is shown for comparison (series resistance subtracted).

Regarding this mid-frequency process, it appears that there is a small feature in the EIS spectra at the same frequency as the τ_{mf} process in the IMVS. This is most evident when the spectra are plotted on a Bode plot as in Figure 5-18. The small deviation at approximately 10 Hz seems to match perfectly with the well resolved time constant in the IMVS measurement. The mid-frequency feature can also be seen on the impedance Nyquist plot, showing as the small distortion between the two large semicircles. This feature has led to several publications in which a finite Warburg element has been used to fit an equivalent circuit[8, 48]. It is not possible to accurately fit or determine a time constant for this process from the EIS spectra, and so the IMVS will be solely used to assess it.

The time constants for the high frequency process are in very close agreement between the two methods. The low frequency process is well resolved in both, with reasonable agreement ($\tau_{lf,\ EIS}$=13 s, $\tau_{lf,\ IMVS}$=9 s).

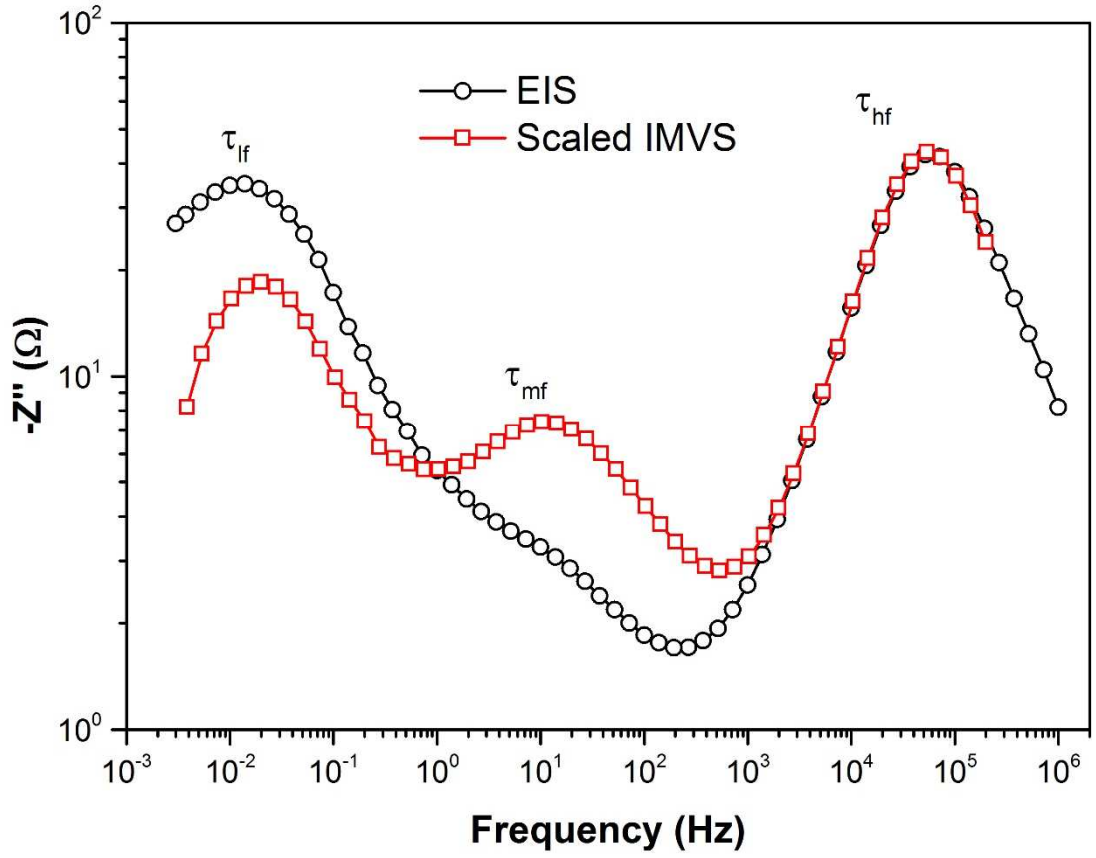

Figure 5-18: Impedance and scaled IMVS spectra plotted on a Bode plot.

After scaling the IMVS by the AC photocurrent at open circuit, it is possible to extract values of the three resistances for the measurements shown in section 1.1.1.4. As previously mentioned, the complete IMVS spectrum was only measured at 3 light intensities, but it gives an indication of the trends expected. Figure 5-19 shows these resistances as a function of light intensity. All 3 appear to increase with decreasing light intensity (this has already been shown for τ_{hf} and τ_{lf} from EIS). The resistance for the mid frequency process also appears to follow a similar trend although perhaps with less linearity.

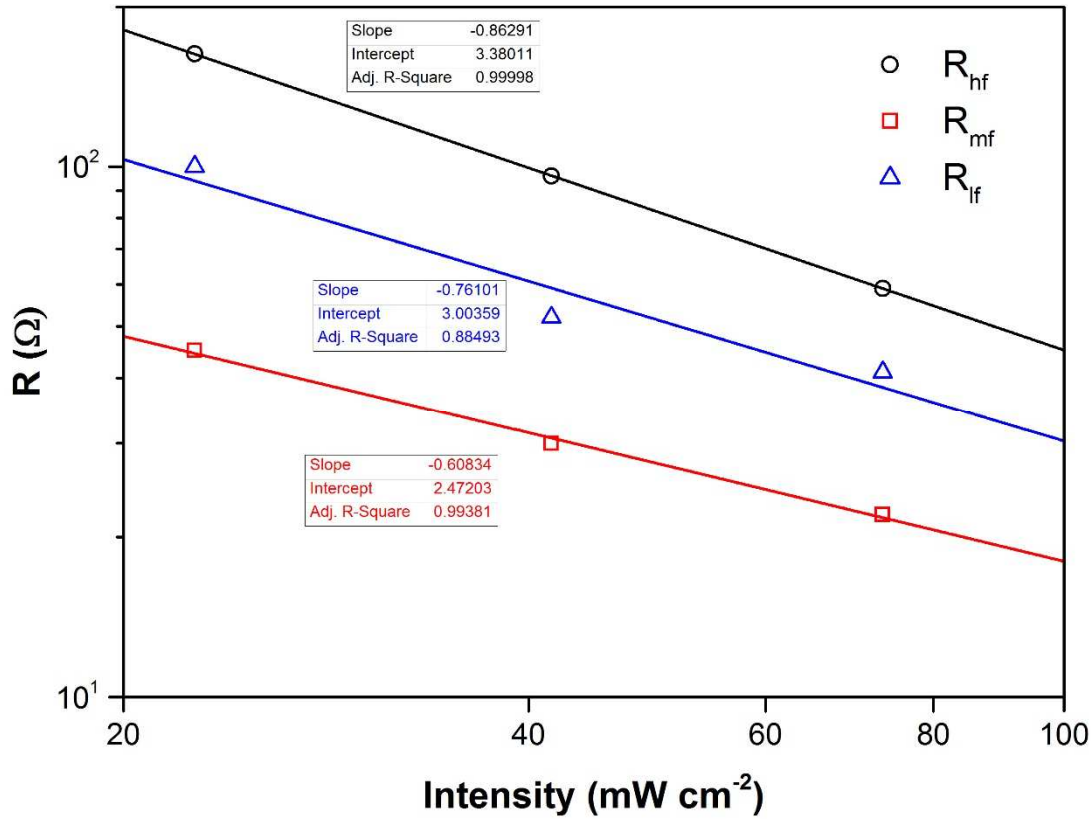

Figure 5-19: Resistances obtained for the three processes observed in the scaled IMVS.

IMVS measurements were performed at all light intensities but not down to such low frequencies. This still allows for analysis of the high and mid-frequency processes (low frequency process to be assessed using EIS data). Unfortunately, the scaling of the IMVS by the AC photocurrent is not possible for this data as the IMPS measurements were not performed under the correct conditions. However, an alternative scaling method has been used. As the capacitance value calculated from the fit to the high frequency arc is constant for all intensities within a very tight range (C_g= 35.4 nF ±0.2 nF), a scaling factor was calculated by which the IMVS needs to be multiplied to give the same capacitance. This is a more reliable method than simply matching the high frequency arc resistance as this will change for any slight difference in intensity/V_{oc} whereas the capacitance is known to be more or less constant at all light intensities. Figure 5-20 shows the resistance values obtained for the high and medium frequency features when the IMVS is scaled in this way. Combining this with the resistance trends of the low frequency feature obtained from the EIS suggests that all three processes are linked to the recombination resistance. This indicates that the recombination resistance is frequency dependent, due to some internal process which modifies the recombination rate on different time scales.

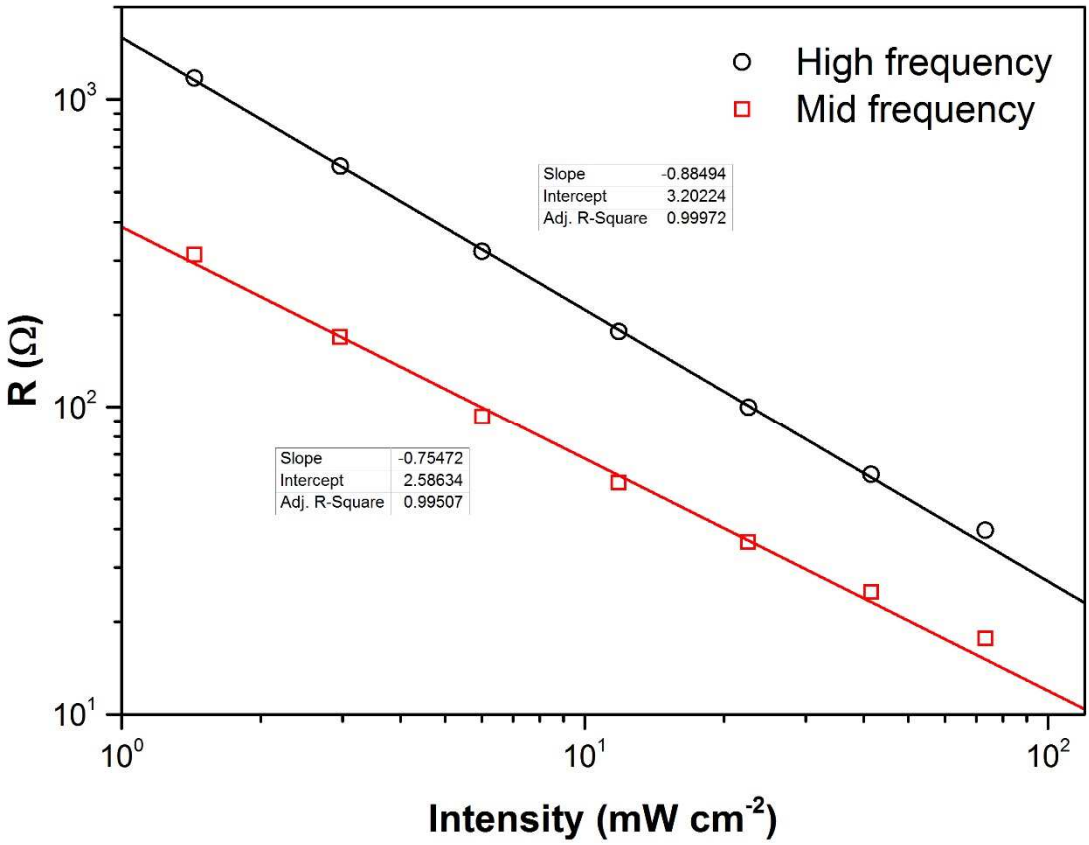

Figure 5-20: Resistance values obtained from a semi-circle fit to the scaled IMVS data at all light intensities studied. IMVS data was scaled so that the high frequency arc yielded the same capacitance as fit to the EIS data.

5.4.5 Temperature dependent low frequency measurements

To further probe what could be responsible for these multiple processes observed in the frequency domain the same impedance and IMVS measurements were carried out as a function of temperature. The temperature was controlled using a peltier element and temperature controller, housed inside a desiccated sample holder to improve device stability and also prevent condensation on the sample at low temperatures. The temperature range used was -25 °C to 65 °C in 10 °C increments. Temperature stability during measurements was to within ±0.01 °C (according to temperature controller manufacturer's specifications) and the control current to the peltier element was pure DC as opposed to PWM which was found to induce interference in the measurement signal.

To perform these frequency domain measurements at open-circuit conditions required the cell to reach steady state under illumination before the measurement was performed. At room temperature this typically took 1-2 minutes of illumination at open-circuit to reach a stable V_{oc} (this can be seen in the slow voltage rise in Figure 5-7). At low temperatures this process could take up to 10 minutes.

The cell was increasingly unstable at temperatures above room temperature, with the impedance measurements above 45 °C starting to be affected by V_{oc} drift due to degradation during the measurement.

Figure 5-21 and Figure 5-22 show Nyquist and Bode plots of the impedance measurements at different temperatures. It is clear that the resistances and time constants associated with both the high and low frequency processes vary with temperature.

The high frequency feature, assigned to the combination of the cells geometric capacitance and recombination resistance can be expected to vary with temperature. The resistance derived from the diameter of the semi-circle is inversely proportional to the recombination rate, and will therefore increase as the cell is cooled and the rate of recombination decreases. This results in the cells V_{oc} increasing at lower temperatures as a result of the decrease in recombination rate.

It is clear that the low frequency process is more strongly affected by temperature, particularly with regards to the time constant. The Bode plot in particular highlights a decrease in the time constant across at least one order of magnitude for just a 40 °C drop in temperature. The time constant of the low frequency process at 45 °C is 4 seconds, whereas for 5 °C it appears to be in excess of 50 seconds as it is not fully resolved even at 3 mHz. It was not possible to measure to lower frequencies due to time/stability constraints. As mentioned above, cell stability became an issue when measuring at temperatures above 45 °C. Fortunately, at the higher temperatures the low frequency process is accelerated significantly, having a time constant of 0.8 ms at 65 °C and therefore not requiring measurements to such low frequencies.

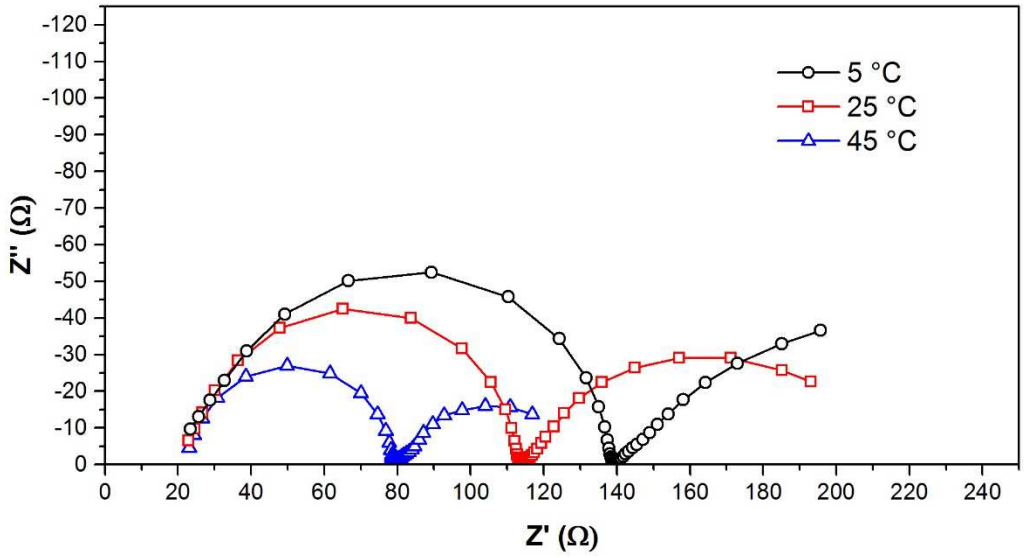

Figure 5-21: Nyquist plot of temperature dependent impedance measurements.

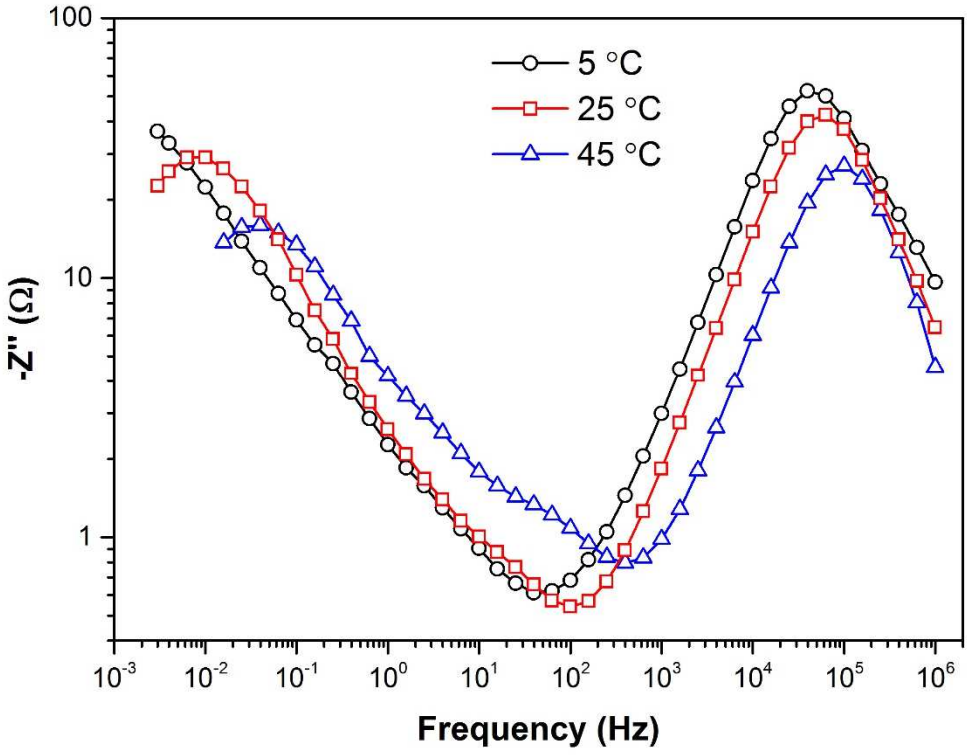

Figure 5-22: Bode plot of temperature dependent impedance measurements.

A similar dependence is observed for the mid-frequency time constant from IMVS as shown in Figure 5-23. The time constant increases from 3 ms at 45 °C to approximately 60 ms at 5 °C.

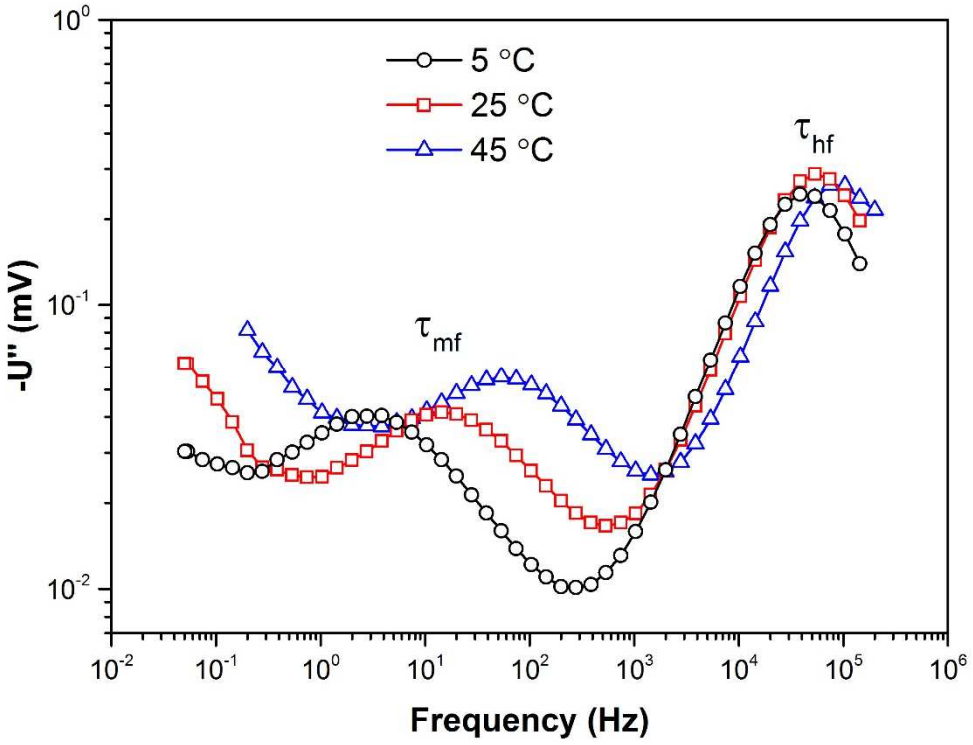

Figure 5-23: Bode plot of IMVS measurements at different temperatures.

The time constants extracted from EIS (τ_{lf}) and IMVS (τ_{mf}) can be used to construct Arrhenius plots (taking the time constant to be the inverse of the rate), from which activation energies for the processes can be derived (it was not possible to resolve the low frequency time constant at temperatures below 15 °C due to the process becoming too slow). These plots are shown in Figure 5-24 and Figure 5-25. The activation energy determined for the low and mid frequency processes are 0.66 eV and 0.55 eV respectively. Attempt frequencies for the two processes can also be calculated from the pre-exponential factor of the Arrhenius equation

$$k = Ae^{-E_A/RT}$$

This gives attempt frequencies for the low and mid frequency processes of 1.2×10^{10} s^{-1} and 1.8×10^{11} s^{-1} respectively.

An activation energy of 0.55 eV is in close agreement with the value calculated for iodide vacancy movement by Eames et al (0.58 eV)[28]. An attempt frequency for ionic species of 1.8×10^{11} Hz is also comparable to that suggested by Eames et al. They used a value of 10^{12} Hz, but considered a slightly higher temperature of 320 K. This close agreement between the experimental values determined here and the

calculated values in literature suggests that the mid frequency process is related to the movement of iodide vacancies in the perovskite.

The low frequency process has both a higher activation energy and lower attempt frequency. One possibility is that this could be related to the movement of methylammonium vacancies in the perovskite lattice. The lower attempt frequency and higher activation energy would agree with the concept that this larger ion would only be able to move through the lead iodide framework when in a particular orientation. Eames et al. calculated an activation energy of 0.84 eV for MA^+ which is significantly higher than the value calculated here. There are other values of activation energies calculated for MA^+ migration in the literature that range from 0.5 eV to 1.1 eV[27, 29, 30]. Due to the dependence on molecular orientation for MA^+ migration it seems that the true values would be at the higher end of these estimates. It is also possible that the two different activation energies calculated in this work relate to iodide vacancy motion in two different environments. For example, iodide migration in the bulk and along grain boundaries.

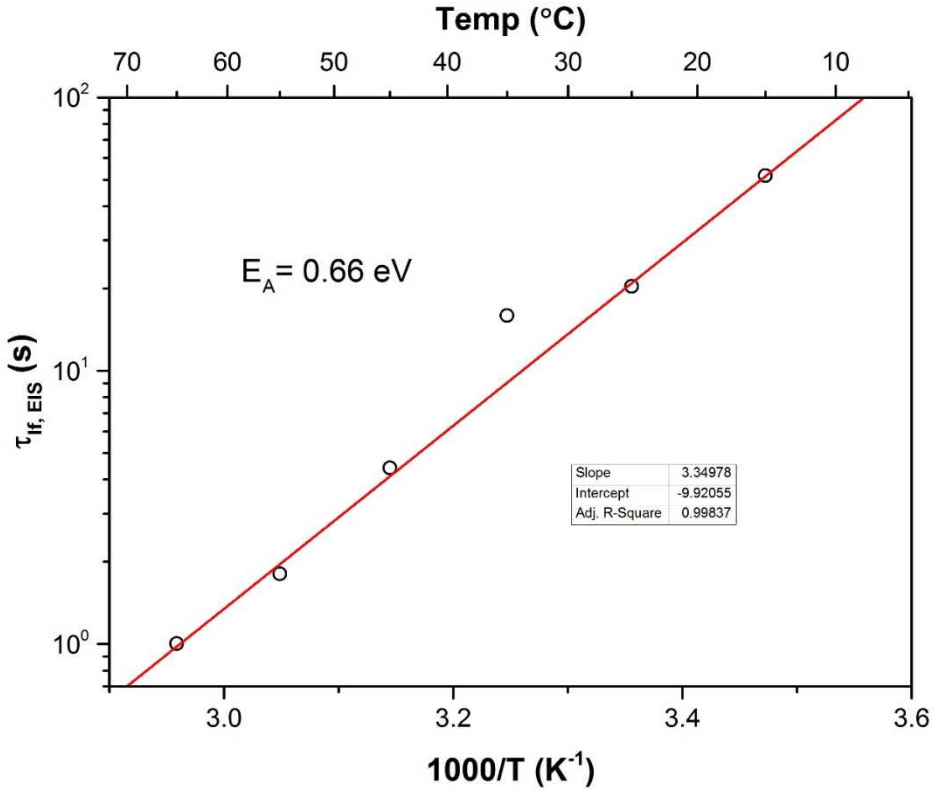

Figure 5-24: Arrhenius plot of the low frequency process using time constants extracted from EIS.

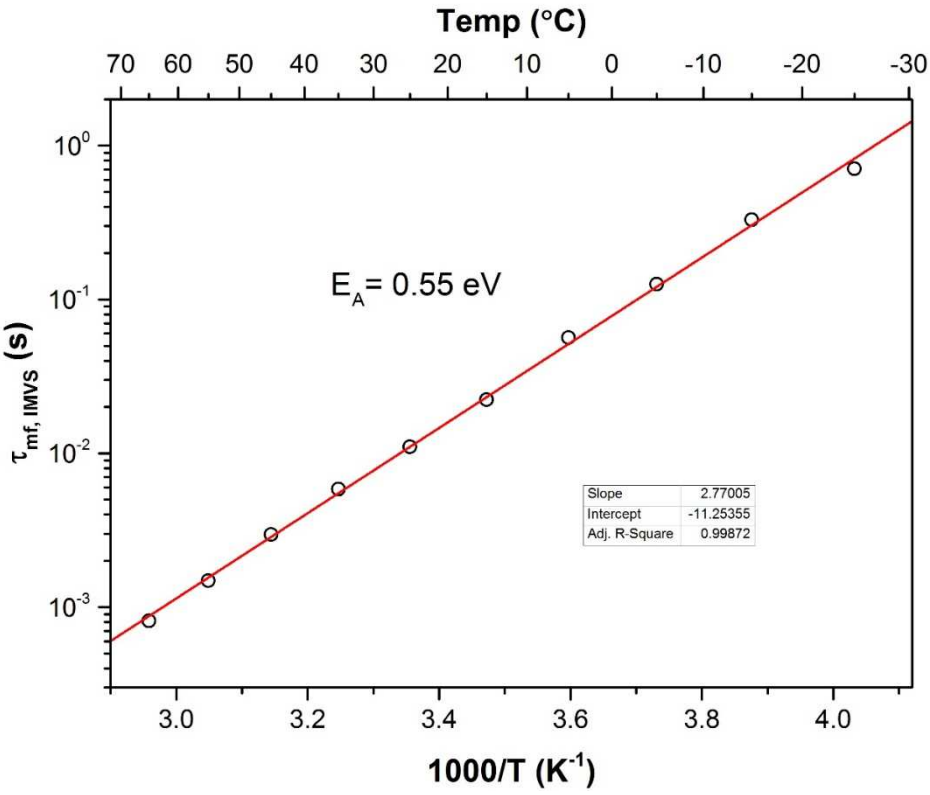

Figure 5-25: Arrhenius plot of the mid frequency process using time constants extracted from IMVS.

5.5 Discussion

The results presented here highlight the range of information that can be obtained from frequency domain measurements. Impedance and IMVS measurements have been combined to reveal the presence of three dominating processes on the timescales measured. At high frequencies the response appears to be determined by purely electronic processes relating to the geometric capacitance of the cell and the recombination resistance. The additional low frequency processes have been shown to be linked to both the recombination resistance, and the presence of mobile ionic species in the perovskite material. In order to help identify the impact of these ions on the electrical characteristics of the device, measurements in the time domain will be presented in the next chapter.

It appears that the recombination rate is dependent on the ionic arrangement within the device. The similar trend in resistance for all 3 processes indicates that they are all linked to recombination. At high frequencies it is reasonable to assume that the ions are immobile and so the high frequency response can be linked to the steady state condition where ions are in a fixed position. At lower frequencies it appears that the ions redistribute causing a reduction in recombination (increase recombination resistance). The recombination resistance increases by a factor of 2-4 depending on the cell. The relative rates of the ionic redistribution processes can be inferred from the time constants measured from EIS and IMVS.

The high frequency time constant shows a large dependence on intensity, as expected from the linear change of recombination resistance with light intensity and constant geometric capacitance. The two lower frequency processes show relatively weak time constant dependences on light intensity despite the increase in recombination resistance. This suggests that the rate of ion movement is only slightly affected by change in light intensity (light intensity affecting electric field has small impact on ions). Temperature dependent measurements show that the lower frequency time constants are greatly affected by temperature. The activation energies of these variations reveal their link to ion motion. As is to be expected, at higher temperature the rate of ion migration is increased, which in turn results in the recombination rate being adjusted more quickly. In other words, it appears that the

rate at which the frequency dependent recombination resistance increases is controlled by the rate of ion motion.

From the evidence gathered here from both light and temperature dependent measurements, the equivalent circuit shown in Figure 5-26 was developed. The circuit represents the series resistance of the cell, together with the cells geometric capacitance and the complex impedance relating to the frequency dependent recombination resistance. This model is consistent with the equivalent circuit presented in the previous chapter for the high frequency response, where R_{rec} replaces the complex impedance Z_{rec} as at high frequencies the recombination resistance is not altered by ionic movement.

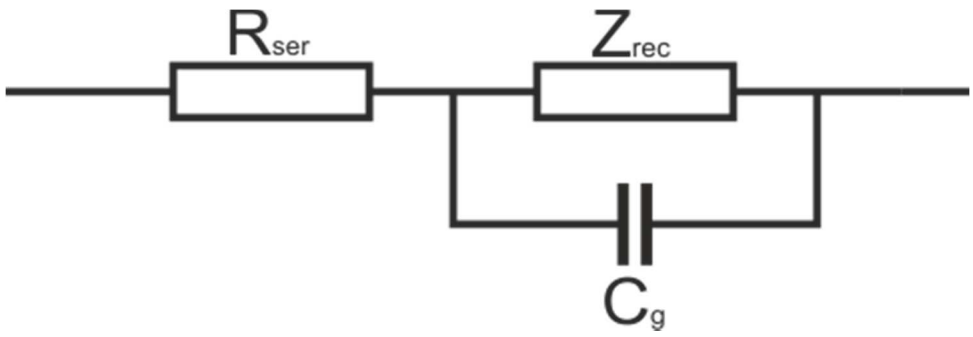

Figure 5-26: Simplified equivalent circuit to describe frequency dependent response of planar perovskite solar cells.

The presence of 3 processes in the frequency response is therefore just a consequence of the change in recombination resistance with frequency. Ionic relaxation on different timescales (milliseconds and seconds) results in the recombination resistance increasing with two different time constants. We are measuring a process governed by ion movement, but not measuring ionic diffusion directly. We observe a semi-circular response as the recombination resistance increases with frequency, but any capacitance value extracted from this time constant is physically meaningless.

At this point it is interesting to consider the coupling of the ionic diffusion and recombination process further. Van Reenen et al. and Richardson et al. both showed that in order to successfully model the observed JV hysteresis of perovskite solar cells, both ion movement and trap-assisted interfacial recombination needed to be included[2, 49]. If trap states are present near to the interface it is reasonable to expect

that ionic charge build up in these regions may alter the recombination rate. This also gives us one possible explanation as to the different effects observed in cells with TiO_2/Spiro contacts and those with organic contacts of PCBM/PEDOT. Organic contact perovskite cells usually show very limited JV hysteresis at room temperature[50, 51].

The change of contact material is unlikely to effect the process of ion movement through the bulk of the perovskite layer, and indeed this has been inferred by the results of Bag et al.[8] Regardless of the fitting procedure that was employed, the extraction of the time constant should still give a reliable estimate of the low frequency process. This gave an activation energy of 0.58 eV. This is very similar to that observed in this work, which was assigned to iodide vacancy migration. The frequency of the low frequency feature in the organic contact cells was higher than for the TiO_2 contact devices. This was consistent with the findings of Bryant et al. who found that a similar hysteresis effect did occur in PCBM contact cells, but at a faster rate[31].

As has been shown in the frequency domain measurements in this chapter, the low frequency impedance response is not a direct measurement of ionic motion. It is related to the modulation of the recombination resistance as ionic species move towards or away from the interfaces. Therefore, due to the similar activation energies seen for both cell types, it can be assumed that the ionic motion is comparable in both. However, the effect on recombination occurs at a different rate. This is possibly due to the different nature of the interfaces. TiO_2 is essentially a flat, hard interface that ions are unlikely to cross or penetrate (although they may adsorb to the surface[52]). PCBM is made up of small molecules so it is possible that ions could penetrate into the layer giving a very different ionic distribution, which may have a different effect on recombination.

5.6 Conclusion

A clear link between recombination and the movement of ions within the perovskite has been observed. The low frequency processes observed on the millisecond and second timescales are shown to be related to the movement of ions by the derivation of activation energies which are comparable to computationally calculated values from literature. These two processes are also shown to be associated with an increase in recombination resistance due to the linear intensity dependence. This shows that the distribution of ions within the perovskite has a substantial effect on recombination. This supports the hypothesis that the slow dynamic behaviour observed (slow voltage rise, hysteresis, etc.) is linked to ionic movement and changes in recombination rate.

5.7 References

1. H. J. Snaith, A. Abate, J. M. Ball, G. E. Eperon, T. Leijtens, N. K. Noel, S. D. Stranks, J. T.-W. Wang, K. Wojciechowski and W. Zhang, *J. Phys. Chem. Lett.*, 2014, **5**, 1511-1515.
2. G. Richardson, S. E. J. O'Kane, R. G. Niemann, T. A. Peltola, J. M. Foster, P. J. Cameron and A. B. Walker, *Energy Environ. Sci.*, 2016, **9**, 1476-1485.
3. A. Baumann, K. Tvingstedt, M. C. Heiber, S. Väth, C. Momblona, H. J. Bolink and V. Dyakonov, *APL Mat.*, 2014, **2**, 081501.
4. B. C. O'Regan, P. R. F. Barnes, X. Li, C. Law, E. Palomares and J. M. Marin-Beloqui, *J. Am. Chem. Soc.*, 2015, **137**, 5087-5099.
5. R. S. Sanchez, V. Gonzalez-Pedro, J.-W. Lee, N.-G. Park, Y. S. Kang, I. Mora-Sero and J. Bisquert, *J. Phys. Chem. Lett.*, 2014, **5**, 2357-2363.
6. S. Chen, X. Wen, R. Sheng, S. Huang, X. Deng, M. A. Green and A. Ho-Baillie, *ACS Appl. Mater. Interfaces*, 2016, **8**, 5351-5357.
7. J. Bisquert, L. Bertoluzzi, I. Mora-Sero and G. Garcia-Belmonte, *J. Phys. Chem. C*, 2014, **118**, 18983-18991.
8. M. Bag, L. A. Renna, R. Y. Adhikari, S. Karak, F. Liu, P. M. Lahti, T. P. Russell, M. T. Tuominen and D. Venkataraman, *J. Am. Chem. Soc.*, 2015, **137**, 13130-13137.
9. E. J. Juárez-Pérez, R. S. Sánchez, L. Badia, G. Garcia-Belmonte, Y. S. Kang, I. Mora-Sero and J. Bisquert, *J. Phys. Chem. Lett.*, 2014, **9**, 2390-2394.
10. A. Guerrero, G. Garcia-Belmonte, I. Mora-Sero, J. Bisquert, Y. S. Kang, T. J. Jacobsson, J.-P. Correa-Baena and A. Hagfeldt, *J. Phys. Chem. C*, 2016, **120**, 8023-8032.
11. K. Miyano, N. Tripathi, M. Yanagida and Y. Shirai, *Acc. Chem. Res.*, 2016, **49**, 303-310.
12. H.-S. Kim, I. Mora-Sero, V. Gonzalez-Pedro, F. Fabregat-Santiago, E. J. Juarez-Perez, N.-G. Park and J. Bisquert, *Nat. Commun.*, 2013, **4**, 2242.
13. V. Gonzalez-Pedro, E. J. Juarez-Perez, W.-S. Arsyad, E. M. Barea, F. Fabregat-Santiago, I. Mora-Sero and J. Bisquert, *Nano Lett.*, 2014, **14**, 888-893.
14. A. Dualeh, T. Moehl, N. Tétreault, J. Teuscher, P. Gao, M. K. Nazeeruddin and M. Grätzel, *ACS nano*, 2014, **8**, 362-373.
15. J. M. Frost, K. T. Butler and A. Walsh, *APL Mat.*, 2014, **2**, 081506.
16. J. M. Frost, K. T. Butler, F. Brivio, C. H. Hendon, M. van Schilfgaarde and A. Walsh, *Nano Lett.*, 2014, **14**, 2584-2590.
17. A. Stroppa, C. Quarti, F. De Angelis and S. Picozzi, *J. Phys. Chem. Lett.*, 2015, **6**, 2223-2231.
18. T. S. Sherkar and L. Jan Anton Koster, *PCCP*, 2016, **18**, 331-338.
19. J. Beilsten-Edmands, G. E. Eperon, R. D. Johnson, H. J. Snaith and P. G. Radaelli, *Appl. Phys. Lett.*, 2015, **106**, 173502.

20. A. M. A. Leguy, J. M. Frost, A. P. McMahon, V. G. Sakai, W. Kockelmann, C. Law, X. Li, F. Foglia, A. Walsh, B. C. O'Regan, J. Nelson, J. T. Cabral and P. R. F. Barnes, *Nat. Commun.*, 2015, **6**, 7124.

21. I. Zarazua, J. Bisquert and G. Garcia-Belmonte, *J. Phys. Chem. Lett.*, 2016, **7**, 525-528.

22. T.-Y. Yang, G. Gregori, N. Pellet, M. Grätzel and J. Maier, *Angew. Chem. Int. Ed.*, 2015, **54**, 7905-7910.

23. C. Li, S. Tscheuschner, F. Paulus, P. E. Hopkinson, J. Kießling, A. Köhler, Y. Vaynzof and S. Huettner, *Adv. Mater.*, 2016, **28**, 2446-2454.

24. Y. Yuan, J. Chae, Y. Shao, Q. Wang, Z. Xiao, A. Centrone and J. Huang, *Advanced Energy Materials*, 2015, **5**, 1500615.

25. Z. Xiao, Y. Yuan, Y. Shao, Q. Wang, Q. Dong, C. Bi, P. Sharma, A. Gruverman and J. Huang, *Nat Mater*, 2015, **14**, 193-198.

26. A. Walsh, D. O. Scanlon, S. Chen, X. G. Gong and S.-H. Wei, *Angew. Chem. Int. Ed.*, 2015, **54**, 1791-1794.

27. J. M. Azpiroz, E. Mosconi, J. Bisquert and F. De Angelis, *Energy Environ. Sci.*, 2015, **8**, 2118-2127.

28. C. Eames, J. M. Frost, P. R. F. Barnes, B. C. O/'Regan, A. Walsh and M. S. Islam, *Nat Commun*, 2015, **6**, 1-8.

29. S. Meloni, T. Moehl, W. Tress, M. Franckevičius, M. Saliba, Y. H. Lee, P. Gao, M. K. Nazeeruddin, S. M. Zakeeruddin, U. Rothlisberger and M. Graetzel, *Nat. Commun.*, 2016, **7**, 10334.

30. J. Haruyama, K. Sodeyama, L. Han and Y. Tateyama, *J. Am. Chem. Soc.*, 2015, **137**, 10048-10051.

31. D. Bryant, S. Wheeler, B. C. O'Regan, T. Watson, P. R. F. Barnes, D. Worsley and J. Durrant, *J. Phys. Chem. Lett.*, 2015, **6**, 3190-3194.

32. N. Sakai, S. Pathak, H.-W. Chen, A. A. Haghighirad, S. D. Stranks, T. Miyasaka and H. J. Snaith, *Journal of Materials Chemistry A*, 2016, **4**, 4464-4471.

33. A. M. A. Leguy, Y. Hu, M. Campoy-Quiles, M. I. Alonso, O. J. Weber, P. Azarhoosh, M. van Schilfgaarde, M. T. Weller, T. Bein, J. Nelson, P. Docampo and P. R. F. Barnes, *Chem. Mater.*, 2015, **27**, 3397-3407.

34. T. A. Berhe, W.-N. Su, C.-H. Chen, C.-J. Pan, J.-H. Cheng, H.-M. Chen, M.-C. Tsai, L.-Y. Chen, A. A. Dubale and B.-J. Hwang, *Energy Environ. Sci.*, 2016, **9**, 323-356.

35. N. J. Jeon, J. H. Noh, Y. C. Kim, W. S. Yang, S. Ryu and S. I. Seok, *Nature Materials*, 2014, **13**, 897-903.

36. A. Pockett, G. E. Eperon, T. Peltola, H. J. Snaith, A. Walker, L. M. Peter and P. J. Cameron, *J. Phys. Chem. C*, 2015, **119**, 3456-3465.

37. S. N. Habisreutinger, T. Leijtens, G. E. Eperon, S. D. Stranks, R. J. Nicholas and H. J. Snaith, *Nano Lett.*, 2014, **14**, 5561-5568.

38. J. Yang, B. D. Siempelkamp, D. Liu and T. L. Kelly, *ACS Nano*, 2015, **9**, 1955-1963.

39. M. Shirayama, M. Kato, T. Miyadera, T. Sugita, T. Fujiseki, S. Hara, H. Kadowaki, D. Murata, M. Chikamatsu and H. Fujiwara, *J. Appl. Phys.*, 2016, **119**, 115501.

40. N. Aristidou, I. Sanchez-Molina, T. Chotchuangchutchaval, M. Brown, L. Martinez, T. Rath and S. A. Haque, *Angew. Chem. Int. Ed.*, 2015, **54**, 8208-8212.

41. F. T. F. O'Mahony, Y. H. Lee, C. Jellett, S. Dmitrov, D. T. J. Bryant, J. R. Durrant, B. C. O'Regan, M. Graetzel, M. K. Nazeeruddin and S. A. Haque, *Journal of Materials Chemistry A*, 2015, **3**, 7219-7223.

42. A. J. Pearson, G. E. Eperon, P. E. Hopkinson, S. N. Habisreutinger, J. T.-W. Wang, H. J. Snaith and N. C. Greenham, *Advanced Energy Materials*, 2016, **6**, 1600014.

43. W. H. Nguyen, C. D. Bailie, E. L. Unger and M. D. McGehee, *J. Am. Chem. Soc.*, 2014, **136**, 10996-11001.

44. U. B. Cappel, T. Daeneke and U. Bach, *Nano Lett.*, 2012, **12**, 4925-4931.

45. T. Leijtens, G. E. Eperon, S. Pathak, A. Abate, M. M. Lee and H. J. Snaith, *Nat. Commun.*, 2013, **4**, 2885-2885.

46. A. R. Pascoe, N. W. Duffy, A. D. Scully, F. Huang and Y.-B. Cheng, *J. Phys. Chem. C*, 2015, **119**, 4444-4453.

47. J. Halme, *PCCP*, 2011, **13**, 12435-12446.

48. M. Bag, L. A. Renna, S. P. Jeong, X. Han, C. L. Cutting, D. Maroudas and D. Venkataraman, *Chem. Phys. Lett.*, 2016, **662**, 35-41.

49. S. van Reenen, M. Kemerink and H. J. Snaith, *J. Phys. Chem. Lett.*, 2015, **6**, 3808-3814.

50. J. H. Heo, H. J. Han, D. Kim, T. K. Ahn and S. H. Im, *Energy Environ. Sci.*, 2015, **8**, 1602-1608.

51. H.-S. Kim, I.-H. Jang, N. Ahn, M. Choi, A. Guerrero, J. Bisquert and N.-G. Park, *J. Phys. Chem. Lett.*, 2015, **6**, 4633-4639.

52. J. R. Jennings and Q. Wang, *J. Phys. Chem. C*, 2010, **114**, 1715-1724.

6 Large amplitude time domain measurements

6.1 Abstract

The behaviour of planar perovskite solar cells was studied in the time domain using open-circuit photovoltage rise and decay measurements. The results of these measurements are shown to compliment the frequency domain measurements, with good agreement between the time constants obtained from the two techniques.

The slow rise and decay in photovoltage was shown to be related to ionic movement through temperature dependent measurements and the calculation of activation energies that were consistent with those obtained in Chapter 5. The results of both the frequency and time domain measurements were used to develop a model to explain the response of planar perovskite solar cells.

Ionic double layers are formed at the interfaces of the perovskite layer, which act to screen the built-in voltage. This leaves a field free region across the bulk of the perovskite. When illuminated the ions redistribute to screen the change in electric field. As the ions move away from the interface the rate of recombination is reduced suggesting that recombination in the region near to or at the interface is the dominant mechanism.

6.2 Introduction

Open-circuit photovoltage decay (OCVD) measurements have been extensively used in a range of solar cell technologies including silicon[1, 2], organic[3] and dye-sensitized solar cells[4-6]. The technique involves illuminating the cell at open-circuit to establish a steady state photovoltage. The light is then switched off and the voltage decay is recorded. Analysis of the rate of decay can give information relating to the carrier lifetime.

In DSSC the electron lifetime is often given by the reciprocal of the derivative of the decay curve normalized to the thermal voltage[7]

$$\tau_n = -\frac{k_B T}{q}\left(\frac{dV_{oc}}{dt}\right)^{-1}$$

This equation gives the effective lifetime of electrons, in the mesoporous TiO_2 conduction band and traps, as they recombine with oxidized species in the electrolyte. This is related to the discharge of the chemical capacitance via the recombination resistance, giving the time constant, $\tau_n = R_{rec}C_\mu$. For large amplitude measurements such as OCVD the rate of recombination may not be linear for all states throughout the decay. Zaban et al. derived the electron lifetime for non-linear recombination[4]. A similar approach has been followed to derive the OCVD lifetime for the case of bimolecular recombination in a low doped, or intrinsic material such as the perovskite. In this instance the lifetime can be calculated using

$$\tau_{OCVD} = -\frac{2k_B T}{q}\left(\frac{dV_{OC}}{dt}\right)^{-1} - \frac{dV_{OC}}{dt}\left(\frac{d^2V_{OC}}{dt^2}\right)^{-1}$$

The derivation of this equation is shown in Appendix B. As shown from EIS measurements (Chapter 4) a chemical capacitance is not observed for the planar cells and so the interpretation of the OCVD lifetime does not relate to the discharge of the chemical capacitance in these cells.

The use of OCVD measurements has not been extensively studied in perovskite solar cells. Time domain measurements have more commonly been restricted to small amplitude perturbation techniques such as transient photovoltage measurements[8-10]. Similarly to the high frequency EIS and IMVS response these measurements give information about the electronic properties of the device. The interpretation of large

amplitude voltage decay measurements is not straightforward as the decays are influenced by other slow processes.

Baumann et al. performed voltage decay measurements on planar perovskite cells with organic type contacts[11]. They observed a fast initial voltage decay which transitioned into a long lived decay lasting for tens of seconds (shown in Figure 6-1). For DSSC a long lived decay can be attributed to the trapping/slow detrapping of electrons in the titania scaffold[5]. However, Baumann et al. observed an interesting trend on the initial intensity in that the slow decay was dependent on the starting point. In a simple trapping model the rate of recombination should only depend on the carrier concentration and not the initial illumination. In other words the traps will empty at the same rate for a given Fermi level regardless of the initial Fermi level position. Also, there is no evidence of significant trap densities in planar perovskite cells[12, 13] (and no charge accumulation was observed in EIS measurements in this work).

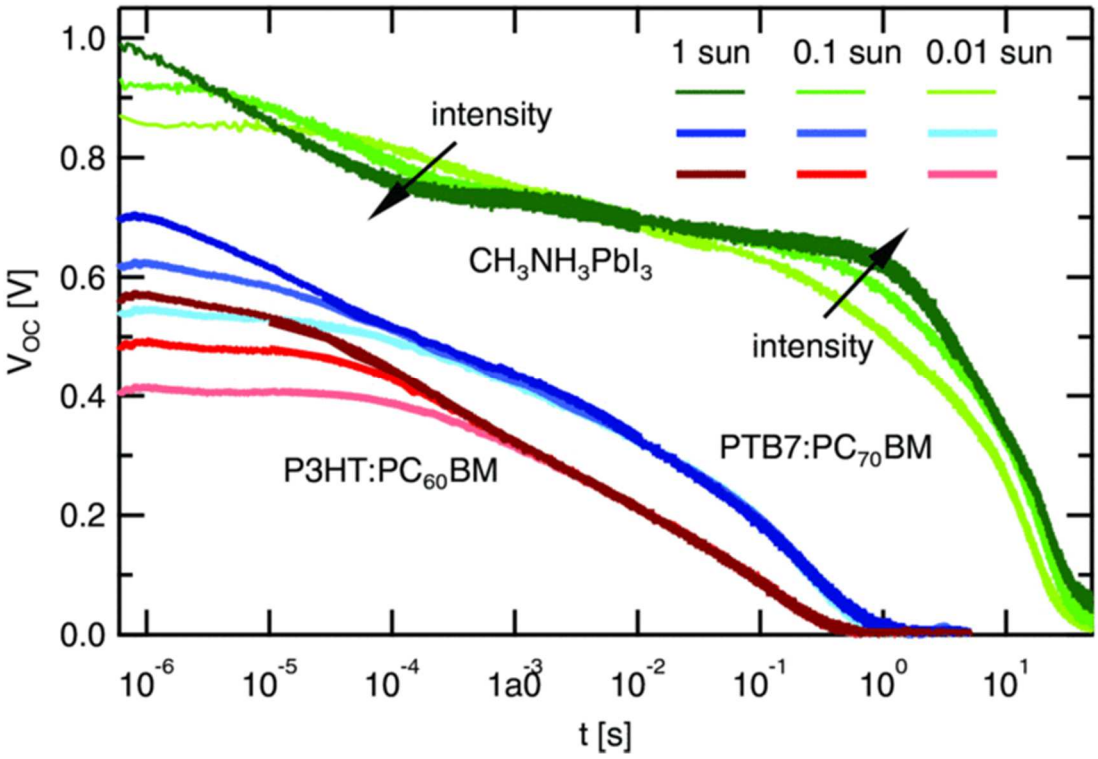

Figure 6-1: Voltage decays measured by Baumann et al. from different light intensities[11]. The persistent photovoltage is dependent on the initial starting conditions for the perovskite cells. OPV cells are used as a comparison showing that after the initial decay, the rate is independent of starting conditions.

Bertoluzzi et al. investigated voltage decays on mesoporous TiO_2 cells, which again presents challenges when trying to separate the influence of the mesostructured layer from the perovskite behaviour[14]. However, they did suggest that the classical method of interpreting OCVD data, using equations such as those shown above to calculate electron lifetimes, may not be suitable with regards to the complete voltage decay. They attributed the fast initial decay to electronic phenomena, i.e. recombination. It was suggested that the subsequent slow decay was as a result of ferroelectric effects.

As mentioned previously, ferroelectric domains have been ruled out as being responsible for the slow dynamic behaviour observed in perovskite solar cells[15, 16]. Strong evidence has been presented that ion migration occurs on timescales comparable to the slow dynamic behaviour. From EIS and IMVS measurements carried out in Chapter 5, activation energies comparable to that for iodide vacancy migration were obtained from the time constants of the low frequency processes. These time constants were shown to be due to the change in recombination rate due to ionic movement. Whilst small amplitude frequency domain measurements have revealed the link between ionic movement and recombination, it is necessary to study the cells using large amplitude time domain measurements in order to determine the effect of the ionic environment on the electronic properties of the cells.

6.3 Experimental

This chapter presents results from the two different batches of cells measured in Chapters 4 and 5. For the measurements on the initial batch of cells from Chapter 4, the OCVD measurements were performed manually using a red LED (630 nm) and function generator to provide the switching signal. The cell was held at open-circuit by a home-built high impedance voltage follower with an input impedance greater than 10^{12} ohms to ensure negligible current flowed during the decay. Transients were recorded on a digital storage oscilloscope. In order to record the fast initial decay at high resolution and still measure the long lived decay, the measurements were repeated under the same conditions using different oscilloscope time bases. These decays were then overlaid and joined together. The complete decays were smoothed using Loess smoothing and fitted to an 11 parameter rational function before calculating the lifetimes.

The remaining measurements carried out in this chapter were performed on the same batch of cells as in Chapter 5. Open-circuit voltage decay measurements were performed using the Solartron ModuLab XM Photoelectrochemical Test System with optical bench attachment. The ModuLab system allows the data sampling rate to be changed during a measurement. This feature was employed to ensure that maximum resolution was achieved when the rate of change of voltage was highest. Immediately after initial light switch on or switch off the sampling rate was set to 1 MS/s to capture the very fast initial rise/decay in photovoltage. After 100 ms the sampling rate was decreased to 100 kS/s, and then to progressively lower sampling rates as the measurement progressed. A minimum sampling rate of 100 S/s was reached from 11.6 seconds onwards. Reduction in the sampling rate as time progressed was utilized to ensure good resolution for the fast parts of the rise/decay whilst being careful not to overload the system's internal data buffer or produce excessively large data files.

Illumination was provided by a 470 nm LED (Thorlabs), at intensities ranging from 73 mW cm^{-2} to 1 mW cm^{-2}. For the temperature controlled measurements an illumination intensity of 42 mW cm^{-2} was used. Cells were illuminated for long enough for the open-circuit voltage to reach a steady state value. This varied from around 1 minute at elevated temperatures to around 30 minutes at low temperature.

Between measurements the cells were held at open-circuit. Measurements were performed inside a light-tight faraday cage to eliminate stray light and electrical interference.

The samples were mounted in a home-built desiccated cell holder with quartz window. Temperature controlled measurements were performed using a home-built sample holder incorporating a Peltier module. The temperature was controlled using a USB controller (Meerstetter Engineering) which delivered a purely DC current to the Peltier module. A different temperature controller was initially tested but its high frequency pulse width modulated (PWM) output signal induced significant interference in the electrical measurements. A 5 kΩ NTC thermistor was placed on the sample surface to monitor the temperature as part of the controllers PID feedback loop. The Peltier element was mounted on a water cooled copper heatsink to extract heat efficiently from the hot side. The water cooling system utilised a pump and radiator with fan that were kept outside of the measurement faraday cage to eliminate sources of interference. The sample holder was also placed inside a desiccated box, with quartz window, to reduce the chances of condensation forming on the cells at low temperatures. The temperature range used was -25 to +65 °C in 10 °C increments. Temperature stability was ±0.01 °C at the set point. Unless stated in the figure captions, all intensity dependent measurements performed on the second cell batch were carried out a controlled temperature of 25 °C. As shown from the temperature dependent measurements, the time constant of the slow process is highly dependent on temperature.

6.4 Results

6.4.1 The fast time domain response

Initial OCVD studies were carried out on the batch of cells studied in Chapter 4. This batch of cells displayed a number of characteristics which separated them into two distinct groups. For example, about half of the cells tested had ideality factors around m=2.6, whilst the other half had ideality factors around m=5.2 as determined from the intensity dependence of the open-circuit voltage. Time constants obtained from EIS and IMVS also showed similarly split dependencies on open-circuit voltage. This trend can be seen to also exist in the open-circuit photovoltage decay measurements, as shown in Figure 6-2. Cell FS43-1 (m=5.3) has a fast photovoltage decay that is complete within approximately 1 second. Cell FB06-1 (m=2.6) has a fast initial decay to around 450 mV, but then a shows a persistent photovoltage lasting in excess of 10 seconds. This behaviour was consistent for all cells in the batch, i.e. only the cells with the lower ideality factors around m=2.6 showed a persistent photovoltage decay.

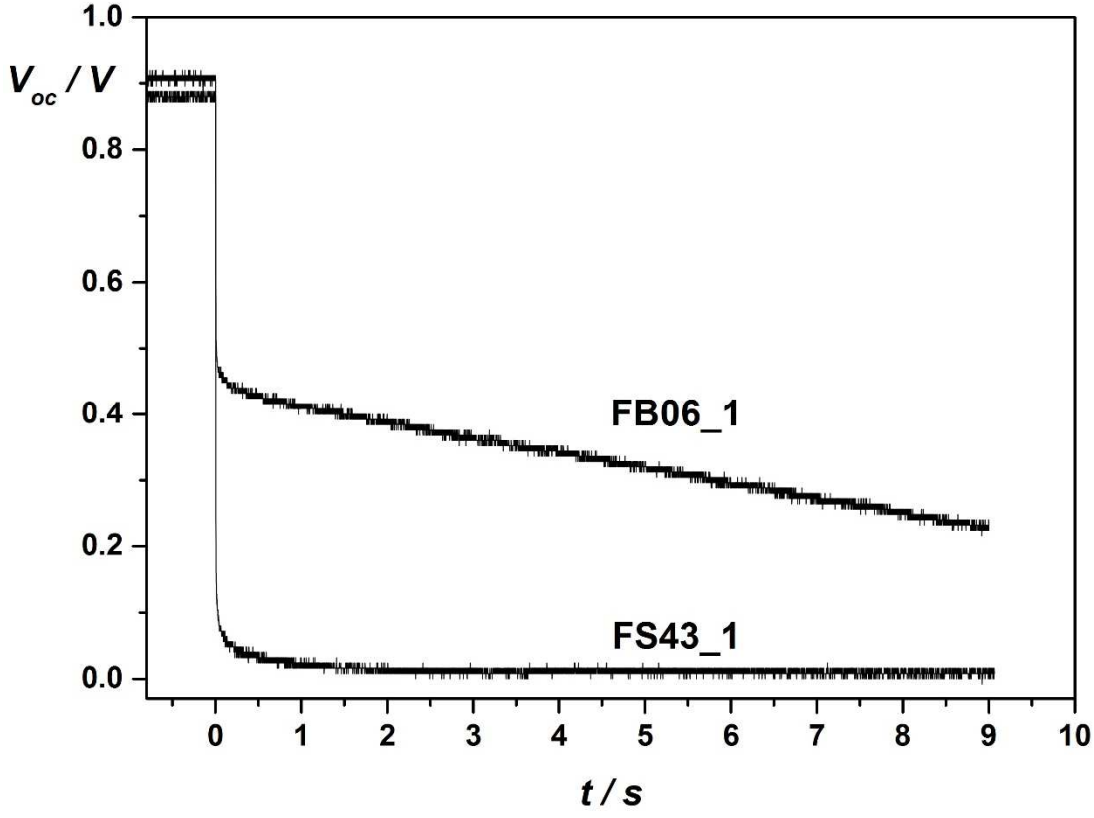

Figure 6-2: Open-circuit voltage decays for cells FB06-1 and FS43-1.

To analyse the decays further the open-circuit voltage was plotted against the logarithm of time as shown in Figure 6-3. The differences between the two types of decay are highlighted in this plot. After 10 ms, the V_{oc} of cell FS43-1 dropped to around 100 mV, compared to cell FB06-1 which maintained a voltage of around 500 mV. After 1 second it appears that the decay for FB06-1 becomes exponential, discharging at a constant rate for several seconds. The long decay for cell FB06-1 is consistent with the results of Baumann et al. who performed similar measurements on perovskite cells with organic contacts[11]. The quicker type of decay for cell FS43-1 has not been previously reported in the literature and suggests increased shunting in the device which would only be evident at low photovoltages, hence the comparable 1 sun performance.

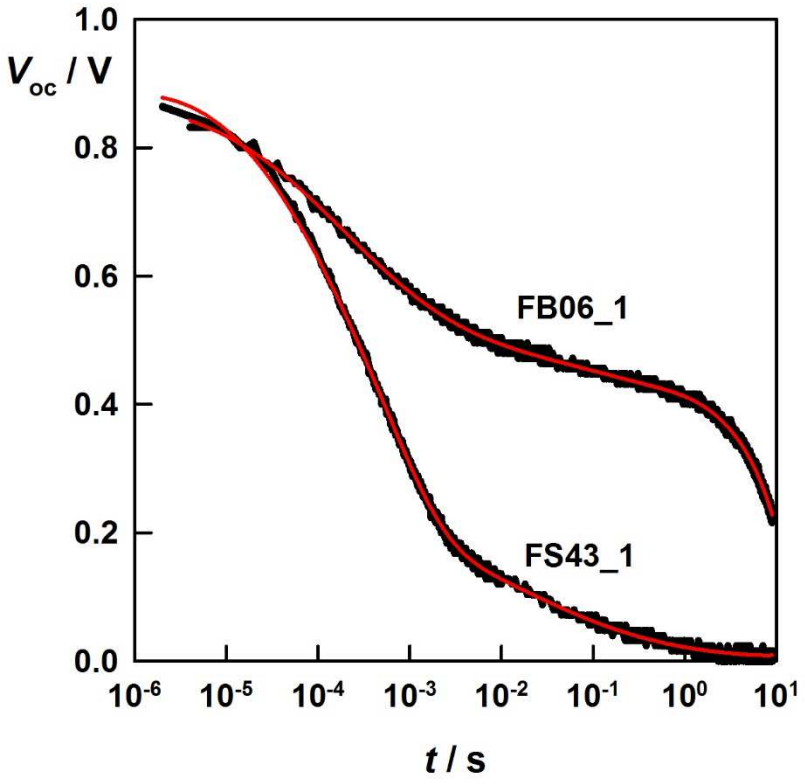

Figure 6-3: Voltage decays on a log(t) axis. Red lines represent fits to an 11 parameter rational function.

The data was smoothed using Loess smoothing to give evenly spaced x-values on the log timescale. This was then fitted to an 11 parameter rational function to get a smooth data function which could be differentiated cleanly (fit displayed in Figure 6-3). This data treatment was important due to the piecewise addition of multiple transients with different timebases.

From this fit, the OCVD lifetime was calculated according to the equation derived for bimolecular recombination (see section 6.2 and Appendix B). The OCVD lifetime is plotted as a function of voltage in Figure 6-4. The lifetimes for each type of decay vary with different slopes at high photovoltages. This is shown to be consistent with the IMVS-V_{oc} dependence. For cell FB06-1 the lifetime rapidly increases below 0.5 V, before becoming constant (monoexponential decay) below 0.4 V. The OCVD lifetimes show good agreement with those obtained from IMVS, indicating that the voltage decays through a set of quasi-stationary states over this voltage range. As in IMVS, at high voltages the OCVD decay is also dictated by the RC time constant of the cells geometric capacitance discharging through the recombination resistance.

At open-circuit voltages below those measured in IMVS the OCVD lifetime increases rapidly to values on the time scale of seconds, seemingly consistent with the slow processes observed in Chapter 5. These results show a clear link between time and frequency domain measurements. The initial fast decay can be related to the high frequency response of the cells which is dominated by the cells geometric capacitance. In order to verify that the apparent slow time domain response is linked to ionic movement within the perovskite layer, as evidenced in the frequency domain measurements, OCVD data for a range of different conditions is presented in the next section.

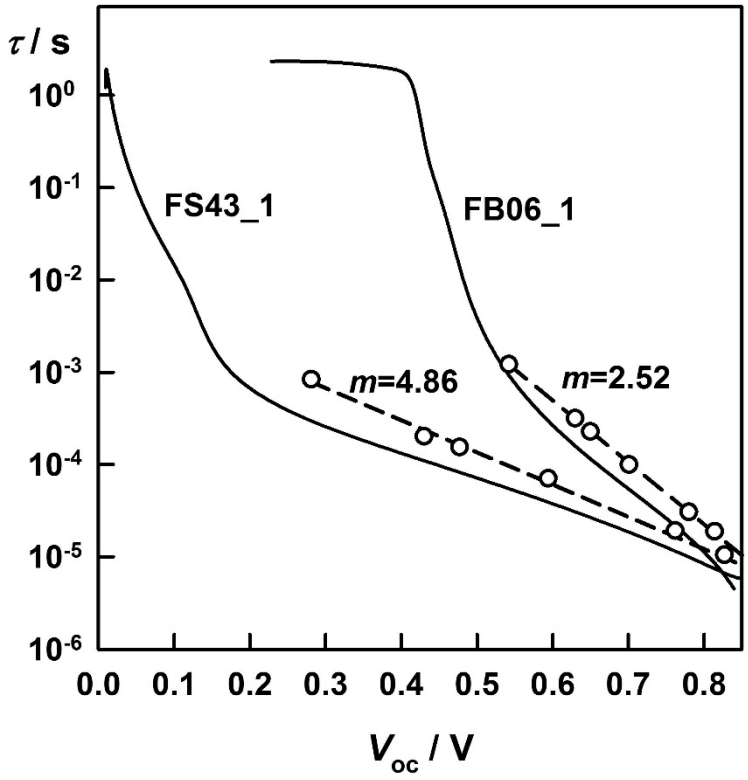

Figure 6-4: Lifetimes as a function of voltage for the two types of cell. The IMVS lifetimes are also plotted for comparison.

6.4.2 The slow time domain response

In order to study the origins of the cells persistent photovoltage a range of measurements were performed under different illumination conditions and at different temperatures. The photovoltage rise was also measured in this part of the experiment.

It is clear from Figure 6-5 that both the rise and decay in photovoltage have a fast and slow component. Upon illumination the V_{oc} rises to 0.55 V in 10 ms. The slow rise to the photostationary V_{oc} takes a further 3 minutes. Similarly to the long decays in the previous section, when the light is turned off the voltage drops to around 0.5 V in the first 30 ms, with the remaining photovoltage decaying over 20 seconds.

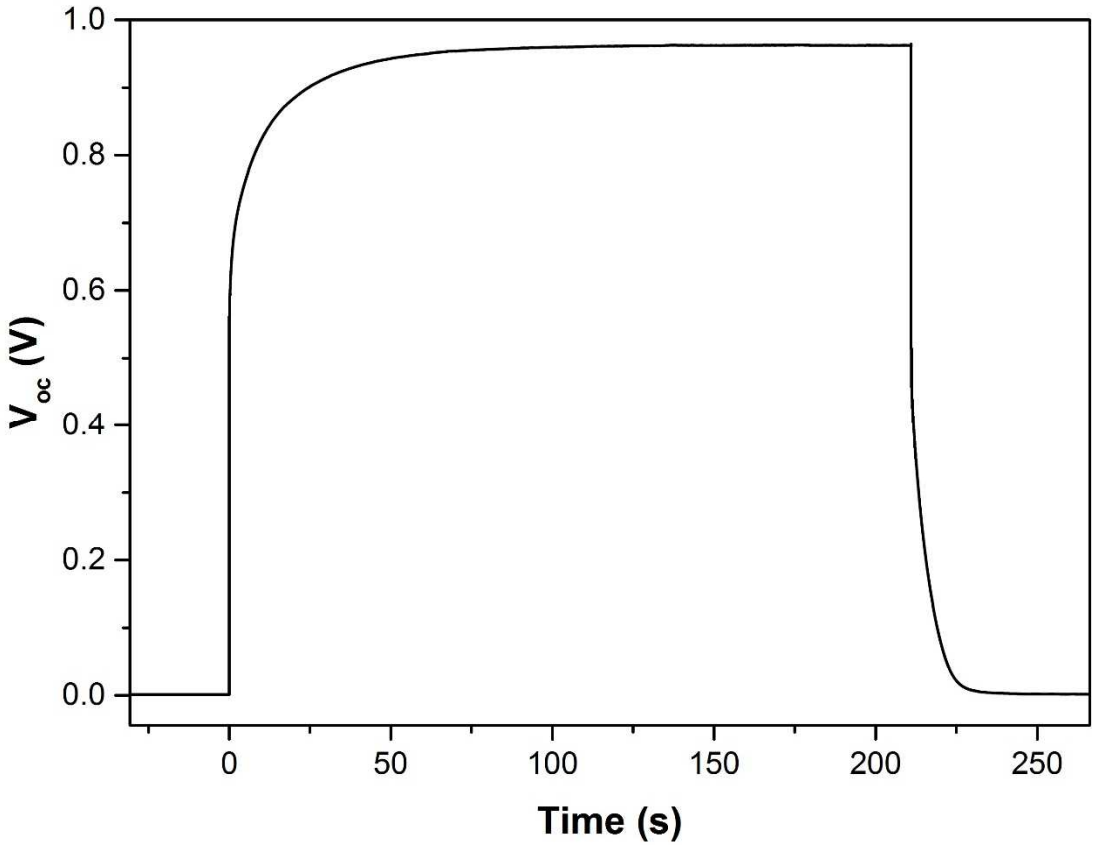

Figure 6-5: Complete OCVD measurement of cell CT-3 under 42 mW cm^{-2} illumination showing fast and slow components to photovoltage rise and fall.

As these slow processes are known to be not purely electronic it would be incorrect to analyse them making assumptions based on recombination mechanisms as for the fast decay in the previous section. In this section time constants will be estimated from the near monoexponential rise and decay processes observed.

1.1.1.5 Intensity dependence

The photovoltage rise shows a clear intensity dependence, seen in Figure 6-6. Firstly, it is clear that for lower intensities the initial photovoltage rise makes up a lower proportion of the final photostationary value. For example, at 42 mW cm^{-2} the initial rise to ~0.55 V represents 57% of the final photostationary value. At 1.4 mW cm^{-2}, the initial rise to ~0.25 V represents only 33% of the final steady state value at that light intensity. The inset of Figure 6-6 also shows that the initial rise becomes faster with increasing intensity.

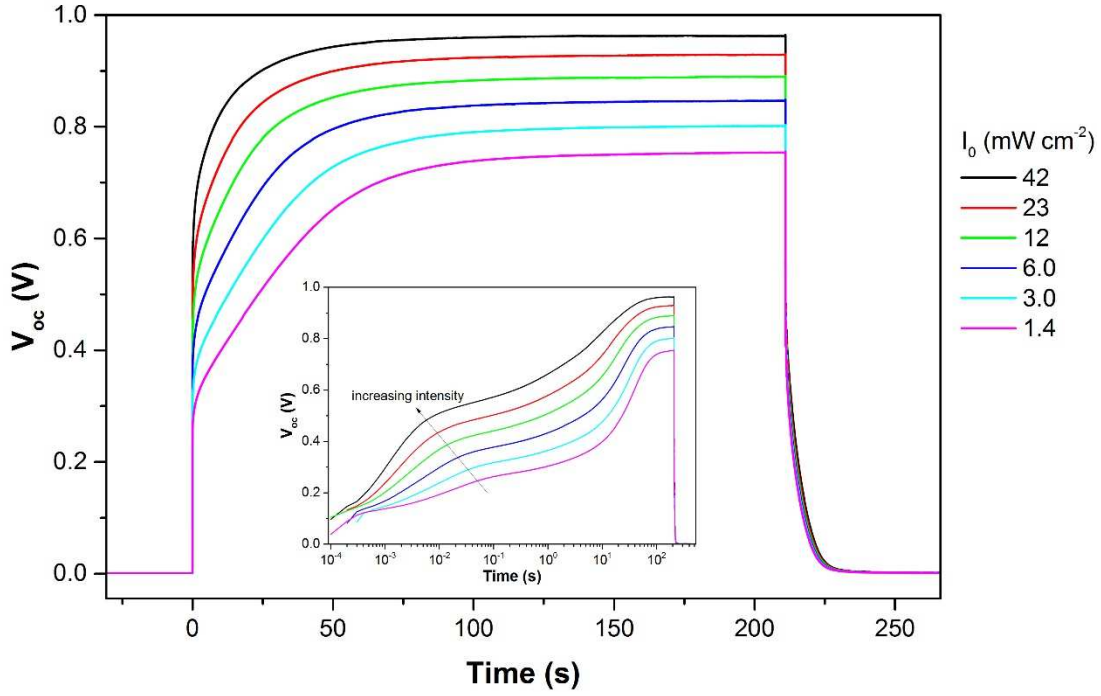

Figure 6-6: OCVD measurement performed at different illumination intensities on cell CT-3. Inset: Photovoltage plotted against a log(t) scale to show multiple components to the voltage rise.

To compare the effect of illumination intensity on the rate of the photovoltage rise it is convenient to plot the data as $\ln\left(1 - V/V_F\right)$ against time, where V_F represents the final photostationary voltage, as shown in Figure 6-7. This shows that the slow rise to steady state appears to be largely independent of light intensity as shown by the similar slopes in the data. A time constant for the rise is estimated by taking a linear fit to the data after the initial rise has taken place, from which point the rise is approximately monoexponential to a maximum value (after the first 10-20 seconds). Time constants around $\tau = 20$ seconds can be estimated for all light intensities. This value is consistent with the low frequency time constants obtained from IMVS/EIS, as is the weak dependence on light intensity.

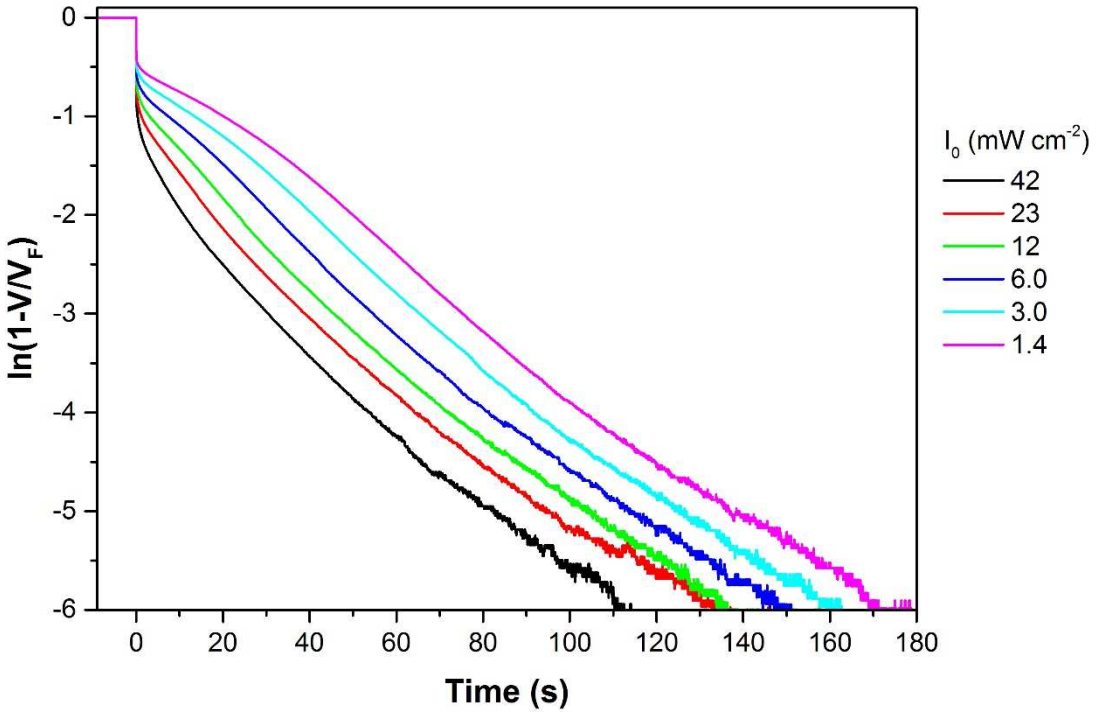

Figure 6-7: Photovoltage rise plotted as ln(1-V/V_F) against time to evaluate the rate of the rise to the final photostationary value, V_F.

The voltage decays show comparable trends to the rise data as shown in Figure 6-8. The initial decay is slightly faster for a higher illumination intensity. There is also a slightly longer lived photovoltage at higher intensities, again consistent with the results of Baumann et al[11]. The time constant extracted from the log(V) versus time plot is approximately 5 seconds, with a slight decrease in lifetime with decreasing light intensity. Again, this is consistent with the low frequency time constant measured using EIS.

The time constant for the decay is several times faster than that obtained from the rise. It is possible that they relate to the same process, i.e. ionic movement, but under different conditions. For example upon illumination photogenerated electron-hole pairs will be formed, splitting the quasi-Fermi levels and altering the electronic band structure. During the decay, electrons and holes will recombine quickly, causing the band structure to relax. This means that ionic movement in the presence or absence of excess electrons and holes will be under the influence of a different electric field.

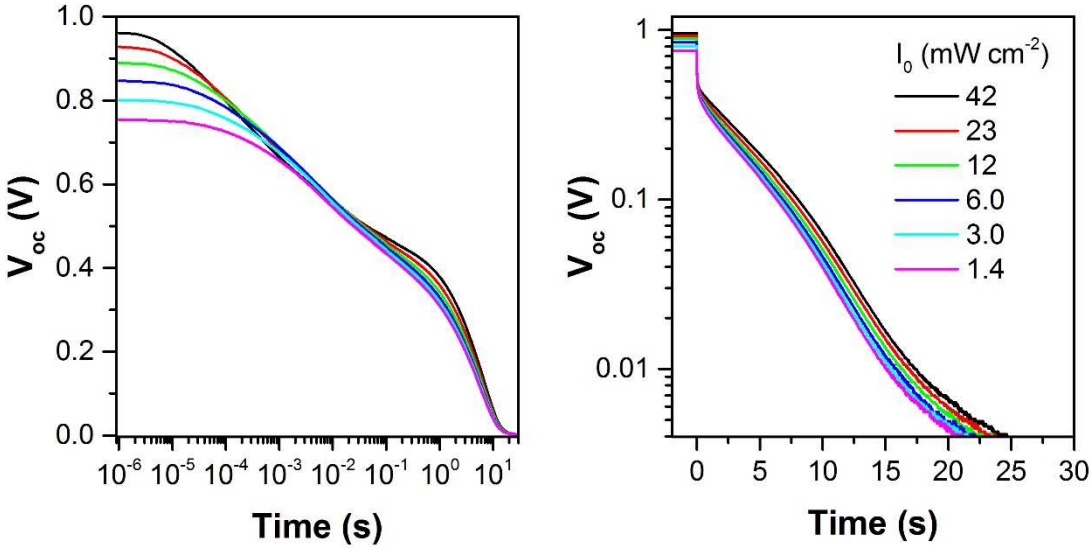

Figure 6-8: Voltage decays at different light intensities on a log(t) scale (left) and log(V) scale (right).

It is essential to note the importance of ensuring a consistent equilibrium starting condition for the voltage rise and photostationary state for the decay in order to obtain reproducible results. Figure 6-9 shows a series of photovoltage transient measurements performed for different illumination times. In order to get the repeated voltage rises to overlay it was necessary to allow the system to relax fully in the dark at open circuit. The V_{oc} was allowed to decay to less than 1 mV before the subsequent measurement was taken. If even a few mV open-circuit voltage remained, the voltage rise was much faster showing that the cell was not at equilibrium.

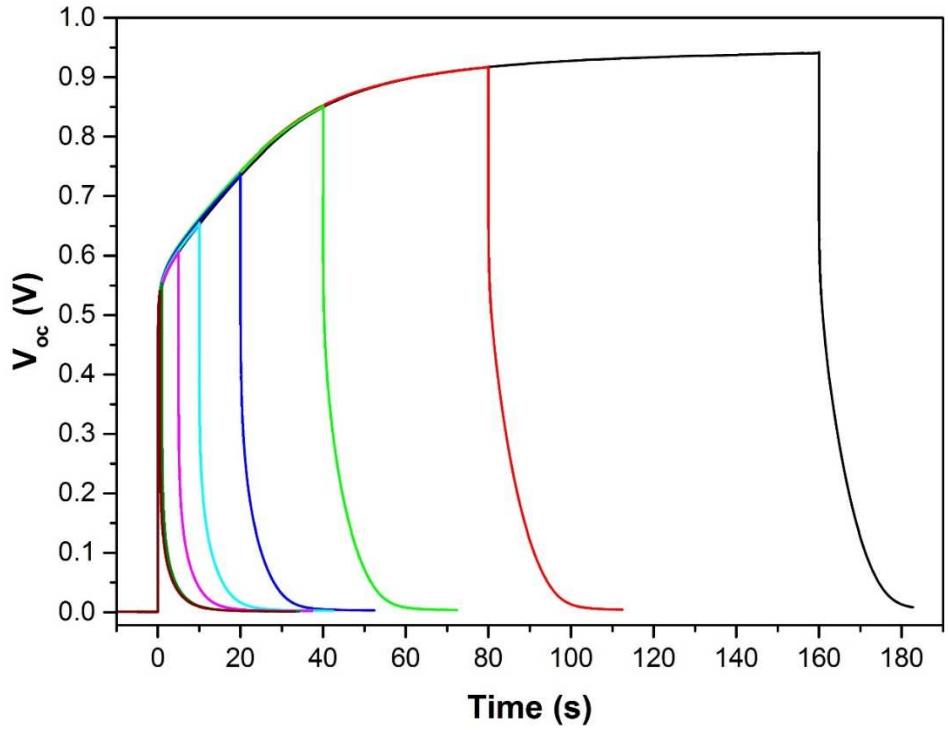

Figure 6-9: Photovoltage transients for different illumination times starting from a well-defined equilibrium condition (i.e. open-circuit in the dark, V_{oc}<1mV).

The voltage decays corresponding to this measurement are shown in Figure 6-10. The decays highlight that a certain condition is built up with increasing illumination time that is allowed to relax when the light is turned off. The slow relaxation takes place at a constant rate regardless of the pre-conditioning as shown by the similar rates of decay after t=1 s for all curves. After longer illumination times the length of the decay increases. To get a true picture of the full relaxation process it is necessary to illuminate for long enough to reach a steady state condition.

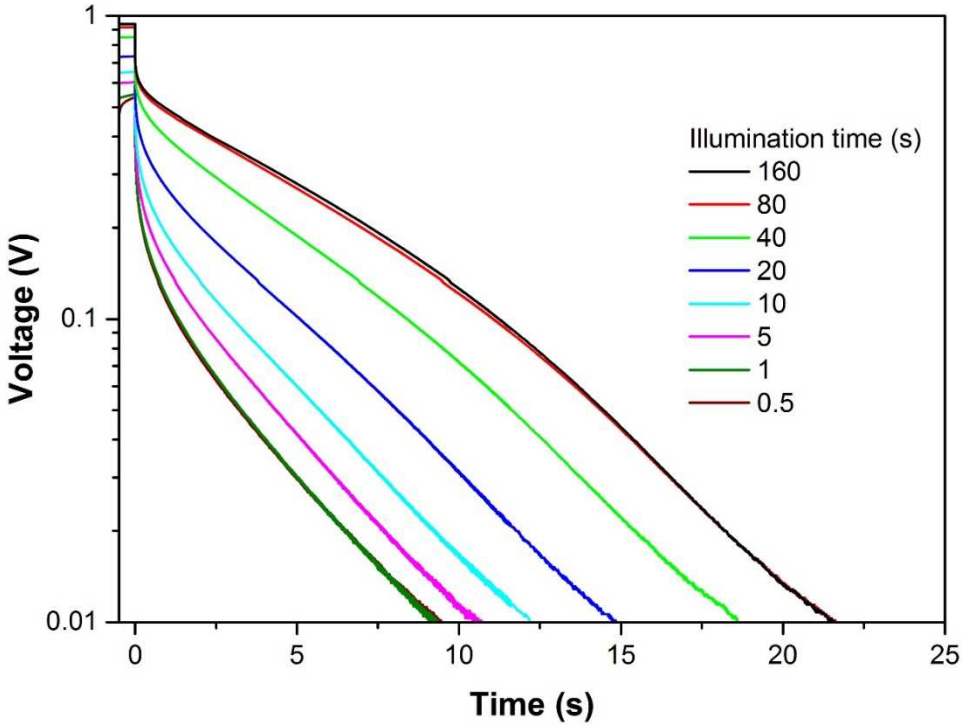

Figure 6-10: Voltage decays after different illumination times for cell CT-3.

For some cells, a ‘bounce-back’ in voltage was observed after the initial fast photovoltage decay as seen in Figure 6-11. This was more prevalent at high intensities. At 73 mW cm^{-2} the voltage increased by 10 mV after the initial decay, before continuing to decrease. This feature is also observed in temperature dependent measurements.

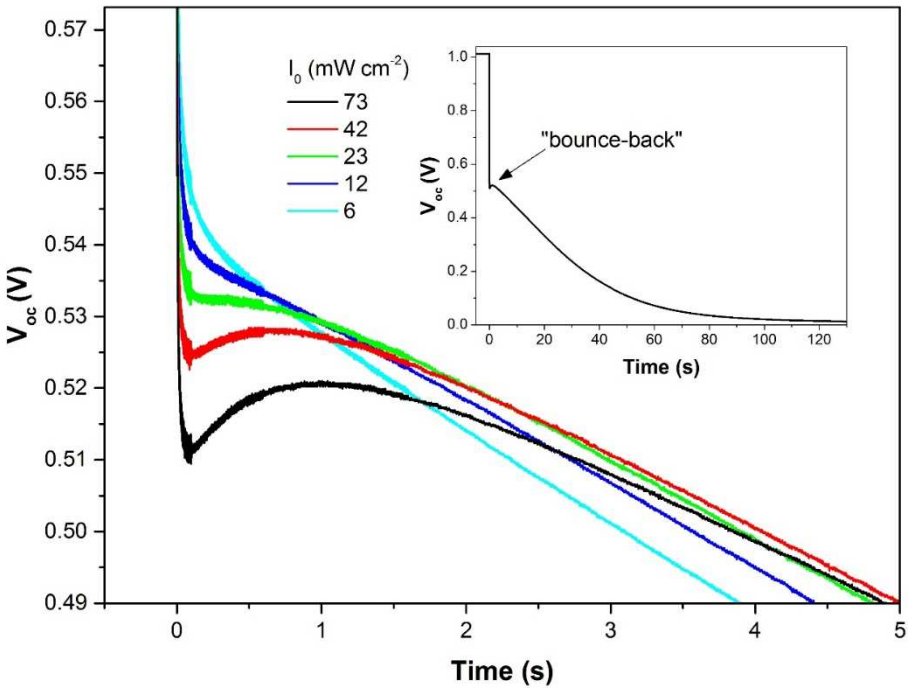

Figure 6-11: Voltage "bounce-back" after initial fast voltage decay. Inset: Full decay from 73 mW cm^{-2} intensity showing position of "bounce-back" at transition from fast to slow decay. Measurement performed at room temperature, ~18 °C, resulting in the slower photovoltage decay.

1.1.1.6 Temperature dependence

As expected from the frequency domain measurements, the slow component of the OCVD measurements shows a significant temperature dependence. Figure 6-12 shows the strong influence temperature has on the rate of the photovoltage rise. At -25 °C the photovoltage takes 30 minutes to reach a photostationary value. Conversely, at 35 °C the voltage has stabilized after just over 1 minute. This is comparable to the time taken for the V_{oc} to stabilize before impedance measurements in the previous chapter. The traces in Figure 6-12 also show a high degree of linearity over long time periods, especially at lower temperatures. This suggests that this slow exponential rise is governed by a single process.

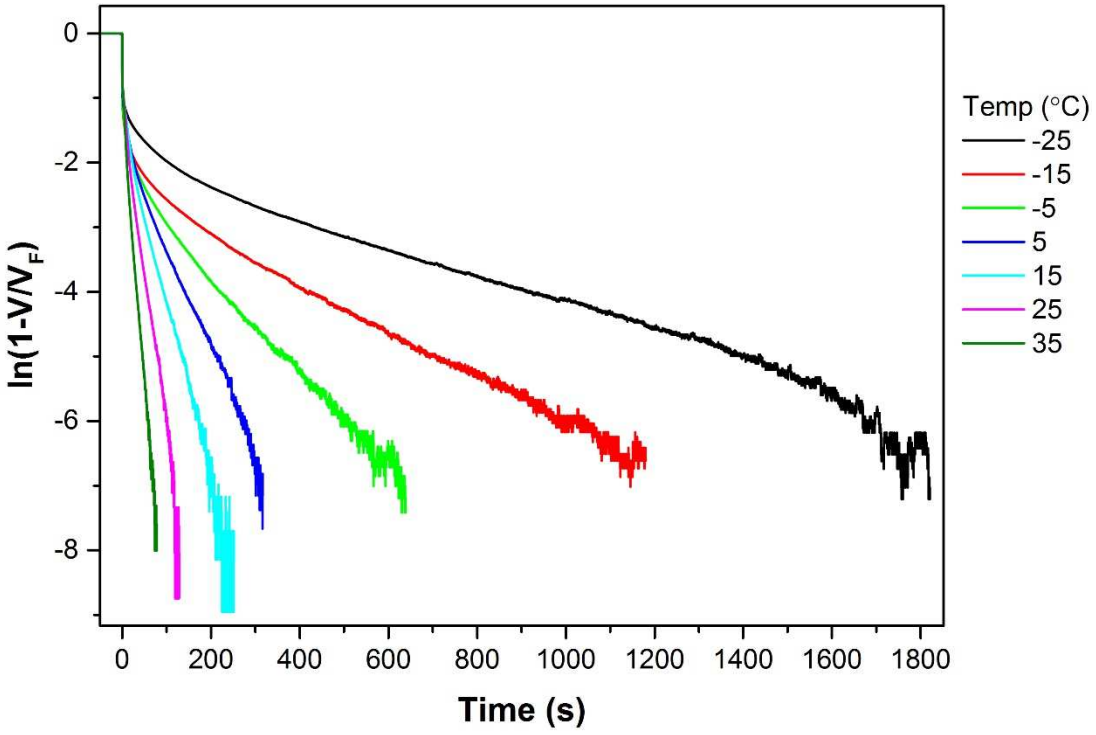

Figure 6-12: Temperature dependent photovoltage rise plotted as ln(1-V/V_F) against time.

The voltage decays show a similar dependence on temperature as seen in Figure 6-13. At -25 °C the photovoltage is still in excess of 0.2 V after 10 minutes. As seen from the linearity of the decays on the log(V) versus time plot, the decays are very close to being monoexponential.

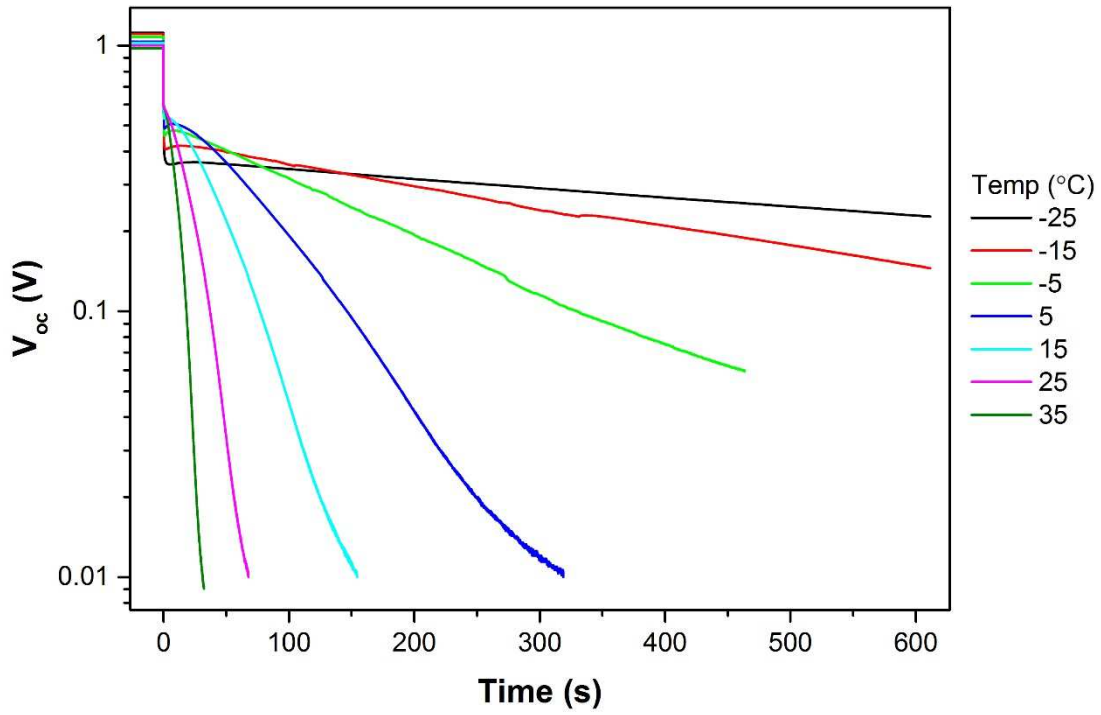

Figure 6-13: Temperature dependent voltage decays.

Time constants have been extracted from both the temperature dependent rise and decay measurements in order to construct Arrhenius plots. The Arrhenius plot for the voltage rise is shown in Figure 6-14. An activation energy of 0.42 eV is calculated from this plot. This is slightly lower than the values calculated from the frequency domain measurements.

The Arrhenius plot for the voltage decay is shown in Figure 6-15. The activation energy agrees well with the activation energies calculated in the frequency domain measurements. The time constants from the low frequency EIS feature are also plotted, showing excellent agreement with the OCVD decay.

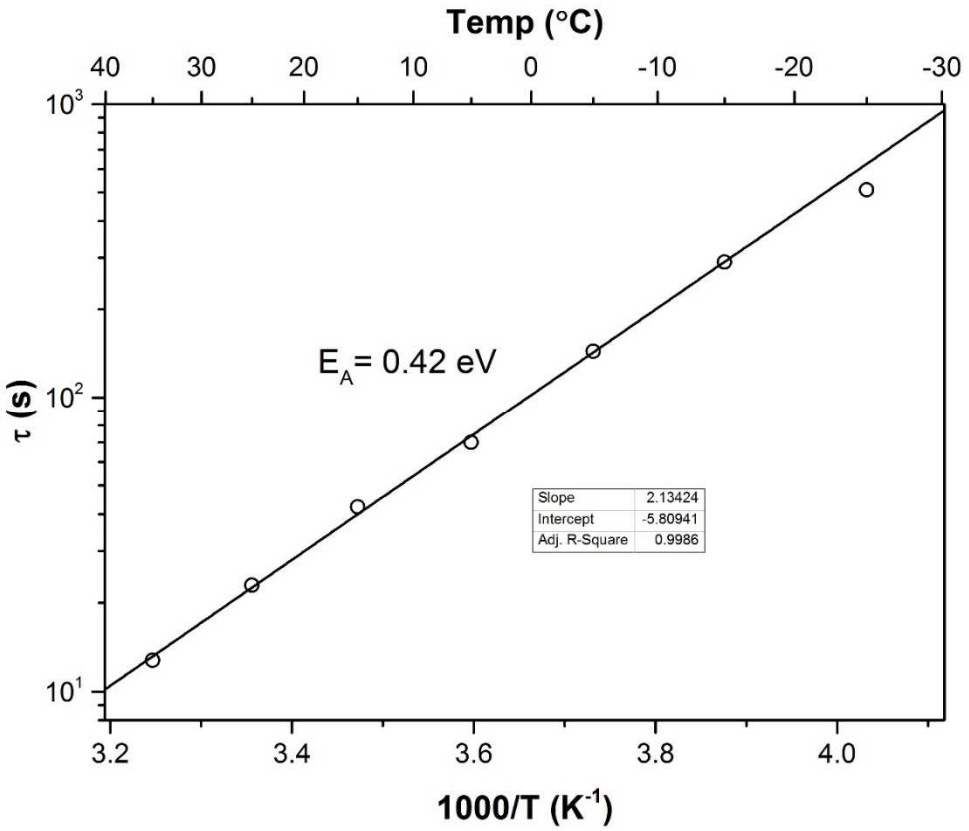

Figure 6-14: Arrhenius plot of the time constant extracted from the slow voltage rise.

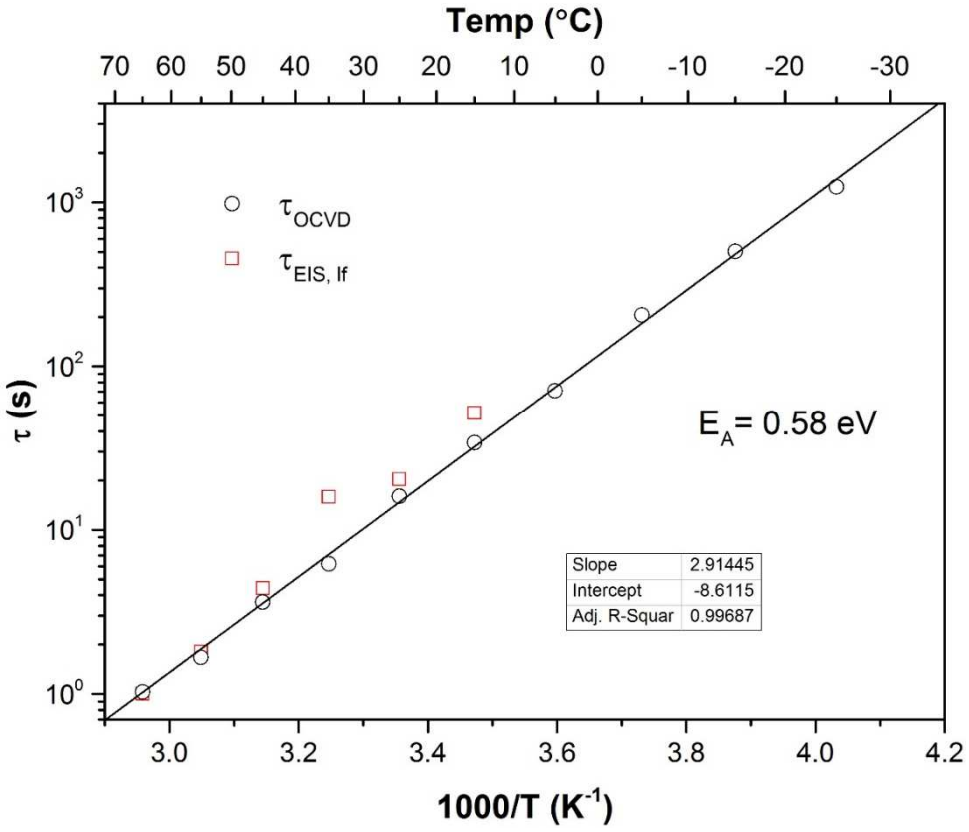

Figure 6-15: Arrhenius plot of the time constant extracted from the slow voltage decay. Also shown are the time constants calculated from the low frequency EIS from the previous chapter.

The “bounce-back” feature was also found to be temperature dependent, shown in Figure 6-16. The peak of the “bounce-back” is delayed as the temperature is reduced, and its effect is prolonged. For example, at 15 °C the peak of the bounce occurs 2.3 seconds into the decay and the effect lasts for approximately 5 seconds (taken to be the length of time for which the voltage is higher than pre-bounce). At -25 °C the peak occurs at 24 seconds into the decay and the effect remains for 45 seconds.

The origin of this feature is not clear, but it is possibly linked to the mid-frequency feature seen in IMVS, and to a lesser extent in EIS. Like the mid-frequency feature, the “bounce-back” occurs between the well-defined high and low frequency processes. It has a strong temperature dependence and slight dependence on intensity. At low intensity the high frequency process in EIS becomes slow enough to obscure the mid-frequency feature as their time constants become comparable. Figure 6-17 shows an EIS measurement under illumination of 0.17 mW cm^{-2} intensity, giving a V_{oc} of 0.56 V. This is close to the voltage at which the “bounce-back” feature is observed in OCVD. It shows that at low intensity the mid-frequency process, typically appearing in the EIS spectra around 10 Hz, becomes completely buried in the transition between the high and low frequency arcs. In fact the high and low frequency arcs start to merge as seen by the phase angle not reaching 0° in the transition between the two. This could also relate to the “bounce-back” being more prominent at higher intensities.

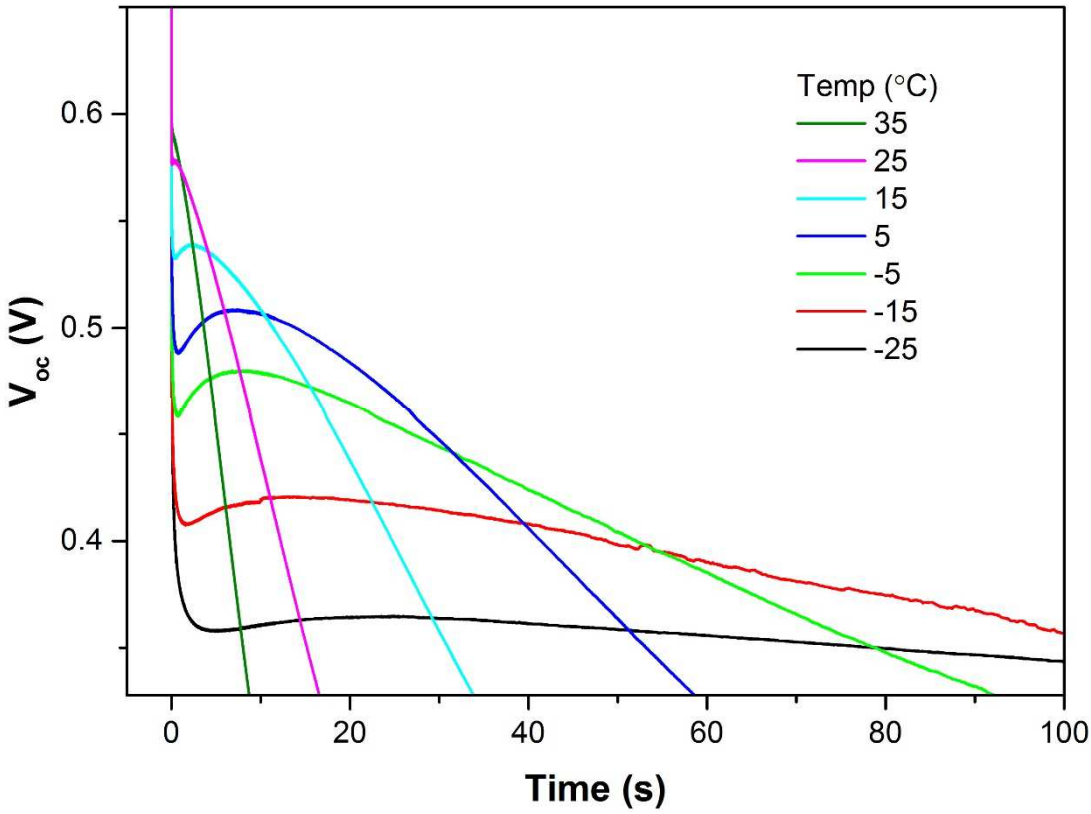

Figure 6-16: Temperature dependence of the "bounce-back" feature.

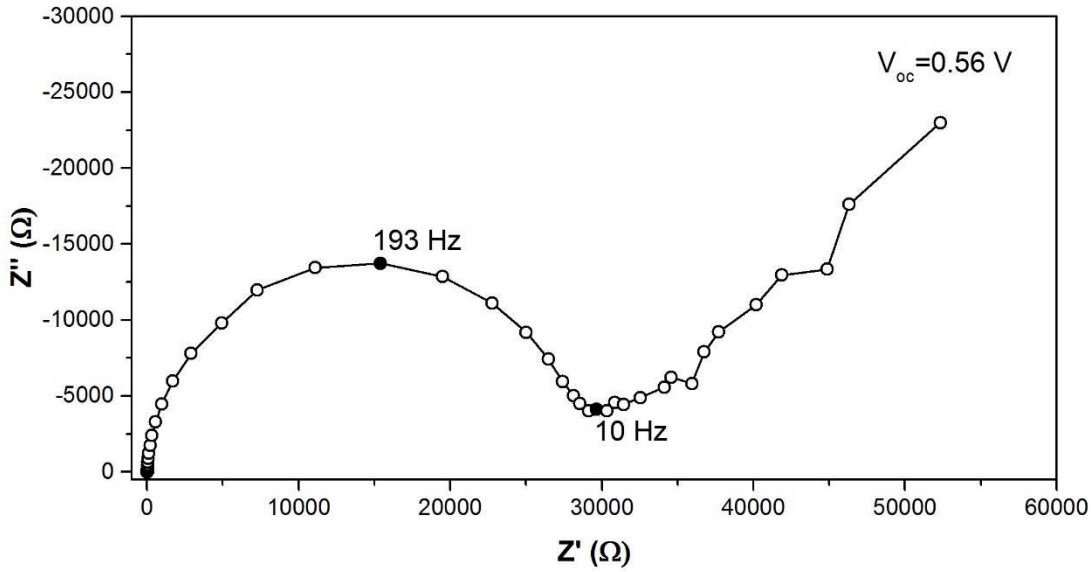

Figure 6-17: Low intensity EIS measurement (0.17 mW cm^{-2}).

6.5 Discussion

This chapter has presented a range of photovoltage transient measurements focusing on both fast and slow processes. These time domain measurements have been shown to correspond well with the frequency domain results presented in the previous chapter. In this discussion, knowledge from both sets of measurements will be used to describe a model to explain the processes that occur in perovskite cells on the microsecond, millisecond and second timescales.

Firstly, the fast initial voltage decay has been shown to correspond to the discharging of the cells geometric capacitance through the recombination resistance. This is verified by comparison to the IMVS lifetimes measured in Chapter 4. There was good agreement between the lifetime-voltage relationships from both IMVS and OCVD for cells with different ideality factors.

It is possible to model the discharge of the geometric capacitance through the cells recombination and shunt (pinhole) resistances. This is compatible with a simple PV model as shown in Figure 6-18. As the recombination resistance is in effect in parallel with the cells shunt resistance, there should be a point in the decay at which the charge begins to predominantly flow through the shunt resistance instead. This occurs when the recombination resistance becomes larger than the shunt resistance.

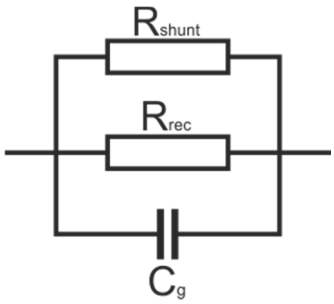

Figure 6-18: Simple PV decay model compatible with the photovoltage decay in perovskite cells in the absence of additional slow effects.

The shunt resistance of similar cells was measured in Chapter 4 (resistance measured in dark impedance at low reverse bias) and found to be of the order of 1 MΩ. The recombination resistance is known to increase exponentially with decreasing voltage at a rate governed by the cells ideality factor

$$R_{rec}(V) = R_0 \cdot e^{(V_0 - V)/mk_BT}$$

Where R_0 is defined to be the recombination resistance at the initial voltage V_0. Therefore if V_0 is equal to the starting value for the decay the recombination resistance can be calculated at each voltage during the decay (assuming ideality factor is constant across entire voltage range). The total cell resistance can be calculated from the parallel combination of the recombination resistance and shunt resistance. The shunt resistance is an intrinsic property of the cell and remains constant. The total resistance tends towards the smallest resistance, and therefore the smallest resistance dominates. For a small voltage drop, dV, the discharge current, dj, flowing through the total resistance can be calculated using Ohm's law. The corresponding decrease in charge is given by dQ = C dV. The time interval, dt, for the discharge of dQ at the rate dj is given by dt = dQ/dj. The time intervals can then be integrated to give the time base for the voltage decay.

Taking values calculated from the EIS and OCVD measurements for the initial voltage, geometric capacitance and recombination and shunt resistances gives the voltage decay shown in Figure 6-19. It can be seen that if the voltage decay followed this simple decay mechanism the voltage would have decayed to zero within 150 ms. The OCVD results presented here show voltage decays lasting for tens of seconds even at room temperature, indicating that an additional process must be occurring.

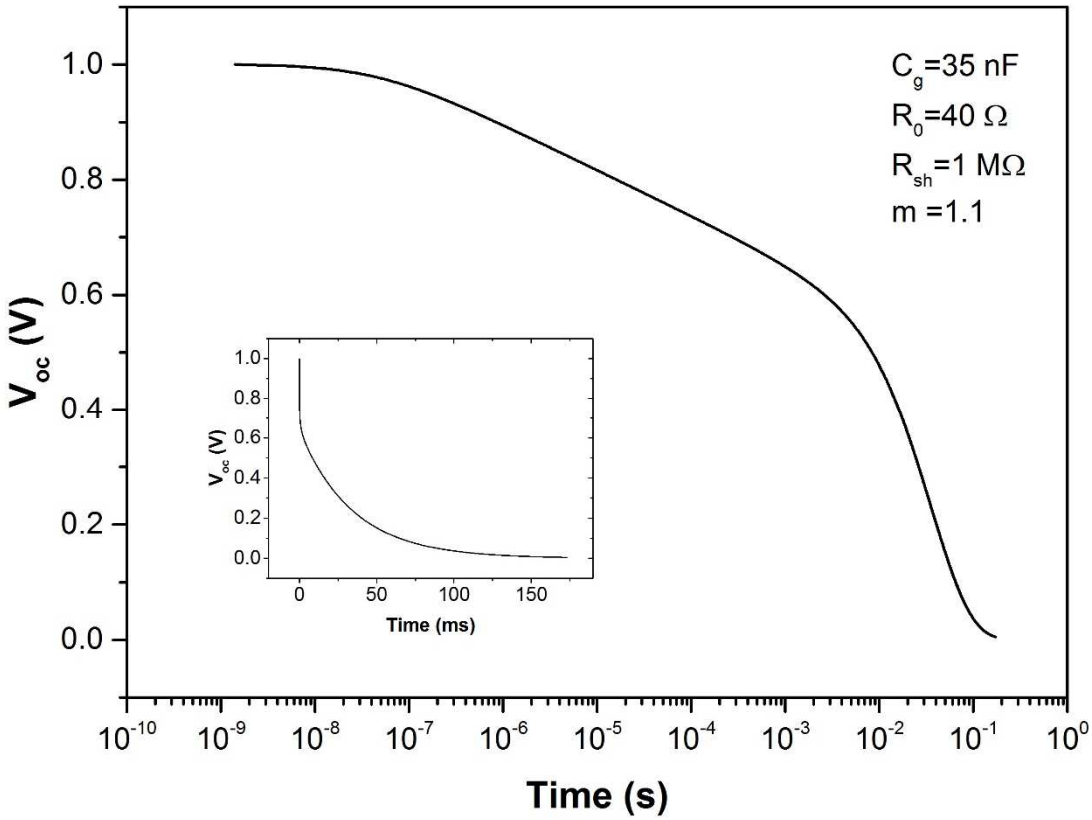

Figure 6-19: Simulated voltage decay using device parameters shown in plot.

From the temperature dependent EIS results obtained in the previous chapter, and the OCVD results presented here, activation energies consistent with values calculated for ionic migration were obtained. It was clear from the frequency domain measurements that this ionic migration had some link to modulating the rate of recombination in the device on different time scales. This is reinforced by the fast initial voltage rise to a value approximately half of the photostationary value, before a slow rise to the maximum. In other words, initially there is a high rate of recombination which slowly reduces over time.

The OCVD results provide a great deal of insight into the mechanisms linking ionic movement to changes in the rate of recombination. The main benefit of performing the large amplitude transient measurements is that it involves measuring the cell between well-defined conditions. Initially the cell is at equilibrium in the dark, it is then illuminated until it reaches a photostationary state before turning off the light and allowing the cell to return to its initial state.

Firstly, to study the case of equilibrium in the dark the formation of the cell must be considered as in Figure 6-20. Upon contact of the n-type and p-type layers to the perovskite, electrons will transfer from the TiO_2 to the Spiro, resulting in the equilibration of the Fermi levels. This produces a built-in voltage across the perovskite layer, V_{bi}. This built-in voltage is taken to be around 1 V from the difference in the Fermi levels in TiO_2 and Spiro contacts[17, 18]. This initial built-in field, $E=V_{bi}/d$ where d is the perovskite layer thickness, will disturb the ionic equilibrium resulting in a redistribution. Negative species (e.g. I^-, V_{MA}) will move towards the TiO_2 interface, whereas positive species (e.g. V_I, MA^+) will move to the Spiro interface. This subsequently causes further electronic redistribution until the electrochemical potentials of all species (ions and electrons/holes) becomes constant across the device. If there is a high concentration of ionic defects, compact double layers will form at the contacts, as shown by Richardson et al[17].

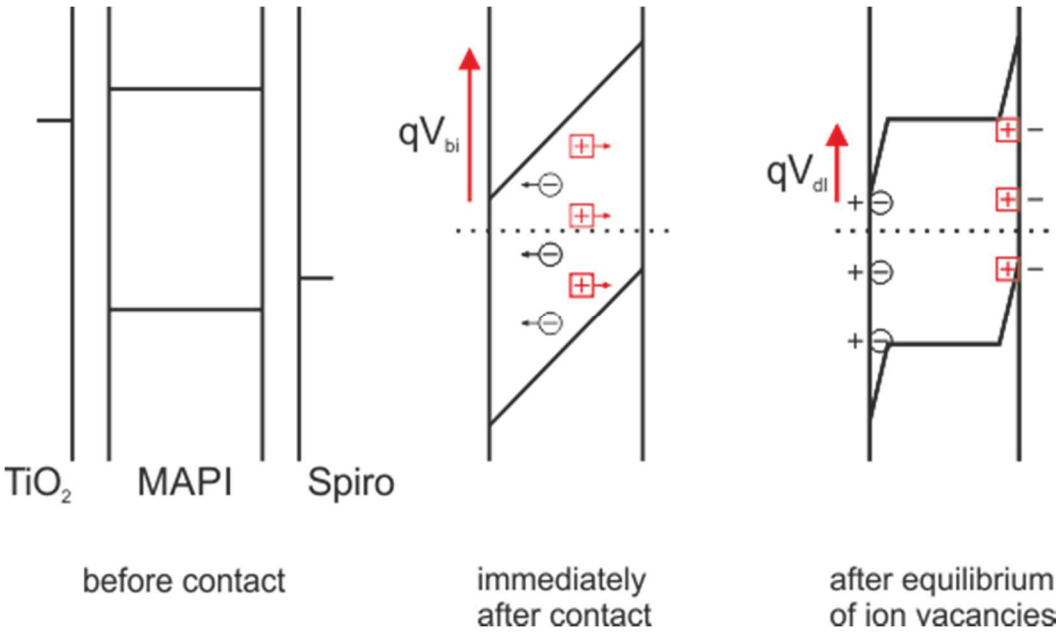

Figure 6-20: Formation of the cell involving equilibration of electrons, holes and ions.

In order for the entire built-in voltage to be compensated for by the double layers, the defect density needs to be high. The Helmholtz capacitance can be calculated from $C_H = \varepsilon\varepsilon_0 / \delta_H$ where ε is the relative permittivity of the perovskite (ε = 24.1) and δ_H is the distance of closest approach of the ion vacancies (taken to be 0.5 nm). This gives a Helmholtz capacitance of 43 μF cm^{-2}. If the voltage drop across each double

layer is equal (i.e. 0.5 V across each) the accumulated ionic charge in each would be 21 μC cm^{-2}. This charge is equivalent to 1.3×10^{14} vacancies per cm^2. Taking an average film thickness to be 500 nm, gives a required vacancy concentration of at least 2.7×10^{18} cm^{-3}.

An estimate for the vacancy concentration can be calculated from the measurements made here. Assuming that the time constant of the slow component in the OCVD relates to the relaxation of the ionic double layer, $\tau = R_{ionic}C_{dl}$, the ionic resistance can be calculated using the double layer capacitance value of 43 μF cm^{-2} calculated above. Taking the time constant to be 10 s (at 25 °C) gives an ionic resistance of 2.3×10^5 Ω cm^2. The ionic conductivity is given by the equation

$$\sigma = \frac{d}{R}$$

Taking d to be the film thickness of 500 nm gives a conductivity of 2.15×10^{-10} Ω^{-1} cm^{-1}. The ionic vacancy concentration can be calculated from the relationship

$$\sigma = Nq\mu$$

Where N is the carrier concentration, q the ionic charge and μ is the ions mobility. Eames et al.[19] estimated the iodide vacancy diffusion coefficient to be of the order of 10^{-12} cm^2 s^{-1} which would relate to a mobility of approximately 4×10^{-11} cm^{-2} V^{-1} s^{-1} using the relationship

$$\mu = \frac{q}{k_B T} D$$

This gives an estimate of the ionic vacancy concentration of 3.3×10^{19} cm^{-3}. Walsh et al.[20] calculated an equilibrium vacancy concentration of 2×10^{19} cm^{-3} from the remarkably low activation energy for vacancy formation of 0.14 eV. The estimate is therefore in good agreement with the theoretically calculated value, and also in excess of the minimum requirement for double layers to compensate the entire built-in voltage. It seems likely therefore that the built-in voltage is dropped across the ionic double layers at the contacts, with little or no electric field in the bulk. This situation relating to equilibrium in the dark is shown in the right hand side of Figure 6-20.

The situation under illumination is considered in Figure 6-21. Illumination quickly leads to the splitting of the quasi-Fermi levels equal to qV_{oc}. Since at equilibrium in the dark there is no field in the bulk, the photovoltage creates an electric field in the film of opposite sign to the built-in voltage (centre image of Figure 6-21). This field will cause ions to move out of the double layers into the bulk until a new ionic equilibrium exists (right hand side of Figure 6-21). Turning off the light will reverse this process and result in the double layers being reformed by vacancies moving back towards the contacts.

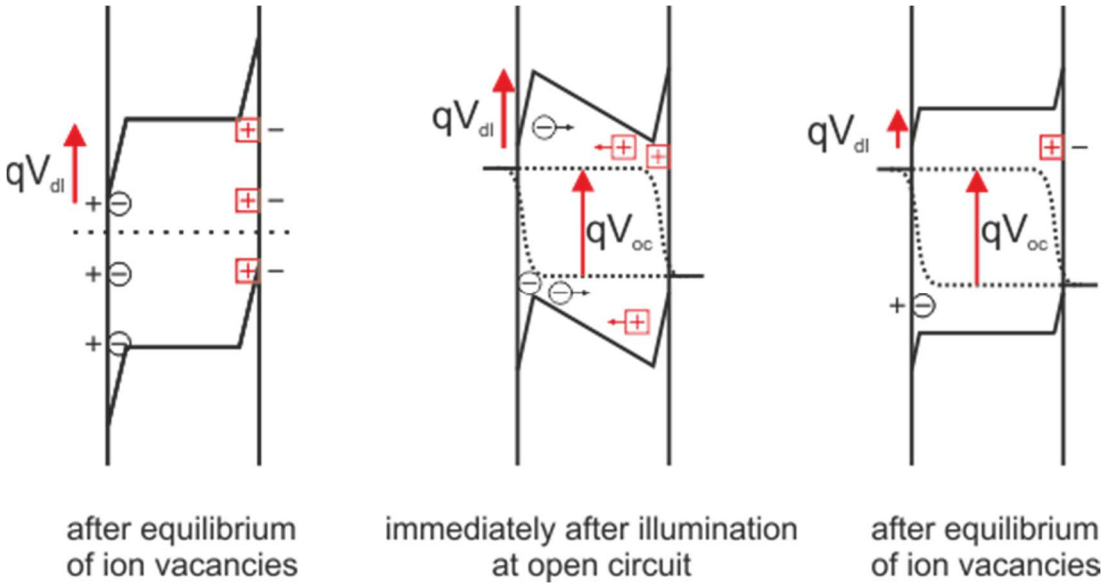

Figure 6-21: Changes to band bending under illumination in the presence of mobile ions.

The slow component of the large amplitude photovoltage transients is therefore related to the discharging of the ionic double layers under illumination, followed by them being recharged during the decay. The rate of charging/discharging is influenced by the ionic resistance (inversely proportional to ionic conductivity). Figure 6-10 illustrates the effect of discharging the double layers to a greater or lesser extent depending on illumination time. The constant decay lifetime irrespective of the extent to which the double layers are discharged is consistent with a constant ionic impedance at a given temperature.

The equivalent circuit which can be used to describe the OCVD transients is shown in Figure 6-22. This model is consistent with the model presented for the frequency domain measurements shown in the previous chapter. As previously mentioned, the smallest resistance in a parallel configuration dominates the response. As the

frequency dependent impedance relating to the recombination resistance, Z_{rec}, is smaller than both the shunt and ionic resistances (both ~1 MΩ) for all intensities studied it will dominate the response. The below circuit can therefore be simplified to the one defined in the previous chapter. This highlights the fact that the ionic resistance is not measured in the EIS measurements at the conditions studied. However, as the ionic displacement is shown to influence the rate of recombination in the device over time, the recombination impedance is modified at a rate related to the charging of the double layer capacitance through the ionic resistance, giving rise to the excellent agreement between the low frequency time constant trends in frequency and time domain measurements.

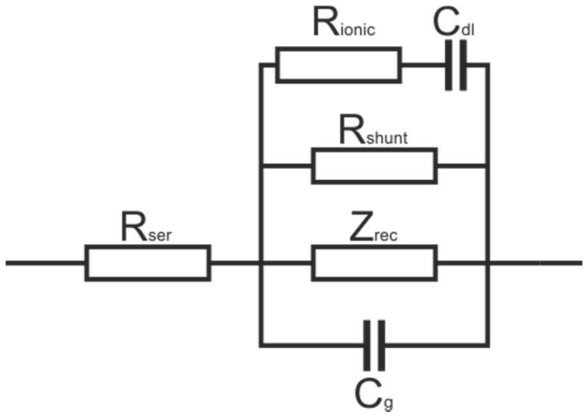

Figure 6-22: Full equivalent circuit model for the perovskite solar cell.

Together with the frequency dependent recombination resistance observed in the EIS/IMVS measurements, the slow rise in photovoltage after a fast initial rise upon illumination corresponds to a decrease in the rate of recombination. For example, a V_{oc} of around 0.5 V is reached after a few milliseconds, with the subsequent slow rise to a steady state photovoltage of around 1 V taking several minutes.

This slow component has been shown to be linked to ionic movement. A large increase in voltage could relate to an increase in Fermi level splitting caused by a decrease in recombination by many orders of magnitude (a V_{oc} increase of 83 mV per order of magnitude decrease in recombination rate would be expected for a cell with ideality m=1.4). This would relate to a decrease in recombination rate of 6 orders of magnitude. Ionic vacancies could be responsible for screening electronic charges or perhaps stabilizing filled traps causing a reduction in non-radiative recombination. Van Reenen et al. reported that in order to simulate hysteresis in JV

curves, a combination of mobile ions and trap states near the interface had to be included in the model[21]. However, such large reductions in recombination rate seem unlikely. It is also possible that band offsets are altered by the ionic environment near to the contacts.

The presence of the mid-frequency process and the "bounce-back" in photovoltage decay indicates that the mobile ions can also alter the rate of recombination on short timescales in the millisecond-second range. As mentioned in the previous chapter this could be related to the movement of different ionic species that are able to move at different rates (i.e. I^- and MA^+, or could possibly include Li^+ from the Spiro or H^+)[22], or perhaps due to one species having different effects depending on its environment. For example, ions moving through the bulk or along grain boundaries. It is also possible that the faster process is a short range relaxation near the contacts with the slow process relating to longer range migration from the bulk of the perovskite.

6.6 Conclusion

By combining the results from the frequency domain measurements, performed in Chapters 4 and 5, with these time domain voltage rise/decay measurements, a model has been developed which describes the operation of the planar perovskite cells. It was shown in Chapter 5 that the slow response of these planar perovskite solar cells was linked to ionic movement, which in turn has an effect on the dominant recombination rate. Starting from a well-defined equilibrium condition (open-circuit in the dark), the time domain measurements show that the response to a large amplitude stimulus (switching on the light) is also governed by these same processes.

The model describes the formation of ionic double layers at the perovskite interfaces which screen the built-in field across the device. The response to a large stimulus is slow as ions must redistribute to screen the change in electric field. It is apparent that as the ions move they also have the effect of reducing the rate of recombination. This suggests that the dominant recombination mechanism is occurring at or near the interface where the change in ionic concentration is highest.

6.7 References

1. M. A. Green, *Solar Cells*, 1984, **11**, 147-161.
2. J. E. Mahan, T. W. Ekstedt, R. I. Frank and R. Kaplow, *IEEE Transactions on Electron Devices*, 1979, **26**, 733-739.
3. A. K. Thakur, G. Wantz, G. Garcia-Belmonte, J. Bisquert and L. Hirsch, *Sol. Energy Mater. Sol. Cells*, 2011, **95**, 2131-2135.
4. A. Zaban, M. Greenshtein and J. Bisquert, *ChemPhysChem*, 2003, **4**, 859-864.
5. A. B. Walker, L. M. Peter, K. Lobato and P. J. Cameron, *J. Phys. Chem. B*, 2006, **110**, 25504-25507.
6. J. Bisquert, A. Zaban, M. Greenshtein and I. Mora-Seró, *J. Am. Chem. Soc.*, 2004, **126**, 13550-13559.
7. J. Bisquert, F. Fabregat-Santiago, I. Mora-Seró, G. Garcia-Belmonte and S. Giménez, *J. Phys. Chem. C*, 2009, **113**, 17278-17290.
8. B. C. O'Regan, P. R. F. Barnes, X. Li, C. Law, E. Palomares and J. M. Marin-Beloqui, *J. Am. Chem. Soc.*, 2015, **137**, 5087-5099.
9. J. M. Marin-Beloqui, J. P. Hernandez and E. Palomares, *Chem. Commun.*, 2014, **50**, 14566-14569.
10. C.-Z. Li, C.-Y. Chang, Y. Zang, H.-X. Ju, C.-C. Chueh, P.-W. Liang, N. Cho, D. S. Ginger and A. K. Y. Jen, *Adv. Mater.*, 2014, **26**, 6262-6267.
11. A. Baumann, K. Tvingstedt, M. C. Heiber, S. Väth, C. Momblona, H. J. Bolink and V. Dyakonov, *APL Mat.*, 2014, **2**, 081501.
12. G. Xing, N. Mathews, S. S. Lim and N. Yantara, *Nature Materials*, 2014, **13**, 476-480.
13. A. Baumann, S. Väth, P. Rieder, M. C. Heiber, K. Tvingstedt and V. Dyakonov, *J. Phys. Chem. Lett.*, 2015, **6**, 2350-2354.
14. L. Bertoluzzi, R. S. Sanchez, L. Liu, J.-W. Lee, E. Mas-Marza, H. Han, N.-G. Park, I. Mora-Sero and J. Bisquert, *Energy Environ. Sci.*, 2015, 910-915.
15. A. M. A. Leguy, J. M. Frost, A. P. McMahon, V. G. Sakai, W. Kockelmann, C. Law, X. Li, F. Foglia, A. Walsh, B. C. O'Regan, J. Nelson, J. T. Cabral and P. R. F. Barnes, *Nat. Commun.*, 2015, **6**, 7124.
16. J. Beilsten-Edmands, G. E. Eperon, R. D. Johnson, H. J. Snaith and P. G. Radaelli, *Appl. Phys. Lett.*, 2015, **106**, 173502.
17. G. Richardson, S. E. J. O'Kane, R. G. Niemann, T. A. Peltola, J. M. Foster, P. J. Cameron and A. B. Walker, *Energy Environ. Sci.*, 2016, **9**, 1476-1485.
18. A. Guerrero, E. J. Juarez-Perez, J. Bisquert, I. Mora-Sero and G. Garcia-Belmonte, *Appl. Phys. Lett.*, 2014, **105**, 133902.
19. C. Eames, J. M. Frost, P. R. F. Barnes, B. C. O/'Regan, A. Walsh and M. S. Islam, *Nat Commun*, 2015, **6**, 1-8.
20. A. Walsh, D. O. Scanlon, S. Chen, X. G. Gong and S.-H. Wei, *Angew. Chem. Int. Ed.*, 2015, **54**, 1791-1794.

21. S. van Reenen, M. Kemerink and H. J. Snaith, *J. Phys. Chem. Lett.*, 2015, **6**, 3808-3814.

22. D. A. Egger, L. Kronik and A. M. Rappe, *Angew. Chem. Int. Ed.*, 2015, **54**, 12437-12441.

7 Investigation of ionic movement in the dark

7.1 Abstract

The slow dynamic behaviour of planar perovskite solar cells was investigated in the absence of light to clarify that the processes observed in previous chapters were not light activated.

Voltage decay behaviour in the dark from a set forward bias potential was shown to be comparable to voltage decays performed under illumination, with a similar activation energy determined for both measurements. The current response to the applied potential also supports the theory that the ionic redistribution modifies the rate of recombination at the interface, as well as potentially modifying charge injection barriers.

7.2 Introduction

The slow dynamic behaviour observed in perovskite solar cells has been shown to be linked to the movement of ionic species[1-3]. It has been shown that these ions are capable of forming double layers at the interfaces of the perovskite layer that can screen the electric field. There is a therefore a coupling between ionic and electronic processes. The previous measurements shown in this work have all been performed under illumination. There are a number of literature reports suggesting that these ionic-electronic processes are light induced.

In their impedance studies on planar perovskite cells with organic contacts, Bag et al. did not observe a low frequency response in the dark[4]. Only one arc with an associated resistance value of around 10^4 Ω is observed in the dark. Under illumination they saw a clear low frequency arc which they linked to ionic migration. They therefore concluded that the ion transport was light induced. However, they only measured the dark impedance at 0 V applied bias. Under these conditions they were likely measuring the cells shunt resistance in parallel with the geometric capacitance, as the recombination resistance will have been large. It is therefore difficult to conclude whether the low frequency process is not occurring or if it is just masked by other effects in the impedance response.

Zarazua et al. reported on a light-induced space charge accumulation layer near to the contacts as being responsible for the observed increase in capacitance at low frequency in their devices[5]. Whilst the results presented in Chapter 5 show that the low frequency response is not related to a true capacitance, merely a time constant relating to a frequency dependent recombination impedance, it has not been determined whether or not it is a light induced effect.

Light induced structural changes were observed by Gottesman et al. in Raman and photoluminescence measurements of uncontacted films[6]. The lack of selective contacts means there is no built-in field as in the complete devices. This would suggest that the observed effects are not the results of ion migration. They suggest that the changes are due to the rearrangement of the Pb-I scaffold as a result of MA cation alignment or increased rotation under illumination. It's not clear what the magnitude of these effects would be on the electronic behaviour of a complete device, in which case ion migration may dominate. Dark measurements have the

advantage that these structural changes can be disregarded. If ion migration is observed in the dark measurements this would indicate these structural changes may not be significant to device operation.

Reversible light activated trap states are also thought to exist in the perovskite, which leads to a reduction in photocurrent[7]. As well as light induced effects in the perovskite there are also known photo-induced effects that occur in the contact layers. Although not an issue using the monochromatic visible wavelength LEDs used in this study, perovskite cells containing TiO_2 are known to be unstable due to UV light induced desorption of surface adsorbed oxygen from the TiO_2 surface[8]. Spiro-OMeTAD is also known to undergo photo-induced oxidation, accelerated by the presence of the commonly used additives Li-TFSI and tBP[9, 10].

This chapter aims to investigate if the ionic movement evidenced from a number of techniques performed under illumination still occurs in the dark. The behaviour of the photovoltage rise and decay in Chapter 6, starting from equilibrium conditions suggested that ionic double layers were present in the dark and were discharged under illumination to compensate for the change in electric field. Calculations of the activation energy for vacancy formation gave a low activation energy of 0.14 eV which was used to determine the equilibrium vacancy concentration of around 10^{19} cm^{-3} at room temperature[11]. It is therefore clear that charged ionic species are present in the device in the dark. This chapter will investigate if they are also able to migrate without the presence of illumination.

7.3 Experimental

The same cell batch as in the previous chapter was used for the measurements shown here. The cells were stored in a nitrogen filled glovebox between measurements with only a single cell removed at a time. Having been stored in the glovebox the cells showed no appreciable sign of degradation over the several weeks of testing, as determined by J-V measurements performed before each round of testing.

The measurements performed in this chapter were carried out using the Solartron ModuLab XM Photoelectrochemical Test System with optical bench attachment. Once again the variable sampling rate feature was employed, in a similar fashion to in the previous chapter. Measurements were performed in the dark starting from equilibrium conditions (judged to be when the residual open-circuit voltage had decayed to less than 1 mV). Once the cell had reached equilibrium in the dark, the cell was held at short-circuit for 10 seconds. The cell voltage was then stepped from 0V to V_{app}. The duration and magnitude of the applied forward bias was varied throughout the measurements, with a typical measurement being 60 s at 1 V. The ModuLab records both the voltage and current signals during the measurement.

The temperature controlled sample holder was again used to control the temperature of the cells over the range -25 °C to +35 °C.

7.4 Results

7.4.1 Dark voltage decays

The initial aim of this section of measurements was to investigate whether the underlying processes linked to the slow dynamic behaviour of the cells was light induced. All characterisation measurements to this point have been performed under illumination. A range of evidence has been presented attributing the slow dynamic behaviour to ionic migration in the perovskite, and its effect on recombination at the interfaces with the selective contacts. So far it has not been shown whether this process is dependent on illumination, and if it can in fact be observed in the dark.

In principal the measurement of voltage decays in the dark is comparable to the conventional open-circuit photovoltage decay measurements performed in the previous chapter, assuming that the presence of illumination does not stimulate additional processes. In these dark voltage decay measurements the system is controlled potentiostatically with the splitting of the Fermi-levels achieved by forward biasing the cell.

Figure 7-1 gives an example of a dark voltage transient for an applied voltage step of 1 V for 60 seconds duration. The cell was kept in the dark at open-circuit between measurements until the residual V_{oc} had decayed to less than 1 mV (this was the condition used to judge when the cell had reached equilibrium, with the V_{oc} reading not dropping further on a consistent basis due to electrical noise/thermal effects). At lower temperatures it took tens of minutes to reach equilibrium. The cell was then short-circuited for 10 seconds, prior to the applied voltage step to V_{app} for a period of time (typically 60 seconds). After this time the cell was switched to open-circuit and the voltage decay recorded.

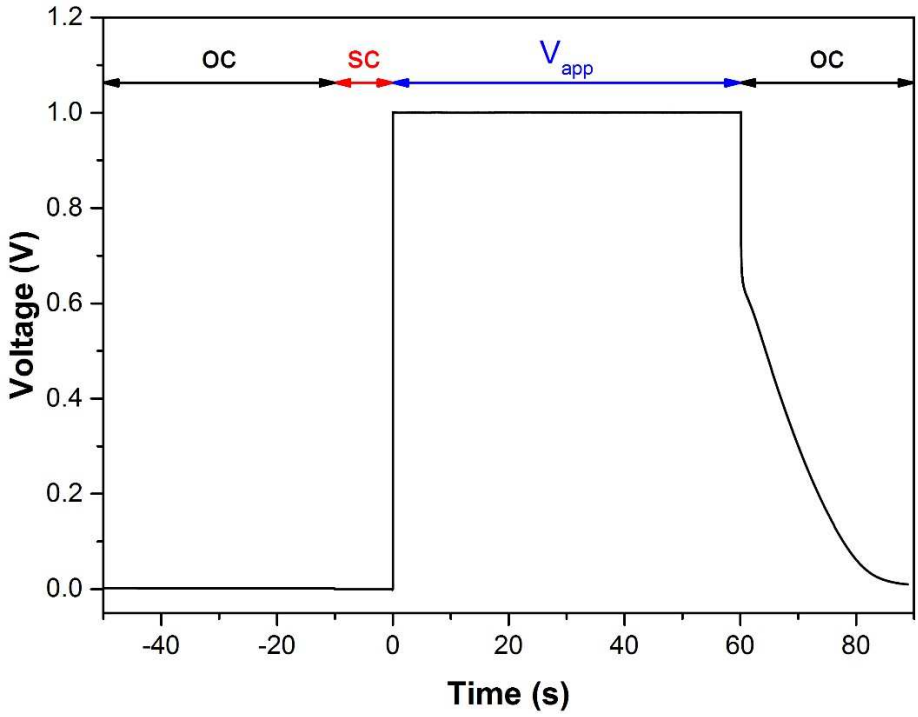

Figure 7-1: Typical dark voltage transient for an applied voltage of 1 V forward bias for 60 seconds at a temperature of 25 °C. The measurement sequence is also illustrated.

Clearly the voltage rise is very different to in the OCVD measurements performed under illumination. In this case the splitting of the Fermi levels is controlled by the potentiostat to give a potential difference of V_{app} between the working and reference electrodes at the cell contacts. In contrast, under illumination at open-circuit the V_{oc} rise is related to the relative carrier generation and recombination rates. In the case of perovskite cells it has been shown here that the recombination rate is time dependent, resulting in the slow rise to a photostationary state.

The voltage decay from the point where the cell is switched to open-circuit from V_{app} appears to follow a similar pattern as observed in the OCVD measurements under illumination. The initial voltage drop to around 0.7 V takes place in approximately 20 ms, comparable to the discharge of the cell capacitance via the recombination resistance as observed previously. The remaining photovoltage decays over a few tens of seconds, again comparable to the results shown previously using light to provide the voltage stimulation.

A series of measurements were performed over a range of voltage step heights (0.4 V to 1 V for a fixed time of 60 s) and different durations (0.5 s to 30 s for a fixed V_{app} of 1 V). Again, to get the repeat measurements to have consistent

behaviour it was essential to start the measurements from an equilibrium condition. Therefore in between measurements the cell was held at open-circuit until any residual V_{oc} had decayed to less than 1 mV.

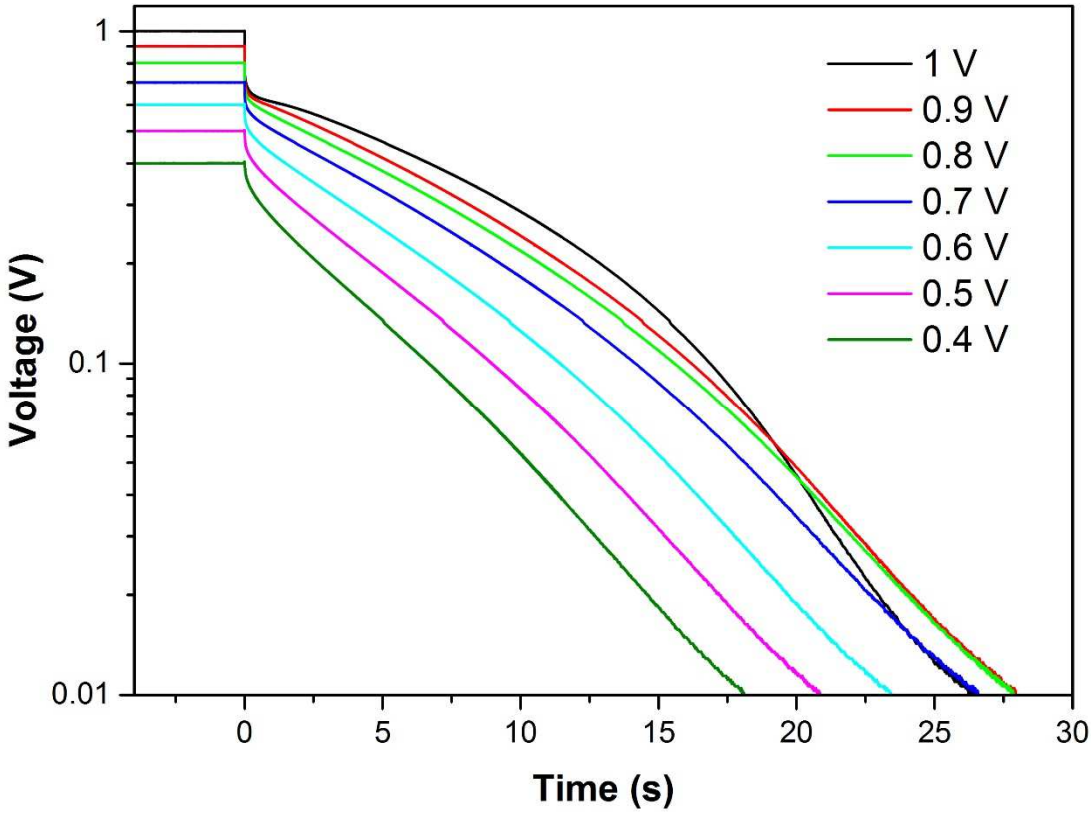

Figure 7-2: Voltage decays from different V_{app} having been applied for 60 seconds.

Figure 7-2 shows the open-circuit voltage decays from different V_{app} levels. The decay from 1 V appears to be anomalous and is due to being the first measurement in the series (decays measured from 1 V downwards), for which the starting equilibrium condition had not quite been met. After the fast initial decay, a similar rate of decay is observed for the slow component regardless of the starting voltage. The time constant extracted from these decays (using a linear fit to the log(V) vs t plot to estimate the lifetime) only varies from around 16 s to 12 s across the V_{app} range 0.9 V to 0.4 V. Not only are these lifetimes comparable to the slow processes observed in the other time and frequency domain measurements, they show a similar insensitivity to the starting Fermi-level splitting as for the light intensity dependence measurements.

There is some evidence of an additional process occurring at the transition from the fast to slow parts of the decay. At the highest forward bias voltages the decay shows a small deflection at this transition point, but is not as pronounced as in the light OCVD measurements. This is not too surprising as it was not resolved in all cells and was only visible for the highest light intensity measurements.

The dark voltage decays for different forward biasing times (all at 1 V) are shown in Figure 7-3. It can be seen that after the initial voltage drop the rate of decay is fairly consistent between all bias times. For longer bias times the initial drop is smaller, before the slow process begins to dominate. This is consistent with the longer bias time allowing a greater extent of ionic movement (discharge of double layers) which then must migrate back to the interface during the decay. This is analogous to a capacitance being charged at a constant rate, with the amount of stored charge being dependent on the length of time that the voltage has been applied.

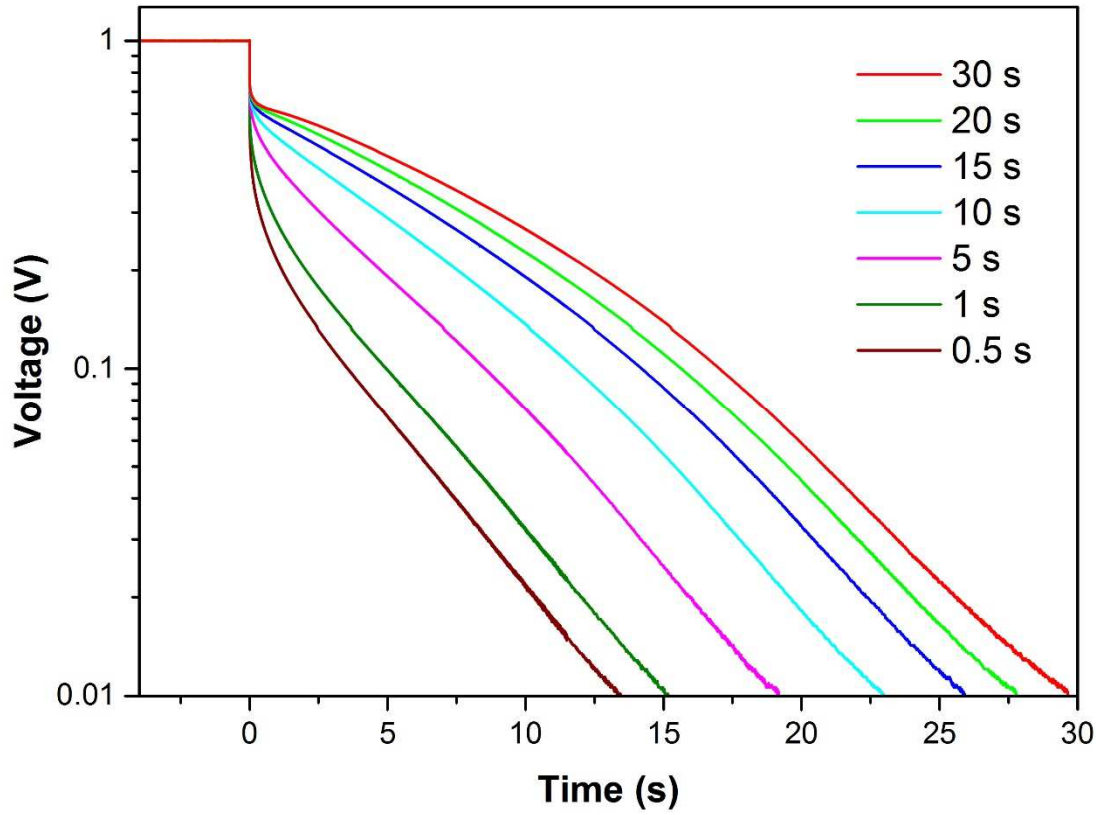

Figure 7-3: Dark voltage decays for different forward bias times.

The slow decay of the dark voltage transients was also strongly temperature dependent. Figure 7-4 shows the decays over a range of temperatures from -25 °C to 35 °C. As shown from Figure 7-3, the consistency of the voltage decay is highly dependent on the cell being at steady state, i.e. the amount of time the cell is forward

biased for before switching to open-circuit. It can also be expected that the time required to reach steady state will be temperature dependent as seen in other measurements. In this method the cell was judged to be at steady state once the dark current had stabilized under forward bias (see next section for discussion on current response). This resulted in a range of forward bias times from 10 minutes at -25 °C to 50 seconds at 35 °C. The decay at -25 °C is not complete after 10 minutes and is extremely linear on the log(V) vs t plot. At 35 °C the voltage decays to below 10 mV within 15 seconds.

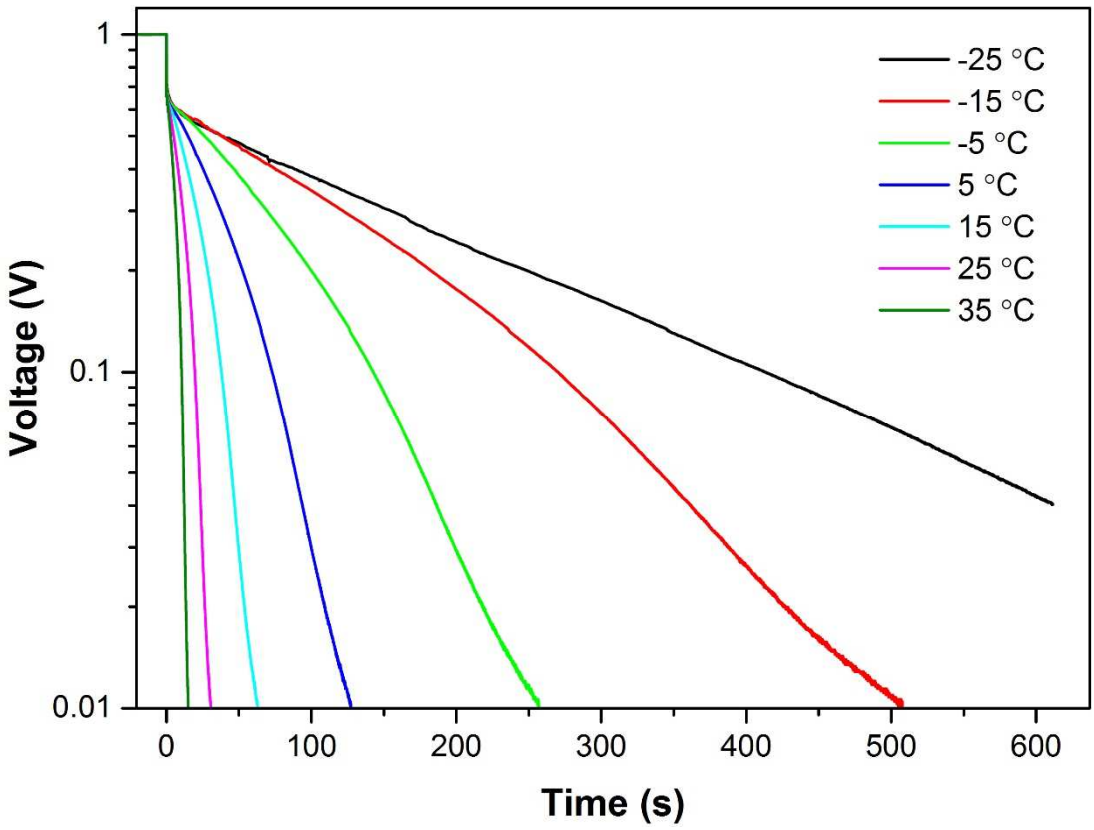

Figure 7-4: Dark voltage decays from 1 V for a range of different temperatures.

Time constants were extracted from Figure 7-4 using a linear fit to the decays. The resulting Arrhenius plot is shown in Figure 7-5, with the activation energy calculated to be 0.45 eV. This is in good agreement with the activation energies extracted using different techniques and under illumination.

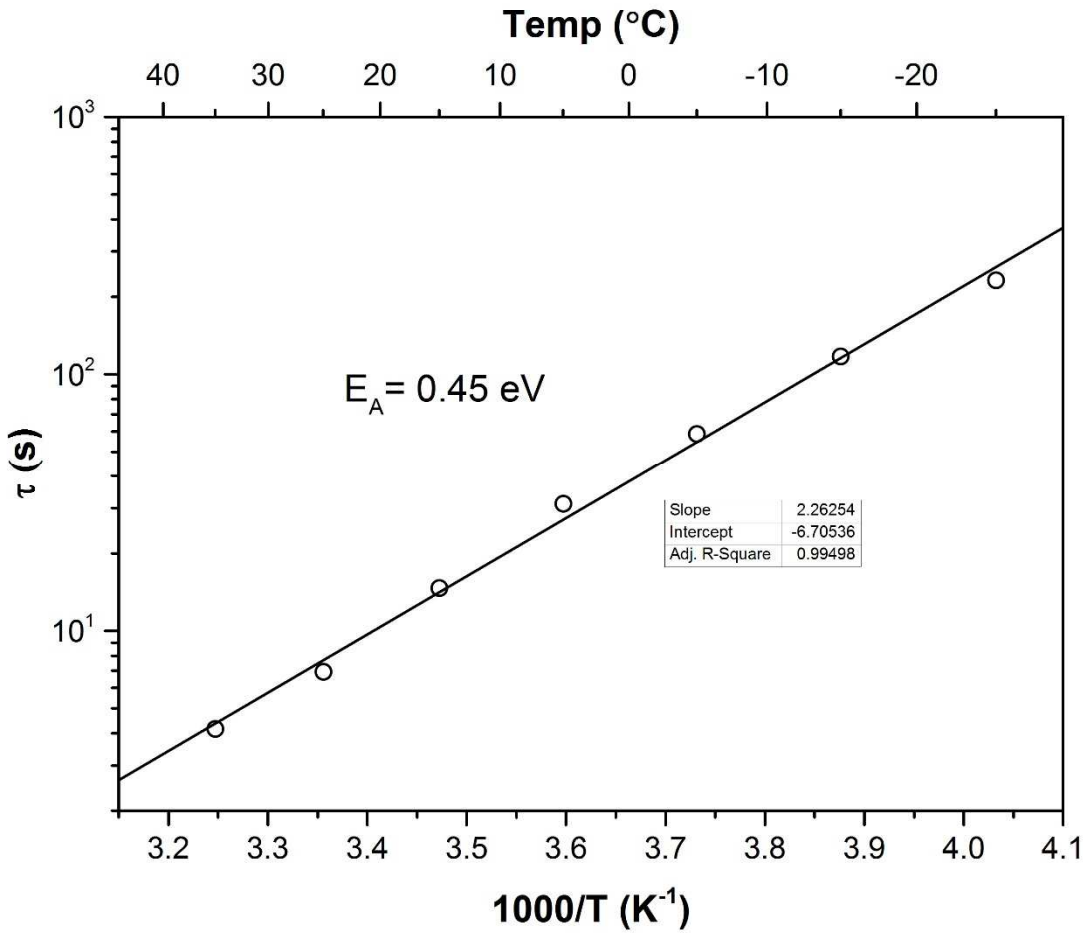

Figure 7-5: Arrhenius plot of time constants extracted from the dark voltage decay measurements.

7.4.2 Dark current response

During the course of performing the dark voltage transient measurements it was noticed that the dark current evolution was more complex than might be expected. The current response at 25 °C to a 1 V potential step is shown in Figure 7-6. Increased dark current is defined as being negative. A number of current maxima/minima are observed as the measured current density changes over time. O'Regan et al. also observed similar, though not as complex, dark current evolution but did not study it in detail[12].

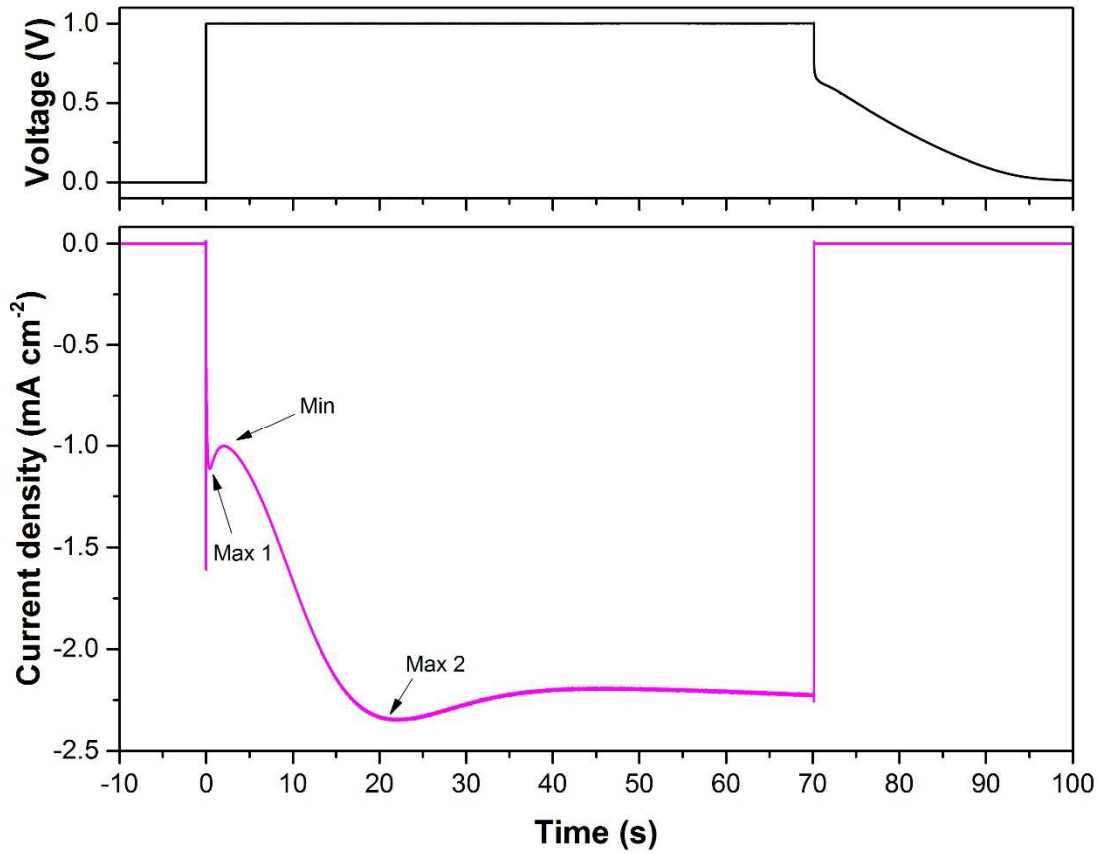

Figure 7-6: Dark current response related to the voltage step shown at 25 °C.

Figure 7-7 focuses on the first few seconds of the current response to highlight the initial changes. There is an initial current spike within the first 20 μs (beyond the resolution of the measurement) which decays quickly. This is assumed to represent the initial charging of the geometric capacitance. The first maximum (labelled 'Max 1') occurs within 0.5 s of the voltage step. The dark current then decreases through a minimum before a more significant increase in current to another maximum ('Max 2') after 20 s. Beyond 40 s the dark current appears to stabilize.

These two slow processes, ‘Max 1’ and ‘Max 2’, occur on similar time scales to those of the two processes observed in both frequency and time domain measurements performed under illumination in this work.

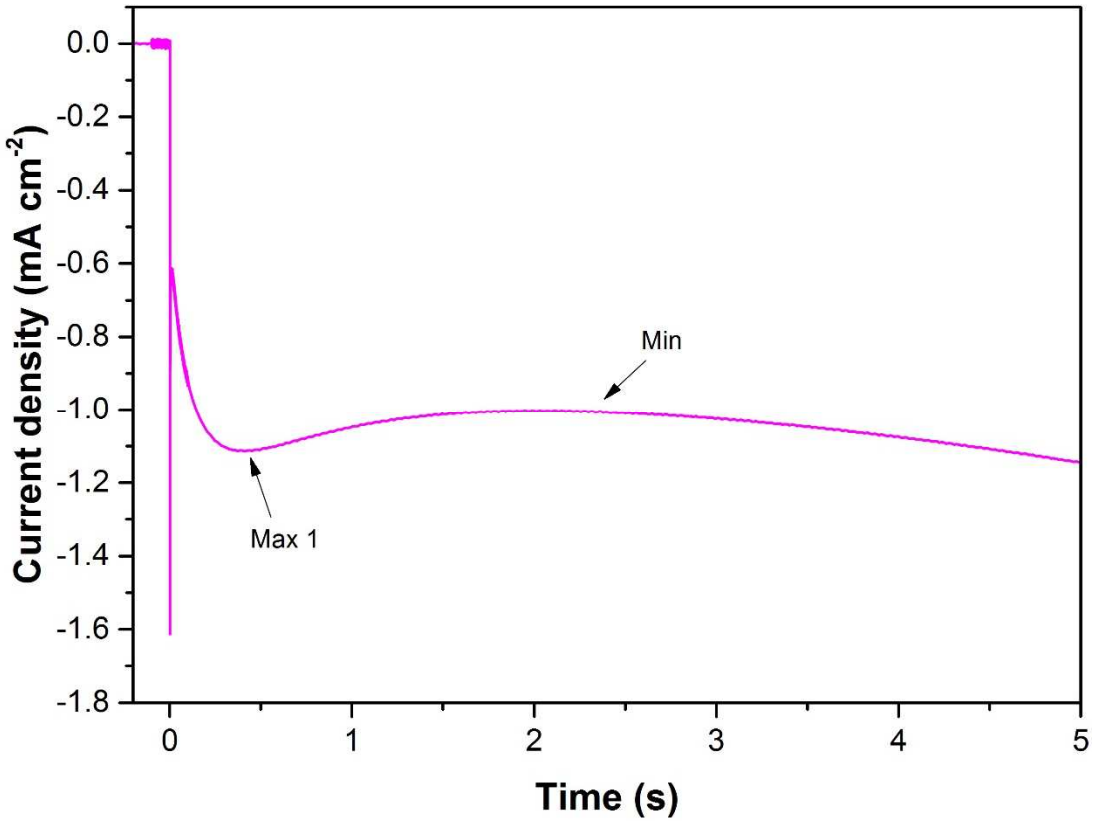

Figure 7-7: First few seconds of the dark current response showing a fast charging current spike before the first maximum at around 0.5 s.

The dark current traces relating to the measurements shown in Figure 7-2 for the different V_{app} levels are shown in Figure 7-8. The first maximum is observed at all bias potentials and occurs at the same time after the voltage step independent of bias level. The slower process occurring after around 20 seconds is strongly dependent on the biasing level. ‘Max 2’ has an amplitude that decreases with decreasing bias voltage, and disappears completely at voltages below 0.85 V.

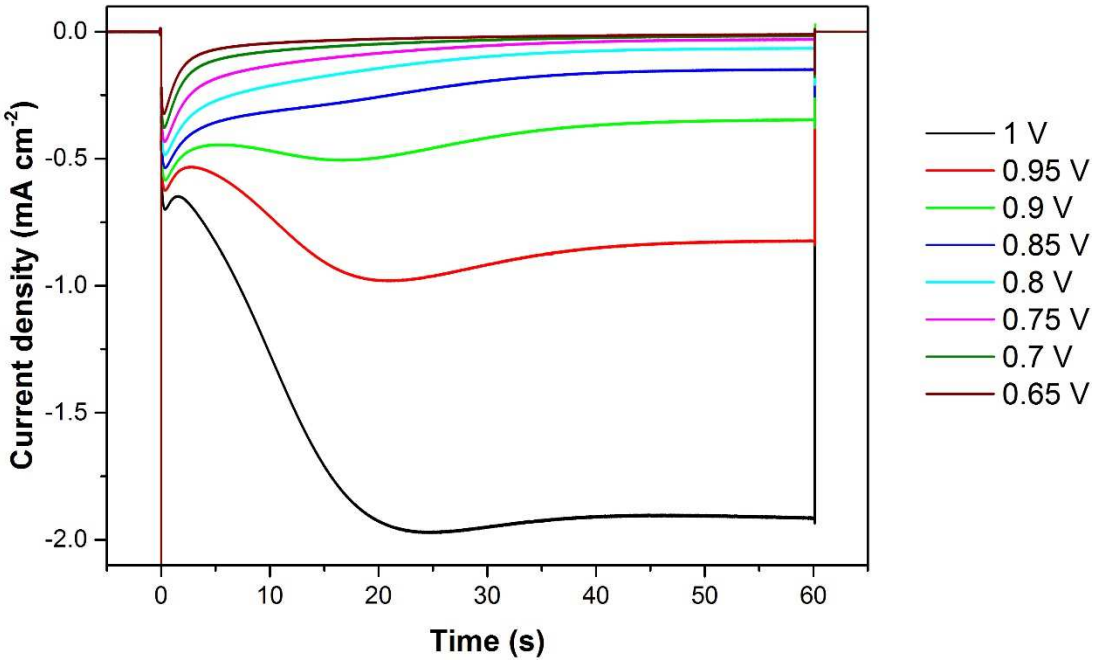

Figure 7-8: Evolution of the dark current for different V_{app} levels (cf. Figure 7-2).

Figure 7-9 shows the reproducibility of this behaviour as seen during the measurement of dark voltage decays after different forward bias times (Figure 7-3). This shows that the system can only be described as having decayed from a steady state for forward bias durations in excess of 30 seconds. The decays from shorter times clearly represent a decay during a dynamic process that is incomplete, i.e. partial discharge of double layers.

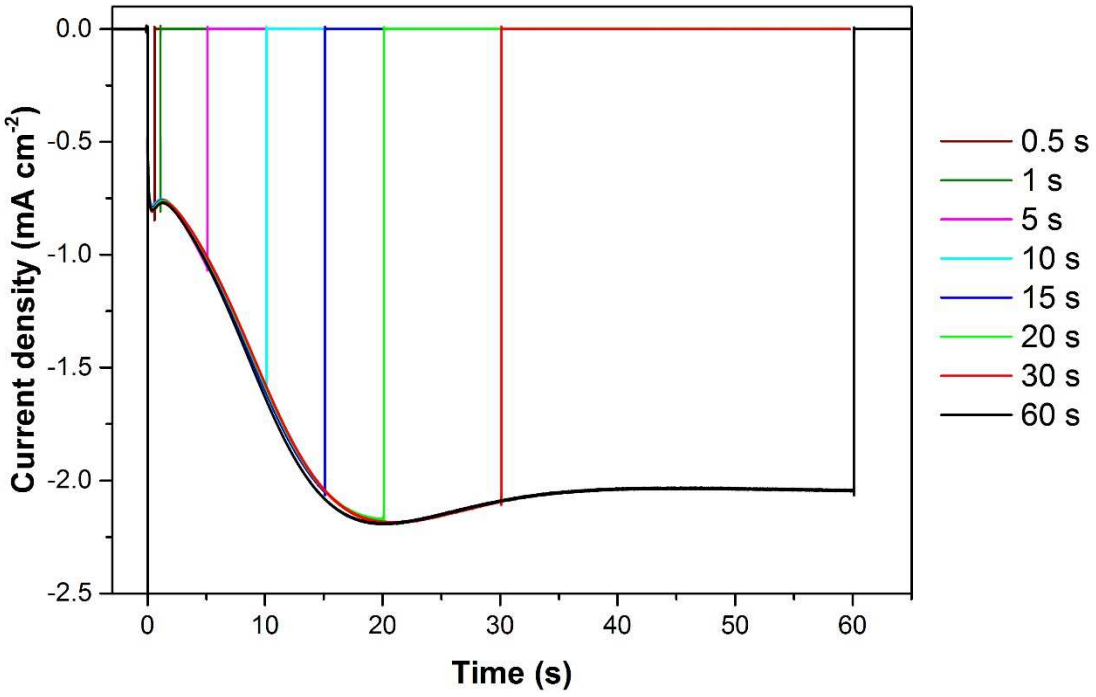

Figure 7-9: Dark current traces showing good reproducibility during experiment with differing forward bias times (cf. Figure 7-3).

The effect of temperature on the rate of this apparent discharge process during the dark forward bias measurements is shown in Figure 7-10. These dark current plots relate to the measurements seen in Figure 7-4. As previously mentioned, during this measurement the cell was held at forward bias until the dark current had stabilized (after 'Max 2'), before the cell was switched to open-circuit. It can be seen that there is a significant increase in dark current with increasing temperature. Also the processes represented by the two dark current maxima occur at shorter times with increasing temperature. This is consistent with an increase in ionic diffusion coefficient with increased temperature.

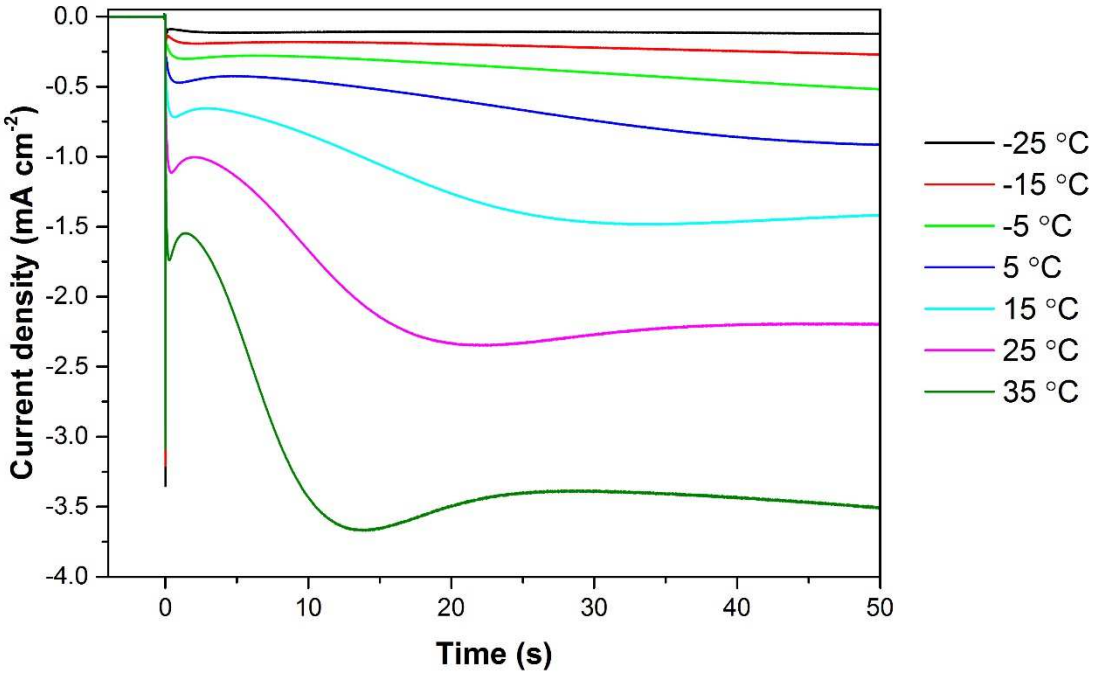

Figure 7-10: Variations in dark current behaviour over time under 1 V forwards bias at different temperatures (cf. Figure 7-4).

For illustration purposes it is clearer to observe the shifts with temperature on a log-log plot of the absolute dark current density against time as the variations in magnitude and timescale are large. This is shown in Figure 7-11. Both current maxima have a similar time dependence on temperature suggesting that they are in fact both linked to a single phenomenon. Again, this is consistent with the findings of the frequency domain measurements in which the mid and low frequency processes both appear to be linked to ionic movement.

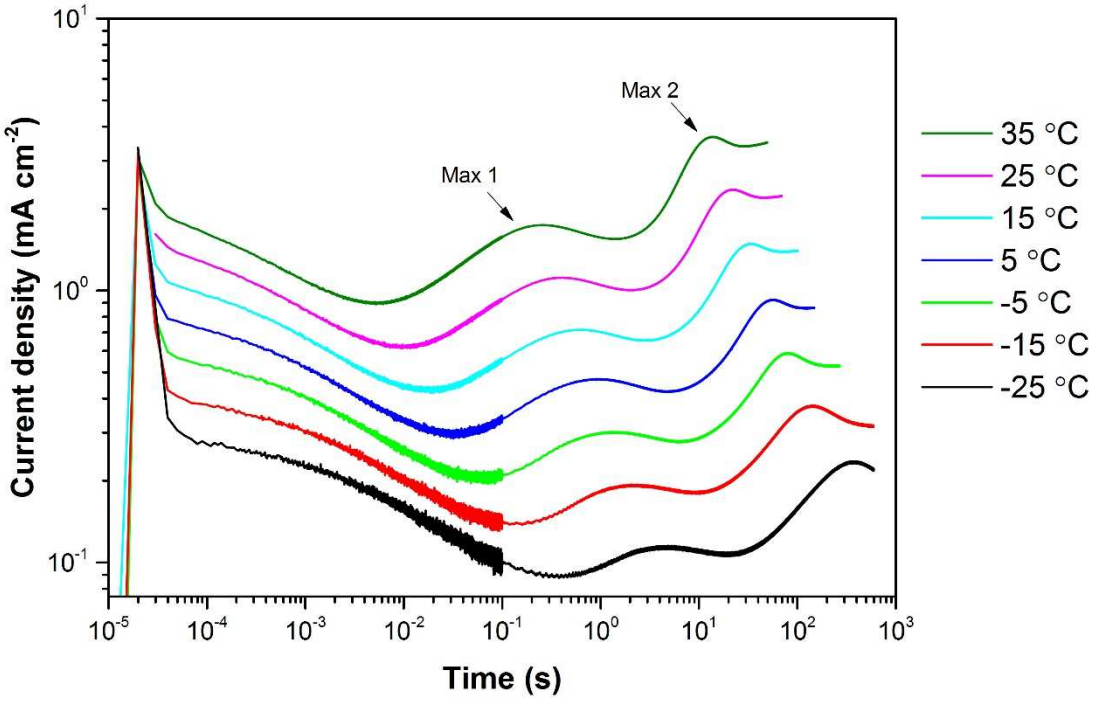

Figure 7-11: Evolution of dark current over time plotted on a log-log plot to show large variations in current magnitude and timescale of slow processes at different temperatures.

7.5 Discussion

These results show a high level of consistency with those obtained using different techniques. The most important aspect of these measurements is the tight control on equilibrium starting conditions and also the simplified measurement protocol. Keeping the cell in the dark and only varying the applied voltage in a single voltage step avoids complications due to the potential for light generated effects (degradation, light induced vacancy formation, etc.) and other dynamic influences.

The fact that the results in the dark and under illumination are consistent shows that the mechanism of splitting the Fermi levels has little or no consequence on the operation of the device. The voltage decay from a steady state shows a similar intensity/V_{app} and temperature dependence both under illumination and in the dark. The activation energy for this decay process is also comparable in both the light (0.58 eV) and the dark (0.45 eV). This indicates that the iodide vacancy migration can still occur in the dark.

During the process of measuring these voltage decays, interesting features were observed in the dark current response to the applied voltage. Deeper analysis of the transient dark current behaviour observed here requires the mechanism of charge transport through the device to be considered. Current flow in the dark is in the reverse direction to photocurrent. In this work the flow of dark current has been defined to be in the negative direction. In other words, under forward bias electrons in the external circuit are pumped from the gold contact to the FTO substrate.

The applied voltage injects electrons into the n-type TiO_2 contact (in the absence of pinholes). Depending on the energetic profile of the cell there are a number of pathways that electrons may take through the cell to complete the circuit. They must either overcome a number of injection barriers into neighbouring materials and/or recombine across interfaces or in the bulk as outlined in Figure 7-12. Due to the large energy offset to the Spiro conduction band, injection is unlikely meaning charge transport must occur via the Spiro valence band. Electrons must cross from the TiO_2 conduction band to the Spiro valence band. There are a number of possible recombination mechanisms that may facilitate this.

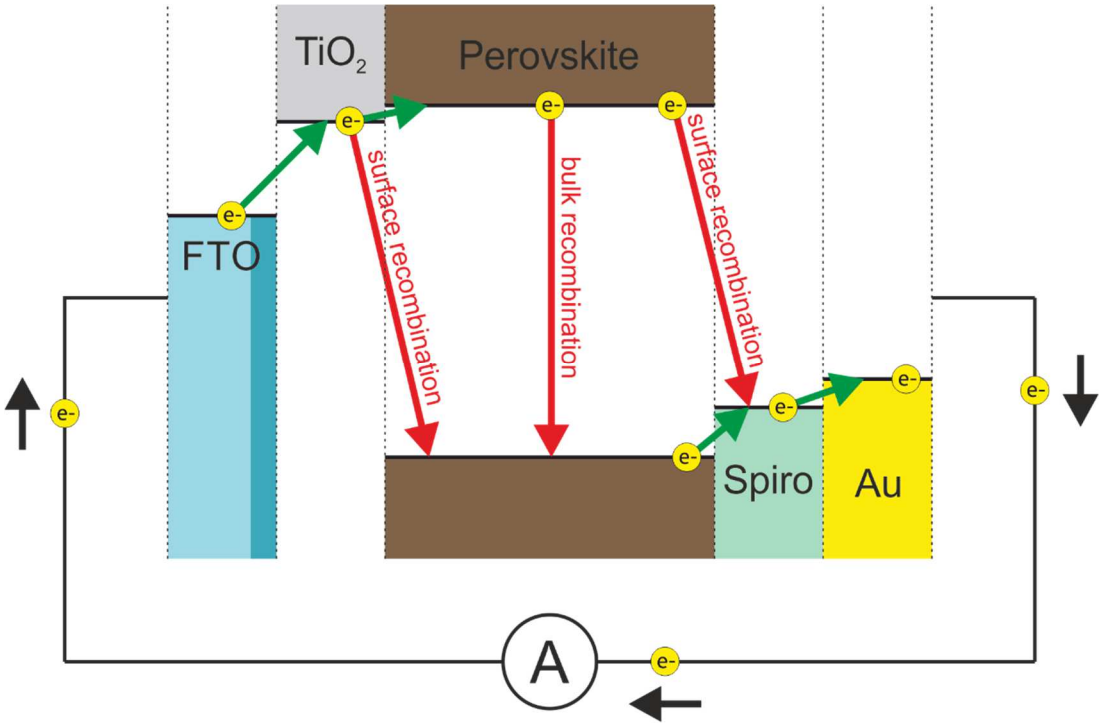

Figure 7-12: Diagram of possible electron pathways though the perovskite solar cell in the dark under forward bias (Green arrows show electron injection, Red arrows represent recombination).

From the TiO_2 conduction band electrons can either be injected into the perovskite conduction band or undergo interfacial recombination with a hole in the perovskite valence band (possibly trap assisted). If injected into the perovskite this recombination could take place in the bulk, or across the perovskite/Spiro interface to the Spiro valence band.

From the above description of the stages of electron transport through a perovskite solar cell in the dark it is clear that the degree of dark current is dependent on the energetic barriers and recombination rates within the device. Lower energetic barriers will results in a higher dark current, as will increased recombination rates. A number of factors that are varied in this work, for example bias levels and temperature, will affect the magnitude of negative current flow as they have significant impact on recombination.

The complex nature of the current response to an applied forward bias voltage step observed here suggests that the recombination rates/injection barriers may be varying with time. Time dependent recombination rates, on timescales associated to ionic movement, have already been observed in the frequency domain measurements

carried out here. The maxima observed in the dark current traces also seem to occur on similar timescales, suggesting recombination rates are also influenced by ions in the dark.

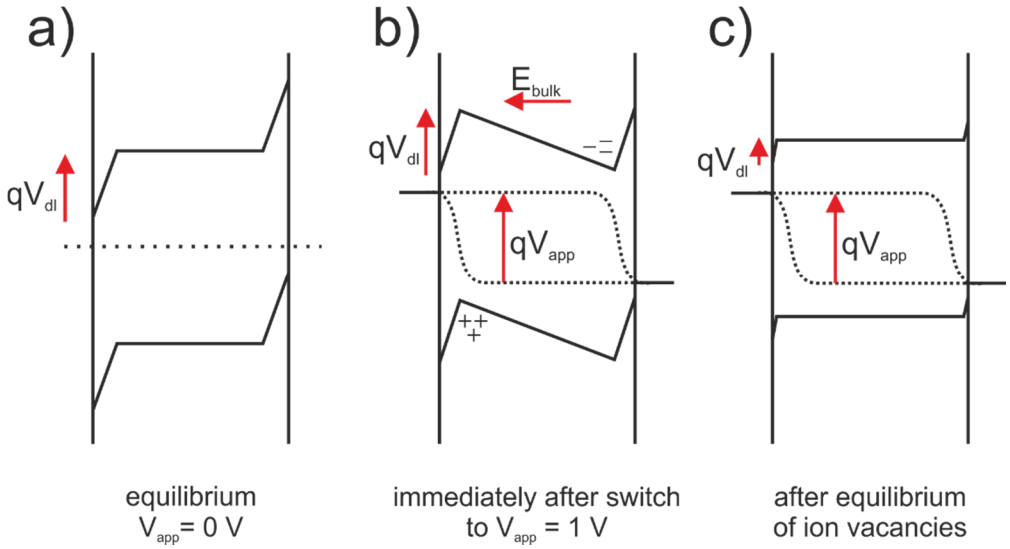

Figure 7-13: Evolution of band bending during the potential step measurements.

The measurements are performed from an equilibrium starting condition (Figure 7-13a). This condition is reached when the cell has relaxed fully in the dark and the built-in voltage has been compensated by the ionic charge stored in the double layers near the interfaces. The potential change across these layers, V_{dl}, is large at equilibrium. Immediately upon applying a forward bias, V_{app}, the electric field, E_{bulk}, is given by $E_{bulk} = -V_{app} / d$ where d is the perovskite layer thickness.

This negative field will have two noticeable effects. Firstly, it will provide a driving force for electrons and holes to drift away from their corresponding selective contact. Electrons will build up near the Spiro interface and holes near the TiO_2 as highlighted in Figure 7-13b, which would lead to an increase in recombination. E_{bulk} will also have an impact on the ionic arrangement as the double layers will discharge to compensate for the applied voltage. This movement of vacancies into the bulk decreases the electric field in the bulk and potential drop across the double layers (Figure 7-13c). The reduction in E_{bulk} reduces the driving force for electron drift and so the dark current will decrease. However the reduction of V_{dl}, and therefore width

of the double layers, increases the electron and hole concentrations near to the TiO_2 and Spiro interfaces respectively. This will lead to an increase in surface recombination. These two competing effects will decrease and increase the dark current at different rates over time.

The effect of E_{bulk} is instantaneous, whereas the discharge of the double layers takes place on timescales proportional to the ionic diffusion coefficient. The initial increase in dark current can therefore be attributed to the effect of E_{bulk} before this decays over the first few seconds. The slow increase in dark current to 'Max 2' may be related to the increased interfacial recombination due to the reduction in the double layer potential. Clearly bias level and temperature will effect these two processes in different ways.

The initial E_{bulk} varies linearly with the applied potential which will result in a higher carrier concentration accumulating near the interfaces thus increasing recombination (increased dark current with increased E_{bulk}). This is reflected in the increased dark current during 'Max 1' for higher V_{app} as shown in Figure 7-8. This recombination reduces as the E_{bulk} is compensated by ionic movement, eventually stabilizing after the field returns to zero.

It appears that the magnitude of the dark current during 'Max 2' is strongly dependent on V_{app}. For applied voltages close to the built-in voltage ($V_{app} > 0.9$ V) 'Max 2' is clearly observed. At lower voltages this process is not clearly observed suggesting that the impact of the double layer potential on recombination rate only dominates when the double layers are close to being depleted. This suggests that the double layers shield interfacial recombination by reducing the carrier concentration close to the interface. As the width of the double layers approaches zero the rate of recombination across the interface increases greatly.

The difference in time scale between the two processes could indicate the relative rates between the two dominating recombination mechanisms, i.e. recombination near the contacts versus surface recombination across the interface. The model presented here could be an oversimplification of the double layer formation and they could indeed be very different at each interface meaning they discharge at different rates or affect recombination at each interface differently.

The temperature dependence supports the theory that ion motion is responsible for the features observed as the timescales of the processes increase greatly with reduced temperature. Eames et al. suggested that the ionic diffusion coefficient increases exponentially with increasing temperature. The fact that the two maxima in dark current show similar dependences on temperature suggests that they are due to a single ionic species having two different effects as opposed to two different ions. The large increase in dark current magnitude at higher temperatures can be attributed to increased rates of recombination due to increased carrier concentrations.

7.6 Conclusion

These results show that ionic distribution has a strong impact on recombination rates. These measurements performed in the dark show very similar behaviour to that observed under illumination, suggesting that ionic motion is not strongly influenced by light. The recombination rate changes on the timescale of ionic movement. It is also possible that the change in the ionic double layers causes changes to injection barriers, with the possibility that ions can adsorb to the interface changing energy level offsets.

7.7 References

1. C. Eames, J. M. Frost, P. R. F. Barnes, B. C. O/'Regan, A. Walsh and M. S. Islam, *Nat Commun*, 2015, **6**, 1-8.
2. S. Meloni, T. Moehl, W. Tress, M. Franckevičius, M. Saliba, Y. H. Lee, P. Gao, M. K. Nazeeruddin, S. M. Zakeeruddin, U. Rothlisberger and M. Graetzel, *Nat. Commun.*, 2016, **7**, 10334.
3. C. Li, S. Tscheuschner, F. Paulus, P. E. Hopkinson, J. Kießling, A. Köhler, Y. Vaynzof and S. Huettner, *Adv. Mater.*, 2016, **28**, 2446-2454.
4. M. Bag, L. A. Renna, R. Y. Adhikari, S. Karak, F. Liu, P. M. Lahti, T. P. Russell, M. T. Tuominen and D. Venkataraman, *J. Am. Chem. Soc.*, 2015, **137**, 13130-13137.
5. I. Zarazua, J. Bisquert and G. Garcia-Belmonte, *J. Phys. Chem. Lett.*, 2016, **7**, 525-528.
6. R. Gottesman, L. Gouda, B. S. Kalanoor, E. Haltzi, S. Tirosh, E. Rosh-Hodesh, Y. Tischler, A. Zaban, C. Quarti, E. Mosconi and F. De Angelis, *J. Phys. Chem. Lett.*, 2015, **6**, 2332-2338.
7. W. Nie, J.-C. Blancon, A. J. Neukirch, K. Appavoo, H. Tsai, M. Chhowalla, M. A. Alam, M. Y. Sfeir, C. Katan, J. Even, S. Tretiak, J. J. Crochet, G. Gupta and A. D. Mohite, *Nat. Commun.*, 2016, **7**, 11574.
8. T. Leijtens, G. E. Eperon, S. Pathak, A. Abate, M. M. Lee and H. J. Snaith, *Nat. Commun.*, 2013, **4**, 2885-2885.
9. R. S. Sanchez and E. Mas-Marza, *Sol. Energy Mater. Sol. Cells*, 2016, **158, Part 2**, 189-194.
10. S. Wang, W. Yuan and Y. S. Meng, *ACS Appl. Mater. Interfaces*, 2015, **7**, 24791-24798.
11. A. Walsh, D. O. Scanlon, S. Chen, X. G. Gong and S.-H. Wei, *Angew. Chem. Int. Ed.*, 2015, **54**, 1791-1794.
12. B. C. O'Regan, P. R. F. Barnes, X. Li, C. Law, E. Palomares and J. M. Marin-Beloqui, *J. Am. Chem. Soc.*, 2015, **137**, 5087-5099.

8 Conclusions and outlook

8.1 Conclusions

This thesis has focused on the characterization of perovskite solar cells using a range of complimentary techniques, which included impedance spectroscopy, intensity modulated photovoltage/photocurrent spectroscopy and open-circuit voltage decay measurements. These techniques had previously been used extensively in the characterization of dye sensitized solar cells. Their application to perovskite solar cells has been shown to be very relevant, although crucially it has been demonstrated that the interpretation of the data needs to be quite different.

Previous characterization of perovskite solar cells had often been performed on cells based on a mesoporous TiO_2 scaffold. This presents problems when trying to assess which of the observed behaviours are due to the perovskite layer, and which can be attributed to the scaffold. The focus here was on planar heterojunction perovskite solar cells utilizing a compact TiO_2 layer as the electron selective contact and Spiro-OMeTAD as the hole transport layer. Cells with this particular architecture are well known for exhibiting a range of slow dynamic responses, most frequently observed as hysteresis in the J-V curve during efficiency measurements. The aim was to gain a better understanding of the underlying physical processes causing this behaviour.

Initial frequency domain measurements revealed a high frequency process that was related to recombination. Unlike in DSSC, transport processes are too fast for the frequency range used in impedance spectroscopy. There was no observed chemical capacitance, or photogenerated charge accumulation, within the device. The high frequency response related to recombination is therefore assigned to the discharge of the cells geometric capacitance (charge stored at contacts) via the recombination resistance. The lifetime for this process was on the order of 1 μs at the highest intensities (0.1 sun equivalent). This same process was observed in both impedance and IMVS measurements. It was also related to the fast initial decay of the photovoltage. This demonstrated that during the fast initial decay, the voltage decayed through the same series of photostationary states as were studied using the frequency domain measurements. This suggested that the process observed at high frequency or on short timescales was purely electronic in nature and was not influenced by the slow effects.

Over the course of these initial measurements it was also found that the device operation can be very sensitive to subtle changes in the manufacturing procedure. In a batch of supposedly identical cells, half exhibited ideality factors around m=2.6, with the other half having ideality factors around m=5.2. They exhibited similar 1 sun performance, but the cells with high ideality factor showed poor low light V_{oc}. This light dependent V_{oc} behaviour was also observed as either a persistent photovoltage (m=2.6) or fast complete decay (m=5.2) in OCVD measurements. This suggested a higher degree of shunting in the cells with poor low-light performance/fast voltage decay. As the cells were supposedly identical this highlights an important issue regarding device consistency, and particularly the need to test cells away from the standard testing conditions at 1 sun to be able to observe underlying losses which are obscured at high intensities.

The measurements were expanded to investigate the low frequency/slow time behaviour that is believed to be linked to hysteresis. The slow processes occur on timescales several orders of magnitude longer than the purely electronic response of the cell. Using temperature dependent measurements it was shown that the slow processes are linked to ionic movement within the perovskite layer. Activation energies around 0.5 eV were obtained from a range of measurements. This agrees closely with values calculated computationally for the migration of iodide vacancies[1, 2]. Activation energies for other vacancy defects are thought to be higher[2].

The low frequency response was shown to relate to the change in recombination rate as the ions move. It is important to stress that the low frequency time constants do not relate to recombination lifetimes, but to the rate at which the recombination rate is altered by the changing ionic environment. These time constants on the order of milliseconds and seconds, gave essentially the same activation energy, suggesting they are both linked to iodide vacancy migration. The exact reasoning behind the two different processes is unclear, but could possibly be due to short and long range migration effects on recombination, or migration along grain boundaries and through the bulk material.

The same process was also investigated in the time domain using large amplitude techniques under illumination and in the dark. The same fundamental process was observed in both situations, showing that at least the fundamental mechanism of ion

migration is not light induced. Other effects of illumination cannot be ruled out, but they appear to have a lesser impact on the measured electrical response of the cell.

Large amplitude open-circuit voltage rise and decay measurements were performed from well-defined equilibrium or steady state starting conditions. This makes interpretation of the observed effects much more straightforward. There is an observed fast response to illumination, followed by a much slower process. This slow process was investigated at different temperatures, and again revealed the same activation energy and time constants as the low frequency process in the frequency domain measurements.

Interpretation of both techniques led to the calculation of a vacancy defect concentration exceeding 10^{19} cm^{-3}. This was shown to be high enough to form ionic double layers at the interfaces which should be able to screen the built-in field of the device. Change in the Fermi-level splitting by either light (IMVS, light OCVD) or applied bias (EIS, dark OCVD) alters the electric field in the bulk which results in ionic redistribution to reach a new equilibrium condition. In turn the ionic redistribution will also impact on recombination and band offsets, giving a closely coupled ionic-electronic interaction. This is consistent with modelling predictions that require both moving ions and recombination at the interface to explain the observed J-V hysteresis[3, 4].

8.2 Outlook

The results presented in this thesis have helped to increase the understanding of both the electronic and ionic nature of perovskite solar cells. The techniques employed show great potential for use in a wide range of investigations.

Further investigation is needed into the relationship between ionic arrangement and recombination. It appears that interfacial properties are critical to controlling the operation of the device. Whilst the observed hysteresis effect does not necessarily imply poor steady state performance, it may present an indication that improvements are possible (potential for further reduction in recombination). In order to make the necessary materials modifications the underlying processes first need to be understood. To do this a range of other contact materials should first be studied.

The careful assessment of the low frequency behaviour could also be applied to studying device degradation. It is likely that ionic motion and the effects on interfaces will be linked to some of the main degradation pathways of the perovskite. The techniques used here are sensitive to subtle changes which might not necessarily be observed in less diagnostic testing, whilst also being directly relevant to the electrical performance of complete devices.

8.3 References

1. S. Meloni, T. Moehl, W. Tress, M. Franckevičius, M. Saliba, Y. H. Lee, P. Gao, M. K. Nazeeruddin, S. M. Zakeeruddin, U. Rothlisberger and M. Graetzel, *Nat. Commun.*, 2016, **7**, 10334.
2. C. Eames, J. M. Frost, P. R. F. Barnes, B. C. O/'Regan, A. Walsh and M. S. Islam, *Nat Commun*, 2015, **6**, 1-8.
3. S. van Reenen, M. Kemerink and H. J. Snaith, *J. Phys. Chem. Lett.*, 2015, **6**, 3808-3814.
4. G. Richardson, S. E. J. O'Kane, R. G. Niemann, T. A. Peltola, J. M. Foster, P. J. Cameron and A. B. Walker, *Energy Environ. Sci.*, 2016, **9**, 1476-1485.

Appendix A – Capacitance of a Perovskite Solar Cell

By Timo Peltola and Alison Walker

We have modelled the cell as a layer of perovskite absorber of thickness *d* between two selective metallic contacts. In the planar cells studied in this paper, these contacts represent the electron extracting contact at the interface between the TiO_2 and perovskite layers, and the hole extracting contact at the interface between the spiro and perovskite layers. The difference in work functions between the spiro and perovskite layers is the built-in electric potential difference, V_{bi}.

The magnitude of the external field across the perovskite layer is $F_{ext} = (V_{bi} - V_{oc})/d$ at the open circuit voltage, V_{oc} , since the external potential that at forward bias opposes V_{bi} is set equal to V_{oc}. We assume that free and trapped carrier concentrations are sufficiently small in the perovskite layer so that the field due to the free charges is much smaller than F_{ext}. The surface charge density per unit area on either of the contact layers arising from F_{ext} is

$$\sigma = \varepsilon_r \varepsilon_0 F_{ext} \qquad \text{(S1)}$$

where ε_r is the relative static dielectric constant and ε_0 is the vacuum permittivity.

At open circuit, the current density is zero so electron and hole quasi-Fermi levels have zero gradient at the electrodes. At most points in the device, charge recombination and generation approximately cancel, leading to zero electron and hole current density gradients from the continuity equations. Therefore, to give an analytical expression for the capacitance arising from the free charge within the perovskite layer, we set these current density gradients to zero at all positions in the device. The electron and hole density profiles $n(x)$, $p(x)$ respectively, where x is the distance from the TiO_2 contact, are determined from Maxwell-Boltzmann statistics:

$$n(x) = n(0)\exp\left\{-\frac{[E_C(x) - E_C(0)]}{k_B T}\right\}, p(x) = p(d)\exp\left\{\frac{[(E_V(x) - E_V(d)]}{k_B T}\right\}. \qquad \text{(S2)}$$

where q is the elementary charge, k_B is the Boltzmann constant, the conduction and valence bands are E_c, E_V respectively and d is the perovskite layer width. Here $n(0) = N_C \exp\{-[E_C(TiO_2) - E_{Fn}(TiO_2)]/(k_B T)\}$, $p(d) = N_V \exp\{-[E_C(\text{spiro}) - E_{Fn}(\text{spiro})]/(k_B T)\}$

With the assumption that the electric field in the device is F_{ext},

$$E_C(x) = E_C(0) + q\frac{(V_{bi}-V_{oc})x}{d}\ ,\ E_V(x) = E_V(d) - q\frac{(V_{bi}-V_{oc})x}{d}. \qquad \text{(S3)}$$

The total free electron and hole charge per unit area in the perovskite layer is then Q_n, Q_p respectively where

$$Q_n = q\int_0^d n\,\mathrm{d}x = qn(0)\int_0^d \exp\left\{-\frac{q(V_{bi}-V_{oc})x}{k_BTd}\right\}\mathrm{d}x = \frac{n(0)k_BTd}{(V_{bi}-V_{oc})}\left(1-e^{-\frac{q(V_{bi}-V_{oc})}{k_BT}}\right) \qquad \text{(S4)}$$

$$Q_p = q\int_0^d p\,\mathrm{d}x = qp(d)\int_0^d \exp\left\{-\frac{q(V_{bi}-V_{oc})x}{k_BTd}\right\}\mathrm{d}x = \frac{p(d)k_BTd}{(V_{bi}-V_{oc})}\left(1-e^{-\frac{q(V_{bi}-V_{oc})}{k_BT}}\right) \qquad \text{(S5)}$$

Figure S0-1 compares Q_n and Q_p with σ and shows that Q_n and Q_p are much less than the surface charge arising from the externally imposed field, σ. This result is consistent with the assumption that the space charge from the free charge present within the perovskite layer is small compared to the surface charge density at either contact. The device is neutral and so the difference between Q_n and Q_p is compensated for by extra charge that appears at the TiO_2/perovskite and perovskite/spiro interfaces.

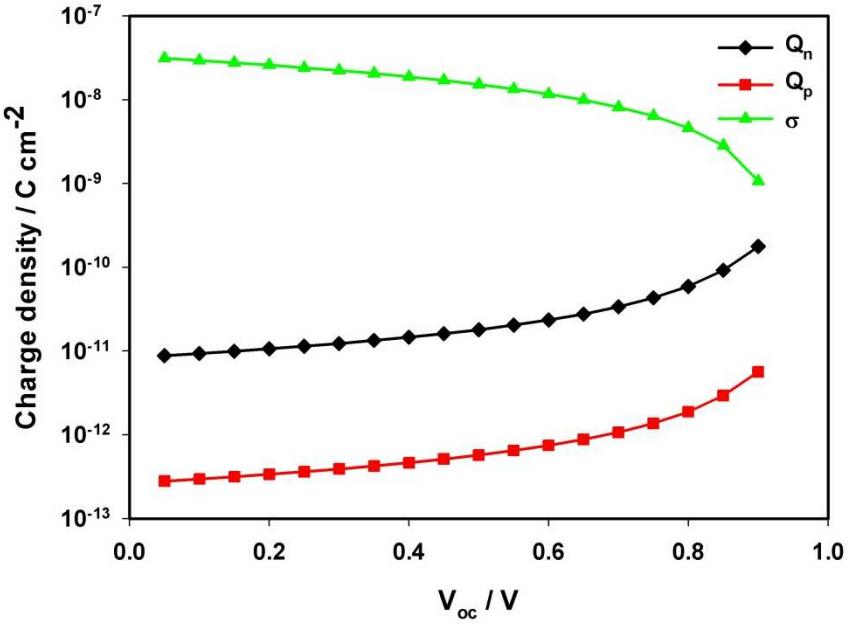

Figure S0-1: Charge density per cm^{-2} across the perovskite layer due to conduction band electrons, Q_n (diamonds), and holes, Q_p (squares), compared to the surface charge density, σ (triangles), at either of the junctions of the perovskite layer with the TiO_2 and spiro layers.

A self-consistent solution of the Poisson equation and continuity equations for the charge density in the device is required to determine the contribution to the device capacitance to the overall capacitance of the cell. Without doing such a calculation, we can estimate the capacitance contribution C_μ arising from changes in Q_n with respect to changes in V_{oc} This contribution is analogous to the chemical capacitance, the capacitance per unit area associated with charge accumulation in a layer [3]. The contribution from Q_n is determined from equation (S4) as

$$C_\mu = \frac{\partial Q_n}{\partial V_{oc}} = \frac{k_B T d n(0)}{(V_{bi}-V_{oc})^2}\left\{ e^{-\frac{q(V_{bi}-V_{oc})}{k_B T}}\left(1+\frac{q(V_{bi}-V_{oc})}{k_B T}\right)-1\right\} \qquad \text{(S6)}$$

This result is only an estimate since the contribution from equation S6, the contribution from Q_p is $C_\mu p(d)/n(0)$ and is not equal to C_μ because it ignores the extra charge needed to neutralise the device referred to above.

As noted in the main text, the geometric capacitance is C_{geo} = 5 nF, or 35nFcm^{-2}. Figure S0-2 shows that even for open circuit voltages close to V_{bi}, C_{geo} exceeds C_μ by more than an order of magnitude. This figure explains the observations that on fitting a simple R_{ser}, R_{rec}, C_{total} equivalent circuit model to the IMVS results that C_{total} took values between 20 and 32 nF for a 0.15cm^2 device that are close to C_{geo}, validating our model. This similarity between C_{geo} and C_{total} also demonstrates that the predicted value of ε_r is a good estimate and that the cell roughness factor is ~3.7. In addition, trapped charge will increase C_{total} showing that our neglect of trapped charge is reasonable.

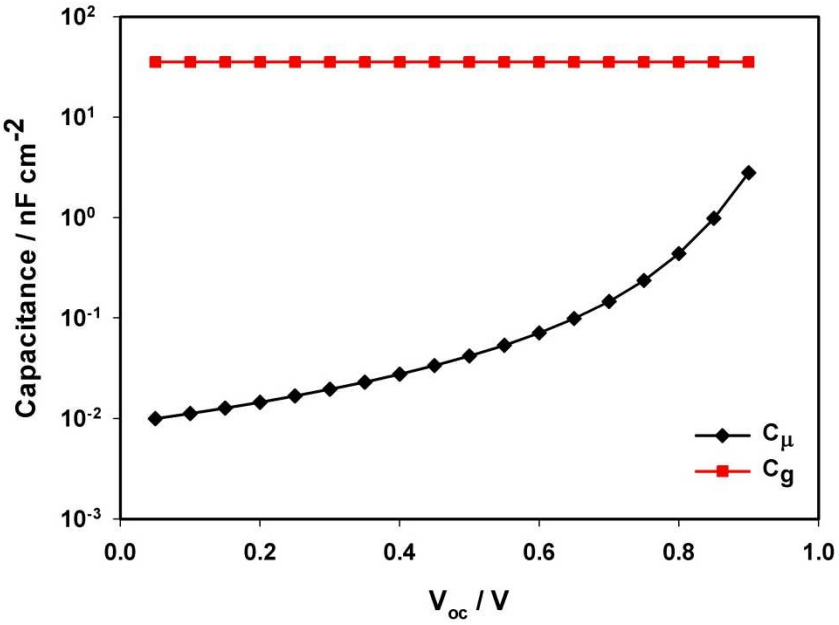

Figure S0-2: Chemical capacitance per unit area, C_μ/A (diamonds), where A is the cell area, arising from Q_n and Q_p, compared to the geometric capacitance per area, C_g/A (squares) due to the surface charge density, σ.

Parameter values

$\varepsilon_r = 24.1$, $d = 600$ nm, $V_{bi} = 0.93$ V [1,2] $E_C(TiO_2)$= -3.75 eV [1] $E_{Fn}(TiO_2)$= -4.07 eV E_V(spiro)= -5.4 eV [2], E_{Fp}(spiro)= -5.0 eV

The perovskite conduction band density of states used was 8.1 x 10^{24} m^{-3} and the valence band density of states was 5.8 x10^{24} m^{-3}. The values are based on the effective masses calculated in references 11 and are derived using a simple free electron gas model. The calculations of the geometric and chemical capacitances were carried out to support the experimental data that showed the dominance of the geometric capacitance.

References

[1] R Lindblad, D Bi, B-W Park, J Oscarsson, M Gorgoi, H Siegbahn. M Odelius, E M J Johansson, H Rensmo J Phys Chem Letts**5** 645 (2014)

[2] P Schulz, E Edri, S Kirmayer, G Hodes, D Cahen, A Kahn Energy Environ Sci **7**, 1377 (2014)

[3] J. Bisquert, Phys ChemChemPhys, **5**, 5360 (2003)

Appendix B – Derivation of carrier lifetime for limiting recombination cases

By Laurie Peter

Open circuit voltage

The open circuit voltage corresponds to the splitting of the quasi Fermi levels for electrons and holes in the device. In the dark, the equilibrium electron and hole concentrations are determined by the Fermi level, E_F.

$$n_0 = N_c e^{-\left[\frac{(E_c - E_F)}{k_B T}\right]} \qquad p_0 = N_v e^{\left[\frac{(E_v - E_F)}{k_b T}\right]} \qquad n_0 p_0 = N_C N_v e^{-\left(\frac{E_g}{k_B T}\right)} \tag{1}$$

Under illumination, the concentration of holes and electrons increases to $n = n_0 + \Delta n$ and $p = p_0 + \Delta p$. n and p are related to the corresponding quasi Fermi levels, and Δn and Δp are the excess electron and hole concentrations.

$$n = N_c e^{-\left[\frac{\left(E_c - {}_n E_F\right)}{k_B T}\right]} \qquad p = N_v e^{\left[\frac{\left(E_v - {}_p E_F\right)}{k_B T}\right]} \tag{2}$$

From 1 and 2, noting that $\Delta n = \Delta p$.

$${}_n E_F - {}_p E_F = q V_{oc} = k_B T \ln\left(\frac{np}{n_0 p_0}\right) = k_B T \ln\left(\frac{\left(n_0 + \Delta n\right)\left(p_0 + \Delta p\right)}{n_0 p_0}\right) = k_B T \ln\left(\frac{\Delta n^2 + \left(n_0 + p_0\right)\Delta n + n_0 p_0}{n_0 p_0}\right) \tag{3}$$

Limiting cases

In the low or undoped case, case where $\Delta n = \Delta p$ is larger than both n_0 and p_0, equation 3 becomes

$$V_{oc} \approx \frac{k_B T}{q} \ln\left(\frac{\Delta n^2}{n_0 p_0}\right) \tag{4}$$

In the doped low intensity case where $\Delta n = \Delta p$ is smaller than the majority carrier density, equation 3 becomes (for p-type as an example, where $p_0 > n_0$, Δn)

$$V_{oc} = \frac{k_B T}{q} \ln\left(\frac{p_0 \Delta n}{n_0 p_0}\right) = \frac{k_B T}{q} \ln\frac{\Delta n}{n_0} \tag{5}$$

Bimolecular electron-hole recombination kinetics

The rate equation for electron hole recombination is (noting again that $\Delta n = \Delta p$)

$$\frac{d\Delta n}{dt} = \frac{d\Delta p}{dt} = -k\left(np - n_0 p_0\right) = -k\left[\left(n_0 + \Delta n\right)\left(p_0 + \Delta n\right) - n_0 p_0\right] = -k\left[\Delta n^2 + \left(n_0 + p_0\right)\Delta n\right] \tag{6}$$

Limiting cases

For the low doped or intrinsic case where $\Delta n > n_0, p_0$

$$\frac{d\Delta n}{dt} \approx -k\Delta n^2 \tag{7}$$

For the doped case where$\Delta n = \Delta p < p_0$ (p-type example) the rate equation becomes pseudo 1st order

$$\frac{d\Delta n}{dt} \approx -kp_0\Delta n = -k'\Delta n \tag{8}$$

We define the recombination rate as

$$R = \frac{d\Delta n}{dt} = \frac{d\Delta p}{dt} \tag{9}$$

The recombination lifetime is then defined as

$$\tau^{-1} = \frac{d}{d\Delta n}\frac{d\Delta n}{dt} = \frac{d}{d\Delta p}\frac{d\Delta p}{dt} = \frac{dR}{d\Delta n} = \frac{dR}{d\Delta p} \tag{10}$$

Deriving the lifetime to the photovoltage decay

We assume that the system decays through a series of quasi-stationary states. Consider first the bimolecular case where the excess carrier densities are higher than the doping concentration. V_{oc} is then given by equation 4. Taking the derivative of equation 4 with respect to time

$$\frac{dV_{oc}}{dt} = \frac{k_BT}{q}\frac{d}{dt}\ln\left(\frac{\Delta n^2}{n_0p_0}\right) = \frac{k_BT}{q}\frac{n_0p_0}{\Delta n^2}\frac{2\Delta n}{n_0p_0}\frac{d\Delta n}{dt} = \frac{2}{\Delta n}\frac{k_BT}{q}\frac{d\Delta n}{dt} = -\frac{2}{\Delta n}\frac{k_BT}{q}R \tag{11}$$

Differentiating equation 11with respect to time

$$\frac{d^2V_{oc}}{dt^2} = -\frac{2k_BT}{q}\frac{d}{dt}\left(\frac{R}{\Delta n}\right) = -\frac{2k_BT}{q}\frac{d}{d\Delta n}\left(\frac{R}{\Delta n}\right)\frac{d\Delta n}{dt} = \frac{2k_BT}{q}R\frac{d}{d\Delta n}\left(\frac{R}{\Delta n}\right) = \frac{2k_BT}{q}R\left(-\frac{R}{\Delta n^2} + \frac{1}{\Delta n}\frac{dR}{d\Delta n}\right) \tag{12}$$

Substituting equation 11 into equation 12 and rearranging to find the inverse of the recombination lifetime defined by equation 10, we obtain

$$\tau^{-1} = \frac{dR}{d\Delta n} = -\left(\frac{dV_{oc}}{dt}\right)^{-1}\frac{d^2V}{dt^2} - \frac{q}{2k_BT}\frac{dV_{oc}}{dt} \tag{13}$$

Appendix C – Publications

1. A. Pockett, G. E. Eperon, T. Peltola, H. J. Snaith, A. Walker, L. M. Peter and P. J. Cameron, *"Characterization of Planar Lead Halide Perovskite Solar Cells by Impedance Spectroscopy, Open-Circuit Photovoltage Decay, and Intensity-Modulated Photovoltage/Photocurrent Spectroscopy"*, J. Phys. Chem. C, 2015, 119, 3456-3465.

2. A. Pockett, G. E. Eperon, N. Sakai, H. J. Snaith, L. M. Peter and P. J. Cameron, "Microseconds, milliseconds and seconds: deconvoluting the dynamic behaviour of planar perovskite solar cells", Phys. Chem. Chem. Phys., 2017.